Title

Development of Photodegradable Polymer Networks: Cellular Applications and Mathematical Models.

Author

Norris, Sam Carsten-Puisis

Publication Date

2019

UNIVERSITY OF CALIFORNIA
Los Angeles

Development of Photodegradable Polymer Networks: Cellular Applications and Mathematical Models.

A dissertation submitted in partial satisfaction
of the requirements for the degree
Doctor of Philosophy in Bioengineering

by

Sam Carsten-Puisis Norris

2019

ABSTRACT OF THE DISSERTATION

Development of Photodegradable Polymer Networks: Cellular Applications and Mathematical Models.

by

Sam Carsten-Puisis Norris
Doctor of Philosophy in Bioengineering
University of California, Los Angeles, 2019
Professor Andrea Marie Kasko, Chair

The field of cell and tissue engineering is far from being systematic. Historically, the field follows a guess-and-test methodology; new materials are produced and tested in search of the "right" combination of material properties, chemical/growth factor concentrations, reactor conditions, etc. While developmental biologists have extensively studied signaling factors, gene expression and other components governing early tissue development, researchers still do not have a full picture of how these signaling cascades are initiated or how spatial and temporal tissue inhomogeneities initially form. To address this issue, new materials must be developed that can mimic the intricacies of native tissue in order to correctly study their behavior. Hydrogels incorporating controlled photodegradation are a novel class of polymeric biomaterials that our group at UCLA has developed. The outstanding benefit of these materials is that their physical and chemical properties can be altered on-demand, in real-time without the presence of toxic compounds, allowing cells to be present during modification. In addition, the degradation, and thus the mechanical properties, is a strict function of the exposure of light (exposure time, wavelength, and intensity) such that the precise spatial and temporal control of the degree of degradation far surpasses that of hydrolytic and enzymatic degradation mechanisms. In this dissertation, I develop new photodegradable materials, find solutions to better characterize their behavior, and expand the techniques necessary for their successful use in cell biology. First, by developing a series of mass-action and kinetic mathematical models, I examine the physical properties of photodegradable gels formed by end-linking gelation. I pay special attention to how diffusion of photoabsorbing byproducts affect degradation. These models are further enhanced by examining the specific microstructure and micro-heterogeniety of the gels formed. Second, I expand the photodegradable materials library. In order to better mimic three-dimensional cellular environments, I successfully synthesize photodegradable protein-based gels and showcase their applicability towards three-dimensional cell culture. I specifically fabricate photodegradable gelatin gels, however, the techniques I develop here more generally aid in the conjugation of hydrophobic moieties to protein materials. Next, I synthesize and fabricate photodegradable polyacrylamide gels. I utilize the flexibility of the polyacrylamide gel system by exploring cell response to both changes in cell binding domain and dynamic softening of the underlying matrix. Finally, I develop the application of maskless photolithography for photodegradable hydrogels. Using this technique, I rapidly pattern grayscale stiffness patterns into photodegradable hydrogels in a highly controlled fashion with sub-micron resolutions. Cell response to complex patterns of grayscale stiffness are tested. Through the developments made in this dissertation, I expand our ability to test cell behavior in spatially and temporally heterogeneous environments.

The dissertation of Sam Carsten-Puisis Norris is approved.

Amy Catherine Rowat

Song Li

Tom Chou

Andrea Marie Kasko, Committee Chair

University of California, Los Angeles

2019

To Mom and Dad

TABLE OF CONTENTS

LIST OF FIGURES

LIST OF TABLES

ACKNOWLEDGMENTS

The long and winding road that brought me to and through this wonderful journey, has been filled with a collection of wonderful people.

To my parents. Never once did they make me feel like the life I was choosing was a bad idea. They let me explore, while always making sure that I could count on them. Thank you for teaching me how to build. Thank you for buying me all those tools and welding equipment even though I never used them all that much. Thank you for taking me dumpster diving. With no one do I share the same level of curiosity about the world. Thanks for letting me forget your birthdays and not getting upset.

To Jim Koutsoures, my highschool manufacturing and welding teacher. Thank you for teaching me the skills that I've built my professional life around (he even to me my first job!). I basically lived in his classroom, built many strange things, drove him a bit crazy, but I always knew I could go to him.

Thank you to Amanda! Her love, support, companionship, willingness to deal with my uncertainties and my inability to plan anything during my PhD, were more important to the completion of this dissertation than any experiment, result, paper, or fellowship. Thank you, thank you, thank you.

It's still amazing to me that from our first interaction – a long distance telephone call – my mentor Andrea Kasko and I instantly and simultaneously wanted to pursue the same research goal, which would become this thesis. I am very grateful for that. I am very grateful that no matter the circumstances, and no matter our disagreements, Andrea always made it clear that she had my back. She was always putting myself and her students before herself.

To Samantha Anderson and Stephanie Delgado. These fine scientists would join me from the beginning, all entering KaskoLab at the same time, all new to a strange city. It was a camaraderie of constant support, laughs, frustrations, excursions, food, and lab shenanigans. These are two faces that no matter my mood could always make me smile in the morning. These are friendships that will never go away.

To Darice Wong and Stephanie Deshayes. These goofy and endlessly enjoyable post-docs taught me everything about academic life, scientific methodology, and pushing me to enjoy life!

To my collaborators Maria D'Orsogna, Jennifer Soto, and Peter Tseng. Thank you for helping me to explore topics I would not have otherwise.

To all my lab members over the years: Ken, Walter, Changying, Thanmayi, Alireza, Shadi, Rodrigo, Manuel, Elli, Brianna, Yu, Patrick, and Brooke. We were all a bit crazy, all in our own way.

To the countless undergraduate students who put up with me. Thanks to those who worked most directly with me: Justin, Tianna, Rogerio, Victoria, and Ruth. You definitely taught me more than I was able to teach you.

To my Bioengineering cohort. The department was not in a good place when we entered. Now it is. That's on us.

To my committee who offered constant support and excitement for my research. To Amy Rowat for the enumerable chats and tangents, all things biophysics. To Tom Chou for always very colorfully entertaining my mathematical inquiries and guiding me through a field unknown to me. To Song Li for his curiosity, and willingness to take risks on projects we really weren't sure about.

Thank you to the National Institutes of Health for granting me my predoctoral fellowship. The freedom it gave me to explore topics and career paths, I would not have otherwise, was unspeakably valuable.

Several chapters of this dissertation contain material from published work with permission:

Figures of Chapter 1 are adapted from:
Thesleff, Tooth organogenesis and regeneration. StemBook, 1–12 (2008).
and
D. T. Butcher, T. Alliston, V. M. Weaver, A tense situation: forcing tumour progression. *Nat. Rev. Cancer.* 9, 108–122 (2009).

Chapter 2 is adapted from Norris, S. C. P. Norris, T. Chou, A. M. Kasko, Diffusion of Photoabsorbing Degradation Byproducts in Photodegradable Polymer Networks. *Macromol. Theory Simulations.* 26, 1700007 (2017).

Chapter 3 is adapted from S. C. P. Norris, A. M. Kasko, T. Chou, M. R. D'Orsogna, Heterogeneity of polymer network micro-regions as formed by end-linking processes, 1–34 (2019).August, 1–34. http://arxiv.org/abs/1908.02957.

Chapter 4 is adapted from Norris, S. C. P. Norris, S. M. Delgado, A. M. Kasko, Mechanically robust photodegradable gelatin hydrogels for 3D cell culture and in situ mechanical modification. *Polym. Chem.* 10, 3180–3193 (2019).

Chapter 6 is adapted from Norris, S. C. P. Norris, P. Tseng, A. M. Kasko, Direct Gradient Photolithography of Photodegradable Hydrogels with Patterned Stiffness Control with Submicrometer Resolution. *ACS Biomater. Sci. Eng.* 2, 1309–1318 (2016).

This work was funded by the National Institutes of Health through the NIH Director's New Innovator Award Program, 1-DP2-OD008533. I gratefully acknowledge support from a Ruth L. Kirschstein Predoctoral Fellowship (NIH - F31DE026356).

VITA

2009	B.S., Materials Science and Engineering University of Illinois Urbana-Champaign
2019	Ph.D., Bioengineering (expected) University of California, Los Angeles, Los Angeles, California

PUBLICATIONS

S. C. P. Norris, A. M. Kasko, T. Chou, M. R. D'Orsogna, Heterogeneity of polymer network micro-regions as formed by end-linking processes, 1–34 (2019).August, 1–34. http://arxiv.org/abs/1908.02957.

S. C. P. Norris, S. M. Delgado, A. M. Kasko, Mechanically robust photodegradable gelatin hydrogels for 3D cell culture and in situ mechanical modification. *Polym. Chem.* 10, 3180–3193 (2019).

S. C. P. Norris, T. Chou, A. M. Kasko, Diffusion of Photoabsorbing Degradation Byproducts in Photodegradable Polymer Networks. *Macromol. Theory Simulations.* 26, 1700007 (2017).

S. C. P. Norris, P. Tseng, A. M. Kasko, Direct Gradient Photolithography of Photodegradable Hydrogels with Patterned Stiffness Control with Submicrometer Resolution. *ACS Biomater. Sci. Eng.* 2, 1309–1318 (2016).

J. Yi, A. J. Radosevich, J. D. Rogers, **S. C. P. Norris**, İ. R. Çapoğlu, A. Taflove, V. Backman, Can OCT be sensitive to nanoscale structural alterations in biological tissue? *Opt. Express.* 21, 9043–59 (2013).

J. Trnka, P. Stoklasová, **S. C. P. Norris**, Detection of Suspicious Mass on Structures by Acoustical Waves. *Exp. Tech.* 36, 14–21 (2012).

S. C. P. Norris, J. Humpolickova, E. Amler, M. Huranova, M. Buzgo, R. Machan,

D. Lukas, M. Hof, Raster image correlation spectroscopy as a novel tool to study interactions of macromolecules with nanofiber scaffolds. *Acta Biomater.* 7, 4195–203 (2011).

CHAPTER 1

Introduction

1.1 Physical changes of tissues in time and space.

It is the aim and challenge of cell biologists and tissue engineers to understand the fundamental principles by which native tissue structures are formed. By mimicking the native environment, through a combination of cell-supporting scaffolds and growth factors, researchers hope to deconstruct the mechanisms of tissue formation. It has long been known that cell behavior is influenced by the surrounding physical environment [1]. As an example, extra cellular matrix (ECM) stiffness has played a vital role in stem cell differentiation, where stiffer substrates promoted the differentiation of stiffer cell lineages [2, 3]. Tissue structures, however, are highly complex and often composed of many different types of cells that can exhibit varying cell phenotypes with precise spatial positions. Cells organize in both time and space to dynamically form interfaces and boundaries in both structure and function [4]. Spatially, changes in tissue physical properties can occur at subcellular lengthscales [5]; temporally, tissue remodeling and physical changes can occur on timescales shorter than the life of a single cell (on the order of a single day) [6, 7].

For example, the role of the dynamic and heterogenous physical properties of the ECM in cancer research has garnered significant attention. Tumors remodel the ECM around them, which is well associated to malignancy and enhanced cell proliferation [8] as well as increased deposition, linearization, and thickening of interstitial collagen [9]. The microenvironment of breast cancer tumors tissues and tumor-adjacent stroma are between 5-20 times stiffer than normal mammary gland tissue [10]. Traction stresses are also significantly higher in cancer cell lines than their non-metastatic counterparts [11], indicating that cancerous cells "feel" their surrounding environment to a greater extent. These cellular forces are transmitted through molecular complexes and actin filaments that eventually reach the nucleus [12], altering transcription and cell fate [2]. As such, it is well known that changes in nuclear shape are a hallmark process of tumorigenesis [13]. Yet, still to be identified are the molecular mechanisms of how force and the physical environment dictate cell fate [14]. In vitro, ECM stiffness has been shown to dictate tumor progression and metastatic potential [10, 15, 16]. Development of breast cancer is strongly correlated with tissue stiffening, where the tumor stiffness increases during cancer progression (Figure 1.1) [17]. In this context, the native tumor environment is neither mechanically static nor homogeneous. However, in vitro studies correlating matrix stiffness to malignancy have relied on ECMs whose mechanical properties cannot be controlled in time nor space [10, 15, 16]. Recent studies have indicated that the mechanical history of the underlying substrate [18, 19, 20] has a significant impact on cell fate. Thus, researchers have become interested in how time-dependent stiffness changes of the surrounding ECM affect tumor development.

As another example, tissue interfaces, such as the alveolar bone to periodontal ligament to tooth transition, are highly anisotropic in structure, composition, and function. Teeth contain gradients in composition and mineral density, which give rise to gradients in the material stiffness [21]. In the articular surfaces of the mandibular condyle, chondrocytes progressively calcify the interterritorial matrix as they approach the stiffer ossification zone, eventually forming mineralized bone. Even within cartilage tissue, chondrocytes spatially transition from a rounded to flat morphology, and the collagen produced transitions from type II to type I, respectively [22].

In the case of dental and craniofacial structures, mesenchymal stem cells (MSCs) have been of interest to researchers due to their multipotent nature. During tooth development, neural crest-derived MSCs have the ability to differentiate into multiple cell types as a function of time and spatial position. In particular, during the bud and subsequent cap stages, MSCs spatially differentiate into odontoblasts that form the tooth pulp and dentin, as well as the dental follice that form the periodontal and cementum tissues (Figure 1.2) [23]. Such MSCs also differentiate into non-dental lineages including osteoblasts and chon-

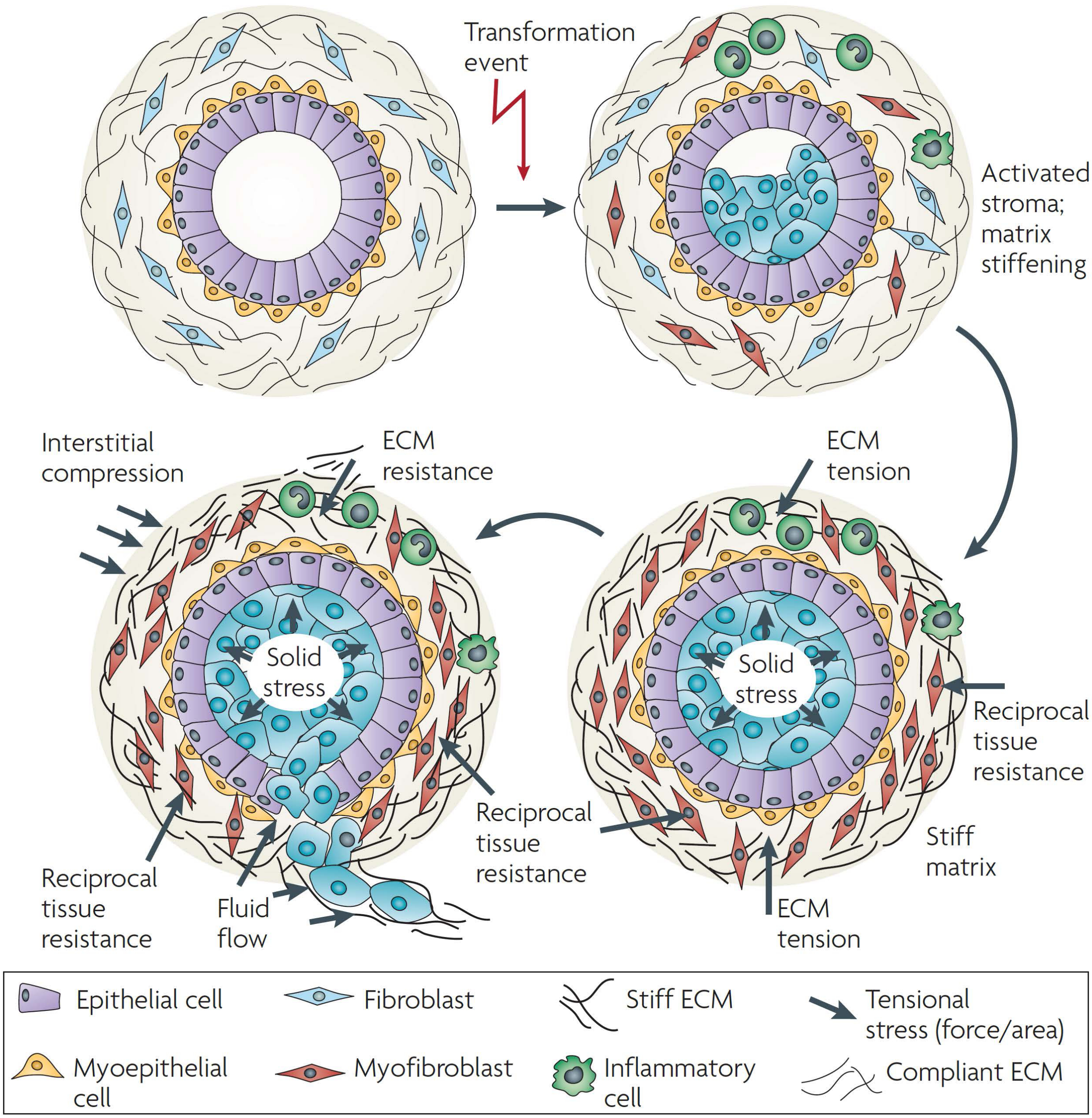

Figure 1.1: **Mechanically active cancerous tissues.**

In adult tissues, significant dynamic changes to the tissue physical properties can occur. One such example is the development of breast cancers. Within the mammary gland, proliferation of luminal epithelial cells is triggered by a transformation event, leading to abnormal pre-neoplastic luminal mammary epithelial cells. Immune cells are stimulated and fibroblasts are activated in the breast stroma which leads to changes in the ECM composition and mechanical properties. Due to genetic modifications and in response to these mechanical changes to the ECM, luminal epithelial cells invade the breast parenchyma. Reproduced, with permission, from Macmillan Publishers Limited. Copyright: (2009) [17].

drocytes, which form bone and cartilage, respectively [24]. This simple spatial segregation of cell types gives rise to the complex structure and the building blocks required to create both a functional tooth and entire orofacial structures [25]. Consequently, MSCs have become an essential cell type to study tissue regeneration. Understanding how MSCs spatially differentiate based on their surrounding environment and how this spatial differentiation affects the formation of tissue interfaces are important problems.

1.2 Exploiting photodegradation

The barrier to understanding how these tissue anisotropies form — for instance tissue polarity, cell orientation, and cell differentiation as a function of time and spatial position — is largely due to lack of proper materials that can reconstitute such complex environments. Ideally, an artificial material should be able to mimic the biophysical and biochemical microenvironment of native tissues, including spatial and temporal control over material properties. To date, research to relate physical microenvironments to cellular response has been largely limited to un-patterned, homogeneous materials in small numbers. Some strategies to microengineer hydrogels [26], incorporate bioresponsive functionalities [27], and integrate metalloproteinase-sensitive structural elements [28] into hydrogel materials have been successful. However, investigators have been largely unable to successfully probe cell behavior in mechanically heterogeneous environments that properly mimic native tissue. For these reasons, researchers have sought to produce novel classes of advanced materials to produce a cell-supporting scaffolds that can achieve spatial and temporal heterogeneity [29].

In order to overcome the inability to modulate the cellular microenvironment as an on-demand process, researchers looked to incorporate photocleavable moieties into the backbone of hydrated polymeric networks. The photoactive *ortho*-nitrobenzyl (*o*-NB) group became an optimal choice as a photocleavable, bi-functional linker due to its high yield photocleavage, relatively simple synthesis, and an absorbance spectrum that was well suited for live cell applications [30]. The unimolecular photocleavage event requires no additional components to proceed, and thus follows first-order rate kinetics. The photodegradable *o*-NB

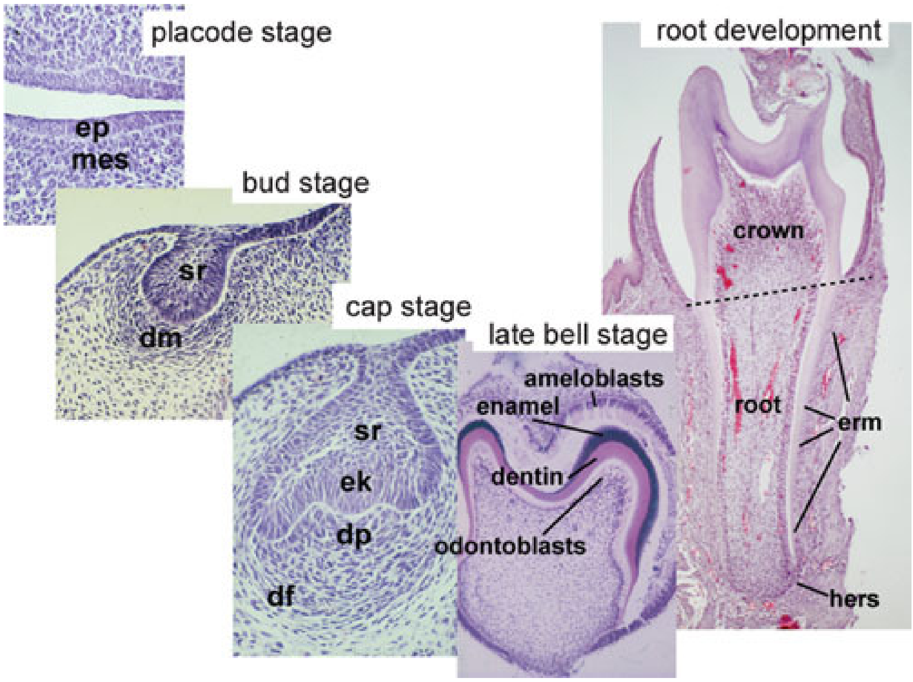

Figure 1.2: **Progressive development of a functional tooth.**
In both time and space, cells organize, forming distinct layers and gradients of cell type and function to form a functional tissue. In early stages of tooth development simple interactions between the epithelium (ep) and the neural crest derived mesenchyme (mes) give rise to a cascade of signalling events. The epithelium segregates into basal cells along the basement membrane and stellate reticulum (sr), the layers of which eventually form the stem cell niche of the epithelium. The dental mesenchyme (dm) splits into the dental papilla (dp), which gives rise to tooth pulp and odontoblasts (dentin formation), and the dental follicle (df) which form into cementoblasts and periodontal tissue. Through these seemingly simple interfaces and changes, the shape of the tooth starts to become apparent. Cells at the epithelial-mesenchymal interface differentiate and secrete mineralizing matrices. Enamel knot (ek), epithelial cell rests of malassez (erm), hertwig's epithelial root sheath (hers). Reproduced, with permission, under the Creative Commons Attribution. Copyright: (2008) Irma Thesleff and Mark Tummers [23].

functionality first found widespread use as a photocleavable protecting group for solid-phase peptide synthesis. Photoremovable *ortho*-nitrobenzyl protecting groups could be conjugated to protect primary amines, carboxyl groups, among a variety of other functional groups [31, 30, 32]. Upon photoirradiation, the protecting group would cleave via a photoinduced intramolecular hydrogen abstraction, releasing the 2-nitrosobenzaldehyde/ketone group and the deprotected functional group, allowing for an additional degree of orthogonality in peptide synthesis. Photocleavable *o*-NB groups have also been used in polymeric applications as a method to photorelease polymeric thin films [33], as positive-type photoresists for microfabrication [34], and as photocleavable linkages in polymer networks [35]. While early use of *o*-NB groups focused on organic chemistry and polymer applications, these photodegradable *o*-NB groups eventually found applications in biomedical fields. Photocleavage of *o*-NB groups has found use in uncaging of fluorophores in the presence of cells [36] and as a sulphydryl protecting group in order to pattern biochemical cues to guide axonal growth in-situ [37].

Looking to utlize the *o*-NB group as a photodegradable linkage within the physical structure of hydrogels, Kloxin, Kasko, et al. incorporated 2-methoxy-5-nitro-4- (1-hydroxyethyl) phenoxybutanoate *o*-NB linker into the backbone poly(ethylene glycol) (PEG) diacrylate macromers (see Figure 1.3) [38]. These macromers, capable of being polymerized by free radical polymerization into polymer network structures, allowed for precise, on-demand material stiffness control. As shown in Figure 1.3, upon illumination with light, cleavage of the *ortho*-nitrobenzyl group occurs, the elastically effective intact network strands break, and the modulus of the gel decreases. To their benefit, *o*-NB moieties can be cleaved at long-wave UV or short-wave visible light. Most commonly, researchers have used the I-line (365 nm) or the H-line (405 nm) of a mercury arc lamp to degrade the *o*-NB linkages. Subsequently, Griffin and Kasko expanded the library of photodegradable hydrogels, taking advantage of different photochemical properties of different *o*-NB moieties to produce different mechanical responses [39]. The outstanding benefit of these materials is that cells can be present not only during fabrication (as is the case with traditional PEG-diacrylate gels), but also during modification via photodegradation. The wavelengths, irradiation intensities, and

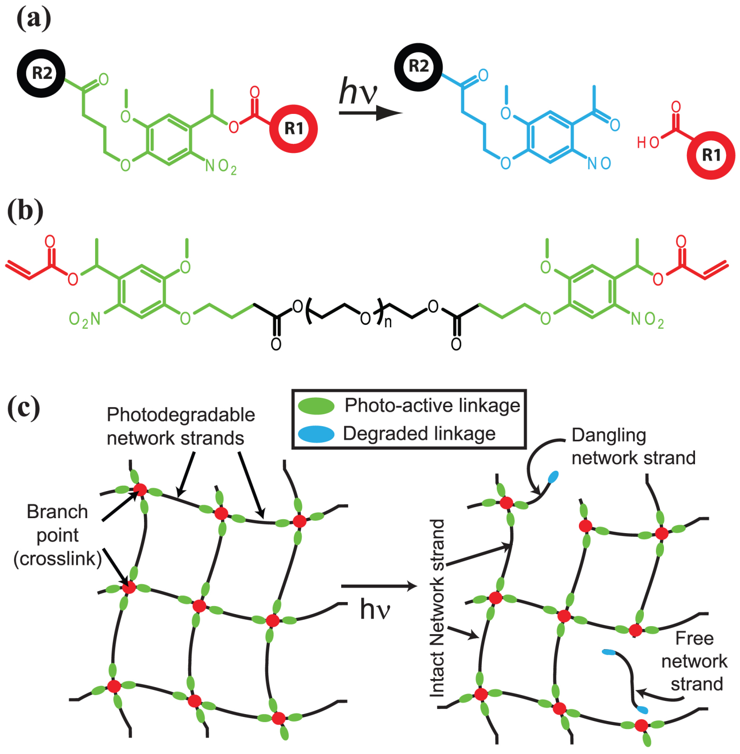

Figure 1.3: **Network structure of photodegradable gels.**
a) Photodegradation of an example *o*-NB molecule: the 4-(4-(1- hydroxyethyl)-2- methoxy-5-nitrophenoxy) butanoic acid chemistry. b) Incorporation of the *o*-NB linkages into the backbone of poly(ethylene glycol) diacrylate macromer to form a photodegradable crosslinking macromer. c) End linking of the photodegradable crosslinking macromer forms a network that can be subsequently degraded. Crosslinks (red dots) are connected to one another by polymeric network strands (black lines) with photodegradable end-groups (green ovals). Exposure to light degrades the photoactive linkages (blue ovals). The photodegradable network strands are left in one of the three states: 1) intact; 2) dangling; or 3) free.

times of degradation used have been shown to be cell compatible [40, 41]. The degradation, and therefore the material stiffness, is a strict function of the exposure to light (exposure time and intensity) [42]. As such, spatial and temporal control of the material stiffness is achieved. This process is far more precise than related mechanisms, such as hydrolysis and enzymolysis. While early reviews on photodegradable polymers have been written [43], a comprehensive look at hydrogels whose structure can be disassembled using light has yet to be fully explored. In this chapter, we explore the applications, novel techniques, exploration of cell behavior, and future perspectives of photodegradable hydrogels.

1.3 Achieving spatial and temporal complexity within photodegradable hydrogels

Since their conception by the lab of Kristi Anseth [38], the use and creation of photodegradable hydrogels has since expanded. As mentioned, one of the greatest advantages to photo-sensitive gels is that the spatial position and time of light exposure is highly controllable. Light can be projected on a two-dimensional surface, or concentrated to a very small volume in three-dimensions with high precision in both time and space. Photolithographic techniques, long utilized in the microfabrication and wafer processing industries, are uniquely applicable to photodegradable hydrogels, where the hydrated polymer networks can be essentially classified as positive photoresists that degrade upon exposure. In the case of photodegradable hydrogels, gels can be patterned to create topological features, or simply softened with light. Both features have found use in cell biology. To mathematically model the degradation process, a combination of polymer physics principles, the Beer-Lambert law, and first order rate kinetics have been applied to model the photodegradation of these gels [42]. Photodegradable hydrogels are unique from other degradable gel types in that the photodegradable moiety absorbs light, thus, light is attenuated along the light path, leading to a differential in the degradation rate along the path of light.

The most simple way to pattern photodegradable hydrogels is through the use of a photomask where geometric patterns block light in some regions and lets it pass in others. As mentioned, the production of low-cost, high quality, precision photomasks, and the tools to "print" using 365 nm light, has been well already established by the photolithography community. Many of the technological advances in the photolithography field are directly applicable to photodegradable hydrogels. Using the combination of photomasks and photodegradable gels, material modulus can be patterned as a function of time and space [38, 44, 45]. More recently, researchers have used photodegradable hydrogels in combination with and polydimethylsiloxane (PDMS) microfluidic devices. Photodegradable PEG hydrogel features within a microfluidic device can be polymerized and subsequently sculpted by photodegradation using a photomask [46]. These devices act as a dynamic method to reconfigure biomicrofluidic systems and have been applied to capture and release specific cell types [47]. These masks, however, only pattern the gels in an on/off manner. Thus, researchers looked to make gradients of photodegradation, which lead to a gradient of intact network strands, and hence modulus [48, 44]. Continuous gradations of material modulus were created by pulling an opaque photomask across the surface of the photodegradable gel during exposure. Regions that experienced longer degradation times were softer, and shorter times lead to stiffer regions. Since mechanical gradients occur throughout our bodies, as mentioned above, this ability was of immense interest.

Such photomasks, however, can only controllable pattern the gels in two-dimensions. In order to expand photodegradable hydrogel patterning in three-dimensions, researchers have taken advantage of laser scanning microscopes typically utilized for confocal microscopy [38, 49, 45, 44]. Using such microscopes, a focused laser beam scans in a custom raster pattern which degrades a single voxel of gel at a time. To increase the three-dimensional resolution of this technique, two-photon absorption can be utilized [38, 49, 45]. Since near-simultaneous absorption of two photons is extremely low, only the exposed regions of the highest flux, and thus the focal point of the laser, cause the two-photon photolysis of the *o*-NB moiety. Since the wavelength of light used for two-photon photolysis is of lower energy (longer wavelength), attenuation of light through the gel is not an issue, allowing degradation to be confined deep into the gel. Degradation can be restricted to a small small volume in three dimensional space $\approx 1\ \mu\text{m}^3$.

To further utilize on photodegradable hydrogels, differential network swelling during photodegradation was capitalized on to create folding hydrogels. The degree to which a polymer network swells is based on a balance between the modulus of the gel, and the osmotic pressure within the gel [50]. Polymer strands within the network attract solvent into the network due to the free energy gain in mixing. The pressure of this inward flow is countered by the elastic energy from the stretching of the gel network. Thus, the degree of network swelling can be controlled by three parameters: 1) the solvent quality for the particular polymer network; 2) the total amount of polymer in the gel; and 3) the stiffness of the network. All three parameters can be controlled spatially and temporally by photodegradation of the networks. As the network degrades, network strands are cleaved which decreases the modulus of the gel. Eventually, polymer strands are completely removed from the system, reducing the total polymer content. After cleavage of the *o*-NB group, a pendant charged carboxylic acid group is left attached to the network that changes the quality of the solvent (water) and thus the osmotic pressure. Researchers have found that upon initial irradiation, the *o*-NB-based PEG gels increase in volume. Eventually as more and more polymer strands are removed, the gel network decreases in volume and eventually undergoes de-gelation where there are not enough intact network strands to form an infinite molecular weight network [51]. This volume expansion and contraction property has allowed researchers to create both positive and negative features within the same gel, only by modifying the exposure conditions [45, 52]. Since the stimulus used is light, such patterns can be controlled spatially using photomasks and modified at different time points. To further explore and utilize the swelling behavior of photodegradable gels, Kapyla et al. exploited the non-uniform degree of degradation along the path of light. Upon irradiation, light is attenuated leading to a gradation of material properties along the path of light. The gel volume at the surface increases while remaining the same deeper into the gel. Given the proper gel geometry and exposure conditions, the gels fold and change their three-dimensional shape [53]; a process that can be induced in the presence of cells. Via the same mechanism, others have utilized the asymmetric swelling of photodegradable networks formed by the copolymerziation of acrylamide (AAm), N -[tris(hydroxymethyl)methyl] acrylamide (THMMA), and a PEG-based photocleavable crosslinker [54].

1.4 Expanding photodegradable hydrogels to alternative material systems

While PEG-based hydrogels have proven to be incredibly effective biomaterials, and well suited to be used in photodegradable systems, researchers have looked towards other material systems incorporating photodegradable linkages. The use of both synthetic and natural polymers has been investigated. Early on, acrylate-terminated *o*-NB moieties were conjugated to naturally-derived dextran polysaccharide polymers [55]. These *o*-NB dextran macromolecules were then crosslinked with dithiolated PEG via a Michael addition between the acrylate and thiol groups. Similarly, looking to produce an injectable hydrogel to release proteins or other biological cargo, heparin, a glycosaminoglycan, was investigated. Heparin was functionalized with maleimide groups and crosslinked via Michael addition with thiol-terminated photodegradable PEG macromers [56]. In order to reduce hydrolysis, the ester bond of the *o*-NB group was replaced with an amide. This amide linkage, however, significantly reduced the photo-sensitivity of the linkage and resulted in much slower photodegradation of the gel, which has been observed previously [57]. Hyaluronic acid (HA) based substrates have also been utilized for photodegradable hydrogels. One of the main advantages of HA is that it has a very high number of functional groups (in the form of a nucleophilic alcohol) per strand: every other monomeric unit. Hyaluronic acid was modified with acrylate terminated photodegradable linkages, methacrylate groups, and RGD domains [58]. Herein, the polymer strands could undergo multiple gelation and degelation reactions: 1) using dithiothreitol, initial gelation occurred through thiol-acrylate Michael addition; 2) exposure to 365 nm light subsequently degrades the *o*-NB linkages, softening the gel; and 3) the methacrylate groups are subsequently photopolymerized.

One of the main drawbacks of many polymeric materials is that they may not be enzymatically active. Cells can not degrade the surrounding network, thus limiting cellular proliferation and restructuring of the matrix. To circumvent this, in combination with photodegradable linkages, metalloproteinase (MMP) sensitive structural elements have been incorporated into the backbone of the PEG hydrogel network [59, 60]. The hydrogels can be specifically degraded with light, and cells can restructure the matrix as well. Along a similar vein, gelatin, a natural material that intrinsically contain MMP sensitive linkages and RGD binding domains has been modified with methacrylate groups (GelMA) and copolymerized with photodegradable PEG [61, 62]. Gelatin has also been directly conjugated with *o*-NB photodegradable crosslinkers to form pure gelatin photodegradable hydrogels [63]. These pure photodegradable gelatin hydrogels suffered from low conjugation efficiency, however.

Another biomaterial that researchers have commonly used is polyacrylamide (PAAm), which has been heavily used in to study cell mechanobiology [64]. As a way to dynamically crosslink PAAm gels, White et al. co-copolymerized acryalmide with a catechol methacrylate group that complexes to iron under basic conditions and forms a bis-catechol crosslink [65]. By adding a photoacid generator (diphenyliodonium chloride) and exposing to 254 nm light, the ferric-phenoxide coordinative bond is protonated and dismantled. While this system is not applicable for cell culture, it has potential applications for photo-reversible adhesives. As described above PAAm-THMMA based photodegradable gels have been synthesized to explore shape-shifting gels [54]. Photodegradable polyacrylamide gels have also been produced by transforming the photoinitiator Irgacure-2959 into a bis-acrylate crosslinker [66]. Again, this photodegradable hydrogel system was not used for cell culture, likely due to the production of harmful free radicals upon irradiation.

Researchers have also looked for different ways to form photodegradable hydrogels. In order to produce more homogeneous network structures, reversible addition-fragmentation chain transfer (RAFT) polymerization was utilized to synthesize hydrogels incorporating the photodegradable *o*-NB group [67]. When compared to conventional PEG-based photodegradable free-radical polymerized hydrogels, RAFT gels display faster degradation kinetics, likely due to their more homogeneous nature. Using a slightly different approach to produce photodegradable hydrogels, the group of Professor Bettinger has investigated block copolymers that disintegrate upon exposure to light[68, 69, 70, 71]. Triblock copolymers composed of a hydrophobic, photolabile blocks (either poly(*o*-nitrobenzyl methacrylate) [68, 71] or poly([6-bromo- 7-hydroxycoumarin-4-yl]methyl methacrylate) [69]) and hydrophilic PEG blocks were synthesized. These block copolymers formed physically crosslinked gels when hydrated. Upon irradiation, the photolabile group was cleaved leaving a pendant carboxyl group on the block copolymer. This cleavage changed the charge density of the polymer chains and rendered the hydrophobic blocks to become hydrophilic. The physically crosslinked networks disintegrated. Other groups have also looked to produce photodegradable physically crosslinked block copolymer gels. Using a very similar approach, a four arm star polymer composed of hydrophilic PEG blocks and hydrophobic, photolabile poly(gamma-*o*-nitrobenzyl-L-glutamate) blocks were synthesized [72]. Again, hydrophobic interactions of the *o*-NB group physically crosslinked the gels and also provided a hydrophobic domain to encapsulate hydrophobic drugs.

1.5 Assaying cell response to changes in matrix mechanics

The great benefit of the photodegradable hydrogels is the ability to ask and answer questions in cell biology that are otherwise inaccessible. As such, detailed protocols, aimed at the cell biology community, to synthesize photodegradable hydrogels, have been established [73]. Since PEG does not inherently contain any cell binding domains, the short peptide arginylglycylaspartic acid (RGD), which is found within many matrix proteins, has been incoproated. RGD domains can either be acrylated and directly incorporated into the gel during formation [74], or a cysteine residue can be added to the RGD peptide which undergoes a Michael addition with a pendant acrylate group on non-photodegradable PEG [75, 53]. Since many of the polymerization mechanisms used are non-toxic, and the wavelength of light used to degrade the gels do not affect gene expression [40] or the proteome more generally [41], cell behavior in photodegradable hydrogels can be studied in both 2D and 3D culture. Using the sliding photomask technique described above, hydrogels with a gradient of elastic modulus were created, and used to analyze valvular interstitial cell (VIC) activation into myofibroblasts [48]. By utilizing a gradation of material properties, specific moduli that suppress VIC activation could be identified. Myofibroblasts could also be dynamically de-activated by softening the matrix stiffness in-situ [48, 74, 76]. Levels of α-smooth muscle actin stress fibers and proliferation could be actively reduced upon substrate softening and reactivated upon addition of TGF-β [74].

The role of dynamic and heterogeneous matrix mechanics on stem cell differentiation has also been explored. Yang et al. found that human mesenchymal stem cells (hMSCs) exhibited “memory” of previous mechanical environments. Using photodegradable PEG-based gels, hMSCs were cultured on initially stiff gels which were then softened upon irradiation. If the culture time on initially stiff hydrogels was long enough (10 days), once the gels were in-situ softened, hMSCs behavior no longer reverted to the behavior observed when cultured on initially soft gels [77]. Research has also shown that cells respond to spatial mechanical cues. Photodegradable PEG gels were patterned with subcellular changes in matrix mechanical properties to study hMSC fate. Different patterns of matrix stiffness lead to disruption of actin organization, altered response of transcriptional regulators, and different cell fate [78]. Cell behavior to topographical signals can also be studied. By pre-softening photodegradable gels, then erroding channels, cell response to dynamic and topological features can be studied: VICs de-activated upon in-situ softening and myofibroblast activation recovered after in situ channel creation [76].

Various methods to explore three-dimensional cell culture using photodegradable hydrogels have also been carried out. By degrading arrays of cell culture wells into photodegradable hydrogels, cell differentiation in response to well geometry was studied. Furthermore, individual cell clusters in adjacent wells could be connected at any time point via controlled two-photon irradiation [59]. Similarly, axon growth of encapsulated embryonic stem cell-derived motor neurons was directed by in-situ creation of user defined tunnels created by two-photon irradiation [57]. Vascular networks have also been explored where, 3D perfusable vessels within photodegradable hydrogels were created via two-photon irradiation. These networks can be readily modified over time, in the presence of cells [60]. Alternatively, photodegradable hydrogels have been used as a way to mold cells into particular shapes. By using the gel folding techniques described above, C2C12 mouse myoblasts were encapsulated into photodegradable gels that could subsequently be folded into tubes at a user-defined time point [53]. Photodegradable hydrogels have also been used as a sacrificial material that can be removed after cell cultures have maturated. Epithelial cells were cultured on the surface of photodegradable hydrogel microspheres, which were then embedded in non-photodegradable gels. The photodegradable component was then eroded away with 365 nm light, leaving a hollow cyst-like architecture that resembled functional epithelial layers [79]. This same technique has been applied to recapitulate the native alveolar tissue architecture [80].

1.6 Limitations

While much research has been performed with photodegradable hydrogels, there are still several factors limiting their development and use. The central theme of this dissertation is to explore these insufficiencies and find potential solutions. The topics I explore all aim to make photodegradable hydrogels more applicable for the study of cell biology. In Chapter 2 I explore mathematical models of photodegradable PEG gels, to more precisely predict their properties. Current models of photodegradable hydrogels are insufficient to properly explore the gel microstructure as well as the complexities surrounding their degradation. I pay special attention to how diffusible photoabsorbing species mediate the degradation of the polymer network. Through a series of mass-action models I show how including the diffusing of photoabsorbing species significantly affects the degradation profile of these gels. The model also examines the experimental conditions in which diffusion of these species is more or less important. Next, in Chapter 3, I precisely model the polymer network microstates being formed (on the order of 100 individual network strands). I create a mathematical model to determine the distribution of network microstates during network polymerization or degradation. The model subsequently explores how networks may be formed if the network bonds can dynamically bind and unbind and thus reach an "equilibrium" state rather than an irreversible (or quenched) network formation process.

While some alternatives to PEG-based photodegradable hydrogels have been explored, there still exist some material-based limitations. In Chapter 4 of my dissertation I explore the fabrication and use of protein-based photodegradable hydrogels. Thus far, most photodegradable hydrogels have been composed of polymers that are not optimal for three-dimensional cell culture. They do not allow for cells to restructure the matrix surrounding them. While some photodegradable gels have incorporated protease-sensitive sites, their fabrication is tedious, and they may not properly mimic the native environment. I explore the use of gelatin, a naturally derived material that contains both enzymatically liable sites and cell binding domains, and synthesize photodegradable gelatin-gels. More generally, this chapter explores the conditions and techniques needed to conjugate hydrophobic moieties to protein macromers at high conjugation efficiency. In Chapter 5 of my dissertation, I explore the synthesis of photodegradable polyacrylamide gels, and their use as a dynamic biomaterial to study cellular mechanotransduction. Polyacrylamide gels the most commonly used hydrogel systems to study mechanobiology. They are easily fabricated, their mechanical properties can be precisely tuned, and any protein of choice can be covalently attached to the gel surface. However, the mechanical properties of polyacrylamide gels for cell culture can not be dynamically tuned. We show that for the particular cell type investigated, cells respond more strongly to dynamic changes in matrix elasticity than the matrix elasticity alone. Furthermore, we utilize the flexibility of polyacrylamide gels to readily attach any protein of choice to the surface. We explore cell response to both cell binding domains and dynamic mechanical changes.

Finally, while simple photomasks and two-photon illumination have been used to pattern photodegradable hydrogels, we find these methods to be limiting. The ability to spatially pattern matrix stiffness to a high degree of control has been challenging. Physical photomasks only allow for binary degraded/nondegraded patterns. While two-photon techniques give perhaps the most control of three-dimensional patterned degradation, they are prohibitively very slow. A very high-powered focused laser beam must scan in a raster-like manner, thus, degradation times run into hours. In Chapter 6 of my dissertation, I explore the use of maskless photolithography as a method to pattern photodegradable hydrogels with custom graphics. Using this technique, I show that photodegradable hydrogels can be patterned rapidly, in a highly controlled fashion with stiffness patterns at the sub-micron scale. Due to the speed of the technique, incredibly fine grayscale patterns can be patterned across length scales spanning several orders of magnitude.

CHAPTER 2

Diffusion of Photoabsorbing Degradation Byproducts in Photodegradable Polymer Networks

2.1 Abstract

Photodegradation of crosslinked, hydrated polymer networks is an important lithographic process in the fabrication of structured biomaterials. In order to better understand the properties of materials fabricated using photodegradation, the process is mathematically modeled, paying special attention to how diffusible photoabsorbing species mediate the degradation of the polymer network. These light-absorbing species may significantly alter light attenuation; thus, understanding the spatial movement of these species is critical in developing a predictive model of photodegradation. Using a series of mass-action models, diffusion of absorbing species is shown to play a significant role in determining the final state of the photodegraded network. The predicted degree of degradation is significantly different when including the effects of diffusion than that predicted when neglecting diffusion. This model also explores degradation profiles that result from different experimental geometries. This model is the most accurate description to date of the relationship between experimental conditions and resulting photodegradation.

2.2 Introduction

In the last decade, reports of photodegradation as a mechanism to control biomaterial properties have steadily increased. Photodegradable moieties can be used as photocages to reveal chemical patterning, and/or can be incorporated into hydrogel backbones to allow physical patterning. Linkages such as the *ortho*-nitrobenzyl (*o*-NB)-based moieties [38, 39] have been used extensively to produce complex cell-culture and targeted drug-release systems. In these systems, photodegradation of the *o*-NB linkages allows for external, real-time, spatial and temporal control of the substrate's properties.[38, 81, 52, 44, 45, 82, 35] The underlying mechanism of *o*-NB degradation consists of an intact *o*-NB linkage attached to two different molecular groups (R1 and R2) that is degraded by exposure to light (**Figure 2.1a**). The two groups are released from one another and result in an irreversible cleavage.

This simple molecular photodegradation procedure has been applied in two ways. First, *o*-NB linkages are used to attach molecular groups – releasable therapeutics, growth factors, or cellular binding domains – to a polymeric network or surface. [83, 84, 85] Second, the *o*-NB linkages are incorporated into the backbone of a crosslinking linear polymer chain such as a poly(ethylene glycol)-diacrylate (PEG-DA) macromer[38, 53, 52, 44, 45] (Figure 2.1b), (the use that is the focus of this study). These photodegradable crosslinking macromers can undergo an end-linking gelation process where the reactive functional groups of the macromers chemically crosslink with one another to form a branch point/crosslink. These crosslinks can be formed by addition polymerization of the reactive end groups or step growth polymerization with a complementary multifunctional linker with a functionality $f > 2$. Here, the functionality f is the number of active sites or the number of network strand attachments to a single branch point. However, the model presented here is not specific to the network formation mechanism. A general network structure with $f = 4$ is shown in Figure 2.1c. Here, the crosslinks (indicated by red dots) are connected to one another by polymeric network strands (black lines) with photodegradable end-groups (green ovals). Using photodegradation, the number density of intact network strands and therefore the elastic modulus of the network, can be modified.

The degradation of the *o*-NB linkages can be externally controlled by exposure to light, allowing physical and chemical patterning of hydrogels. However, measurement of interior physical and chemical properties is difficult, if not impossible, with current characterization techniques. Mathematical models assist in understanding and predicting of the physical and chemical properties of such patterned materials and provide an additional tool to guide

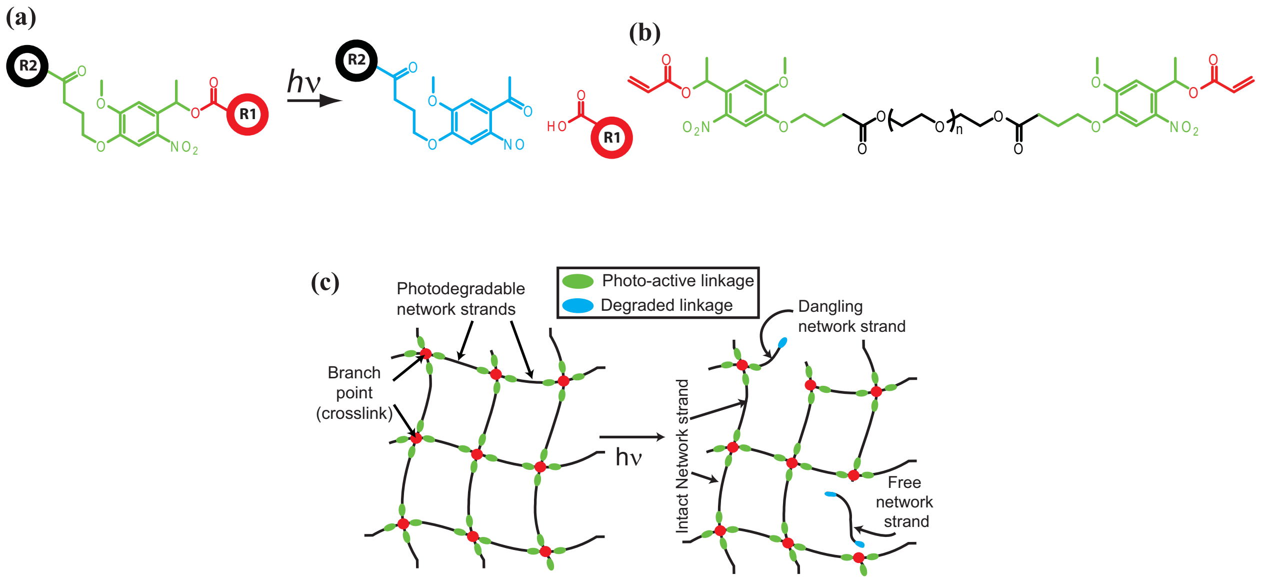

Figure 2.1: **Network Structure.**

(a) Photodegradation of an example *o*-NB molecule: the 4-(4-(1-hydroxyethyl)-2-methoxy-5-nitrophenoxy) butanoic acid chemistry. **(b)** Incorporation of the *o*-NB linkages into the backbone of a poly(ethylene glycol) diacrylate to form a photodegradable crosslinking macromer. **(c)** End linking of the photodegradable crosslinking macromer forms a network that can be subsequently degraded. Crosslinks (red dots) are connected to one another by polymeric network strands (black lines) with photodegradable end-groups (green ovals). Exposure to light degrades the photoactive linkages (blue ovals). The photodegradable network strands are left in one of three states: 1) intact; 2) dangling; or 3) free.

in their design, synthesis and characterization. In this paper, we focus on modeling the photodegradation of nitrobenzyl-based linkages, yet our mathematical model is sufficiently general to be applicable to all systems containing photodegradable linkages.

2.2.1 Photochemical Reaction Kinetics

Previous mass-action kinetic models have been developed to characterize and predict hydrolytically and enzymatically degradable hydrogels that undergo bulk degradation.[86, 87] These models consist of first-order, spatially *homogeneous* rate equations. They do not account for spatially *heterogeneous* rate equations or the spatial diffusion processes present in a photochemical reaction. In a hydrolytically degradable hydrogel, it is reasonable to assume that water is uniformly distributed throughout the network, resulting in a constant rate of degradation. In contrast, in a typical photochemical reaction, light is attenuated along the beam path. As the local intensity of light changes, so does the degradation rate of the photosensitive *o*-NB linkages. The attenuation of light is modeled by the Beer-Lambert law, in which the intensity of light $I(x,t)$ at a given position x and time t is expressed as

$$I(x,t) = I_0 \exp\left[-\sum_j \alpha_j \int_x^\infty c_j\left(x',t\right)\,\mathrm{d}x'\right], \tag{2.1}$$

where I_0 is the incident light intensity (mW cm^{-2}) at the entrance to the system. Any light absorbed or scattered above this point is assumed to be negligibly small. The concentration (M) and molar absorptivity (M^{-1}cm^{-1}) of the j^{th} photoabsorbing species are denoted c_j and α_j, respectively. Any variations in the light intensity, calculated by Equation 2.1, are directly caused by variations in concentrations of photoabsorbing species. **Figure 2.2** shows a basic schematic of the model. The water-swollen polymer network occupies the space between $0 < x < L$. Above this network, in the space $x > L$, exists a water layer where degradation products (Figure 2.1c) may readily diffuse. Light enters the system in the negative-x direction, and enters the photodegradable polymer network at the $x = L$ surface. In this analysis, we assume that all photon absorption is single-photon and that

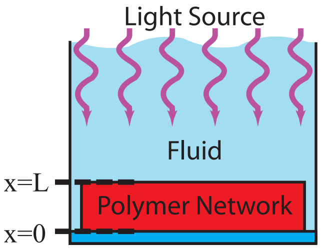

Figure 2.2: **Basic model schematic.**
A photodegradable polymer network occupies the space $0 < x < L$. Above, exists a fluid layer where degradation products may readily diffuse. Light enters the system in the negative-x direction.

the relaxation time of the photoabsorbing species is negligibly small, i.e., the photoabsorber instantly relaxes after absorbing a photon, immediately allowing it to continuously absorb subsequent photons.

In nitrobenzyl-based systems, only two photoabsorbing species exist: the undegraded, photodegradable/photoactive linkage and the degradation product(s) (i.e., *o*-nitrosoketone), as shown in Figure 2.1a. This assumes only one possible photodegradation product, which may not be true for all o-NB linkers or other photoreactive species. In this paper, the concentrations of these two species are denoted as c_{pd} and c_{deg}, respectively. This work assumes that absorption of photons by degraded *o*-NB linkages causes no further chemical changes to the system. Since the photochemical reaction rate is proportional to the local intensity of light, variations in the light intensity create spatial heterogeneities in the chemical kinetics. This heterogeneity is substantial when using high concentrations of photodegradable species with large extinction coefficients.

Photo-based network reconstruction mass-action models that account for light attenuation have been developed previously to examine: 1) photoinitiation during photopolymerization;[88, 89] 2) individual reaction steps such as propagation, chain transfer, and termination of thiol-vinyl photopolymerizations;[90, 91] and 3) mass transport during photopolymerization.[92] The kinetics of crosslinking photopolymerizations have also been well studied experimentally in order to investigate the various factors (chemical and physical) that dominate mechanisms of network formation.[93] These explicit models, while helpful to determine the effects of individual experimental parameters on output polymer structure, are limited in applied settings where many of the factors involved are difficult to measure experimentally. To this end, coarse-grained or "minimal" models have been created.[94] These models condense factors important to photopolymerization and rely on measurable quantities. They have been used to study parameters such as thermal diffusion[95] and mass transport[96] on the kinetics of photopolymerization.

To investigate the effects of light attenuation on photodegradable hydrogels, Tibbitt et al.[42] adapted coarse-grained bulk-degradation models[87] and set the degradation rate to be proportional to the light intensity $I(x,t)$. The one-dimensional form of this equation is

$$\frac{\partial c_{\mathrm{pd}}(x,t)}{\partial t} = -kI(x,t) \cdot c_{\mathrm{pd}}(x,t), \tag{2.2}$$

where the light intensity-independent kinetic constant is defined as

$$k = \frac{\alpha_{\mathrm{pd}} \lambda \phi}{N_A 2\pi\hbar c}, \tag{2.3}$$

where α_{pd} is the molar absorptivity of the undegraded o-NB linkage ($\mathrm{M}^{-1}\mathrm{cm}^{-1}$), λ is the wavelength of light (cm); $N_A = 6.022 \times 10^{23}\mathrm{mol}^{-1}$; $\hbar \approx 1.055 \times 10^{-30}\mathrm{cm}^2\mathrm{kg\ s}^{-1}$ is Planck's constant; $c \approx 3 \times 10^{10}\mathrm{cm\ s}^{-1}$ is the speed of light; and ϕ is the quantum yield (events per photon absorbed). In previous work by Griffin and Kasko[39] a factor of 10^{-6} is included in the kinetic degradation rate equation for unit conversion. We assume that the quantum yield of individual o-NB linkages is unaffected by light absorption-induced temperature changes, or the functionality of the branch point. From conservation of mass, the mass-action equation of the degraded species is simply $\partial c_{\mathrm{deg}}/\partial t = -\partial c_{\mathrm{pd}}/\partial t$. Analysis of this degradation process typically assumes the initial conditions $c_{\mathrm{pd}}(x,0) = c_{\mathrm{pd},0}$ for $0 < x < L$ and $c_{\mathrm{deg}}(x,0) = 0$ for all x. The solution to Equation (2.2) has been widely used to describe the spatial and temporal properties of network photodegradation and properly matches the corresponding experimental data.[42]

Table 2.1: Summary of variables used.

Symbol	Representation	Units	Value	Definition
I	Light intensity	mW cm^{-2}		Eq. (2.1)
I_0	Incident intensity	mW cm^{-2}	Experimental variable	
α_j	Molar absorptivity of species j	M^{-1}cm^{-1}	$\alpha_{\text{pd}} = 8061$, $\alpha_{\text{deg}} = 6073$	
c_j	Concentration of species j	M		
$c_{\text{pd},0}$	Initial o-NB linkage concentration	M	Experimental variable	$c_{\text{pd}}(x, t = 0)$
t	Time	s		
x	Coordinate	cm		
k	Kinetic degradation constant	mW^{-1}cm^{2}s^{-1}	3.3×10^{-4}	Eq. (2.3)
D	Diffusion coefficient	cm^{2}s^{-1}	Experimental variable	
L	Thickness of substrate	cm	Experimental variable	
h	Quiescent layer thickness	cm	Experimental variable	
I^*	Dimensionless light intensity			I/I_0, Eq. (2.11)
α_j^*	Initial absorbance parameter, species j			$\alpha_j c_{\text{pd},0} L$
C_j	Dimensionless concentration, species j			$c_j/c_{\text{pd},0}$, (Eq. 2.9)$^{a)}$
τ	Dimensionless time ("degree of degradation")			ktI_0
X	Dimensionless coordinate			x/L
H	Dimensionless quiescent layer thickness			h/L
D^*	Dimensionless diffusion coefficient			$D/(kI_0L^2)$
ΔC_j	Diffusion-induced degradation discrepancy			Eq. (2.18)
$(\alpha^*)^2 D^*$	Ratio of time scales (degradation/diffusion)			$\alpha_{\text{pd}}^2 c_{\text{pd}}^2 D/(kI_0)$, Eq. (2.4)

$^{a)}$The dimensionless concentration of the network strands is $2c_j/c_{\text{pd},0}$ to account for two o-NB linkages per network strand.

2.2.2 Movement of Photoabsorbing Network Components

Diffusion of photoabsorbing network strands. As indicated in Figure 2.1c, after photodegradation has occurred each photodegradable network strand will exist in one of three states: 1) neither of the o-NB end groups are cleaved, and the network strand remains fully "intact" and continues to contribute to the elastic integrity of the network; 2) one of the o-NB end groups is cleaved and the network strand "dangles" from the network backbone, unable to bear stress; or 3) both of the o-NB end groups are cleaved and the network strand is "free" from the network. Additionally, partially degraded dangling network strands can be further photolyzed to become "free" network strands. Typically, the molecular weight of polymer-based network strands is 1-10 kDa. At this size, "free" network strands will readily diffuse.[97] These free network strands continue to absorb light through their two degraded o-NB end groups and may significantly affect the light intensity profile of the gel. While the work by Tibbitt et al.[42] has been fundamental in the study of photodegradable networks, it does not account for the diffusion of the photoabsorbing free network strands.

In order to quickly evaluate whether spatial rearrangement of free network strands is significant during photodegradation of polymer networks, we compare time scales of degradation and diffusion. Diffusive transport of photoabsorbing species along the light path will be significant when the dimensionless parameter, δ, is greater than 1:

$$\delta = \frac{\alpha_{\text{pd}}^2 c_{\text{pd}}^2 D}{kI_0} = \frac{\text{degradation time scale}}{\text{diffusion time scale}} > 1, \tag{2.4}$$

where D is the diffusion coefficient of the free network strands and $1/(kI_0)$ can be thought of as the time scale of degradation. Accordingly, $1/(\alpha_{\text{pd}}^2 c_{\text{pd},0}^2 D)$ can be thought of as the time scale of diffusion, where $1/(\alpha_{\text{pd}} c_{\text{pd},0})$ is the distance over which the concentration of the diffusing species changes significantly. As the optical density increases, this distance decreases. Thus, we can think of δ as a ratio of the reactive and diffusive time scales. If δ is large, the diffusion of photoabsorbing species will be significant during the photodegradation reaction.[92, 96] Given typical experimental conditions of $\alpha_{\text{pd}} \approx 5000\ \text{M}^{-1}\text{cm}^{-1}$, $c_{\text{pd},0} \approx 0.05$ M, $D \approx 100\ \mu\text{m}^2\text{s}^{-1}$, $k \approx 3 \times 10^{-4}\ \text{cm}^2\text{mW}^{-1}\text{s}^{-1}$, and $I_0 \approx 10\ \text{mW cm}^{-2}$: $\alpha_{\text{pd}}^2 c_{\text{pd},0}^2 D/(kI_0) \approx 20$. Thus, diffusion of photoabsorbing molecules is expected to be significant and impact the light intensity profile.

Movement of larger network structures. As photodegradation proceeds, large finite-size aggregations of branch points and network strands may separate from the network. For example, as shown in Figure 2.1c, a branch point can be freed from the network if all network strands surrounding the branch point are dangling or free. This forms a soluble cluster that includes a branch point and any dangling network strands attached. For networks formed through addition polymerization, the branch point can have a functionality of $f \approx 15 - 20$ depending on fabrication conditions.[42] The molar mass of these finite-size clusters can be significant. Additionally, larger aggregates of multiple branch points, connected by intact network strands, can break off if there is no connecting path to the parent gel. In the work presented here, it is assumed that these soluble photoabsorbing aggregates do not diffuse throughout the system. This is due to the much larger molar masses and diffusion coefficients involved. Only the free photoabsorbing individual network strands are assumed to be mobile.

Model considerations. In order to quantitatively understand the effects of network strand diffusion in photodegradable gels, we develop and analyze a mathematical model of the process. In this model, the effects of the following variables are examined: 1) initial photodegradable group concentration $c_{\mathrm{pd},0}$; 2) incident light intensity I_0; 3) sample thickness L; 4) diffusion coefficient D of the free network strands; and 5) the imposed boundary conditions. This work focuses on the 4-(4-(1-hydroxyethyl)-2-methoxy-5-nitrophenoxy) butanoic acid chemistry,[39] as it is the most common nitrobenzyl linkage used and easiest to synthesize. 1,3-Di(hydroxymethyl)-2-nitrobenzene[39] is also heavily used, however, due to its large kinetic constant of degradation and low photoabsorbance in both the intact and degraded state, the effect of its degraded byproducts diffusing throughout the system is minimal and insignificant for the applications discussed. This chemistry has the following photochemical properties at $\lambda = 365$ nm, which have been measured previously:[39] $\alpha_{\mathrm{pd}} = 8061\ \mathrm{M}^{-1}\mathrm{cm}^{-1}$, $\alpha_{\mathrm{deg}} = 6073\ \mathrm{M}^{-1}\mathrm{cm}^{-1}$, and $k = 3.3 \times 10^{-4}\ \mathrm{cm}^2\mathrm{mW}^{-1}\mathrm{s}^{-1}$ (see **Table 2.1**). These values are used in this study. The values for α_j given above assume that the Beer-Lambert law uses the Napierian (e-based) form. These coefficients are easily converted from their decadic (10-based) form ϵ_j as given by Griffin and Kasko.[39]

However, any photodegradable chemistry can be used with this model as long as the rate constant of degradation and the molar absorptivities of the intact and degraded species are known.

In this work we demonstrate that the diffusion of photoabsorbing free network strands strongly affects the network degradation profile. This is particularly true when the photolabile linkage degrades slowly, the degraded linkage is optically dense, and/or the freely diffusing species is highly mobile. These criteria are fulfilled by the *o*-nitrobenzyl class of linkages.[39] Moreover, we demonstrate that diffusion is important in systems with steep concentration gradients of the diffusing species. These steep gradients can arise from sharp variations of micro-patterned structures,[81, 52] sample surfaces that quickly remove the degraded byproducts, and/or spatial degradation gradients caused by the strong attenuation of light along the beam path.[53]

2.3 Mathematical Model

2.3.1 Diffusionless Model

We examine the degradation of the photoactive *o*-NB linkages in one dimension, x, along the path of light propagation using mass-action kinetics. Shown in Equation (2.2), the kinetic equation for the *o*-NB linker is a first-order equation and proportional to the intensity of light. In the context of this work, light is attenuated as it passes through the sample and is absorbed by each type of photoabsorbing species present, including both degraded and undegraded species. To simplify this analysis, we nondimensionalize (see Table 2.1) our equations by introducing dimensionless time $\tau \equiv ktI_0$, position $X \equiv x/L$, concentration $C_j \equiv c_j/c_{\mathrm{pd},0}$, and a dimensionless initial absorbance parameter $\alpha_j^* \equiv \alpha_j L c_{\mathrm{pd},0}$ where $c_{\mathrm{pd},0}$ is the intital concetration of intact photodegradable linkage. The light intensity (Equation (2.1)) is thus rewritten in dimensionless form as

$$I^*(X,\tau) = \frac{I(x,t)}{I_0} = \exp\left[-\int_X^\infty \left\{\alpha_{\mathrm{pd}}^* C_{\mathrm{pd}}\left(X',\tau\right) + \alpha_{\mathrm{deg}}^* C_{\mathrm{deg}}\left(X',\tau\right)\right\} \mathrm{d}X'\right]. \tag{2.5}$$

The dimensionless mass-action integro-differential equations for the photodegradable and degraded groups are

$$\frac{\partial C_{\mathrm{pd}}(X,\tau)}{\partial \tau} = -I^*(X,\tau)\cdot C_{\mathrm{pd}}(X,\tau), \tag{2.6a}$$

$$\frac{\partial C_{\mathrm{deg}}(X,\tau)}{\partial \tau} = -\frac{\partial C_{\mathrm{pd}}(X,\tau)}{\partial \tau}, \tag{2.6b}$$

with the initial condition: $C_{\mathrm{pd}}(0 \leq X < 1, \tau = 0) = 1$, where $C_{\mathrm{pd}}(X, \tau = 0) = 0$ otherwise and; $C_{\mathrm{deg}}(X, \tau = 0) = 0$. For the remainder of this paper, we use the nondimensionalized form shown above unless otherwise stated. In the case where the degraded products do not

Table 2.2: Representation of different species concentrations. Below, $C_{\mathrm{deg}} \equiv C_{\mathrm{f}} + C_{\mathrm{d}}/2$ represents the sum of degraded *o*-NB photoabsorbing species.

Symbol	Representation	Units
c_{pd}	Photodegradable linkages	(M)
c_{deg}	Degraded linkages	(M)
C_{pd}	Photodegradable linkages	unitless
C_{deg}	Degraded linkages	unitless
C_{i}	Intact network strands	unitless
C_{d}	Dangling network strands	unitless
C_{f}	Free network strands	unitless

absorb light, the solution to this equation has been solved analytically by Wegscheider:[98]

$$C_{\mathrm{pd}}(X,\tau) = \left[1 - e^{-\alpha^*_{\mathrm{pd}}(1-X)}\left(1 - e^{\tau}\right)\right]^{-1}. \tag{2.7}$$

While this solution is not applicable to the photodegradable *o*-NB linkages presented here, it is used to validate the accuracy of the numerical method and calculate the error.

2.3.2 Kinetic Equations for Network Strand Types and Added Diffusion

In this model, concentrations of absorbing species change in one of two ways: 1) through the photodegradation reaction; or 2) through diffusion. We first examine the production of network strands absent diffusion. A coupled system of differential equations is created, where each equation in the system pertains to an individual network strand type. Once the kinetic contribution to the individual network strand types has been established, diffusion of individual network strands can be incorporated.

In order to accurately model all network strand concentrations rather than just the concentration of the intact *o*-NB linkages, we decompose the population according to the three network strand types seen in Figure 2.1c. The relationship between the network strand concentrations and the concentrations of the photodegradable linkages is calculated using combinatorial statistical arguments. This relationship assumes a random photodegradable linkage degradation as seen previously for similar hydrolyzable networks in Metters et al.[87]

In the thermodynamic limit, the probability that a randomly chosen o-NB linkage has been degraded approaches the fraction of degraded o-NB linkages. The linkages are assumed to be broken in an identical, independent manner. No spatial correlations exist. The probability that within a region of space at position X a linkage is degraded is

$$\begin{aligned} P(X,\tau) &= C_{\mathrm{pd}}(X,0) - \frac{c_{\mathrm{pd}}(X,\tau)}{c_{\mathrm{pd},0}} \\ &= C_{\mathrm{pd}}(X,0) - C_{\mathrm{pd}}(X,\tau). \end{aligned} \tag{2.8}$$

Recall that an intact network strand requires that both end groups remain intact, a dangling network strand requires one end group to be degraded while the other remains intact, and a free network strand requires that both end groups are degraded. Therefore, the local probability of finding a particular network strand is related to the local probability that a photodegradable linkage is degraded, assuming no network strand diffusion. The dimensionless concentrations of the network strand types (**Table 2.2**) are expressed as

$$C_{\mathrm{i}}(X,\tau) = C_{\mathrm{pd}}^2(X,\tau), \tag{2.9a}$$

$$C_{\mathrm{d}}(X,\tau) = 2C_{\mathrm{pd}}(X,\tau)\left(C_{\mathrm{pd}}(X,0) - C_{\mathrm{pd}}(X,\tau)\right), \tag{2.9b}$$

$$C_{\mathrm{f}}(X,\tau) = \left(C_{\mathrm{pd}}(X,0) - C_{\mathrm{pd}}\left(X,\tau\right)\right)^2, \tag{2.9c}$$

where C_{i}, C_{d}, and C_{f} are the dimensionless concentrations of the intact, dangling, and free network strands, respectively (Figure 2.1c). The dimensionless time rate of change of these concentrations is:

$$\frac{\partial C_{\mathrm{i}}(X,\tau)}{\partial \tau} = 2C_{\mathrm{pd}}(X,\tau)\frac{\partial C_{\mathrm{pd}}(X,\tau)}{\partial \tau}, \tag{2.10a}$$

$$\frac{\partial C_{\mathrm{d}}(X,\tau)}{\partial \tau} = 2\left(C_{\mathrm{pd}}(X,0) - 2C_{\mathrm{pd}}(X,\tau)\right)\frac{\partial C_{\mathrm{pd}}(X,\tau)}{\partial \tau}, \tag{2.10b}$$

$$\frac{\partial C_{\mathrm{f}}(X,\tau)}{\partial \tau} = 2\left(C_{\mathrm{pd}}(X,\tau) - C_{\mathrm{pd}}(X,0)\right)\frac{\partial C_{\mathrm{pd}}(X,\tau)}{\partial \tau}. \tag{2.10c}$$

For the remaining equations in this section, we have suppressed the dependence on (X,τ) for brevity. Since the concentrations of intact and degraded o-NB linkages are calculated from the concentrations of the different network strand types ($C_{\mathrm{pd}} = C_{\mathrm{i}} + C_{\mathrm{d}}/2$ and $C_{\mathrm{deg}} = C_{\mathrm{f}} + C_{\mathrm{d}}/2$, respectively), the dimensionless intensity profile (Equation (2.5)) is expressed as

$$I^* = \exp\left[-\int_X^{\infty}\left\{\alpha^*_{\mathrm{pd}}\left(C_{\mathrm{i}} + \frac{C_{\mathrm{d}}}{2}\right) + \alpha^*_{\mathrm{deg}}\left(C_{\mathrm{f}} + \frac{C_{\mathrm{d}}}{2}\right)\right\}\mathrm{d}X'\right], \tag{2.11}$$

where I^* is integrated from X to ∞ to account for free network strands that may have diffused out of the hydrogel, into the surrounding fluid (in the space $X > 1$), but still attenuate light. The differential equation of the photodegradable group (Equation (2.6a)) becomes

$$\frac{\partial C_{\mathrm{pd}}}{\partial \tau} = -I^*\left(C_{\mathrm{i}} + \frac{C_{\mathrm{d}}}{2}\right). \tag{2.12}$$

Now, Equation (2.10) and (2.12) are combined such that the kinetic equations are functions of only the network strand type. Without diffusion, all network strand species remain within the polymer network space ($0 \leq X < 1$). The differential equations for the network strand concentrations due to photodegradation within and only within this space are:

$$\frac{\partial C_{\mathrm{i}}}{\partial \tau} = -2I^*\left(C_{\mathrm{i}} + \frac{C_{\mathrm{d}}}{2}\right)^2, \tag{2.13a}$$

$$\frac{\partial C_{\mathrm{d}}}{\partial \tau} = -2I^*\left(\left(C_{\mathrm{i},0} + \frac{C_{\mathrm{d},0}}{2}\right) - 2\left(C_{\mathrm{i}} + \frac{C_{\mathrm{d}}}{2}\right)\right)\left(C_{\mathrm{i}} + \frac{C_{\mathrm{d}}}{2}\right), \tag{2.13b}$$

$$\frac{\partial C_{\mathrm{f}}}{\partial \tau} = -2I^*\left(\left(C_{\mathrm{i}} + \frac{C_{\mathrm{d}}}{2}\right) - \left(C_{\mathrm{i},0} + \frac{C_{\mathrm{d},0}}{2}\right)\right)\left(C_{\mathrm{i}} + \frac{C_{\mathrm{d}}}{2}\right), \tag{2.13c}$$

where I^* is given in Equation (2.11), $C_{\mathrm{i},0} = C_{\mathrm{i}}(X, 0)$, and $C_{\mathrm{d},0} = C_{\mathrm{d}}(X, 0)$. Equation (2.9), (2.10), and (2.13), however, only account for the number of network strands as produced by the photodegradation reaction. Any contribution to the number of network strands via diffusion must be considered separately. As expected, whether or not free network strands diffuse in or out of a given region, the kinetics of the photodegradation reaction (Equation (2.6a)) do not change. Production of network strands through photodegradation, as seen in Equation (2.13), does not depend on the local concentration of free network strands. Only the local light intensity (Equation (2.5) and (2.11)), which can be considered independently, is subject to change.

In order to fully quantify the entire process, we must account for network strands that have been added or subtracted from a region of space by diffusion. For the polymer networks described, the intact and dangling network strands are immobile – only free network strands diffuse with diffusion coefficient D. In this case, intact and dangling network strands remain only within the polymer network space ($C_{\mathrm{i}}(X,\tau) = C_{\mathrm{d}}(X,\tau) = 0$, for $X \geq 1$) while free network strands are able to diffuse out of the polymer network into the space $X \geq 1$. The contribution of diffusion to the free network strand concentration is simply

$$\frac{\partial C_{\mathrm{f}}}{\partial \tau} = D^* \frac{\partial^2 C_{\mathrm{f}}}{\partial X^2}, \qquad \text{for } X \geq 0, \tag{2.14}$$

where $D^* \equiv D/(kI_0L^2)$ is a dimensionless diffusion coefficient of the free network strands. Within the polymer network ($0 \leq X < 1$), the dimensionless time rate of change, including both photodegradation and diffusion, of the network strands is now:

$$\begin{aligned}
\frac{\partial C_{\mathrm{i}}}{\partial \tau} &= -\, 2I^* \left(C_{\mathrm{i}} + \frac{C_{\mathrm{d}}}{2} \right)^2, & \text{(2.15a)}\\
\frac{\partial C_{\mathrm{d}}}{\partial \tau} &= -\, 2I^* \left(\left(C_{\mathrm{i},0} + \frac{C_{\mathrm{d},0}}{2} \right) - 2 \left(C_{\mathrm{i}} + \frac{C_{\mathrm{d}}}{2} \right) \right) \left(C_{\mathrm{i}} + \frac{C_{\mathrm{d}}}{2} \right), & \text{(2.15b)}\\
\frac{\partial C_{\mathrm{f}}}{\partial \tau} &= -\, 2I^* \left(\left(C_{\mathrm{i}} + \frac{C_{\mathrm{d}}}{2} \right) - \left(C_{\mathrm{i},0} + \frac{C_{\mathrm{d},0}}{2} \right) \right) \left(C_{\mathrm{i}} + \frac{C_{\mathrm{d}}}{2} \right) + D^* \frac{\partial^2 C_{\mathrm{f}}}{\partial X^2}. & \text{(2.15c)}
\end{aligned}$$

Outside of the polymer network, in the space $X \geq 1$, only diffusion contributes to changes in C_{f}. For $X \geq 1$, $C_{\mathrm{i}}(X,\tau) = C_{\mathrm{d}}(X,\tau) = 0$ and Equation (2.15c) simplifies to Equation (2.14). Here, we assume the substrate is an infinite slab with finite thickness and that network strand densities vary only along the normal direction. Subsequent analysis assumes the following initial conditions:

$$C_{\mathrm{i}}(X, \tau = 0) = \begin{cases} 1 & \text{if } 0 \leq X < 1 \\ 0 & \text{otherwise} \end{cases}, \tag{2.16a}$$

$$C_{\mathrm{d}}(X, \tau = 0) = C_{\mathrm{f}}(X, \tau = 0) = 0. \tag{2.16b}$$

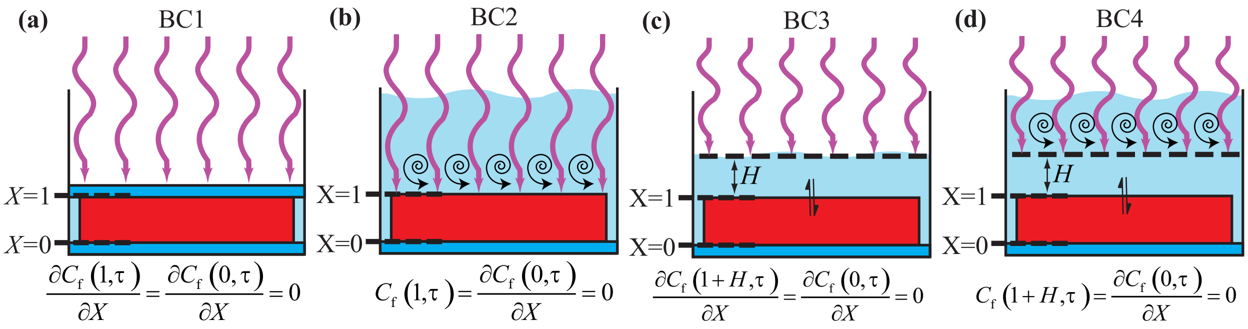

Figure 2.3: **Boundary conditions.**
(a) The substrate is bounded on surfaces ends by no-flux (Neumann) boundary conditions, e.g., two glass slides. **(b)** The top surface is directly exposed to an instantly absorbing sink (Dirichlet) boundary condtion ($C_f = 0$). The bottom surface retains the no-flux condition. **(c)** The substrate has an overlying unmixed fluid of dimensionless height H into which mobile species can diffuse. **(d)** Mixing of fluid in the upper unbounded reservior is not perfect, giving a quiescent, unmixed fluid layer of height H above the substrate.

2.3.3 Experimental Geometry and Boundary Conditions

During an experimental degradation, varying laboratory conditions will cause the boundary conditions to change. This impacts the overall result. **Figure 2.3** shows four different boundary conditions that are motivated by experimental applications:

- BC1: When the polymer network sample is sandwiched between two glass plates (Figure 2.3a) no flux of free network strands occurs at the boundaries. The conditions at both boundaries are no-flux (Neumann) conditions as described by Equation (2.17a) below. In this case, free network strands diffuse throughout the sample and are not removed from the system.

- BC2: If the top surface of the sample is unconstrained and exposed to an "instantly absorbing sink" (Figure 2.3b), we set the concentration of free network strands to zero (Dirichlet condition) at $X = 1$ (Equation (2.17b)). Such a condition is physically realized by a large fluid reservoir that is well mixed or is quickly being replaced by pure medium.

- BC3: If the experimental sample involves an unmixed fluid of fixed thickness h (in dimensionless form $H = h/L$) above the top surface of the sample (Figure 2.3c), we allow free diffusion up to $X = 1 + H$. Since the fluid-air interface at $X = 1 + H$ reflects free network strands, no-flux (Neumann) boundary conditions are applied at both $X = 0$ (bottom glass plate) and $X = 1 + H$, as represented in Equation (2.17a) below.

- BC4: If mixing or fluid replacement in an unbounded upper reservoir is not perfectly efficient, there will be a quiescent, unmixed fluid layer above the sample (Figure 2.3d). This quiescent layer has a typical thickness of $h \sim D/V$, where V is the typical fluid mixing velocity. Beyond this distance, the diffusing species are in the well-mixed medium in which their concentrations are approximately constant (Equation (2.17b)). An absorbing sink condition is imposed at an effective distance h. In general, the size of h depends on how the mixing process is experimentally implemented.

For this set of experimental conditions, the boundary conditions are set as:

two no-flux boundary conditions (BC1 & BC3):

$$\frac{\partial C_{\mathrm{f}}\left(X = 1 + H, \tau\right)}{\partial X} = \frac{\partial C_{\mathrm{f}}\left(X = 0, \tau\right)}{\partial X} = 0, \tag{2.17a}$$

asymmetric boundary conditions (BC2 & BC4):

$$C_{\mathrm{f}}\left(X = 1 + H, \tau\right) = \frac{\partial C_{\mathrm{f}}\left(X = 0, \tau\right)}{\partial X} = 0. \tag{2.17b}$$

If no medium exists above the top surface of the polymer network (BC1, Figure 2.3a) or the solution is very well mixed (BC2, Figure 2.3b), $H \approx 0$. For boundary conditions BC3 and BC4, we must consider that the diffusion coefficient is not necessarily constant throughout the region of interest. The diffusion of macromolecules within a swollen hydrogel matrix will be restricted compared with their movement in water ($D_{\mathrm{gel}} \leq D_{\mathrm{water}}$). Additionally, spatial differences in the diffusion coefficient may arise from a degradation-induced change in the hydrogel mesh size or a local temperature change due to light absorption. Spatially-dependent diffusion coefficients can be computed as a function of the mesh size,[99] temperature as given by the Einstein-Smoluchowski equation, or measured experimentally.[97] However, for simplicity, we assume a uniform diffusion coefficient in this work.

2.3.4 Numerical approach

In order to numerically model the degradation process, the problem is discretized spatially and temporally. During each time step, three computations are performed: first, the light intensity profile integral (Equation (2.11)) is evaluated by the trapezoid rule; second, the kinetic equations (Equation (2.15) - excluding diffusion) are evaluated by Newton iteration; and third, the diffusion of the free network strands (diffusion term of Equation (2.15c)) is analyzed implicitly by the Crank-Nicolson method which is second order accurate in time. Matrix inversion is performed through a tridiagonal matrix algorithm. Due to the wide range of model parameter values (see **Table 2.3**), a large number of time steps (100,000) and small mesh size ($\Delta X = 1/50,000$) are required in order to keep the error low.

When a particular model parameter is examined, all other model parameters are fixed (Table 2.3). For example, if D is varied from 0.1 to 10,000 μm^{2}s^{-1}, then L, I_0, and $c_{\text{pd},0}$ are fixed at 2000 μm, 5 mW cm^{-2}, and 0.05 M, respectively. To compare the effects of diffusion-mediated degradation across different experimental conditions, the dimensionless time parameter $\tau = ktI_0$ is fixed. That is, if the value of I_0 is varied as a model parameter, the illumination time t must be appropriately adjusted to maintain the same degree of degradation since k is a fixed material property. This dimensionless time parameter τ is considered the time integrated "degree of degradation." All numerical computations were performed in MATLAB.

Table 2.3: Range of variable model parameters.

Model Parameter	Variable Minimum	Variable Maximum	Fixed Value
D (μm^2 s^{-1})	0.1	10,000	100
L (μm)	1	10,000	200
I_0 (mW cm^{-2})	0.05	5,000	5
$c_{\text{pd},0}$ (M)	10^{-3}	10	0.05
h (μm)	0.5	5,000	0

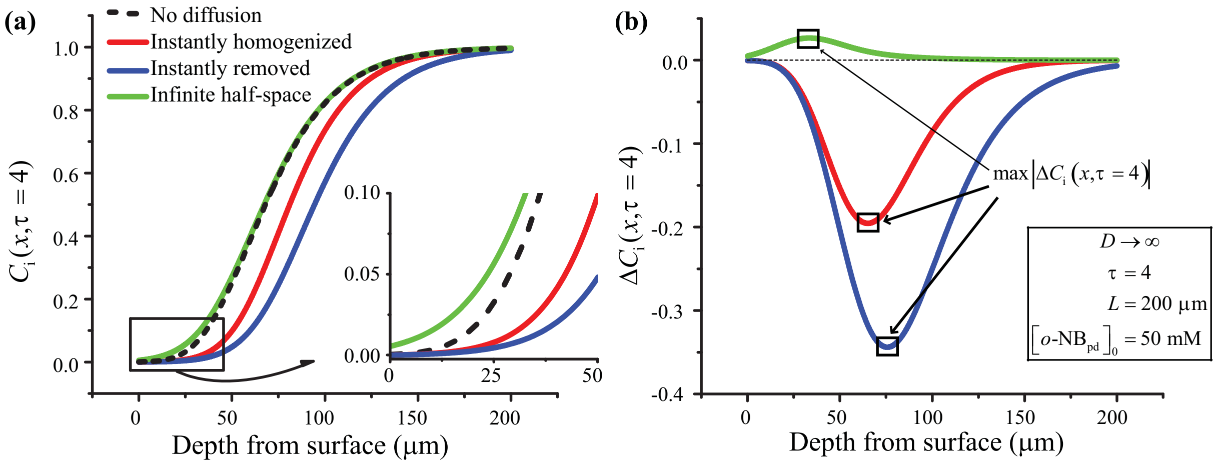

Figure 2.4: **Instantaneous diffusion. (a)** Intact network strand concentration profiles for three different boundary conditions. Results for $D \to \infty$ are compared to those for $D = 0$ (dashed black curves). 1) For the asymmetric boundary conditions in which one boundary is an absorbing sink, an infinitely fast diffusivity leads to instantaneous removal of free network strands from the system (blue curves). 2) When both boundaries are no-flux, fast diffusion quickly leads to a uniform/homogenous free network strand concentration throughout the sample (red curves). 3) When an infinite half-space exists above the sample surface, free network strands diffuse into this region. Accordingly, when diffusion is infinitely fast, all free network strands diffuse into the overlying medium (green curves). **(b)** A plot that shows the diffusion-induced discrepancy (ΔC_i) as defined by Equation (2.18) for each boundary condition.

2.4 Results and Discussion

2.4.1 Limit of Instantaneous Diffusion

We first consider a simple limiting model in which the mobile species diffuses instantaneously: $D \to \infty$. This allows us to quickly and easily estimate whether diffusion has an effect on the degradation profile and determine the upper bound of the diffusion-induced changes to the network. While an infinitely large D is not physically realizable, recall that the dimensionless diffusion parameter ($D^* = D/(kI_0L^2)$) is inversely proportional to kI_0. That is, for sufficiently small kI_0, diffusion is fast compared to the photodegradation reaction. Photodegradation using low incident light intensities, or photodegradable linkages with low k, are both realistically accessible experimental parameters. Small L also causes D^* to increase, however, the substrates are virtually transparent ($I(x,t) \to I_0$) as $L \to 0$, regardless of the distribution of light absorbing species. Three cases, each based on a particular boundary condition, are represented:

Case 1) Diffusion occurs throughout the sample bulk with two no-flux boundary conditions (BC1, Figure 2.3a). In this case, the diffusable species is contained within the sample boundary. When diffusion is infinitely fast, the concentration of the mobile species instantly reaches a spatially uniform value that increases with time – i.e., the free network strands are "instantly homogenized" (**Figure 2.4**) throughout the sample bulk.

Case 2) One of the sample boundaries obeys a fixed concentration (Dirichlet) boundary condition (BC2, Figure 2.3b, $C_\mathrm{f}(X = 1) = 0$). When diffusion is infinitely fast, the flux of mobile species across the Dirichlet boundary will be infinitely large, and all mobile species will be "instantly removed" (Figure 2.4) from the sample.

Case 3) Above the sample is an infinitely large upper reservoir of medium into which free network strands diffuse (BC3/BC4, Figures 2.3c & 2.3d, $H \to \infty$). We consider this as a theoretical simplification of the boundary condition when the unmixed and unreplenished fluid above the sample surface is very large. Unlike the case with two no-flux boundary conditions, the diffusable species are not restricted to the sample boundaries but are able to move into the medium above. This medium is considered an "infinite half-space" (Figure 2.4). Since the mobile species are instantly distributed throughout both the sample and the infinitely large upper reservoir, all mobile species instantly reside in the overlying medium. Light is, accordingly, attenuated before reaching the sample surface.

Each case is compared to a degradation model without diffusion where there is no change in the total number of network strands at every point in space and time: $C_\mathrm{i} + C_\mathrm{d} + C_\mathrm{f} = C_\mathrm{i}(t = 0)$. Without diffusion, degraded photoabsorbing species accumulate at the optical entrance of the substrate where the light intensity is the greatest. This accumulation prevents degradation from propagating deep into the substrate. The diffusion-induced degradation discrepancy is defined as the change in concentration of a network strand species when diffusion is applied:

$$\Delta C_j(X,\tau) = \underbrace{C_j(X,\tau)}_{\text{with diffusion}} - \underbrace{C_j(X,\tau)}_{\text{without diffusion}} \quad . \tag{2.18}$$

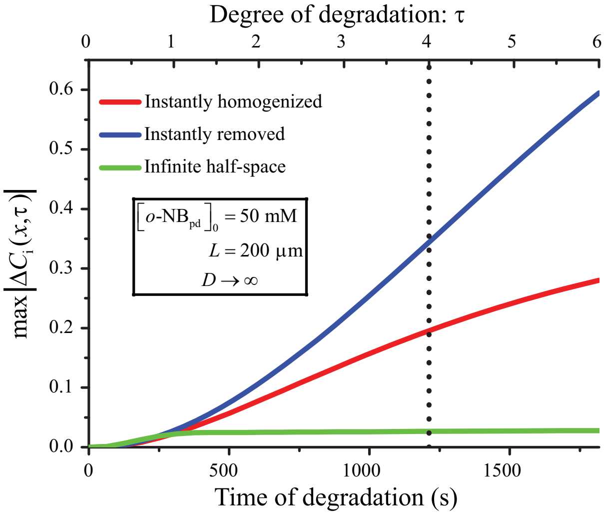

Figure 2.5: **Maximum diffusion-induced network change.**
Plot of the maximum change of intact network strand concentration across the sample depth max$|\Delta C_\mathrm{i}|$ from Figure 2.4b as a function of the degree of degradation τ and time of degradation t. Free network strands diffuse instantaneously. The dotted line indicates the degree of degradation used in this study: $\tau = 4$. Here, as the degree of degradation increases – due to some combination of time, light intensity, or reaction kinetics – the movement of free network strands increasingly affects the final state of the network.

As demonstrated in Figure 2.4a, homogenization (Case 1) or removal (Case 2) of diffusable species leads to increased light penetration and greater degradation (reduction of C_i) along the optical path. This occurs since the photoabsorbing mobile species are diluted (Case 1) or removed from (Case 2) the uppermost region of the substrate, allowing deeper light penetration through that region. Accordingly, instant removal of the diffusable species leads to a greater depth of degradation than instant homogenization. When the free network strands instantly diffuse into the overlying medium (Case 3), they attenuate light before the light reaches the sample surface. Unlike cases 1 and 2, the depth of degradation decreases with respect to the diffusionless model ($\Delta C_\mathrm{i} > 0$) when the photoabsorbing species are allowed to diffuse into the overlying medium. This difference is most pronounced near the sample surface (Figure 2.4b). Figure 2.4, however, represents only one fixed “degree of degradation” ($\tau = 4$).

For larger τ the magnitude of the diffusion-induced discrepancy $|\Delta C_\mathrm{i}|$ is expected to increase. In Figure 2.4b, the maximum of $|\Delta C_\mathrm{i}|$ for a particular τ is indicated as $\max|\Delta C_\mathrm{i}(x, \tau = 4)|$. In **Figure 2.5**, max$|\Delta C_\mathrm{i}|$ is plotted as a function of τ for the three

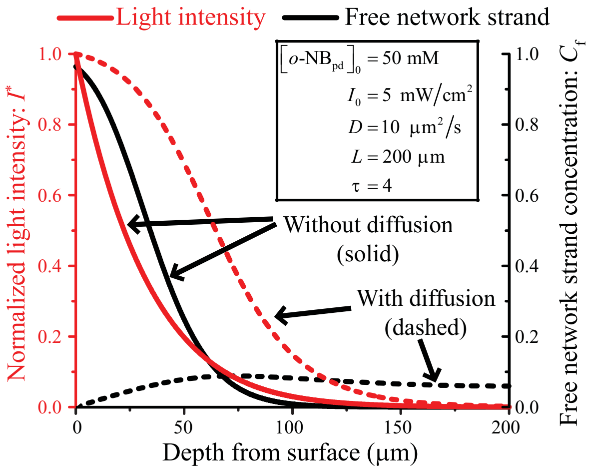

Figure 2.6: **Finite diffusion coefficients.**
The free network strand concentration and light intensity profiles with and without diffusion. A fixed concentration boundary condition is applied at the sample surface $C_{\text{f}}(X = 1, \tau) = 0$. When free network strands are removed from the sample surface, light is able to penetrate further into the sample.

different boundary conditions with $D \to \infty$. As seen within this range of τ, $\max|\Delta C_{\text{i}}|$ increases with larger τ. In both Case 1 and Case 2, when degree of degradation τ is large, diffusion plays a significant role in the degradation behavior. When an infinite half-space of medium exists above the sample (Case 3), almost no deviation from the diffusionless model occurs even at large degrees of degradation. Still unknown, however, are the experimental conditions under which ΔC_{i} will be significant.

2.4.2 Finite Diffusion Coefficients

In network photodegradation, photoabsorbing free network strands are relocated via diffusion, which changes the light intensity profile. **Figure 2.6** shows a sample network degradation with and without diffusion. It plots the light intensity profile $I^*(x, \tau = 4)$ and the free network strand concentration profile $C_{\text{f}}(x, \tau = 4)$ across the sample's physical depth. At the sample surface, a fixed concentration boundary condition $C_{\text{f}}(X = 1, \tau) = 0$ is applied which decreases the concentration of free network strands close to the surface. This redistribution of free network strands allows light to penetrate further into the network. As such, the degradation of intact linkages is affected.

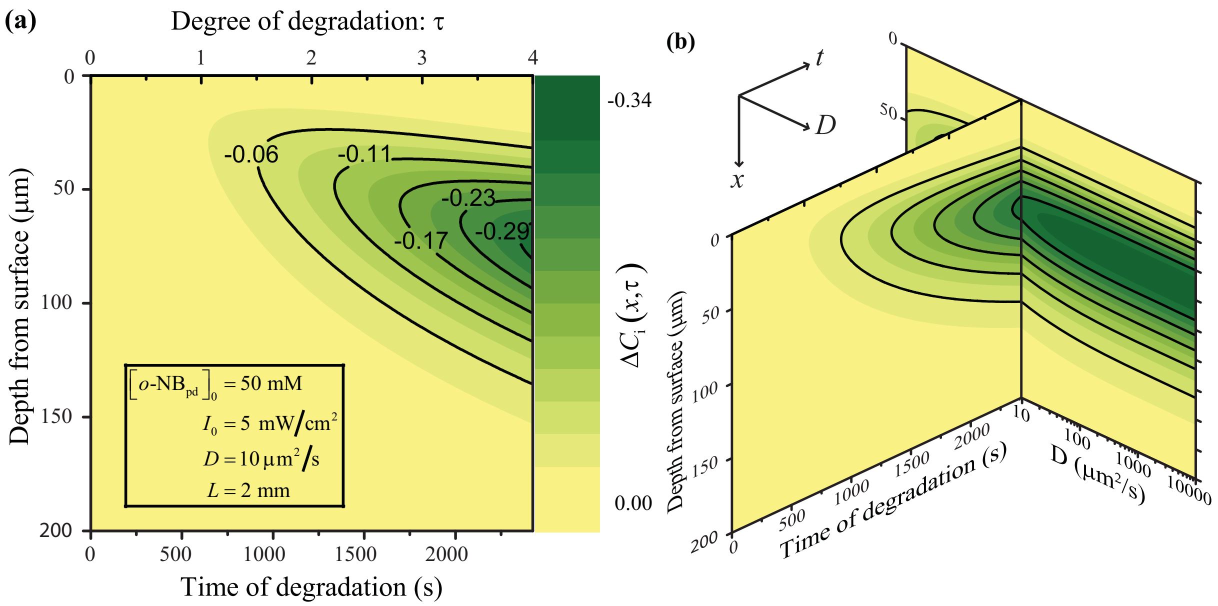

Figure 2.7: **Depicting changes to network degradation.**
(a) A representative contour plot of the diffusion-induced discrepancy of the intact network strand concentration (ΔC_i) as a function of time and depth with $D = 10\ \mu\mathrm{m}^2\ \mathrm{s}^{-1}$ and asymmetric boundary conditions (BC2). **(b)** This plot is expanded across a range of diffusion coeffients. ΔC_i is plotted as a function of the depth and D at a fixed degree of degradation $\tau = 4$.

Figure 2.7a shows $\Delta C_\mathrm{i}(x,\tau)$ as a function of the degradation time and depth from the sample surface. While this time-dependent degradation profile is important, we are more interested in what impact experimental factors have on ΔC_i. We calculated ΔC_i as a function of the following variables: 1) the diffusion coefficient D, 2) the incident light intensity I_0, 3) the initial concentration of the photodegradable linkages $c_{\mathrm{pd},0}$, 4) the total sample thickness L, and 5) the quiescent layer thickness h. To examine the effect of the diffusion coefficient, we expand Figure 2.7a – which pertains only to a single coefficient $D = 10\ \mu\mathrm{m}^2\ \mathrm{s}^{-1}$ – over a range of coefficients and plot $\Delta C_\mathrm{i}(x, \tau = 4; D)$ as a function of D and x. Figure 2.7b shows how these two plots are related, where $\Delta C_\mathrm{i}(x,\tau;D)$ is plotted as a function of all three variables and the two plots connect at $\tau = 4$ and $D = 10\ \mu\mathrm{m}^2\ \mathrm{s}^{-1}$.

2.4.2.1 Double No-Flux Boundaries (BC1/BC3)

First, we examine the geometry of a sample is bounded by two no-flux boundaries (Figure 2.3a, 2.3c and Equation (2.17a)). In the following analyses, unless otherwise stated, the experimental parameters are fixed at $I_0 = 5\ \mathrm{mW\ cm}^{-2}$, $c_{\mathrm{pd},0} = 0.05$ M, $L = 200\ \mu$m, $D = 100\mu\mathrm{m}^2\ \mathrm{s}^{-1}$, and $h = 0\ \mu$m (Table 2.3). The dimensionless time parameter, or degree of degradation, is again fixed at $\tau = 4$. In **Figure 2.8**, we see that ΔC_i changes across the sample depth. Thus, the physical location where $|\Delta C_\mathrm{i}|$ is largest is indicated by a dashed red line on the contour plots. The value of $\max|\Delta C_\mathrm{i}|$ is plotted as a function of the respective experimental variable above each contour plot. Since both D and I_0 are included in the dimensionless diffusion coefficient $D^* = D/(kI_0L^2)$ their effect on the network degradation can be combined into a single figure (Figure 2.8a). When either D increases or I_0 decreases, D^* becomes larger. As δ increases, diffusion has a greater impact on the system. When the diffusion coefficient is varied, we see higher D^* corresponds to greater degradation of the sample ($\Delta C_\mathrm{i} < 0$). At very large D^*, ΔC_i approaches an asymptotic value: $\lim_{D^*\to\infty} \max|\Delta C_\mathrm{i}| \to 0.19$. Free network strand diffusion starts to become a significant factor at $D \approx 100\mu\mathrm{m}^2\ \mathrm{s}^{-1}$ or larger. Similar values for D are exhibited by 10kDa macromolecules in hydrogels.[97] In the case of incident radiation intensity variability, lower I_0 leads to increased degradation ($\Delta C_\mathrm{i} < 0$). At low intensities, the degradation time required

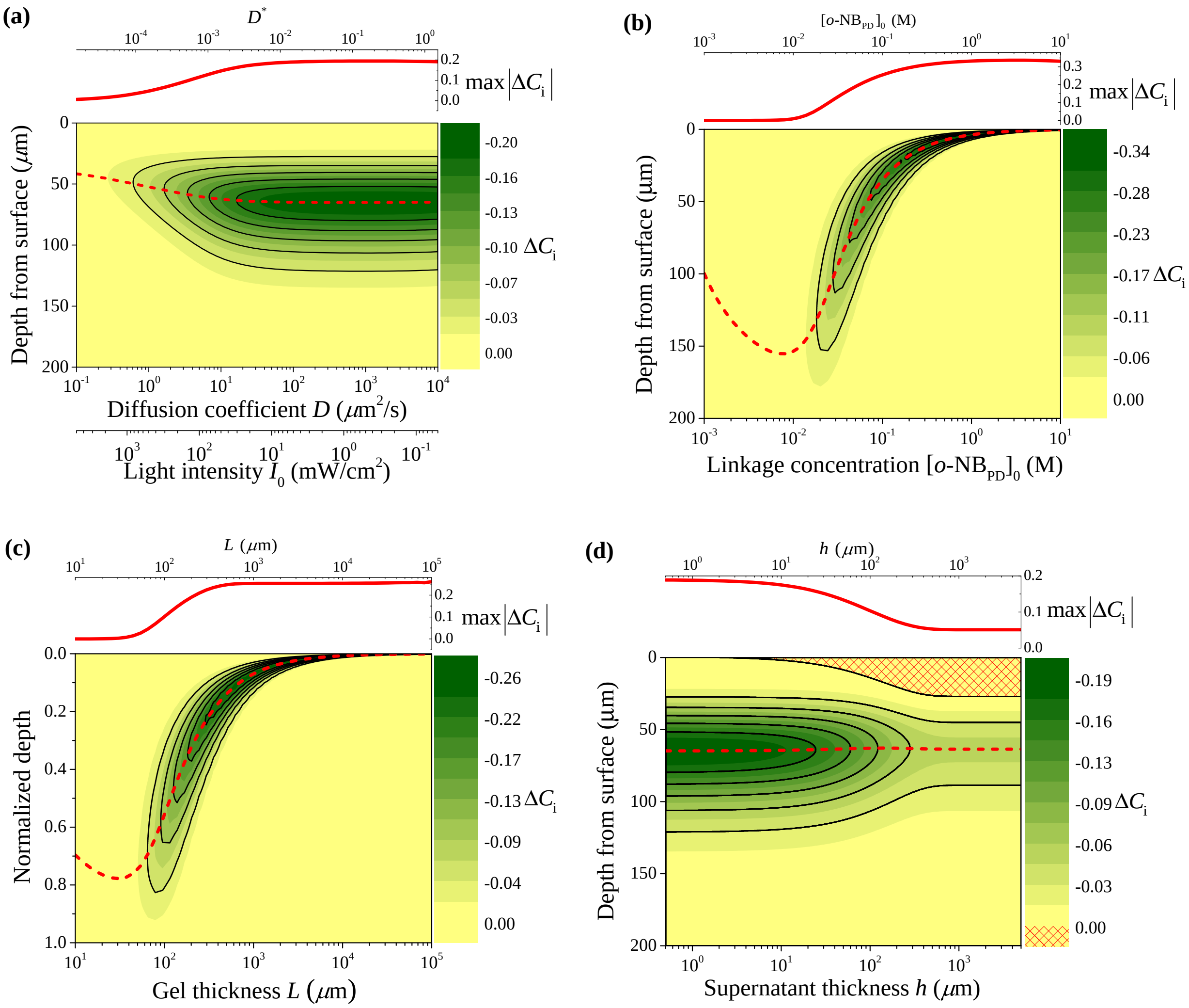

Figure 2.8: **Two no-flux boundary conditions.**
These contour plots show ΔC_i as a function of the sample depth and the experimental variable of choice. The dashed red line indicates the location of the maximum discrepancy $\max|\Delta C_\mathrm{i}|$ across the sample depth. This maximum discrepancy value is plotted as a function of the particular experimental variable: **(a)** the diffusion coefficient and incident light intensity, **(b)** the concentration of the photodegradable linkage, **(c)** the sample thickness, and **(d)** the quiescent layer thickness, where the red crosshatch marks indicate regions where diffusion of photoabsorbing species causes less degradation of the substrate ($\Delta C_\mathrm{i} > 0$).

is long; thus, the mobile species are able to sufficiently move throughout the network and alter the light intensity profile. Conversely, at higher intensities, the degradation time required is much smaller and the effect of diffusion is negligible. We see that diffusion becomes significant around $I_0 \approx 10$ mW cm^{-2}, which is within the range of intensities used experimentally for network degradation.[39] In Figure 2.8a, increases in ΔC_i are first seen at $D \approx 1$ μm^{2}s^{-1} or $I_0 \approx 500$ mW cm^{-2} which corresponds to $\delta \approx 1$. As predicted, above $\delta = 1$, diffusion becomes increasingly fast compared to the photodegradation reaction. Changes in ΔC_i are also seen across the sample depth. Near the surface, the light intensity profile is nearly uniform, regardless of δ, and diffusion of attenuating species has limited effect. At deeper regions, there is very little degradation due to significant light attenuation. The magnitude of ΔC_i, accordingly, decreases.

When increasing the initial concentration of the photodegradable linkages ($c_\mathrm{pd,0}$, Figure 2.8b), $|\Delta C_\mathrm{i}|$ grows and eventually reaches the asymptotic value: $\lim_{c_\mathrm{pd,0} \to \infty} \max|\Delta C_\mathrm{i}| \to 0.33$. With larger $c_\mathrm{pd,0}$, the majority of the degradation is localized to a thin region near the sample surface due to a substantial optical attenuation. This degradation localization increases the concentration gradient of mobile species and their diffusive flux. As $c_\mathrm{pd,0}$ is further increased, the degradation is limited to an infinitesimally thin region at the surface, and the flux of mobile species increases. In the limit of $c_\mathrm{pd,0} \to \infty$, the dimensionless flux $|D^* \nabla C_\mathrm{f}| \to \infty$. Increasing $c_\mathrm{pd,0}$ also has the effect of increasing the dimensionless parameter δ (see Equation (2.4)). Diffusion is predicted to occur faster than the photodegradation reaction. Conversely, as $c_\mathrm{pd,0}$ is lowered, the light intensity and degradation profiles approach uniformity along the light path and the flux decreases: as $c_\mathrm{pd,0} \to 0$, $D^* \nabla C_\mathrm{f} \to 0$. The ratio δ decreases, and diffusion will be much slower than the photodegradation reaction. Again, we see a region where diffusion becomes a significant factor and occurs at concentrations of $c_\mathrm{pd,0} \approx 0.05$ M, which is also well within the range of values used experimentally. In this example, $\delta = 1$ when $c_\mathrm{pd,0} \approx 5 \times 10^{-3}$ M; above which $|\Delta C_\mathrm{i}|$ increases.

Considering sample thickness L (Figure 2.8c), we notice that thicker samples increase $|\Delta C_\mathrm{i}|$, with $|\Delta C_\mathrm{i}|$ becoming significant around $L \approx 100 \mu$m. Thicker samples allow the mobile species to spread across a larger depth, leading to greater diffusion of photoabsorbing species away from the zone of degradation. Accordingly, the ratio of timescales δ does not depend on L. Diffusion does not become faster or slower with respect to the photodegradation reaction as $L \to \infty$. At large L, only the dilution of the free network strands changes where $\lim_{L\to\infty} C_\mathrm{f} \to 0$ at equilibrium. The maximum effect a change in sample thickness has on the diffusion-induced discrepancy is: $\lim_{L\to\infty} \max|\Delta C_\mathrm{i}| \to 0.26$.

When comparing the effects of the diffusion coefficient, the photodegradable linkage concentration, and the sample thickness, the maximum discrepancies are different and obey the following sequence: $\max|\Delta C_\mathrm{i}|_{c_{\mathrm{pd},0}\to\infty} > \max|\Delta C_\mathrm{i}|_{L\to\infty} > \max|\Delta C_\mathrm{i}|_{D\to\infty}$. As mentioned, with very large $c_{\mathrm{pd},0}$, the degradation is limited to a very thin region at the sample surface. This results in a large diffusive flux. With large L, light is able to penetrate further into the sample since the diffusable photoabsorbing species are more diluted. Yet, the diffusive flux does not increase greatly. When the diffusion coefficient D is large, the mobile species move quickly. However, the dilution of these photoabsorbing species is limited and significant attenuation of light occurs before reaching the zone of degradation.

When an unmixed, unreplenished quiescent fluid layer of height h is imposed above the substrate, mobile network strands can diffuse into this layer. When the free network strands reside in this layer they absorb light and reduce the degree of degradation within the underlying sample (Figure 2.3c). Increasing h allows for a greater number of mobile photoabsorbing species to reside in the layer, which further increases the attenuation of light. As a result, larger quiescent fluid layers increase the concentration of intact network strands within the sample below (Figure 2.8d). As shown, a fluid layer as thin as $h \approx 30$ μm will have a significant effect on the degradation profile. This condition most noticeably differs from that of the other variables (D, I_0, L, and $c_{\mathrm{pd},0}$) in that ΔC_i is positive near the substrate surface (as indicated by the red crosshatch marks). As shown in Figure 2.4 and 2.5, when $D \to \infty$ and $h \to \infty$, ΔC_i never reaches large positive values. During photodegradation, most free network strands are produced at the sample surface and attenuate light. If these free network strands diffuse further upbeam (into the overlying medium), the degradation of intact photodegradable linkages below remains relatively unchanged. Only when photoabsorbing free network strands diffuse downbeam (negative X-direction) or are removed completely from the uppermost regions of the substrate does the rate and depth of degradation increase.

2.4.2.2 Asymmetric Boundary Conditions (BC2/BC4)

When asymmetric boundary conditions are applied across the sample (BC2, Figure 2.3b), the fixed concentration (Dirichlet) boundary condition at the sample surface acts as the primary sink for diffusing species. The mobile photoabsorbing species produced at the sample surface are quickly removed through the high-flux Dirichlet boundary at $X = 1$. In contrast, models with two zero-flux boundary conditions (BC1/BC3), do not allow for the complete removal of mobile photoabsorbing species. This difference between the two boundary conditions leads to key distinctions in the photodegradation behavior (**Figure 2.9**). When a fixed concentration boundary condition is applied at $X = 1$, diffusion becomes significant across a larger range of experimental variables. We find that $|\Delta C_\mathrm{i}|$ increases at lower diffusion coefficients ($D \approx 1\ \mu\mathrm{m}^2\ \mathrm{s}^{-1}$ Figure 2.9a), higher light intensities ($I_0 \approx 100$ mW cm^{-2}, Figure 2.9a), lower photodegradable linkage concentrations ($c_{\mathrm{pd},0} \approx 0.01$ M, Figure 2.9b), and thinner sample thicknesses ($L \approx 30\ \mu$m, Figure 2.9c). As shown, diffusion significantly alters the degradation of the resulting network under practical experimental conditions.

Since a perfectly absorbing boundary condition is not physically realizable, the “instantly absorbing sink” boundary condition (BC2) is only an approximation. To more accurately model the effects of stirring in the supernatant, we impose an unmixed layer of thickness h (BC4, Figure 2.3d, Equation (2.17b)). The exact relation between the height of the unmixed layer thickness h and the “speed” or “vigor” of mixing is not well characterized, but approximated to be inversely proportional: $h \propto 1/V$, where V is the approximate velocity of mixing. The results given in Figure 2.9d indicate that the amount of fluid mixing has an effect on the final state of the degraded substrate. The thickness of the unmixed medium layer, at which $|\Delta C_\mathrm{i}|$ drops significantly, is larger when applying asymmetric boundary conditions ($h \approx 200\ \mu$m) than when applying two no-flux boundaries ($h \approx 30\ \mu$m).

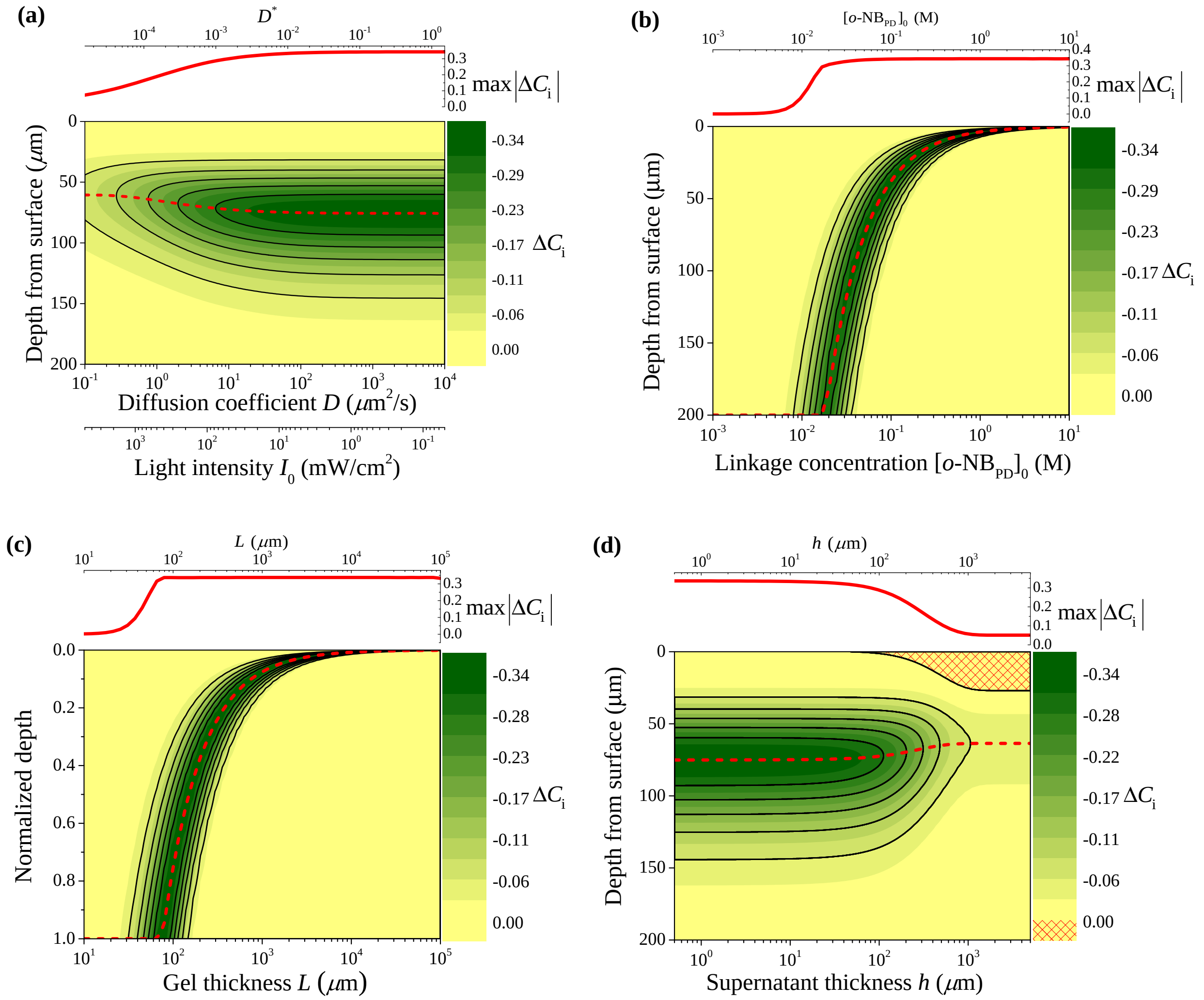

Figure 2.9: **Mixed boundary condition.**
These contour plots are analogous to those in Figure 2.8 except that they represent results computed for systems with asymmetric boundary conditions. As shown, when an absorbing sink boundary condition is added at the sample surface, diffusion becomes a more significant factor than when two no-flux conditions are applied. Again, the experimental variables shown are **(a)** the diffusion coefficient and incident light intensity, **(b)** the concentration of the photodegradable linkage, **(c)** the sample thickness, and **(d)** the quiescent layer thickness. The red crosshatch marked regions are where diffusion of mobile species causes less degradation of the network.

2.4.3 Effects of *o*-NB chemical properties

In addition to the model parameters presented here, it is also possible to elucidate the dependence of the model on linkage-specific chemical properties. The molar absorbtivity α_j is related to $c_{\mathrm{pd},0}$ through the dimensionless initial absorbance parameter $\alpha_j^* = \alpha_j c_{\mathrm{pd},0} L$. Hence, figures with variable $c_{\mathrm{pd},0}$ (Figures 2.8b and 2.9b) can predict changes in the network degradation as a function of α_j. With higher α_j^*, the zone of degradation is limited to a very thin region near the sample surface and diffusion is much faster than the photodegradation reaction. Both the diffusive flux and diffusion-induced discrepancy increase. Variation in the kinetic degradation constant k can be directly related to I_0 through dimensionless time $\tau = ktI_0$ and the dimensionless diffusion coefficient $D^* = D/(kI_0L^2)$. With increasing k, the time a diffusing species has to travel is shortened. At large k the degradation happens quickly and not enough time is allowed for diffusion have a significant effect. Conversely, when k is small, the mobile species are given sufficient time to diffuse. This behavior is predicted by a decrease in δ as k increases. Figures 2.8a and 2.9a predict changes in the network degradation as a function of k, for different values of D^*. For example, certain *o*-NB linkages have very low molar absorbtivity or very high rate constants of degradation such as the 1,3-dihydroxymethyl-2-nitrobenzene or 4-(3-(1-hydroxyethyl)-4-nitrophenoxy) butanoic acid moieties respectively.[39] For these linkages, diffusion is predicted to have diminished influence on the system.

2.5 Summary and Conclusions

The concentration of intact network strands C_i is an important attribute of water-swollen polymeric networks since it determines physical properties of the network such as the modulus E, swelling ratio Q, and network mesh size ξ. As photodegradable hydrogels gain use in lithography, accurate spatio-temporal modeling of these physical network properties is necessary. In photodegradable hydrogels, network strands freed by degradation continue to absorb light. When these photoabsorbing free network strands are removed and/or redistributed by diffusion, the light intensity profile is altered. As a direct consequence, photodegradation models incorporating diffusion give significantly different results than models not incorporating diffusion. We show that the degree of this difference strongly depends on certain experimental variables such as the incident light intensity I_0, diffusion coefficient D, photodegradable linkage concentration $c_{\mathrm{pd},0}$, and thickness of the substrate L. Accordingly, we demonstrate the importance of the boundary conditions during an experimental degradation. We find that if a no-flux (BC1) or absorbing sink (BC2) boundary condition is applied at the sample surface, the concentration of intact network strands is lowered (i.e., the hydrogel undergoes a greater degree of degradation). In a system containing an unmixed, unreplenished fluid layer of thickness h above the sample surface, mobile photoabsorbing species diffuse into this layer and attenuate light. As a result, less degradation of the underlying substrate takes place in certain regions.

Guide for Design and Optimization. Changes in the final network state, as caused by the diffusion of mobile photoabsorbing species, may or may not be desirable. When mass transfer by diffusion is accounted for, the shape of the $C_{\mathrm{i}}(x,t)$ profile changes and the concentration gradient of intact network strands along the beam path is more shallow (Figure 2.4). As photoabsorbing species are removed, the light intensity profile of the sample becomes more uniform. Thus, the diffusion of byproducts can be used to manipulate the mechanical gradation through the depth of the sample. Here, we classify $c_{\mathrm{pd},0}$ and α_j as "length scale altering" properties. Variation of $c_{\mathrm{pd},0}$ or α_j changes the attenuation length of the photons throughout the sample, as given by Beer's law. This influences the degradation rate profile along the sample depth and, consequently, the mobile species flux profile. However, $c_{\mathrm{pd},0}$ and α_j are inherent chemical properties of the *o*-NB linkages.It is possible to alter α_j somewhat by changing the chemistry of the photodegradable linkage.[39] They are not useful tools to controllably alter the degradation of the substrate. Likewise, D and I_0 are classified as "time scale altering" properties. These properties change the normalized characteristic time it takes a diffusing particle to travel a given distance. The diffusion coefficient D changes the travel speed of a molecule and I_0 changes total degradation time (lower I_0 requires a longer degradation time). The light intensity, which is externally controllable over several orders of magnitude, is the most reasonable way to use diffusion to alter the network strand density profile.

Model Limitations and Future Considerations. Recall that when hydrogel network strands are broken, the equilibrium swelling ratio Q increases, modulus E decreases, and mesh size ξ increases. These physical properties can be estimated from attributes of the polymer network.[100] In this model we do not account for how dynamic changes to the network physical properties might impact the degradation. For example, as the mesh size increases, mobile species diffuse more freely. However, we assume constant diffusion coefficients during the degradation process. As the volume of the network increases due to swelling, the diffusive species must also travel longer distances. These factors may play a significant role in the degraded state of the network. As an improvement, a more dynamic model accounting for changing physical properties can be constructed. This work also assumes that larger degradation products consisting of finite-sized aggregations of crosslinks and network strands are immobile. At large degrees of degradation or low branch point functionality f, the gel transitions from an highly crosslinked insoluble polymer network to an assembly of highly branched soluble polymeric aggregates. Thus, aggregate diffusion becomes more reasonable. While complete modeling of this process is complex, appropriate models can be created that account for aggregate diffusion.

2.6 Acknowledgments

Funding for this work was provided by the National Institutes of Health through the NIH Director's New Innovator Award Program, 1-DP2-OD008533. Tom Chou acknowledges support from the NSF through grant DMS-1516675.

CHAPTER 3

Stochastic-induced heterogeneities of end-linking polymer gel microstates

3.1 Abstract

Polymerization and formation of crosslinked polymer networks in an important process in manufacturing, materials fabrication, and in the case of hydrated polymer networks, biomedical materials, drug delivery, and tissue engineering applications. While considerable research has been devoted to the modeling of polymer networks to determine "average" properties in the mean-field, studies that specifically examine the variance and distribution of the polymer network micro-states are limited. In the present study, we mathematically model polymer networks composed of bifunctional A2 network strands that undergo an end-linking gelation process to a multi-functional crosslink center. The distribution of the network microstates is examined as a function of the extent of reaction. We specifically looked at how the micro/nano-structure of polymeric end-linking gels is formed, and the heterogeneity of these micro-regions in the gel (on the order of 100 individual network strands). We find that simply by the randomness of polymer strand end-linking, micro-regions within a larger gel network show high variability in terms of their crosslink density and topology. Adding to the strength of this model, we explore how such micro-regions are affected by the dynamics and kinetics of end-linking gelation. We allow the end-groups to reversibly bind and control the specific reactivity of the end-groups. As a result, we are able to better characterize the heterogeneous topology of polymer network microstates.

3.2 Introduction

The study and development of crosslinked polymer networks has been important in a wide range of applications from heavy industry to biomedical [101, 102, 50, 100, 103, 104, 105, 106]. Crosslinked polymer networks can be formed by various techniques, leading to different structures and properties. Of these network types, considerable attention has been paid to those formed by a process termed "end-linking". During end-linking gelation, polymer strands with two or more reactive ends bind at branch points/cross-links to form an infinite polymer network [107, 108]. For example, polyethylene glycol (PEG) based hydrogels are typically formed through the reaction of its end-groups. The end-groups of the bifunctional A_2 PEG polymer precursor can either react through 1) a binary condensation reaction with a multifunctional (> 2) junction/crosslink/branchpoint; or 2) if the end-groups are polymerizable, to multiple other end-groups – e.g., free-radical polymerization of vinyl end-groups. As this end-linking process proceeds, the respective reactive polymeric strands may exist in one of many states. In the case of bifunctional A_2 polymeric strands, each polymeric strand may exist in one of three states (see Figure 3.1): 1) the strand may be "free" where neither of the reactive ends have bound; 2) the strand may "dangle" where only a single end has bound and the strand dangles from the rest of the network; or 3) the strand may be "intact" where both ends are bound to the larger polymer network and bridge two different crosslink centers [109]. Strands with both ends bound, may form a loop, where both ends are bound to the same crosslink center [110]. In water-swollen polymeric networks, the proportion of these network strand states has important implications with regards to the material modulus, mesh size, and swelling[50].

3.2.1 Examination of polymer network microstates

While the average number of network strand states in the mean-field can be calculated as a function of the extent of reaction (p) [101, 102, 111, 112, 109], there is no bijective relation between the number of end-groups that have bound and the exact tallies of respective network strand states. This holds true for both the bulk network and the individual

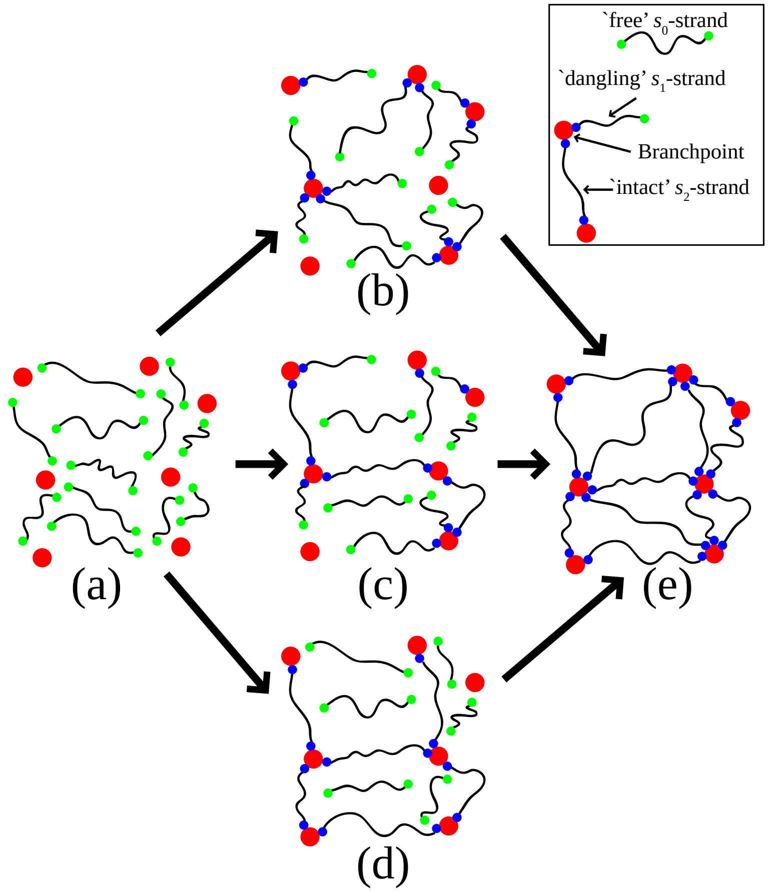

Figure 3.1: **Schematic of polymer network microstate evolution.** During the formation of a end-linking polymer network composed of A_2 polymeric strands, the network strands may exist in one of three states: "free" – neither end group is bound (s_0-strand); "dangling" – a single end group is bound (s_1-strand); or "intact" – both end groups are bound (s_2-strand). **(a)** During network formation, all network strands are initially in the s_0-state. **(b-d)** As end-linking proceeds, the composition of network strands can follow many paths. For example, when the extent of reaction $p = 0.5$, the is a finite probability that many different network microstates will exist. At the extremes, the different microstates could be composed of network strands that **(b)** all exist as s_1-strands, **(c)** exist as a combination of s_0-, s_1-, and s_2-strands, or **(d)** exist only s_0- and s_2-strands. **(e)** When the extent of reaction of complete ($p = 1$), only one microstate is possible where all network strands exist in the s_2-state.

micro-regions within the gel. A single extent of reaction, will instead, only give a probability that a specific set of network strand states exist (Figure 3.1). Thus far, researchers have mainly calculated the "average" number of network strand states, but not individual probabilities of individual sets of network strand states. Such "average" models, however, do not account for larger heterogeneities in the network structure that can occur though thermal concentration fluctuations of network strands (termed "frozen concentration fluctuation"), or heterogeneous distribution of crosslinking[113, 114, 115]. While network formation simulations have been performed to examine certain topological heterogenieties of the networks [116, 117, 118, 119, 120, 121, 122], they rely on Monte Carlo simulations, and do not study the probability distributions of large polymer network microstate configurations. In this work, we expand on these models: the dynamics and probability distributions of network microstates due to random end-linking is examined mathematically to find analytical solutions.

As proposed by Stepto and coworkers [123, 124, 125] the population of molecular species in the network-forming polymerizing mixture may be realized as a population of the states, or "subgraphs," of the monomeric network strands, where only a subset of the states is needed to describe the polymerization process. The existence probabilities of these states can be formulated. This subset of states approach has been expanded to examine topological defects of the polymer networks[126]. However, to the best of our knowledge, there is a lack of investigations examining analytical solutions to higher order combinations of network strands, e.g., where the number of network strands in each individual microstate/subgraph is $\gtrsim 10$. The study of the heterogeneity and distribution of microstates with high-network strand numbers is particularly important when the extent of reaction (p) is incomplete ($p < 1$), where p is defined as the fraction of end-groups that have bound to the network. At incomplete extents of reaction, variability of microstate populations will be highest. In this work, we consider and model the formation of very large microstate "subgraphs" of polymer network strands.

We consider the reaction of bifunctional A_2 polymer precursors, and also look more generally at higher order functional polymer precursors A_N where N is the number of reac-

Table 3.1: Summary of variables used.

Symbol	Representation	Value	Definition
N	Number of reactive end-groups per polymer precursor	2	-
ℓ	Number end-groups that have bound per polymer precursor	0, 1, 2	-
s_ℓ	Designation of strand type with ℓ bound end-groups	-	-
N_s	Number polymer strands per microstate	variable	$n_0 + n_1 + n_2$
n_0	Number of s_0-polymer strands (no bound end-groups)	variable	-
n_1	Number of s_1-polymer strands (a single bound end-group)	variable	-
n_2	Number of s_2-polymer strands (two bound end-groups)	variable	-
m	Number of end-groups that have bound per microstate	variable	$n_1 + 2n_2$
p	Extent of reaction	variable	$m/(N_s N)$
$P(n_1, n_2)$	Probability of microstate with composition $\{N_s - n_1 - n_2, n_1, n_2\}$	variable	(see Master Equation)

tive end-groups on each polymer precursor. For simplicity, we consider the reaction of the multifuctional A_N polymer precursor that combine at their end-groups without restriction to the number of end-groups that can combine at the crosslink/branchpoint (Figure 3.1). Accordingly, the total number of branchpoints in a single microstate has no effect on this model and can be incorporated afterwards to determine network physical properties. We simply examine the distribution of network strand states only. Based on models examining stochastic self assembly and nucleation [127, 128], we produce a Master Equation that is more complete than current mathematical methods to not only find average quantities of the network strand states, but also the entire probability distribution. This Master Equation allows us to further calculate quantities such as variance and first passage times. We also use the Master Equation to account for different reactivities of the different network strands during gelation, and devise a model where the network strand end groups can dynamically bond to the network.

3.3 Current combinatoric models

3.3.1 Bounded strand probability

Thus far the most common analyses of networks formed by end-linking of multi-functional strands have used combinatoric approaches which we here review [129, 130, 109, 42, 131]. For convenience, we refer to the different strand types in the network as s_ℓ-strands where ℓ is the number of strand end-groups that have bound to a branchpoint/crosslink center and, thus, to the greater network. We also assume that a maximal number of N end-groups per strand can bind the network so that $0 \leq \ell \leq N$. Hence, an unbound "free" strand where no reactive ends have bound is an s_0-strand; a singly-bound "dangling" strand where only one end-group has bound is a s_1-strand; a k-bound "partial" strand with $k < N$ end-groups bound is a s_k-strand. Finally, if all N end-groups have reacted and bound we have a fully integrated s_N-strand. It is typical to define the extent of reaction p as the percentage of all possible end-groups bound to the network at equilibrium. The value of p can also be interpreted as the probability that any end-group has joined the overall network. We can evaluate the probability $P_\ell(p)$ of finding s_ℓ-strands with $0 \leq \ell \leq N$ bound end-groups as

$$P_\ell(p) = \binom{N}{\ell} p^\ell (1-p)^{N-\ell} \tag{3.1}$$

which assumes that of N end-groups ℓ are bound and $N - \ell$ are not. The binomial formula ensures that the above probabilities are normalized to one

$$\sum_{\ell=0}^{N} P_\ell(p) = \sum_{\ell=0}^{N} \binom{N}{\ell} p^\ell (1-p)^{N-\ell} = (p + 1 - p)^N = 1. \tag{3.2}$$

This combinatoric approach yields the probability of observing a given total number of different network strand states at equilibrium assuming that the fraction of bound end-groups is fixed. In Figure 3.2 we show schematics of A_2 and A_3 networks and corresponding plots of $P_\ell(p)$ of finding s_ℓ-strands as a function of the extent of reaction p. Equation 3.2 is the basis for many other end-linking gelation models which assume that all end-groups carry the same reactivity α, regardless of the state of the strand they are attached to. This may not always be the case in realistic scenarios. For example, end-groups of an unbound strand might bind more readily than a dangling, partially bound strand, since diffusion may allow the unbound strand to more freely navigate the environment and find appropriate reaction sites. Conversely, in other realizations, the unbound end-group of a dangling strand might more readily bind due to its proximity to the overall polymerizing network, especially when the polymer concentration is dilute.

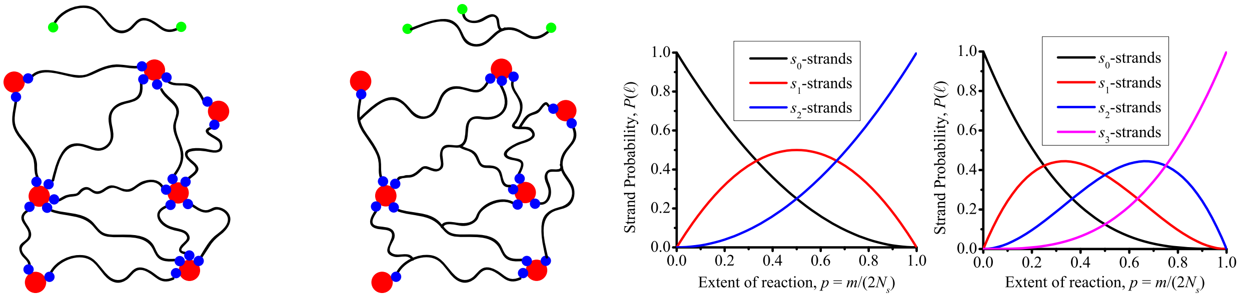

(a) (b) (c) (d)

Figure 3.2: **Representation of A_2 and A_3 networks.**
Representation of **(a)** A_2 and **(b)** A_3 network strands and the corresponding networks that are formed from these strands, respectively. Such networks can be modeled in the mean-field where the probability $P(\ell)$ of the different s_ℓ-strand types is plotted as a function of the extent of reaction p for **(c)** A_2 and **(d)** A_3 network strands.

Furthermore, network formation (or induced degradation) may occur in a different settings: it may be an irreversible or “quenched” forward processes that follows a specific path, and that is highly dependent on the initial conditions; but it may also be a reversible phenomenon, and rearrangements may also be possible. Finally, one may be interested in the probability distribution for a specific microstate configuration, where the number of nul, single, k, or N bound end-groups is specified, or in the time-evolution of the system. The goal of this paper is to present a mathematical framework to allow for a more detailed analysis of the system that can go beyond Equation 3.2. We will do this via a Master Equation where different reactivities of unbound or partially bound end-groups are specified and where reversible or irreversible binding events will be considered and where explicit time-dependence will be included.

3.3.2 Equilibrated distribution

Before introducing our Master Equation, we determine the equilibrium probability distribution for a given network microstate based on combinatoric arguments and under complete reversibility of the system. We consider a pool (or solution) of N_s polymeric network strands, where at most N end-groups per strand can bind, resulting in a total of N_sN available end-groups. For simplicity we set $N = 2$, the most representative experimental scenario [107].

Our goal is to determine the number of ways one can distribute n_0 unbound s_0-strands, n_1 singly bound s_1-strands, and n_2 doubly bound s_2-strands among the total number of strands N_s, given that a specific number of end-groups m have bound. The above quantities are related by $n_0 + n_1 + n_2 = N_s$ since all strands must be accounted for, and by $n_1 + 2n_2 = m$ to include the contribution of each strand type to the total end-group count. Hence a given microstate $\{n_0, n_1, n_2\}$ can be equivalently described by $\{N_s, m, n_2\}$. The extent of reaction p can also be determined from $\{N_s, m, n_2\}$ via $p = m/NN_s = m/2N_s$; by definition $0 \leq p \leq 1$ since the number of bound end strands m cannot exceed the total number of available ones $2N_s$. If we now assume that the reactive end-groups bind and unbind reversibly while maintaining constant m, we can write the number of ways $\mathcal{N}(n_0, n_1, n_2)$ to realize a given microstate $\{n_0, n_1, n_2\}$ at equilibrium through a simple combinatoric argument

$$\mathcal{N}(n_0, n_1, n_2) = 2^{n_1} \binom{N_s}{n_0\, n_1\, n_2}. \tag{3.3}$$

Here the 2^{n_1} factor arises from the fact that bound end-groups on s_1-strands can be arranged in two configurations per strand. The above can be rewritten using $n_0 = N_s - m + n_2$ and $n_1 = m - 2n_2$ as follows

$$\mathcal{N}(N_s, m, n_2) = \frac{2^{m-2n_2} N_s!}{(N_s - m + n_2)!(m - 2n_2)!n_2!} \tag{3.4}$$

Upon summing over n_2 we derive $Z_{N_s,m}$ the partition function for all possible configurations, once N_s, m are fixed

$$Z_{N_s,m} = \sum_{n_2=0}^{[m/2]} \mathcal{N}(N_s, m, n_2) \tag{3.5}$$

where $[\cdot]$ indicates the integer part of its argument. The equilibrium probability distribution can now be calculated as $P_{N_s,m}(n_2) = \mathcal{N}(N_s, m, n_2)/Z_{N_s,m}$, from which we can calculate the following average strand populations

$$\langle n_2 \rangle = \sum_{n_2=0}^{[m/2]} n_2 P_{N_s,m}(n_2) \tag{3.6a}$$

$$\langle n_1 \rangle = m - 2\langle n_2 \rangle \tag{3.6b}$$

$$\langle n_0 \rangle = N_s - m + \langle n_2 \rangle \tag{3.6c}$$

The expression for $P_{N_s,m}(n_2)$ can be useful to also determine other quantities of interest, such as the variance and higher moments. So far, we have assumed that the binding and unbinding of any strand end-group is independent of the number of bound end-groups already present on a strand. At times, however, bound end-groups may promote or hinder the binding of other end-groups, leading to so called cooperative or uncooperative binding. For example, two s_1-strands may more easily link, forming an extra s_2-strand due to the proximity of their unbound end-groups. Cooperative binding is at play here ; the opposite case may also emerge, wherethe formation of an s_2-strand from two s_1-strands is instead hindered by negative allosteric effects. We thus write

$$\mathcal{N}(N_s, m, n_2, \alpha) = \frac{(2/\alpha)^{m-2n_2} N_s!}{(N_s - m + n_2)!(m - 2n_2)!n_2!}. \tag{3.7}$$

Here, $\alpha > 1$ represents cooperative binding, which penalizes configurations with $n_1 = m - 2n_2$ partially bound end-groups, thus favoring $s_1 \to s_2$ events. The case $\alpha < 1$ represents the opposite case of uncooperative binding. Finally, the probability distribution at equilibrium $P_{N_s,m,f}(n_2)$ can be written as

$$P_{N_s,m,\alpha}(n_2) = \mathcal{N}(N_s, m, n_2, \alpha) \Bigg/ \sum_{n_2=0}^{[m/2]} \mathcal{N}(N_s, m, n_2, \alpha). \tag{3.8}$$

3.4 Master Equation

In this section we introduce the Master Equation to describe the time evolution for the probability $P(n_0, n_1, n_2, t)$ of finding the polymer network in a given $\{n_0, n_1, n_2\}$ microstate at time t. The transition rates between states are dictated by a reaction matrix as we will outline below. Since the total number of strands is constant, the overall constraint $n_0 + n_1 + n_2 = N_s$ will be obeyed. We will consider various realizations, including irreversible/reversible binding, and the possibility of cooperativity. We will compare equilibrium or steady state solutions to Equation 3.1 and Equation 3.7; where possible we will also determine the full time-dependent solution.

3.4.1 Irreversible end-group binding to the network

The first case we consider is that of irreversible attachment, whereby once an end-group has bound to the network, it will not detach. We also assume the binding rate λ is constant, although cooperative binding effects may be included. Under these conditions, the Master Equation for the probability $P(n_1, n_2, t)$ of a microstate with n_1 network strands bound at one end and n_2 network strands bound at both ends at time t, evolves according to

$$\begin{aligned}\frac{dP(n_1,n_2,t)}{dt} =& 2\lambda(N_s - n_1 - n_2 + 1)P(n_1 - 1, n_2, t) + \\ & \lambda\alpha(n_1 + 1)P(n_1 + 1, n_2 - 1, t) - \\ & \lambda[2(N_s - n_1 - n_2) + \alpha n_1]P(n_1, n_2, t),\end{aligned} \tag{3.9}$$

where we have explicitly used the $n_0 = N_s - n_1 - n_2$ constraint. The parameter α represents possible cooperative effects: $\alpha > 1$ implies that the $s_1 \rightarrow s_2$ binding event is more likely than the $s_0 \rightarrow s_1$ one; the reverse is true for $\alpha < 1$. The first term on the right hand side of Equation 3.9 represents the process of an unbound strand attaching to the network structure to form a singly bound dangling strand ($s_0 \rightarrow s_1$, Figure 3.3), which gives the microstate transition $\{n_0 + 1, n_1 - 1, n_2\} \rightarrow \{n_0, n_1, n_2\}$ (See Figure 3.4). The multiplicative factor $N_s - n_1 - n_2 + 1$ represents the number s_0-strands in the previous microstate that have

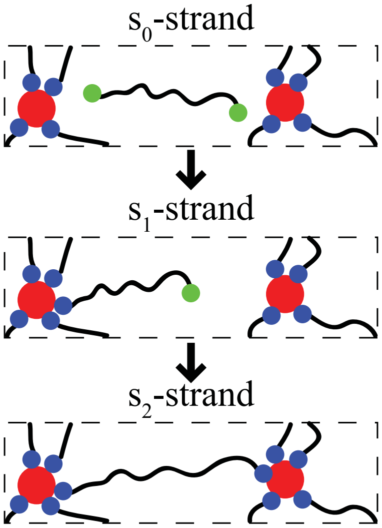

Figure 3.3: **Schematic of the process of end-group binding to the overall network and network strand transition.**
An unbound s_0-strand initially binds to the overall network at one of it's two end groups to form a s_1-strand. This s_1-strand can undergo further binding via the unbound end-group to form a s_2-strand that is fully bound to the network.

the ability to bind to the network; the 2 prefactor is also included since a s_0-strand can bind to the network at either of its two unbound end-groups. Similarly, the second term represents an unbound end-group from a singly bound strand binding to the network and forming a doubly bound strand ($s_1 \to s_2$, Figure 3.3). The related transition is $\{n_0, n_1 + 1, n_2 - 1\} \to \{n_0, n_1, n_2\}$ (Figure 3.4). The multiplicative factor $n_1 + 1$ represents the number of s_1-strands that can bind to the network to form an s_2-strand. Finally the last term describes the processes that drives the system out of the $\{n_0, n_1, n_2\}$ microstate, where either an $s_0 \to s_1$ transition, with $\{n_0, n_1, n_2\} \to \{n_0 - 1, n_1 + 1, n_2\}$, or a $s_1 \to s_2$ transition, with $\{n_0, n_1, n_2\} \to \{n_0, n_1 - 1, n_2 + 1\}$, occur (Figure 3.4). Due to the irreversibility of the dynamics, at $t \to \infty$ the system will consist of only s_2-network strands $P(n_1, n_2, t \to \infty) = 0$ for all $\{n_1, n_2\} \neq \{0, N_s\}$ and $P(0, N_s, t \to \infty) = 1$ (Figure 3.1f). For simplicity we rescale time in Equation 3.9 via $\lambda \alpha t \to t'$ to give

$$\begin{aligned}\frac{dP(n_1, n_2, t)}{dt} =& z(N_s - n_1 - n_2 + 1)P(n_1 - 1, n_2, t) + \\ & (n_1 + 1)P(n_1 + 1, n_2 - 1, t) - \\ & [z(N_s - n_1 - n_2) + n_1]P(n_1, n_2, t),\end{aligned} \tag{3.10}$$

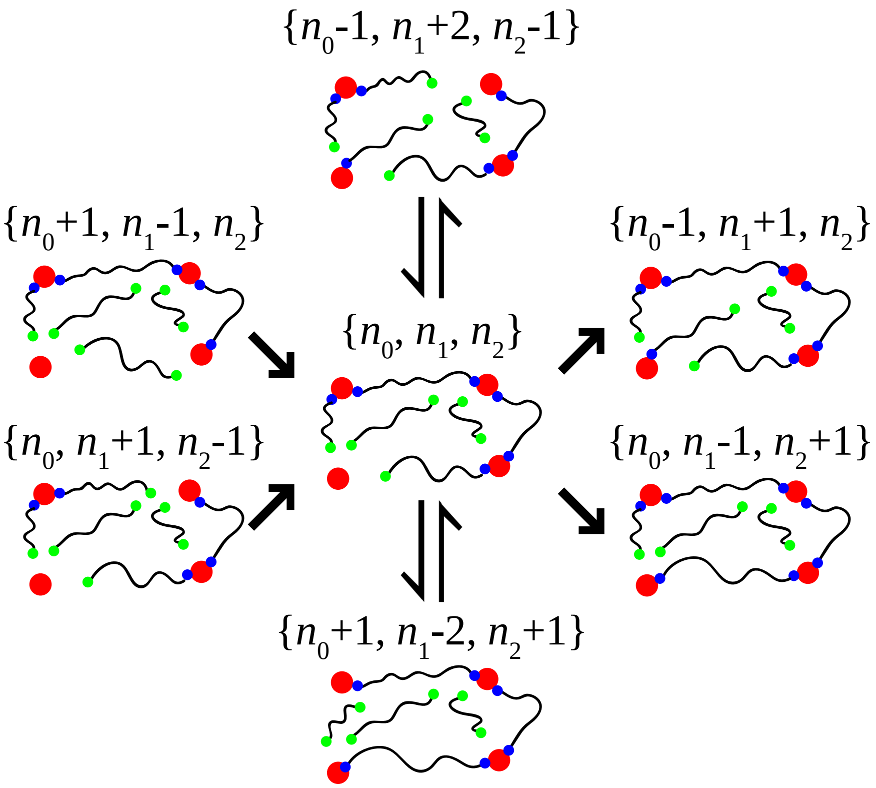

Figure 3.4: **Schematic of potential microstate transitions where $N_s = 6$ network strands.**
In this schematic we examine, as an example, the "ground state" where $\{n_0, n_1, n_2\} = \{2, 2, 2\}$, and the paths in which the microstate can transition. Microstate transitions from left-to-right represent the process of more end-groups binding to the network. The $\{n_0, n_1, n_2\}$ microstate can be formed, or dismantled. In the case of reversible end-group rearrangement, the number of bound groups is constant, but the microstate changes form (vertical direction).

where $z = 2/\alpha$ and where we have dropped the prime notation ($t' \to t$) for simplicity. We can now define the average number of strand types $\langle n_\ell(t) \rangle$ via

$$\langle n_\ell(t) \rangle = \sum_{n_1, n_2} n_\ell P(n_1, n_2, t), \tag{3.11}$$

for $\ell = 1, 2$, under the constraint that $0 \leq n_1 + n_2 \leq N_s$. The corresponding mass action equations can be derived by multiplying Equation 3.10 by n_ℓ and by summing over n_1, n_2

under the same constraint so that

$$\begin{aligned}\frac{d\langle n_0(t)\rangle}{dt} &= -\,z\langle n_0\rangle, && (3.12a)\\ \frac{d\langle n_1(t)\rangle}{dt} &= z\langle n_0\rangle - \langle n_1\rangle, && (3.12b)\\ \frac{d\langle n_2(t)\rangle}{dt} &= \langle n_1\rangle, && (3.12c)\end{aligned}$$

Equation 3.12 can be solved under the initial condition $n_0(0) = N_s$, modeling an initially totally unbound network. We find

$$\begin{aligned}\langle n_0(t)\rangle &= N_s e^{-zt}, && (3.13a)\\ \langle n_1(t)\rangle &= N_s\frac{z}{z-1}(e^{-t} - e^{-zt}), && (3.13b)\\ \langle n_2(t)\rangle &= N_s\left(1 + \frac{e^{-zt} - ze^{-t}}{z-1}\right) && (3.13c)\end{aligned}$$

from which it can be seen that $\langle n_\ell(t \to \infty)\rangle \to 0$ for $\ell = 0, 1$ and $\langle n_2(t \to \infty)\rangle \to N_s$. To connect Equations 3.13 to Equation 3.1 we evaluate $\langle m\rangle = \langle n_1\rangle + 2\langle n_2\rangle$ to find

$$\langle m(t)\rangle = \frac{N_s}{z-1}\left[[(2-z)e^{-zt} - ze^{-t} + 2(z-1)\right]. \tag{3.14}$$

Inverting the above transcendental equation is not possible, however upon setting $z = 2$, that is, under neutral cooperative conditions $\alpha = 1$, we find

$$\langle m(t)\rangle = 2N_s[1 - e^{-t}], \tag{3.15}$$

which can be inverted to yield

$$e^{-t} = 1 - \frac{\langle m(t)\rangle}{2N_s} = 1 - \langle p\rangle, \tag{3.16}$$

where we have identified the average extent of the reaction $\langle p\rangle$ with $\langle p\rangle = \langle m(t)\rangle/2N_s$, and where t and $\langle p \rangle$ are monotonic functions of each other. Equations 3.13 can be now recast as

$$\langle n_0(p) \rangle = N_s(1 - \langle p \rangle), \tag{3.17a}$$

$$\langle n_1(p) \rangle = 2N_s \langle p \rangle (1 - \langle p \rangle), \tag{3.17b}$$

$$\langle n_2(p) \rangle = N_s \langle p \rangle^2. \tag{3.17c}$$

As can be seen upon comparison with Equation 3.1, Equations 3.17 obey the following identity $\langle n_\ell(p) \rangle = N_s P_\ell(p)$, implying that the standard combinatoric approach is recovered when we consider a time-dependent irreversible deposition process described by Equation 3.10 without cooperative effects, $\alpha = 1$. The Master Equation 3.10 however is much more powerful as it allows us to follow the time dynamics of the system and offers much more information than Equation 3.1. For example, Equation 3.10 can be solved directly to find the microstate distribution at all times, $P(n_1, n_2, t)$. To do this we introduce the generating function $G(x, y, t)$ defined as

$$G(x, y, t) = \sum_{n_1, n_2} P(n_1, n_2, t) x^{n_1} y^{n_2}, \tag{3.18}$$

under the constraint $0 \leq n_1 + n_2 \leq N_s$. Upon multiplying Equation 3.10 by $x^{n_1} y^{n_2}$ and summing over n_1, n_2, under the same constraint, we find the following differential equation for $G(x, y, t)$

$$\frac{\partial G}{\partial t} = -z(x - y)\frac{\partial G}{\partial x} - (y - 1)\frac{\partial G}{\partial y}. \tag{3.19}$$

Equation 3.19 is coupled to the corresponding initial condition $G(x, y, t = 0) = x^{N_s}$. Using the method of characteristics we find

$$G(x, y, t) = \left[x e^{-zt} + \frac{zy}{z - 1}(e^{-t} - e^{-zt}) + \left(1 - \frac{1}{z - 1}(z e^{-t} - e^{-zt}) \right) \right]^{N_s}. \tag{3.20}$$

After performing a Taylor series expansion in x, y and upon comparison with Equation 3.18

we find

$$P(n_1,n_2,t) = \binom{N_s}{n_1,n_2} e^{-z(N_s-n_1-n_2)t} \left(\frac{ze^{-t}-ze^{-zt}}{z-1}\right)^{n_1} \left(1-\frac{ze^{-t}-e^{-zt}}{z-1}\right)^{n_2}. \tag{3.21}$$

Note that $P(n_1, n_2, t \to \infty) = 0$ for $\{n_1, n_2\} \neq \{0, N_s\}$ and that $P(0, N_s, t \to \infty) = 1$ as expected from an irreversible process. Also note that the time-dependent solution for $P(n_1, n_2, t)$ in Equation 3.21 depends on the initial conditions.

3.4.2 Reversible end-group rearrangement/redistribution

We now include an equilibration process that allows the bound end-groups to dynamically rearrange their binding sites on the network if the extent of reaction is not complete and $m < NN_s$ (Figure 3.4). Note that we are assuming that the total number of bound-ends $m = n_1 + 2n_2$ is fixed, and that the system readjusts the manner in which these bound-ends divide into singly-bound, or doubly-bound. Since the equilibration process yields a distribution that is independent of the initial configuration, we can select any starting point that yields m bound-ends. We write the equilibration Master Equation for $P(n_1, n_2, t)$ as follows:

$$\begin{aligned}\frac{dP(n_1,n_2,t)}{dt} =& 2\kappa\alpha^2\binom{n_1+2}{2}P(n_1+2,n_2-1,t)+\\ & 4\kappa(N_s-n_1-n_2+1)(n_2+1)P(n_1-2,n_2+1,t)-\\ & 2\kappa\alpha^2\binom{n_1}{2}P(n_1,n_2,t)-\\ & 4\kappa n_2(N_s-n_1-n_2)P(n_1,n_2,t).\end{aligned} \tag{3.22}$$

where κ is the rate at which network strand end-groups move within the network which we assume for simplicity to be constant. The first term on the right hand side of Equation 3.22 accounts for the process of forming a s_2-strand and a s_0-strand from two s_1-strands ($2s_1 \to s_0 + s_2$; Figure 3.4). In this process the bound end-group of one of the two s_1-strands "hops" to the unbound end-group of the other s_1-strands to give the microstate transition $\{n_0 - 1, n_1 + 2, n_2 - 1\} \to \{n_0, n_1, n_2\}$. The combinatorial factor accounts for how many pairs of s_1-strands are available for this process, while the 2 prefactor is due a bound end-group being able to hop from either of the two s_1-strands to the other. The binding factor α is squared, since the formation of an s_2-strand arises from the binding of two s_1-strands. The second term on the right hand side represents the reverse process, a bound end-group "hops" from a s_2-strand and relocates to an unbound end-group on a s_0-strand, $\{n_0 + 1, n_1 - 2, n_2 + 1\} \to \{n_0, n_1, n_2\}$ (Figure 3.4), giving rise to two s_1-strands. The factors $(N_s - n_1 - n_2 + 1)(n_2 + 1)$ represent the number of unbound and doubly bound network strands available, respectively. The 4 prefactor accounts for the number of possible bond movements: either of the two bound end-groups on the s_2-strand can relocate to either of the two unbound end-groups of the s_0-strand, yielding a total of four combinations. The last two terms represent the the same two processes described above, but driving the system away from the configuration $\{n_0, n_1, n_2\}$ as shown in Figure 3.4. Note that in Equation 3.22 there are no terms that represent the process of network bonds leaving a s_2-strand to populate a s_1-strand; this transition would not change the overall the microstate configuration $\{n_0, n_1, n_2\}$. Finally, the probability $P_{\mathrm{b}}(m, t)$ of having m bound-ends at time t can be written as

$$P_{\mathrm{b}}(m, t) = \sum_{n_2=0}^{[m/2]} P(m - 2n_2, n_2, t) \tag{3.23}$$

where the weight of all possible n_1, n_2 combinations that yield $m = n_1 + 2n_2$ bound-ends are added. Equation 3.22 ensures that $dP_{\mathrm{b}}(m, t)/dt = 0$; that is that m does not change once the rearrangement dynamic is at play as expected.

In addition to the $n_1 + 2n_2 = m$ constraint, the number of strands is also fixed so that $n_0 + n_1 + n_2 = N_s$. As a result of these two relationships we can cast Equation 3.22 in terms of only one of the network strand populations $\{n_0, n_1, n_2\}$. We choose n_2 and determine the steady state $P(n_2, t \to \infty) \equiv P^*(n_2)$ by imposing detailed balance between the first and the last term on the right hand side, or equivalently, the second and the third. One can verify that the conditions are the same. We find

$$\frac{P^*(n_2-1)}{P^*(n_2)} = \frac{4n_2(N_s-m+n_2)}{\alpha^2(m-2n_2+2)(m-2n_2+1)} \tag{3.24}$$

which can be solved to yield

$$P^*(n_2) = \frac{1}{Z_{m,N_s}}\frac{(2/\alpha)^{m-2n_2}N_s!}{(m-2n_2)!n_2!(N_s-m+n_2)!}, \tag{3.25}$$

where Z_{m,N_s} is the normalization constant

$$Z_{m,N_s} = \sum_{n_2=0}^{[m/2]} \frac{(2/\alpha)^{m-2n_2}N_s!}{(m-2n_2)!n_2!(N_s-m+n_2)!}. \tag{3.26}$$

As can be seen, this result is the same as in Equation 3.7, confirming that the combinatoric result evaluated through the equilibrated distribution, is equivalent to allowing for relaxation on the network with a fixed number of bound end-strands m.

3.5 Numerical Results And Discussion

3.5.1 Equilibrated distributions using the partition function

In this section we present and discuss results from the numerical evaluation of the equilibrated distribution in Equations 3.4 and 3.7 and related quantities. The equilibrium microstate distribution $P_{m,N_s}(n_2)$ for a given extent of reaction $p = m/2N_s$, but for different numbers of n_2 s_2-strands is plotted in Figures 3.5a – 3.5c for three different values of the cooperative factor α. We choose this representation since the number of "intact" or "elastically effective" s_2-network strands determines both the mechanical modulus and swelling behavior of the polymer network [50].

Note that as α increases, the probability of finding microstates with more s_2-strands, at lower values of m, increases as might be expected. Accordingly, in Figure 3.5d we plot the average strand fractions $\langle n_\ell \rangle / N_s$ as evaluated via Equations 3.6 for $N_s = 40$ and as a function

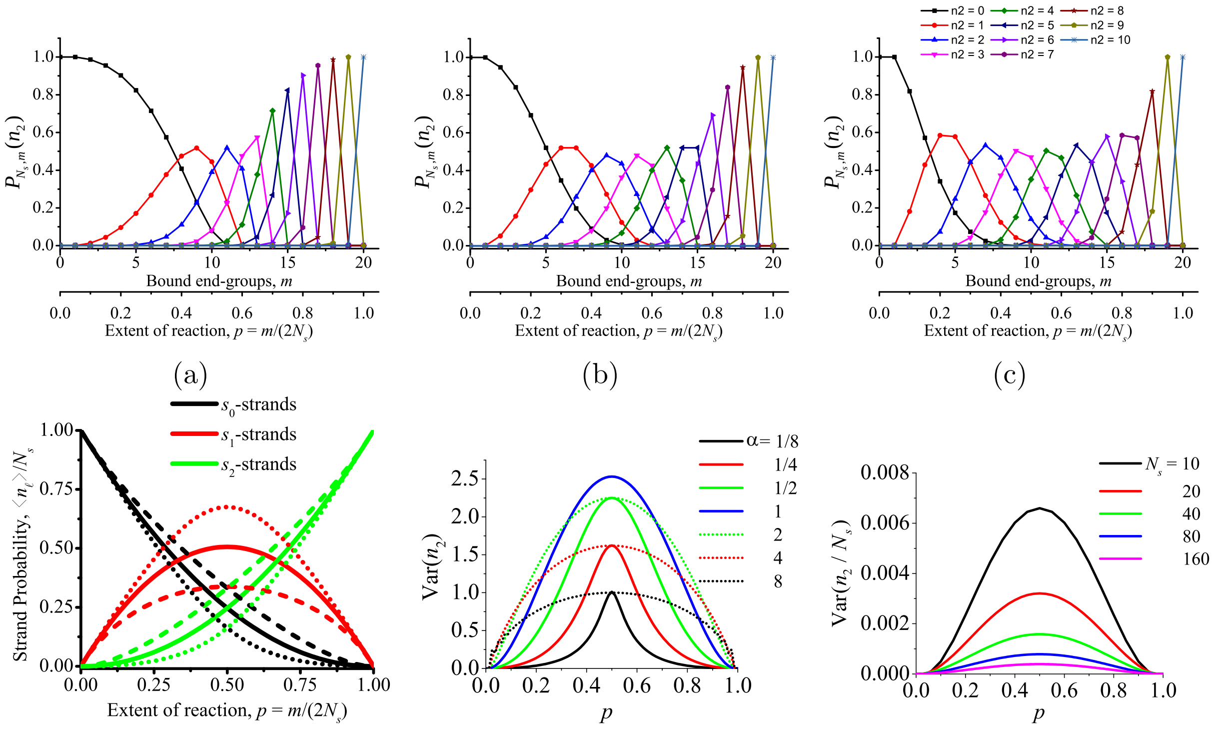

(a) (b) (c)

(d) (e) (f)

Figure 3.5: **Microstates as produced by the equilibrated distribution.** **(a-c)** Distribution of microstates in a system with 10 network strands as a function of the extent of reaction p. Each data point represents a different microstate $\{n_0, n_1, n_2\}$. The individual microstate probabilities are calculated given **(a)** $\alpha = 0.5$, **(b)** $\alpha = 1$, and **(c)** $\alpha = 2$. Microstates with the same number of s_2-strands are connected with lines. **(d)** Average microstate strand populations $\langle n_\ell \rangle / N_s$ when $N_s = 40$ given (dotted line) $\alpha = 0.5$, (solid line) $\alpha = 1$, and (dashed line) $\alpha = 2$. **(e)** The variance of n_2 as a function of p with variable α and $N_s = 40$. Dotted lines indicate the inverse value of the solid lines of the same color. **(f)** To compare the strand variance across microstates of increasing N_s, the variance of the fraction of strands in the s_2-state (n_2/N_s) is plotted. The fractional strand variance across the possible microstates maintains a maximum at $p = 0.5$ and decreases as the microstate grows in size.

of the extent of reaction p. Under neutral conditions, for $\alpha = 1$, the resulting average strand probabilities closely follow that of Figure 3.2c as calculated by the combinatorical approach in Section 3.3.1. Similarly to Equations 3.6 one can also calculate the second moments of the strand populations $\langle n_\ell^2 \rangle = \sum_{n_\ell=0}^{N_s}[n_\ell^2 P_(n_\ell)]$ and the resulting variance $\mathrm{Var}(n_\ell) = \langle n_\ell^2 \rangle - \langle n_\ell \rangle^2$. Figure 3.5e shows $\mathrm{Var}(n_2)$ as a function of p for different values of α. In each panel, the maximum variance occurs when half of all possible end groups have bound. As α deviates from 1, the bias towards certain bond types causes the variance to decrease. Interestingly, when α is equal to a number and that number's reciprocal, the maximum variance is equal. The shape of the two curves, however, differ as shown by the solid and dotted lines of the same color. We also examine how the size of the microstate affects the variance of microstate topologies. The variance of the fraction of s_2-strands $\mathrm{Var}(n_2/N_s)$ is shown in Figure 3.5f at different values of N_s. Clearly, as the number of strands in the microstate increases, the variance in the fraction of strands in the s_2-state decreases.

3.5.2 Solution to the Master Equation

3.5.2.1 Irreversible end-group binding

While the equilibrated distribution method is an improvement over the combinatoric approach, it still assumes that end-group bonding is reversible in order to achieve thermodynamic equilibrium. Thus, the model's results are independent to the path/history in which the network was formed and not representative of networks formed by "quenched" (non-reversible) end-group binding. Additionally, end-group binding is a stochastic process. At a single time point, each individual microstate within the network will not have the same number of bound end-groups as every other microstate. Rather, there will be a probability distribution of m across the microstates as a function of time. The equilibrated distribution approach only gives the microstate probability distribution when m is fixed.

Evaluation of Equation 3.13 is shown in Figures 3.6a-c. The average strand number fractions $\langle n_\ell \rangle / N_s$ are plotted as a function of time where $N_s = 40$ at different values of α. Similar to the statistical mechanics approach, formation of s_1-strands is favored at smaller

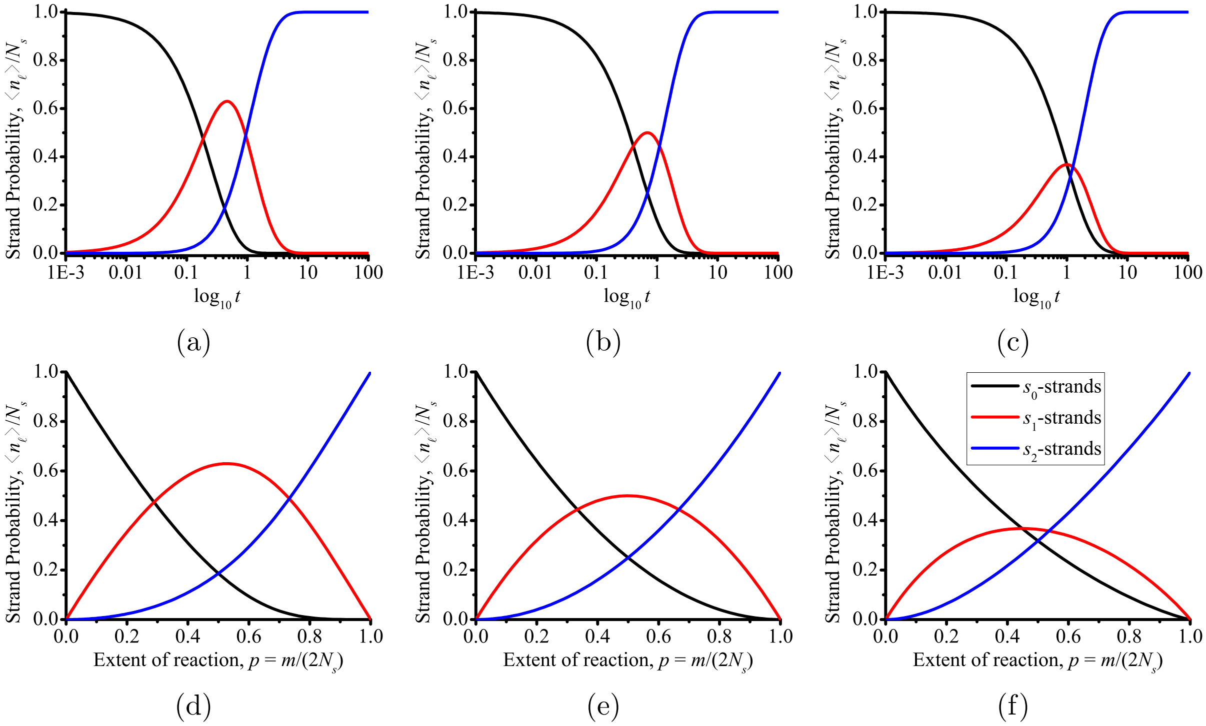

(a) (b) (c)

(d) (e) (f)

Figure 3.6: **Solutions to Equation 3.13.**
Solutions to Equation 3.13 as a function of **(a-c)** time and **(d-f)** p, where **(a,d)** $\alpha = 0.5$, **(b,e)** $\alpha = 1$, and **(c,f)** $\alpha = 2$.

α, and formation of s_2-strands is favored at higher α. These figures can subsequently plotted against the average extent of reaction $\langle p \rangle$ of the system (Figure 3.6d-f), where

$$\langle p(t) \rangle = \frac{2\langle n_2(t) \rangle + \langle n_1(t) \rangle}{2N_s}. \tag{3.27}$$

When plotted in this manner, the strand probabilities take on a distinctly different shape from previous models when $\alpha \neq 1$. Most noticeably, the $\langle n_1 \rangle$ probability loses its symmetric behavior as observed previously in Figure 3.5d and becomes skewed (Figures 3.6d,f). As shown in Figure 3.9d, this skewed behavior of $\langle n_1 \rangle$ as evaluated by Equation 3.21 exists at all $\alpha \neq 1$. Dotted lines represent $\langle n_1 \rangle$ evaluated by Equations 3.6 and 3.7 with variable α and solid lines represent the corresponding evaluations of Equation 3.21.

Evaluation of the Master Equation allows us to directly calculate the probability distribution of individual microstates. Figure 3.7 shows the probability of individual microstates $P(n_1, n_2)$ plotted against $\langle p \rangle$ at different values of α where $N_s = 3$. Due to the stochastic

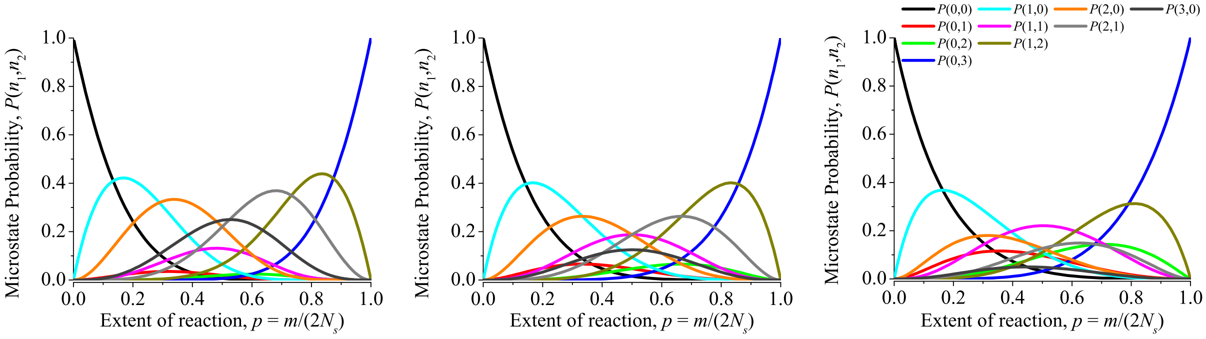

(a) (b) (c)

Figure 3.7: **Solutions to Equation 3.21.**
Solutions to Equation 3.21 to find the individual microstate probabilities $P(n_1, n_2)$, where (a) $\alpha = 0.5$, (b) $\alpha = 1$, (c) $\alpha = 2$.

nature of end group binding, we find that at even very small values of $\langle p \rangle$ there exists a small, but finite, probability that all network strands will be in the s_2-state, $P(n_1 = 0, n_2 = 3)$. As an example, we can solve for $P(n_1, n_2)$ when $N_s = 3$, $\alpha = 1$, and $\langle p \rangle = 0.5$ to give:

$$\begin{aligned} P(0,0) &= 0.0143, & P(1,1) &= 0.1874, \\ P(0,1) &= 0.0455, & P(1,2) &= 0.0994, \\ P(0,2) &= 0.0482, & P(2,0) &= 0.1820, \\ P(0,3) &= 0.0171, & P(2,1) &= 0.1930, \\ P(1,0) &= 0.0883, & P(3,0) &= 0.1249. \end{aligned} \tag{3.28}$$

One of the main benefits of this Master Equation, is our ability to explore the behavior of microstates with very high strand numbers and investigate their probability distribution and variability. Figure 3.8 plots the microstate probabilities $P(n_1, n_2)$ with increasing N_s. When $N_s = 50$, there exists 1326 distinct $\{n_0, n_1, n_2\}$ microstates, all with a non-zero probability when $t > 0$. Calculation of microstate probabilities when N_s is larger than 50 is possible, but graphically difficult to display.

From these microstate probabilities we can, again, look at the microstate variance. Figure 3.9a plots $\mathrm{Var}(n_2)$ at different values of α when $N_s = 40$. In comparison to Figure 3.5e, we notice two main distinctions. First, the variance of n_2 is larger for the microstates cal-

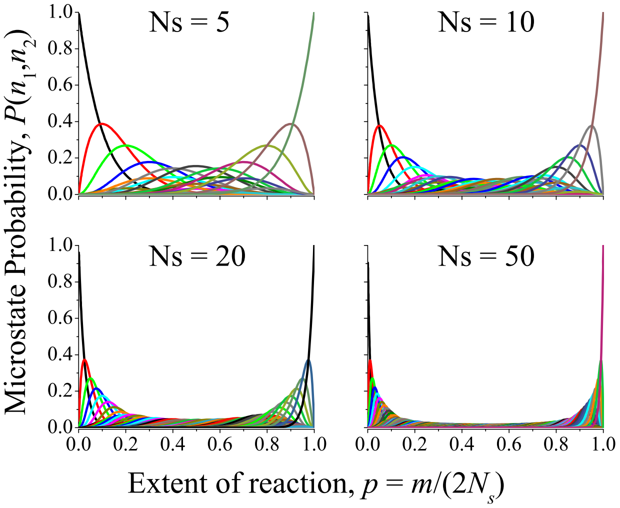

Figure 3.8: **Microstate Probability with high N_s.**
Microstate probability distributions for microstates with higher network strand numbers where $\alpha = 1$. Each line represents an individual microstate probability.

culated using the Master Equation when N_s is fixed. This makes sense. At each time point (and thus at each individual value of $\langle p \rangle$), there exists a probability distribution, not only of the different possible combinations of $\{n_0, n_1, n_2\}$ for a single value of m, but a distribution of m itself. The total number of possible microstates at any given point in time further increases. Figure 3.9b shows the variance of m, again, with variable α when $N_s = 40$. Var(m) reaches a maximum as $\alpha \to \infty$ and a minimum as $\alpha \to 0$, the latter of which gives a bimodal distribution of Var(m). When $\alpha \ll 1$ all end-group binding will initially only occur on s_0-strands. Therefore, when $p = 0.5$ all network strands will have transitioned to the s_1-state and the variance is at a minimum. Second, we notice that the variance of n_2 is no longer symmetric with $\langle p \rangle$ for all α. Rather, when $\alpha = 1$ the variance reaches a maximum when $p \approx 0.7$. Similar to Figure 3.5f, Figure 3.9c shows that as N_s increases and the microstate size increases, Var(n_2/N_s) decreases. The shape of the Var(n_2/N_s) does not change as the size of the microstate increases, only decreases in magnitude.

3.5.2.2 Reversible end-group binding

From here, we can use the Master Equation to observe a system where the network bonds are able to bind and unbind, eventually reaching thermodynamic equilibrium [132]. For

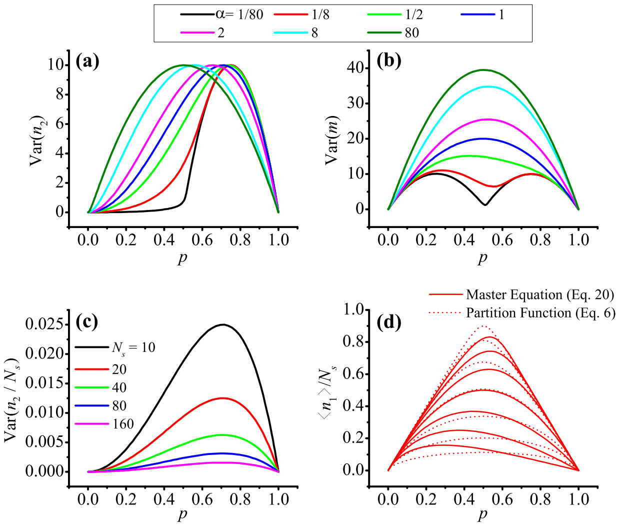

Figure 3.9: **Microstate variance**

The variance of the number of **(a)** s_2-strands and number of **(b)** bound end groups m across the various possible microstates with variable α and $N_s = 40$. For $\alpha > 80$ and $\alpha < 1/80$ the variance curves to not change significantly from those displayed. **(c)** The variance of the fraction of s_2-strands $\mathrm{Var}(n_2/N_s)$ across the various possible microstates with variable N_s and $\alpha = 1$. **(d)** Comparison of $\langle n_1 \rangle$ as calculated using (dotted lines) the thermodynamic equilibrium approach and (solid lines) the Master Equation with variable α.

example network end-groups can be bound together by reversible hydrazone bonds [133], imine bonds [134], or guest-host interactions [135]. Under the condition that the total number of bound end-groups in each microstate remains constant, microstate transitions occur according to Equation 3.22. The solution of which is the same as found through the use of the equilibrated distribution (Equation 3.25). We combine the bond formation and bond redistribution differential equations (Equations 3.9 and 3.25, respectively) to model both processes simultaneously. A simplified version of the solution to this equation (as is the case for Equation 3.21) could not be found. In Figure 3.10 we compare the results of the Master Equation with and without reversible end-group binding. The solution and evaluation to the system of coupled linear differential equations $dP(n_1, n_2, t)/dt$ is plotted against $\langle p \rangle$ and shown in Figure 3.10b with $N_s = 3$, $\alpha = 2$, and $\kappa \gg \lambda$. This solution is directly compared to the case where end-group binding is quenched ($\kappa = 0$, Figure 3.10a). Figure 3.10b shows the redistribution of microstate probabilities due to the reversibility of the bonds. To evaluate this redistribution, we looked at the variance of the different strand types $\mathrm{Var}(n_\ell)$. When $\alpha = 1$, bond reversibility produces no change in the variance

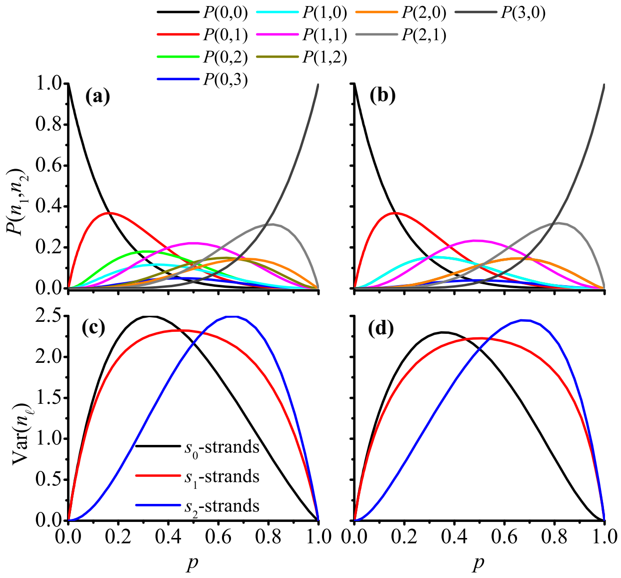

Figure 3.10: **Microstate probabilities $P(n_1, n_2)$ are plotted against $\langle p \rangle$.** Microstate probabilities $P(n_1, n_2)$ are plotted against $\langle p \rangle$ for **(a)** quenched end-group binding ($\kappa = 0$), and **(b)** reversible end-group binding ($\kappa \gg \lambda$) when $\alpha = 2$ and $N_s = 3$. The variance in the number of strand types $\mathrm{Var}(n_\ell)$ is plotted for **(c)** quenched end-group binding and **(d)** reversible end-group binding. For the variance plots, $\alpha = 2$ and $N_s = 10$.

curves. When $\alpha = 2$, bond reversibility produces only slight differences in the variance curves (Figure 3.10d) as compared to the quenched case (Figure 3.10c). As α deviates further from 1, the magnitude of $\mathrm{Var}(n_\ell)$ for networks with reversible bonds decreases slightly, and the shape of the variance curves deviate more. In this sense, the bond reversibility works to "anneal" the microstates when $\alpha \neq 1$.

This "annealing" process can be more closely observed if we plot only the microstates where m is fixed. Figure 3.11 shows the microstate probabilities $P(5, 0)$, $P(3, 1)$, and $P(1, 2)$ plotted against $\langle p \rangle$ for a $N_s = 5$ system. When bond reversibility is introduced (solid lines), the probability curves shift, and become scalar multiples of one another. That is, the ratio $P(5, 0)$:$P(3, 1)$:$P(1, 2)$ is fixed for all time, and hence all $\langle p \rangle$. This result is expected given the steady-state microstate probabilities when m is fixed. Equation 3.25 calculates the distribution of microstate probabilities with fixed m and is independent of the network's average extent of reaction, or the time of the network formation process. This equilibration process only requires that t be sufficiently large or $\kappa \gg \lambda$ in order for equilibration of microstate probabilities to occur.

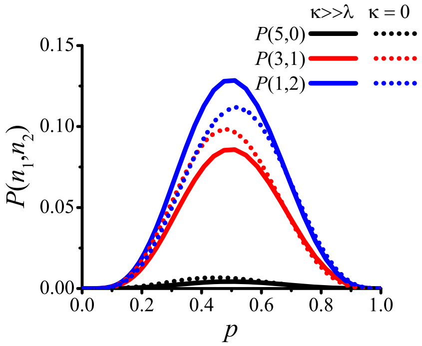

Figure 3.11: **Probability of microstates with reversible binding.** The probability of individual microstates $P(n_1, n_2)$ when $\alpha = 2$, and $N_s = 5$. Only the microstates with fixed $m = 5$ are shown ($\{n_0, n_1, n_2\} = \{0, 5, 0\}$, $\{1, 3, 1\}$, or $\{2, 1, 2\}$). Comparison is drawn between microstates formed with reversible end-group binding (solid lines) and quenched end-group binding (dotted lines).

Redistribution of microstate probabilities can be further observed when the average strand probabilities $\langle n_\ell \rangle / N_s$ are calculated according to Equation 3.11 as shown in Figure 3.12. Similar to Figure 3.6d-f the strand probabilities are plotted when $\alpha = 0.5$, 1, or 2. As expected, when $\alpha = 1$, we find that reverible end-group bonding has no effect on these curves. However, when $\alpha \neq 1$, introduction of binding reversibility reverts this solution back to the solution observed using the equilibrated distribution (Figure 3.5d). The most noticeable feature being they symmetry of $\langle n_1 \rangle$ with $\langle p \rangle$ even when α has deviated far from 1 (Figure 3.12d).

3.6 Conclusions and applications in polymer science

3.6.1 Probability distribution of microstates as spatial heterogeneity.

In this work we use the Master Equation to produce probability distributions of polymer network microstates. This model can now be applied towards modeling the composition of larger polymer networks. We imagine the microstates as three-dimensional subspaces that make up the greater polymer network, all with the same number of network strands. Once we have calculated the probability distribution of the network microstates, we can translate this distribution of probabilities into a spatial distribution of microstates. That is,

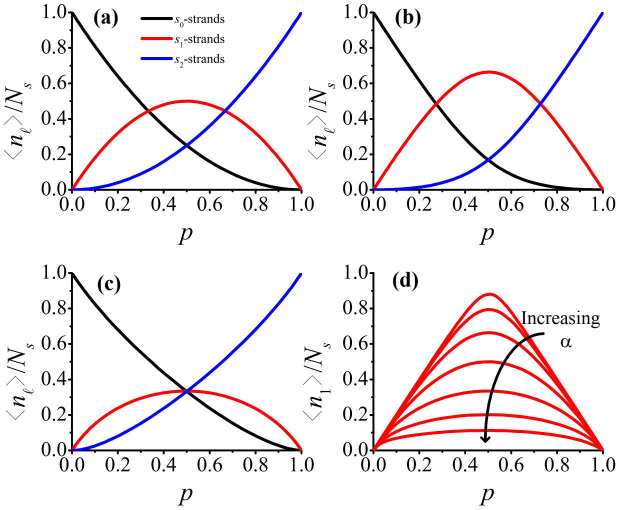

Figure 3.12: **Strand probabilities when with bond reversibility.** The average strand fractions $\langle n_\ell \rangle / N_s$ for networks with reversible end-group binding. Strand probabilities are plotted for **(a)** $\alpha = 1$, **(b)** $\alpha = 0.5$, and **(c)** $\alpha = 2$. **(d)** When bond reversibility is introduced, the plot of $\langle n_1 \rangle / N_s$ becomes symmetric with $\langle p \rangle$ for all α. For all figures, $N_s = 10$.

the number density of specific microstates $\{n_0, n_1, n_2\}$ within the larger network will follow the probability distribution of microstates.

For example, in Equation 3.28 we give the probability distribution of microstates for an $N_s = 3$ system where $\langle p \rangle = 0.5$ and $\alpha = 1$. If we spatially divide the network into subspaces of three network strands each, we expect that the makeup of microstates will follow the aforementioned probability distribution. Thus, we can create a spatial map of microstates and examine the spatial heteroginiety of the network. Taking this concept a step further, we can model microstates with a large number of network strands to the point where the microstates modeled are of tangable size. For example, we examine a network that consists of 5 w/v% polymer where the polymer strands are 10 kDa each. For a space of $(50\text{ nm})^3$, we expect ≈ 375 strands, which is a reasonable number of network strands to input into the Master Equation.

We can then formulate a reasonably large network made up of $(50\text{ nm})^3$ subspaces, where each individual subspace is given a specific microstate $\{n_0, n_1, n_2\}$ dictated by the probability distribution. This tool is useful to investigate the heterogeneity of networks across multiple length scales when the extent of reaction is not complete. The model does not examine heterogeneous mixing, but fixes each microstate to have the same N_s. Instead, local changes in network strand concentration will subsequently shrink and expand the physical size of the microstate which can be subsequently modeled in future iterations.

3.6.2 Elasticity

According to the phantom network theory, the shear modulus G of an ideal network is related to the number density of "elastically effective" network strands ν by $G = (1-2/f_{\mathrm{cross}})\nu k_{\mathrm{B}}T$ where α_{cross} is the functionality of the network's crosslink/branchpoint centers, k_{B} is the Boltzmann constant, and T is the absolute temperature [50]. In this simple estimation, we assume that all s_2-strands are elastically effective, and that there is no formation of loops. Loops do not act as elastically effective strands, however, the formation of loops can be incorporated into the Master Equation in future models [136]. By creating a spatial distribution of microstates with different numbers of s_2-strands we can create a spatial distribution map of elasticity using this above relationship.

3.6.3 Models of network degradation

In the past two decades, degradable sites have been increasingly incorporated into end-linking polymeric network strands that allow for a de-gelation process that can occur after the initial gelation process. The degradable sites typically degrade by enzymatic, hydrolytic, photolytic, or other chemical mechanisms. Initially, the network strands exist in the "intact" state where both ends are considered "un-reacted." After a single end has reacted/degraded, the network strand is a "dangle," and after both ends have reacted/degraded, the network strand is "free." To mathematically model the degradation of such networks, researchers have applied similar principles and methods as the mathematical models of gelation where the "un-binding" process is now modeled. In particular, our group is interested in photodegradable networks [39, 131]. End-groups are degraded by exposure to light, a process that follows exponential decay.

Mathematical models of photodegradable networks have been proposed [42, 131], but lack the the intricacies of models we examine in this work: calculation of network microstates distributions, quenched network de-gelation reactions, and incorporation of a bias factor where certain network strands react more readily than others. In the case of network degradation, one might assume that the undegraded end-groups of a network strand that is bound at both ends to the network, might degrade more readily due to the stress that is normally induced in swollen polymeric networks. Once one of the end-groups has cleaved, and the network strand dangles, the stress is removed rendering the remaining undegraded end-group less susceptible to degradation. This cooperative process can again be modeled by the bias factor α. Models that predict de-gelation behavior largely ignore this notion.

Furthermore, in such degradable networks, incomplete extents of reaction are especially important and useful where network heterogeneity is highest. For example, photodegradable gels have been used to pattern network stiffness as a function of time and space [81]. As we have shown in this work, simple combinatoric models do not properly model such polymer networks. This model can be very simply applied to degradable networks by labeling "intact" network strands as s_0-strands (0 degraded end groups), "dangling" network strands as s_1-strands (1 degraded end group), and "free" network strands as s_2-strands (2 degraded end groups).

CHAPTER 4

Mechanically robust photodegradable gelatin hydrogels for 3D cell culture and in situ mechanical modification

4.1 Abstract

Recent developments in photodegradable (PD) hydrogels have allowed researchers to study cell behavior in response to spatial and temporal changes to the extracellular environment. To date, most PD hydrogel systems have been composed of poly (ethylene glycol) (PEG) based macromers that crosslink via end-linking gelation. PEG-based hydrogels, however, are not optimal for three-dimension cell culture, as they neither allow for cellular proliferation nor restructuring of the matrix. Unlike PEG-based hydrogels, gelatin, a naturally derived material, contains enzymatically degradable sites and cell binding domains, making it an attractive biomaterial for three-dimensional cell culture. To this end, researchers have modified gelatin to contain methacrylamide groups (GelMA). This allows the gels to be chemically crosslinked, rendering them stable at physiological temperatures. A few groups have also reported the synthesis of PD gelatin, but the incorporation of photodegradable groups is hampered by poor conjugation efficiency and poor solubility, leading to insufficient mechanical properties. In this work, we develop a PD gelatin hydrogel system that is mechanically robust and can be easily produced in large quantities. Specifically, we chemically modify the gelatin with highly hydrophilic groups which, in turn, adjust the isoelectric point and charge density of the protein. This modification results in a highly soluble PD-gelatin that can be crosslinked into a gel and subsequently degraded with exposure to light. These PD-gelatin gels exhibit mechanical properties similar to GelMA gels, but with the extra ability to be spatially and temporally patterned with light. Photodegradation of the gels can

be done either before cell seeding or in the presence of cells. We show that cells respond to both patterned structures and in situ softening of the network in 2D, while in situ softening in 3D does not affect morphology at the compositions and time scales investigated.

4.2 Introduction

Engineering a dynamic cell microenvironment that mimics the native ECM is of great clinical interest for tissue (or organ) repair and replacement [137]. Hydrogels are extensively investigated as two- and three-dimensional scaffolds for cells because of their high water content, tunable mechanical and physicochemical properties and their ability to be formed in the presence of biological materials such as cells, proteins and DNA [138, 139, 140, 141, 142, 143]. Largely due to advances in hydrogel development, researchers have been able to elucidate fundamental phenomena, such as how cells feel and respond to the mechanical properties of their substrate [144, 145].

Hydrogels are most commonly fabricated from synthetic water-soluble polymers or from modified natural polymers (most commonly proteins or polysaccharides). Synthetic hydrogels including those fabricated from poly(acrylamide) (PAAm) and poly(ethylene glycol) (PEG) typically require the addition of peptides or proteins to encourage cell adhesion [146]. Synthetic peptides are readily reactively incorporated, but can be tedious to synthesize, and may induce unwanted cell signaling cascades or atypical adhesion [147, 148]. Proteins can also be entrapped, adsorbed, or covalently conjugated to hydrogels. In both cases, the concentration of the adhesive peptide or protein may be difficult to quantify. Furthermore, synthetic hydrogels lack the intrinsic ability to be restructured by cells. Many authors believe that this ability for the cells to either mechanically [149] or proteolytically [150] remodel the matrix surrounding them is important for cellular differentiation and/or tissue development. Researchers typically introduce either hydrolytically degradable groups or enzyme degradable peptide sequences into synthetic hydrogels to mimic natural remodeling, although this approach does not fully recapitulate the complexity of degradable sites in the ECM.

As an alternative to synthetic hydrogels, protein-based hydrogels inherently contain both cell binding domains and enzymatically degradable sites[151, 152]. Protein-based hydrogels not only provide structural integrity, but also provide essential biochemical properties in the cellular microenvironment through the binding and release of cellular mediators [153]. One such protein that has gained traction as a biomaterial in recent years is gelatin. Gelatin, which is derived from collagen and contains both enzymatically degradable sites and cell binding domains is inexpensive, readily available in large quantities and can be chemically modified. Indeed, several groups have reported modification of gelatin with polymerizable groups such as glycidyl methacrylate [154] or (meth)acrylic anhydride [155, 156, 157, 158, 159, 160] to produce gelatin methacrylate and gelatin methacrylamide (GelMA), respectively. These crosslinking groups enhance the mechanical stability of gelatin gels. Among many applications, GelMA gels have been used to study cardiac [161], vascular[162], and epidermal [163] tissues; they have been used as antimicrobial hydrogels [164]; and they have been utilized for 3D projection stereolithography [165] and modular biomaterials [166].

In addition to introducing polymerizable groups, researchers may wish to add more complex functionalities to hydrogel materials, such as functional groups that allow dynamic control of the physical and chemical properties of the hydrogel. Chemical and mechanical changes to the ECM occur during cell differentiation, morphogenesis, tissue development, repair, and disease progression [167, 168, 168, 169], and replicating such dynamic changes in biomaterials may be critical for controlling cell fate. For example, changes in environmental rigidity, structure, and cellular adhesion have been reported relative to the development and progress of several types of cancer[170, 171, 172]. Changes in tension applied to the vasculature by blood pressure changes can lead to diseases such as vasospasm and cerebral aneurysms[173]. Several recent reviews have focused on different aspects of dynamic biomaterials design [174, 175, 176, 177, 178, 179, 180, 181].

To this end, our lab has developed a platform of photodegradable linkers that can be used to control the chemical and physical properties of hydrogels. We designed and synthesized a series of photodegradable *ortho*-nitrobenzyl (*o*-NB) groups, characterized their absorptivity (including degradation products) and quantified their degradation rates via photorheology [39]. We developed a predictive model of (multi-stage) photodegradation and release[182, 131]. Using several different lithographic techniques, we demonstrated precise mechanical and topographical patterning of these gels [52, 53, 81]. We have also demonstrated the utility of these hydrogels for live stem cell encapsulation and release. We have demonstrated that doses of light used to achieve photodegradation do not induce any changes in gene expression of human mesenchymal stem cells [40]. Importantly, we have reported significant changes in gene expression by mesenchymal stem cells when encapsulated within a hydrogel (3D construct) compared to culturing the cells on a chemically identical hydrogel a 2D cell sheet. While these photodegradable systems are highly reproducible and easy to synthesize and fabricate, there are several limitations. First, like most synthetic hydrogels require the addition of a cell-adhesion peptide or protein. Additionally, PEG hydrogels lack the ability to be restructured by cells. A few groups have produced photolabile, enzymatically degradable PEG-based hydrogels [183, 59, 60, 184] but the MMP-sensitive linkages and the RGD cell adhesion domains can be tedious to produce and purify, and their incorporation is difficult to quantify.

A few groups have attempted to incorporate photodegradable *o*-NB linkers into gelatin-based hydrogels by crosslinking GelMA with photoclevable PEG[185, 61]. However, the storage moduli of these gels is extremely limited (< 1 kPa), likely due to the fact that PEG precipitates gelatin out of solution above a certain concentration[186]. Additionally, one group has attempted to directly link the photodegradable *o*-NB linker to gelatin [63], however, the synthesis this photodegradable gelatin is inefficient, and the degree of modification is significantly limited due to the limited solubility of the *o*-NB moiety in aqueous solution.

To improve the modification of natural polymers such as gelatin, we have developed a bioconjugation chemistry to enhance its solubility prior to functionalization with (relatively) hydrophobic groups. In this report, we first describe the conjugation of cysteic acid to gelatin, followed by functionalization with methacrylamide groups to produce soluble gelatin methacrylamide with a high degree of functionalization. Second, as proof-of-concept of the wider applicability of this technique, we functionalize the cysteic-acid modified gelatin with photodegradable *o*-NB groups to produce highly soluble crosslinkable, photodegradable gelatin.

4.3 Experimental

4.3.1 Materials, Chemicals, and Reagents

Hydrochloric acid (Fisher, concentrated), sodium hydroxide (Fisher, ACS grade), *N*-hydroxysuccinimide (NHS) (Alfa Aesar, 98+%), 3-(3-Dimethylaminopropyl)-1-ethyl-carbodiimide hydrochloride (EDC-HCl) (Chem-Impex, 99.23%), sodium chloride (Fisher, ACS grade), dioxane (Acros Organics, 99.8%, Extra Dry, stabilized), *N,N*'-dicyclohexylcarbodiimide (DCC) (Anaspec), methacrylic anhydride (Alfa Aesar, 94%, stabilized), anhydrous magnesium sulfate (Fisher, certified), L-cysteic acid (Acros Organics, 99%), anhydrous sodium carbonate (Fisher, ACS certified), sodium bicarbonate (Amresco, ACS grade), sodium tetraborate decahydrate (Fisher, reagent grade), 9-fluorenylmethoxycarbonyl chloride (Fmoc-Cl) (Oakwood Chemical), acetonitrile (BDH, ACS grade), granular fish gelatin (J. T. Baker, 250 bloom), acetone (BDH, ACS grade), piperidine (Alfa Aesar, 99%), *N,N*-diisopropylethylamine (DIEA) (Fisher, peptide synthesis grade), 2,4,6-trinitrobenzene sulfonic acid (TNBS) (G-Biosciences, 1% solution in methanol), CBQCA protein quantification kit, (Molecular Probes), lithium phenyl-2,4,6-trimethylbenzoylphosphinate (LAP) (Sigma-Aldrich, ¿95%), deuterated solvents (D_2O, $(CD_3)_2SO$, and $CDCl_3$) (Cambridge Isotope Laboratories), and silica gel 60 thin-layer chromatography plastic plates (EMD Millipore, F_{254}) were used as received. Dichloromethane (DCM) (Fisher, 99.9%) was distilled under argon (Ar) and stored under Ar in a dry, air-free flask. Dimethyl sulfoxide (DMSO) (Fisher, ACS certified) was dried by storing over dried $4\AA$ molecular sieves (Fisher, grad 514, 8-12 mesh beads) twice. Anhydrous *N,N*-dimethylformamide (DMF) was dispensed from a Grubb's-type Phoenix Solvent Drying System and stored under Ar in a dry, air-free flask. Regenerated cellulose dialysis membranes (Fisher, nominal MWCO 3500) were hydrated in deionized (DI) water for 30 minutes prior to use.

4.3.2 Chemical Synthesis Techniques

All reactions were performed under argon atmosphere using a Schlenk line unless noted otherwise. ^{1}H NMR spectra (δ ppm) of the small molecules were recorded on a Bruker Biospin Ultrashield (either 300 or 500 MHz) NMR spectrometer. All spectra were recorded in D_2O, $(CD_3)_2SO$, or $CDCl_3$ using tetramethylsilane (TMS) as an internal standard. NMR spectra of gelatin samples was performed at 40°C. 4-(3-(Acryloyloxymethyl)-2- nitrobenzyloxy)-4-oxobutanoic acid and 4-(4-(1-(acryloyloxy)ethyl)-2-methoxy-5-nitrophenoxy)butanoic acid photodegradable linkers were synthesized as described previously [39].

4.3.3 Synthesis of 4-(3-(Acryloyloxymethyl)-2- nitrobenzyloxy)-4-oxobutanoic acid succinimide (1).

4-(3-(Acryloyloxymethyl)-2- nitrobenzyloxy)-4-oxobutanoic acid (1.413 g, 4.193 mmol), NHS (0.965 g, 8.38 mmol), and EDC-HCl (1.607 g, 8.838 mmol) were dissolved in DCM (20 mL) and the reaction mixture was stirred overnight at room temperature (RT). The reaction mixture was washed with saturated brine (4×), dried with $MgSO_4$, filtered, and concentrated to yield a pale yellow waxy substance (yield 1.922 g, 4.425 mmol, quantitative). ^{1}H NMR (300 Mz, $CDCl_3$) $\delta = 7.53$ (3H, m, **ArH**), 6.43 (1H, d, $OC(O)CH\mathbf{CH_2}$), 6.13 (1H, q, $OC(O)\mathbf{CH}CH_2$), 5.90 (1H, d, $OC(O)CH\mathbf{CH_2}$), 5.32 (2H, s, $Ar\mathbf{CH_2}OC(O)CHCH_2$), 5.28 (2H, s, $Ar\mathbf{CH_2}OC(O)CH_2CH_2$), 2.98 (2H, t, $ArCH_2OC(O)\mathbf{CH_2}CH_2$), 2.83 (4H, s, COO**NHS**), 2.78 (2H, t, $ArCH_2OC(O)CH_2\mathbf{CH_2}$).

4.3.4 Synthesis of 4-(4-(1-(acryloyloxy)ethyl)-2-methoxy-5-nitrophenoxy)butanoic acid succinimide (2).

4-(4-(1-(acryloyloxy)ethyl)-2-methoxy-5-nitrophenoxy)butanoic acid (696 mg, 1.97 mmol), NHS (459 mg, 3.99 mmol), and EDC-HCl (771 mg, 4.022 mmol) were dissolved in DCM (25 mL) and the reaction mixture was stirred overnight at room temperature. TLC shows the formation of the product and no left over starting compound. The reaction mixture was washed with brine (4×), dried over $MgSO_4$, filtered, and concentrated to yield a yellow oil (869 mg, 1.93 mmol, 97.9%). ^{1}H NMR (300 Mz, CDCl3) δ = 7.65 (1H, s, **ArH**), 7.06 (1H, s, **ArH**) , 6.59 (1H, q, Ar-**CH**(CH_3)O), 6.49 (1H, d, O(CO)CH**CH_2**), 6.21 (1H, q, O(CO)**CH**CH_2), 5.92 (1H, d, O(CO)CH**CH_2**), 4.21(2H, t, ArO**CH_2**$CH_2$$CH_2$), 3.98 (3H, s, ArO**$CH_3$**), 2.95 (2H, t, ArO$CH_2$$CH_2$**$CH_2$**), 2.90 (4H, s, COO**NHS**), 2.33 (2H, quin, ArOCH_2**CH_2**CH_2), 1.71 (3H, d, ArCH**CH_3**).

4.3.5 Synthesis of Fmoc-Cys(O_3H)-OH (4).

Synthesis of Fmoc-Cys(O_3H)-OH followed a similar synthesis procedure for Fmoc-β-Ala(SO_3H)-OH as previously published [187, 188]. Briefly, L-Cysteic acid **3** (4.215 g, 24.92 mmol) and Na2CO3 (4.083 g, 38.52 mmol) were dissolved in water (14 mL) and the reaction mixture was cooled in an ice bath. Fmoc-Cl (5.875 g, 22.71 mmol) was dissolved in dioxane (10 mL) and this solution was added dropwise to the cysteic acid solution. The reaction mixture was allowed to come to RT and stirred overnight. Formation of the product was confirmed by TLC. The reaction mixture was then acidified with 2 M HCl to pH = 1, and the product was dried by rotary evaporator. The resulting solid was triturated with acetonitrile (20 mL) twice, filtered, then dissolved in water (10 mL) and recrystallized at 4° C. The resulting product was filtered, washed with cold water to remove residual salts, and then lyophilized to dryness to give the purified product (yield 5.892 g, 15.05 mmol, 66.3%). ^{1}H NMR (300 Mz, (CD3)$_2$SO) δ = 12.54 (1H, s, COO**H**), 7.86 (2H, d, **ArH**), 7.66 (2H, d, **ArH**), 7.42 (2H, t, **ArH**), 7.38 (1H, s, **NH**), 7.30 (2H, t, **ArH**), 4.23 (1H, t, **CH**CH_2O), 4.21 (2H, d, CH**CH_2**O), 4.17 (1H, d, -NH**CH**COOH), 2.83 (2H, d, CH**CH_2**SO_3H).

4.3.6 Synthesis of Gelatin-Cys(O3H)-NH2 (sulfo-gelatin) (8).

(a) Preparation of N-hydroxysuccinimidyl ester (5). [187, 188] A combination of **4** (1.739 g, 4.444 mmol) and NHS (507 mg, 4.405 mmol) were dried under vacuum at 40° C for 2h. The solution was brought to RT, backfilled with argon, and the compounds were dissolved in dry DMF (20 mL). To this solution, DCC (897 mg, 4.347 mmol) was added and the reaction mixture was stirred at RT overnight. The next day, the reaction mixture was quite cloudy due to the production of the dicyclohexylurea (DCU) byproduct. The solution was transferred into centrifuge tubes and centrifuged to remove the major amount of DCU precipitate. The colorless and transparent eluent, containing the activated NHS ester, was used without further purification. The reaction yield was assumed to be quantitative using DCC as the limiting reagent.

(b) Coupling reaction to gelatin (7). In a separate round bottom flask, fish gelatin **6** (5.000 g, 0.73 mmol lysine residues) and DIEA (1.2 mL, 6.89 mmol) were mixed with DMSO (40 mL) under argon atmosphere and heated to 60° C while stirring to dissolve the gelatin. Once the gelatin was dissolved, the reaction mixture was cooled to RT. The DMF solution containing **5** was then added to the gelatin solution dropwise and stirred overnight at RT. Conjugation of the Fmoc-Cys(O_3H) group to the gelatin was checked by TLC. A small aliquot of this solution was removed and precipitated in acetone for future analysis. This precipitate was collected, dissolved in water and dialyzed against DI water to give **7**. The yield was assumed to be quantitative.

(c) De-protection of primary amine (8). To the remaining solution of **7**, piperidine (10 mL) was added and the reaction mixture was stirred for 15 minutes to cleave the Fmoc protecting group. Cleavage of the Fmoc group from the gelatin compound was checked by TLC. The reaction mixture was then added to 550 mL of cold acetone. This mixture was acidified with 2 M HCl, added dropwise, until the pH of the solution became acidic and the gelatin precipitated out of solution. The mixture was placed in the freezer to further precipitate. The precipitate was collected by centrifugation, dissolved in DI water, and dialyzed against water at RT for 5 days, with two water changes per day. The aqueous solutions were lyophilized to give the pure product 8 (yield 3.954 g, 79.1%). ^{1}H NMR shows complete reaction of lysine residues to cysteic acid.

4.3.7 Synthesis Acryl-*o*NB-sulfo-gelatin (*o*NB-Gel) (9).

A mixture of **8** (471 mg, 0.0687 mmol primary amine) was dissolved in DMSO (20 mL) at 65° C. Once dissolved, the reaction mixture was brought down to 35° C. Compound **1** (76 mg, 0.175 mmol) was added and the reaction mixture was stirred overnight. The conjugation of the *o*-NB group to the gelatin was checked by TLC. The reaction mixture was precipitated in acetone (200 mL) and acidified with 2 M HCl until the gelatin was fully precipitated. The product was collected by centrifugation, washed twice with 20 mL acetone, dissolved in water, and then titrated with 0.1 M NaOH (aq.) until the solution reached pH=7.0. The solution was then dialyzed against water for 36 hours with four water changes and lyophilized to yield a colorless foam **9** (yield 456 mg, 96.8%, 0.105 mmol *o*-NB per gram gelatin).

Acryl-*o*NB-sulfo-gelatin incorporating a 4-(4-(1-hydroxyethyl)-2-methoxy-5-nitrophenoxy) butanoate linker instead of a 1,3-di(hydroxymethyl)-2-nitrobenzene (acryl-oNB-sulfo-gelatin (**10**)) is described in the supporting information.

4.3.8 Synthesis of Gelatin Methacrylamide (GelMA) (11-12).

Two different procedures were used to produce GelMA.

(a) Standard aqueous method using native gelatin. Synthesis of gelatin methacrylamide followed a procedure previously published [189]. Briefly, sodium carbonate (159 mg 1.50 mmol) and sodium bicarbonate (293 mg, 3.49 mmol) were dissolved in water. To this buffered solution, fish gelatin (2.000 g, 0.292 mmol lysine) was added and the mixture was heated to 60° C to dissolve the gelatin. Once fully dissolved, the mixture was cooled to 40° C, the pH was adjusted to pH = 9 using 2 M HCl, and methacrylic anhydride (0.2 mL, 1.35 mmol) was added. The reaction mixture was stirred at 40° C for three hours. The gelatin methacrylamide was then purified by dialyzing against water at 40° C for three days with two changes of water per day. The solution was filtered and lyophilized to give a white foam **11** (yield 1.787 g, 89.4%, 0.259 mmol methacrylamide groups per gram gelatin).

(b) High Conjugation Method in DMSO/DIPEA using gelatin-Cys(O_3H)-NH_2. To obtain a higher conjugation efficiency of methacrylic groups to the gelatin strands, we modified the above procedure. We performed the reaction under anhydrous conditions to reduce hydrolysis of the methacrylic anhydride. This reaction was first attempted using non-sulfo (native) gelatin, but the reaction was inconsistent, often formed a gel-like product during the reaction, and crashed out of solution during dialysis. Fish gelatin-Cys(O_3H)-NH_2 (200 mg, 0.0292 mmol primary amine) was added and the mixture was heated to 60° C to dissolve the gelatin. Once fully dissolved, the mixture was cooled to 35° C and DIEA (100 μL, 0.471 mmol) followed by methacrylic anhydride (82 μL, 0.533 mmol) were added. The reaction mixture was stirred at 35° C overnight. We noticed that the resultant reaction mixture remained a viscous liquid and did not form a gel-like texture as we had observed when performing this reaction with native gelatin. The reaction mixture was added to acetone (50 mL) where the mixture turned cloudy but did not form as cohesive of a precipitate. The mixture was acidified with 2 M HCl to fully precipitate the gelatin. The product was collected by centrifugation, dissolved in water and titrated with 0.1 M NaOH (aq.) till the solution reached pH=7.0. Unlike the analogue reaction using native fish gelatin, the centrifuged product dissolved very quickly in water and the solution remained transparent, without any cloudiness after titration. The solution was then dialyzed against water for 48h with 4 water changes and lyophilized to yield a colorless foam **12** (yield 192 mg, 96%, 0.759 mmol methacryl groups per gram gelatin).

4.3.9 Primary amine quantification.

The concentration of primary amine groups on the different gelatins was determined using two methods:

(a) Quantification using the CBQCA assay. The CBQCA assay was performed according the manufacturer's protocol. All samples tested were dissolved in a 0.1 M sodium borate buffer, pH 9.3. The pH of each sample solution was checked to insure the solutions pH did not deviate from 9.3. Briefly, 5 μL of a 20 mM KCN solution was added to 135 μL of the different gelatin solutions (0.5 mg/mL in buffer) in a 96-well plate. To this, 10 μL of a 2 mM CBQCA working solution was added and incubated at RT. A standard curve of glycine in buffer (167, 83, 62, 42, 21, and 0 μM) was used to quantify primary amine concentration. For comparison, we also created a standard curve of cysteic acid in buffer (167, 83, 62, 42, 21, and 0 μM) to calculate the concentration of primary amines. After 1 hour (as suggested by the manufacturer), the fluorescence of the samples was measured with an excitation at 465 nm and emission at 550 nm. We noticed, however, that the cysteic acid standard curve was very weakly fluorescent. The incubation was allowed to proceed for 11 more hours, before measuring again. The fluorescence reading for the cysteic acid samples greatly improved, and the fluorescence intensity values for all other samples remained relatively unchanged. Data reported in this work used the readings after 12 hours of incubation.

(b) Quantification using the TNBS assay. The TNBS assay was performed according the manufacturer's protocol. All samples tested were dissolved in a 0.1 M sodium barcarbonate buffer, pH = 8.5. The pH of each sample solution was checked to ensure they remained at pH = 8.5. Briefly, 250 μL of a 0.01% TNBS working solution in buffer was added to 500 μL of the different gelatin solutions (0.5 mg/mL in buffer) and incubated at 37° C for 2 hours. The reaction was stopped by adding 250 μL 10% sodium dodecyl sulfate and 125 μL 1M HCL. A standard curve of glycine in buffer (167, 83, 62, 42, 21, and 0 μM) was used to quantify primary amine concentration. Absorbance at 340 or 405 nm was used to measure the chromogenic product of the reaction.

4.3.10 Iso-Electric Point.

The iso-electric point of the different gelatin macromers was calculated using a PROTEAN) i1$^{\text{TM}}$ isoelectric focusing system. Briefly, 5 μg of gelatin was loaded to each iso electric focusing gel (BioRad ReadyStrip$^{\text{TM}}$ IPG Strip 17 cm pH 3-10) by allowing the gels to soak in the gelatin solutions overnight. Isoelectric focusing was performed according the manufacturer's instructions with a total of 57.5 kVh over 12 hours. The gelatin was visualized on the focusing gels using standard silver staining for gel electrophoresis. Gels were scanned using a transparency scanner (Epson Perfection V700).

4.3.11 Titration Curves.

The titration curves of gelatin were performed using a previously described method [190]. Briefly, 150 mg of each gelatin sample tested was dissolved in 15 mL distilled water, heated to 40° C, and the pH was measured with a digital pH meter. The solutions were first acidified using 300 μL 2 M HCl then back titrated by adding 0.1 M NaOH while recording the pH. Sufficient time between additions was given for the pH reading to stabilize. A blank titration in 15 mL pure distilled water was performed using the same conditions as above. From this data, combined ions could be quantified using a calculation as described previously [190]. The titration curves were then spline fit to remove noise from the data. The limits of the displayed titration curves was set at pH's 1.33 and 11.82 since pH values of the gelatin and water only solutions beyond this point were so small that even the slightest deviation of the pH gave wildly inaccurate results.

4.3.12 Glass Silanization.

(a) To covalently adhere the hydrogels to a glass substrate, round pieces of coverglass (12 mm diameter, Fisher) were functionalized with methacrylate groups using the following procedure. The coverglass was first cleaned with hexanes, acetone, water and methanol (in that order), dried, and activated with oxygen plasma (Plasma Prep II, SPI Supplies) for 5 minutes. The activated coverglass was then reacted with 3-(trimethoxysilyl)propyl methacrylate (0.5 mL) in 25 mL of a (Ethanol and acetic acid) solution for 30 minutes. The coated coverglass was then washed with methanol three times before drying. Silanized coverglass pieces were used within two hours of functionalization.

(b) Glass slides were rendered hydrophobic, and thus non-adherent to the polymerized hydrogels, by wiping a drop of Gel Slick (Lonza) on the slide surface. This process was repeated once to ensure a sufficient coating. The slides were then briefly rinsed with DI water to clean the surface and dried before use.

4.3.13 Hydrogel Fabrication.

Stock solutions of GelMA (13.3 w/w%), *o*NB-Gel (13.3 w/w%), and LAP (0.1, 1.0, or 4.0 w/w%) in phenol red-free cell culture media were prepared and mixed together at different compositions to form the pre-polymer solutions. Gels with *o*-NB content were polymerized with 0.25% LAP, and pure GelMA gels were polymerized with 0.025% LAP. Gels containing both *o*-NB and GelMA content used the traditionally synthesized GelMA (**11**). To prepare the gelatin stock solutions, the stocks were heated in a 55° C water bath until dissolved and then centrifuged to remove any bubbles. Since the gelatin used was fish-based, once dissolved the stock solutions remained liquid at room temperature for approximately one hour. If the gelatin stock solutions underwent physical gelation, they could easily be re-liquefied in a 40° water bath. The pre-polymer solution was polymerized, and thus chemically crosslinked, into a hydrogel using a collimated light source (EXFO Omnicure S1000) filtered with a 405 nm bandpass filter (Newport) with an output intensity of 4.8 mW/cm^2 as measured by a spectroradiometer (International Light Technologies, ILT950) between 350 and 500 nm. All gels were polymerized for 5 minutes. To subsequently degrade the gels containing photodegradable gelatin macromer, gels were exposed to the same collimated light source, but filtered with a 365 nm bandpass filter (Newport) with an output intensity of 7.8 mW/cm^2 for a specified amount of time. Striped photomasks were used to block light from reaching certain regions of the gels as prescribed.

4.3.14 Cell Culture.

NIH/3t3 mouse fibroblast were obtained from ATCC (CRL-1658). 3T3 mouse fibroblast cells were thawed and expanded according to ATCC's recommended protocol. Cells were grown in complete growth medium made up of DMEM (Corning, high glucose) supplemented with 10% fetal bovine serum (Corning) and 1% Penicillin-Streptomycin (Life Technologies). For steps requiring photo-irradiation, DMEM without phenol red (GE HyClone, high glucose) was used instead. Cells were incubated and grown at 37° C, 5% CO2. Cells were removed from the cell culture flasks using Trypsin-EDTA (Corning). From here, cells could either be seeded on the surface of sterilized gels or encapsulated as described below.

4.3.15 3D Cell Encapsulation.

To encapsulate cells, media was aspirated from the cell culture plates which were then washed with PBS. Cells were dissociated from the plates with trypsin-EDTA, pelleted via centrifugation (5 min, 0.2 relative centrifugal force (RCF)), resuspended in cell culture media, and counted with a hemocytometer. The necessary volume of media corresponding to the desired number of cells was calculated, and the corresponding amount of cell suspension was pipetted into a 1.5 mL Eppendorf tube. These cell suspensions were centrifuged (5 min, 0.2 RCF) and the media was removed carefully, paying special attention to remove as much of the media as possible. The cell pellets were then resuspended in the corresponding pre-polymer solution (4 million cells/mL). The suspension (5.0 μL per gel) was pipetted between a hydrophobically modified glass slide and 12 mm round glass coverslips functionalized with methacrylate groups that were separated by 200 μm spacers, and polymerized. The resultant cell-hydrogel discs were then placed into 24-well plates, covered with culture media, and incubated at 37° C and 5% CO2. The cell culture media was replaced with phenol red-free media when the gels were exposed to light.

4.3.16 Hydrogel and Cell Imaging.

All samples were imaged with a fluorescence microscope (10×, Axiovert Observer Z1, Zeiss) in PBS. For live/dead analysis LIVE/DEAD viability/cytotoxicity kit (ThermoFisher) was used where calcein AM was used as the live stain, and ethidium homodimer-1 (EthD-1) to stain dead cells. Staining was performed according the manufacturer's instructions. For *o*NB-Gel gels, a higher concentration (10×) of EthD-1 was required to properly stain dead cells. A series of Z-stack images were collected across the sample depth. An orthogonal projection across the Z-direction was produced and the quantification of live and dead cells was performed using a customized pipeline (CellProfiler). For the live/dead assay, we tested three different gels for each condition and imaged the cells at five unique locations at both the gel interior and edge. For cytoskeletal and nuclear staining, the gels were fixed with 4% paraformaldehyde (Fisher), permeabilized with 0.1% Triton X-100 (Fisher), and blocked with 1% bovine serum albumin (BSA; Fisher). The samples were then incubated with fluorescein-isothiocyanate-conjugated phalloidin (Invitrogen) for 2 h. Nuclei were stained with 4',6-diamino-2-phenylindole (DAPI; Invitrogen).

4.3.17 Atomic Force Microscopy.

Prepolymer solutions (10 μL) were pipetted between a hydrophobically modified glass slide and 12 mm round glass coverslips functionalized with methacrylate groups that were separated by 200 μm spacers. The glass slide/prepolymer/coverglass sandwich was then immediately polymerized. After polymerization, the coverglass (with the attached hydrogel) was pried off the glass slide, and submersed in 1× PBS to swell overnight. The next day, the gels were exposed to 365 nm light or left unexposed. The gels were then submersed in 1× PBS to swell overnight. Surface topography and elastic modulus were measured using Atomic Force Microscopy (AFM) in PBS using a JPK Nanowizard 4a BioScience AFM using the force spectroscopy mode in the Nano and Pico Characterization Laboratory at California Nanosystems Institute, UCLA. A CP-qp-CONT-SiO-B probe with a 3.5 μm diameter SiO_2 sphere (sQube) was used to indent the sample. For the quantitative measurements of moduli, the spring constant of the cantilever was measured using the AFM's internal contact-free thermal tuning method. Single indentations were performed with a total force of 4.0 nN. At least 15 indentations were performed at 15 unique locations across the gel surface. All AFM force curve analysis was performed using the JPK Data Processing software. The Young's modulus was calculated by using a Hertz/Sneddon spherical fit with a Poisson's ratio of ν = 0.5.

4.4 Statistical analysis

All statistical calculations were performed in Origin(Pro), OriginLab Corporation. All error bars indicate standard deviations of the mean. To calculate statistical significance, two-sample t-tests were performed. Significance is indicated by *, **, or n.s. for $p < 0.05$, 0.01, or not significant, respectively.

4.5 Results and discussion

4.5.1 Synthesis of Gelatin Macromers.

One limitation of modifying gelatin with polymerizable groups is that solubility generally decreases as degree of modification increases [191, 192, 193, 194, 195]. Because the number of crosslinkable groups is limited, the crosslink density is limited, and therefore the mechanical properties of the hydrogels are limited. For example, we synthesized gelatin methacrylamide using anhydrous DMSO as a solvent, an excess of methacrylic anhydride, and diisopropylethylamine (DIEA) as a base. We purified the reaction by dialysis against water, and during this process the product crashed out of solution and could not be dissolved in water, even at elevated temperatures. Our group also pursued photodegradable gelatin by conjugating an *o*-NB group to unmodified, native gelatin. However, this conjugation resulted in insoluble macromers that precipitated from solution during dialysis purification (Figure 4.11, similar to when a high degree of methacrylation was attempted) and the resultant macromers could not be redissolved in aqueous solution. Other groups have observed similar effects on gelatin solubility after modification [63]. In order to enable modification of gelatin with hydrophobic groups such as methacryloyl or *o*-NB, we sought to further enhance its aqueous solubility prior to functionalization. Sulfonate groups have been used extensively in chemistries for biological applications to vastly improve water solubility of highly hydrophobic compounds.[188, 187] Drawing inspiration from this approach, we used cysteic acid, a naturally occurring amino acid generated by the oxidation of cysteine, to improve the aqueous solubility of gelatin. Our approach is depicted in Scheme 4.1. Fish gelatin is used due to its greater solubility at lower temperatures [196]. First, we protected the amine group of cysteic acid with Fmoc, and subsequently formed the *N*-hydroxylsuccinimidyl (NHS) ester at the carboxylate group using dicyclohexylcarbodiimide and NHS. Next, we reacted the Fmoc-protected cysteic NHS ester with lysine residues in gelatin to form hydrolytically

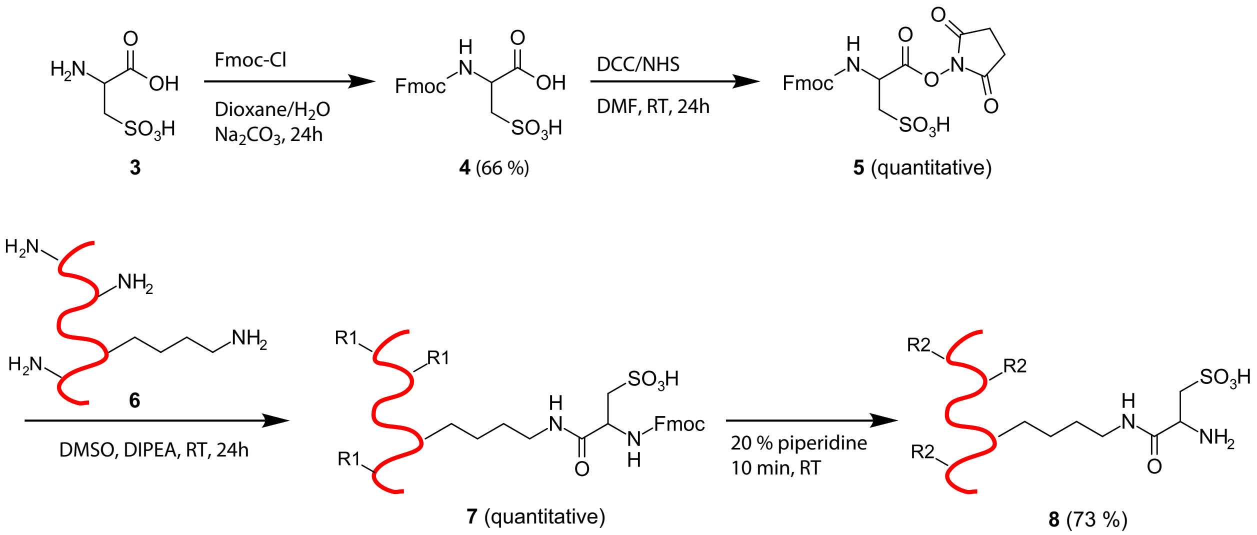

Figure 4.1: **Production of Gelatin-Cys(O_3H)-NH_2 sulfo-gelatin through the attachment of Fmoc-Cys(O_3H)-OH and subsequent Fmoc deprotection.**

stable amide linkages. Finally, we deprotected the amine using piperidine. This amine is then available for further functionalization. To produce gelatin methacrylamide (GelMA), we reacted the cysteic-acid modified gelatin with methacrylic anhydride.

To produce photodegradable gelatin (*o*NB-Gel), we reacted cysteic-acid modified gelatin with the NHS ester derived from (1,3- dihydroxymethyl)-2-nitrobenzene), as depicted in Scheme 4.2. (We also synthesized *o*-NB-Gel with the more frequently used 4-(4-(1-hydroxyethyl)-2-methoxy-5-nitrophenoxy) butanoate linker (Figure 4.12)). All macromers are quite easy to purify, as gelatin has very limited solubility in solvents other than water or DMSO. Simply diluting the reaction medium with acetone precipitates the product while any excess reactants or side products remain in solution.

4.5.2 ^{1}H NMR Characterization.

We characterized the gelatin-based macromers via ^{1}H NMR spectroscopy. Applying a previously reported technique [197], the amino acids valine, leucine, and isoleucine can be considered chemically inert, and their methyl peak at 1.2ppm is easily separated from the rest of the ^{1}H NMR peaks in gelatin; we can therefore use this peak as an internal standard when quantifying conjugation to the gelatin macromer (Figure 4.13, Table 4.3). GelMA, (**11**)

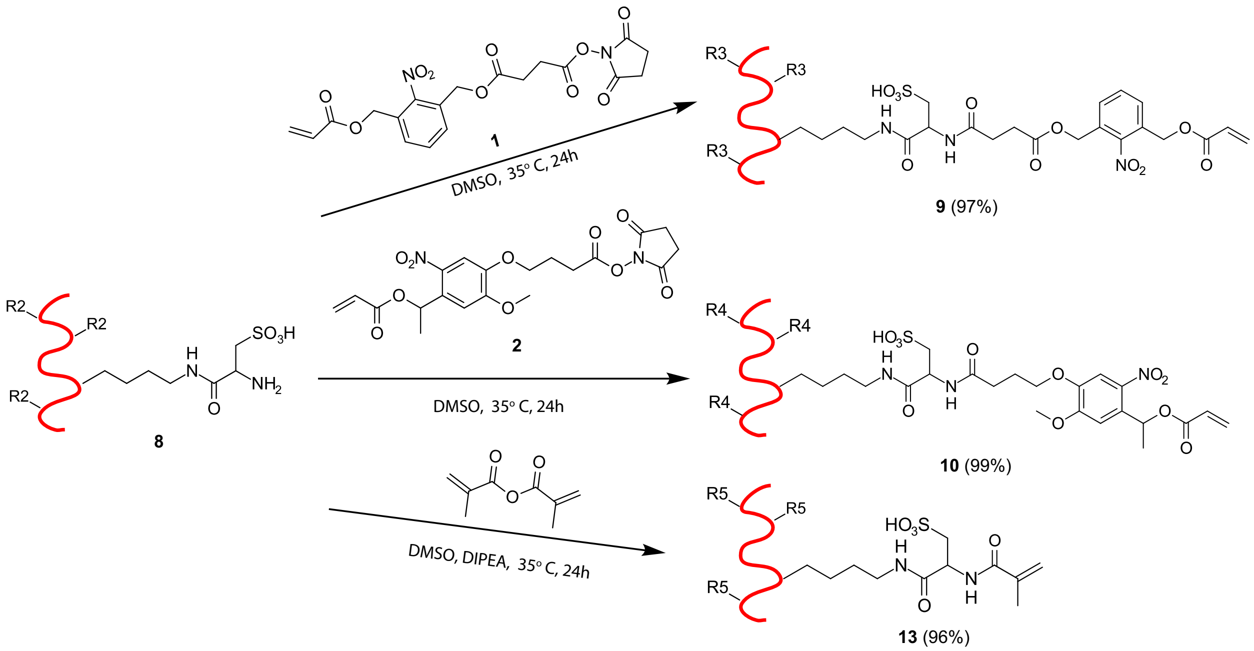

Figure 4.2: **Attachment of hydrophobic linkages to Gelatin-Cys(O_3H)-NH_2 in anhydrous conditions.**

shows the expected methacrylamido peaks at ≈5.25-5.75 ppm (Figure 4.14). Notably, there are small peaks approximately 0.5 ppm downfield of the major olefinic peaks, suggesting that in addition to reacting with lysine residues, some methacrylic anhydride may react with other amino acids. When gelatin is modified with cysteic acid, the peak for the ϵ-methylene group in lysine disappears, and new peaks for cysteic acid appear (Figure 4.15). When sulfo-gelatin is reacted with methacrylic anhydride, the sulfo-gelatin methacrylamide (sulfo-GelMA, **12**), the olefinic peaks from the methacrylamide shift downfield since the methacrylamide is on the cysteic acid α-amine rather than on the ϵ-amine of the lysine for typical GelMA (Figure 4.16). Also, there are additional olefinic peaks, indicating conjugation of the methacryloyl moieties to other side groups on the gelatin. These other side groups are most likely the alcohol groups on serine, threonine, and possibly tyrosine.

Figure 4.3 shows the ^{1}H NMR spectra of native fish gelatin used in this study compared to *o*NB-Gel; additional ^{1}H NMR spectra are available in Supporting Information (Figure 4.17 & 4.18) . The protons of the aromatic ring of the *o*-NB group appear around 7.5 ppm, and the acrylate peaks appear at 5.75-6.25 ppm. The methylene group of cysteic acid is at

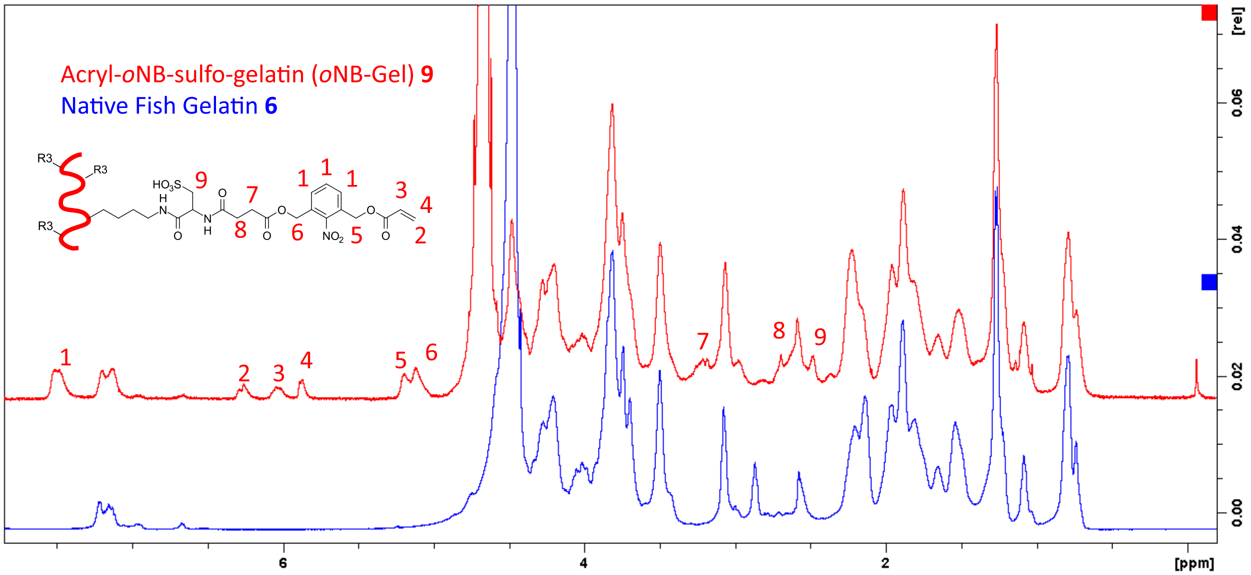

Figure 4.3: ^{1}**H NMR spectra of native fish gelatin and acryl-*o*NB-sulfo-gelatin.** Peaks corresponding to the *o*-NB moiety are indicated. Loss of the native gelatin lysine peak is observed at 2.93 ppm.

≈2.5 ppm, and the methylene peaks from the succinimidyl linker are visible at 2.75 and 3.25 ppm, indicating successful conjugation. Table 4.1 summarizes the conjugation efficiency of the functionalization of gelatin with methacrylamide alone (GelMA), sulfo-methacrylamide (sulfo-GelMA), and two different syntheses of oNB-Gel.

Table 4.1: Conjugation efficiencies of the specified gelatin macromolecules using the valine, leucine, and isoleucine residues as an internal standard.

	Conjugation (mmol/g gelatin)
acryl-*o*NB-sulfo-gelatin (**9**)	0.105
acryl-*o*NB-sulfo-gelatin (**10**)	0.098
GelMA (**11**)	0.259
Sulfo-GelMA (**12**)	0.759

Briefly, we normalized the integration of the methyl peak from the isoleucine, valine and leucine residues to the number of these residues in reported composition of gelatin [197], which allowed us to calculate the number of free lysine groups in this gelatin. We then integrated the protons for methacryloyl or acryloyl or groups to determine the extent of conjugation of the GelMA, *o*NB-Gel and sulfo-GelMA, respectively. Significantly, the degree of functionalization of the sulfo-GelMA is artificially high since we see a variety of peaks in the methacryloyl region, indicating that groups other than the amine of the cysteic acid may be methacrylated. This indicates that the sulfo-gelatin may have better solubility during this reaction, allowing a higher degree of modification than is possible during methacrylation of native gelatin.

4.5.3 Primary Amine Assay

We initially used a TNBS assay to quantify primary amines in our modified gelatins, as it is commonly used to calculate conjugation efficiencies in GelMA synthesis. However, we observed that the assay produces an unusual pinkish hue when used with the sulfo -gelatin, (**8**) (Figure 4.21). Quantitatively, the TNBS assay showed a large decrease in primary amine concentration for Fmoc-sulfo-gelatin (**7**) as expected, but only indicated partial recovery of primary amine groups after deprotection to give the sulfo-gelatin (**8**) (Figure 4.20). Since the TNBS assay should only give varying levels of a yellow chromogenic product we suspected the sulfonated groups, which are in close proximity to the primary amine, may somehow interfere with the assay. We therefore performed a CBQCA assay. The CBQCA assay (CBQCA: 3-(4-carboxybenzoyl)quinoline-2-carboxaldehyde) is commonly used to quantify the concentration of proteins in solution and can be used to quantify the number of free primary amines in protein samples. Using glycine as a standard for the calibration curve, the CBQCA assay indicates that the conjugation of the Fmoc-cysteic acid moiety (**7**) nearly removes all free amino groups from the gelatin (0.76% remaining, Figure 4.4). Once the Fmoc group is cleaved to reveal the free amino group of cysteic acid (**8**), the CBQCA assay only indicates a partial recovery of primary amines (6.78%), similar to the results of the TNBS assay. However, if cysteic acid is used to produce a standard curve instead of glycine, the resultant calibration curve is significantly different (Figure 4.19), with a lower signal at a given amine concentration for cysteic acid compared to glycine. Applying the cysteic acid standard curve, we observe 125% recovery of the primary amines on the sulfo-gelatin (compared to native gelatin). While 125% recovery is not possible, we believe that this value represents both amines from the cysteic acid functionalization, as well as other amines in the gelatin (i.e., even a very small amount of unreacted free amines from the lysine residues will contribute disproportionately to the assay readout based on the difference between the glycine and cysteic acid calibration curves). That is, different primary amines exist in sulfo-gelatin, and a single calibration curve (either using glycine or cysteic acid as a standard) is not sufficient to quantify the free amine content. None-the-less, the data presented in Figure 4.4 indicate nearly quantitative conjugation of free amines in gelatin with cysteic acid (Fmoc-sulfo-gelatin(**7**)), recovery of primary amines upon deprotection (sulfo-gelatin(**8**)), and a subsequent reduction in amine content upon functionalization with the *o*-NB group (*o*NB-Gel (**9**)), comparable to GelMA (**11**). Taken together with the ^{1}H NMR data (which shows complete disappearance of the lysine primary amine after conjugation to Fmoc-cysteic acid, and also complete disappearance of the Fmoc peaks after deprotection as well as appearance of cysteic acid peaks), we believe that that the de-protected cysteic acid moiety has successfully, and fully, conjugated to the gelatin strands via the lysine residues.

4.5.4 Iso-Electric Point

To further characterize the gelatin macromers, we performed isoelectric focusing to determine their pI (Figure 4.22). We found that native fish gelatin has an isoelectric point of pH 6, which is within the range given by the manufacturer. We expect that incorporation of the highly acidic sulfonic acid group in cysteic acid (pKa $\approx$ 1.3) will drastically reduce the isoelectric point. We were unable to observe a pI for sulfo-gelatin, however this is not unexpected. The pKa of protonated lysine is around 10, while the pKa of the sulfonate group of cysteic acid is close to 1.3. The isoelectric focusing gels can only probe for protein isoelectric points in the range from pH = 3-10. Likely, the sulfonate acid group, and the loss of the lysine primary amine, lowered the isoelectric point below this range. Therefore, the disappearance of the isoelectric point for the modified gelatin is an indirect indication of successful modification.

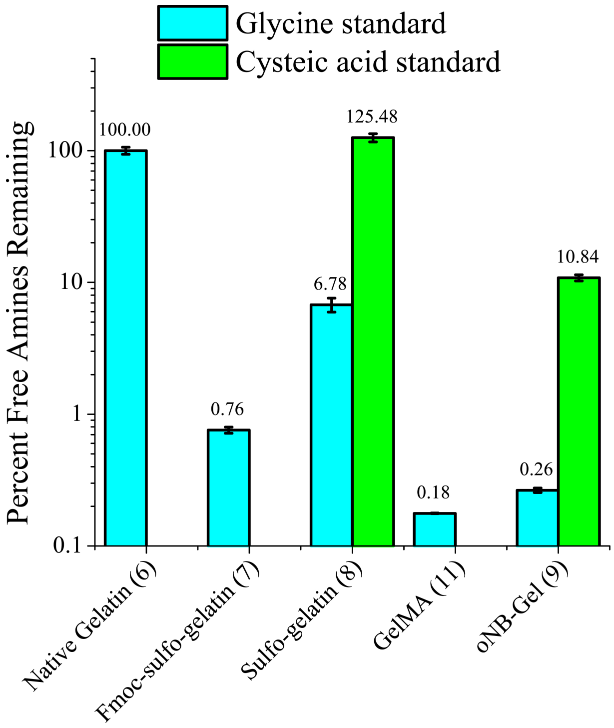

Figure 4.4: **Results from the CBQCA Assay.**

To calibrate the amine quantification we used both glycine and cysteic acid to form the standard curve (see supporting information). Conjugation of the Fmoc-cysteic acid clearly reduces the amount of primary amines. Partial recovery of primary amines is visible after Fmoc deprotection using the glycine standard curve, however when calibrated against the cysteic acid standard curve, full recovery of primary amines is observed. Both the gelatin methacrylamide and *o*-NB gelatin clearly have a reduced number of primary amines.

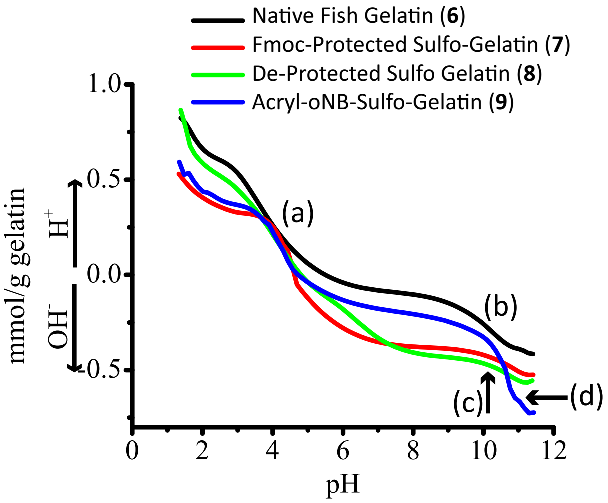

Figure 4.5: **Titration curves of various gelatin macromers.**
(a) All macromers show protonation of Glu and Asp carboxylic acid side groups. **(b)** Native gelatin shows protonation of lysine amine side group. **(c)** Both the fmoc-protected sulfo-gelatin and de-protected sulfo-gelatin show modification of Lys primary amine and loss of Lys protonation. Protonation of α-amino group of sulfo-gelatin could possibly be at the small inflection point at approximately pH 6.5. **(c)** Progressive addition of base eventually degrades the ester groups in the acryl-*o*NB-sulfo-gelatin.

4.5.5 Titration Curves

We also characterized the native and modified gelatin via titration. Titration curves can provide more information about individual charged groups within the protein, instead of an overall average like isoelectric points. As shown in Figure 4.5, all macromers show a region of protonation of the carboxylic acid groups around pH=3.5-4, which correlates well with the pKas of glutamic and aspartic acid. Native gelatin (**6**), shows the protonation of the primary ϵ-amine of lysine around pH = 10.5. Once the gelatin is modified with cysteic acid (7 & 8) the protonation of the lysine disappears. Appearance of the protonation of the primary α-amine of cysteic acid appears around pH $\approx$7; this is expected since the sulfonate group is electron withdrawing. Once the *o*-NB moiety is conjugated to the sulfo-gelatin, we no longer see the protonation of the α-amine on cysteic acid, nor do we see the protonation of the primary ϵ-amine of lysine. Instead, we see degradation of the ester groups on the *o*-NB group at pH $\approx$ 11, which is very sharp and very pronounced, and not observed for any other gelatins.

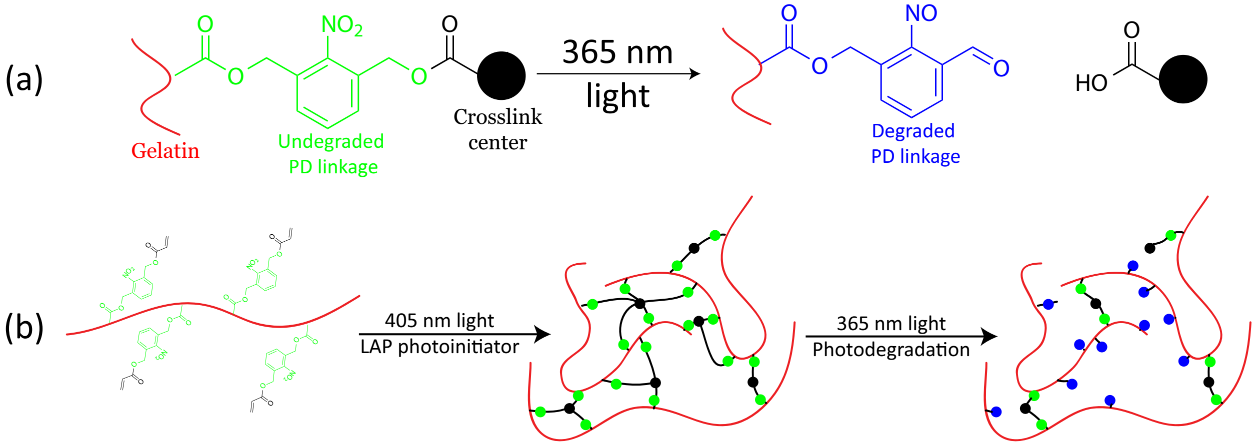

Figure 4.6: **Schematic of hydrogel formation and degradation.**
(a) The *ortho*-nitrobenzyl heterobifunctional groups link the gelatin backbone to a polymerizable acrylate end group that forms a crosslink center when polymerized. **(b)** These acrylate end groups can be polymerized via the visible light (405 nm) initiation mechanism of LAP to form the network. These networks can be subsequently degraded by a shorter wavelength of light (365 nm) to cleave the *o*-NB linkages which subsequently degrade and softens the network.

4.5.6 Fabrication of hydrogels.

While there are many different o-NB groups available, we chose the o-NB linker based on 1,3-di(hydroxymethyl)-2-nitrobenzene due to its low molar absorptivity. It absorbs virtually no light at 405 nm49, allowing photopolymerization using LAP. Furthermore, since this o-NB group also exhibits relatively low absorptivity at 365, light is not significantly attenuated during degradation and degradation is therefore more uniform throughout the gel. Figure 4.6 depicts the formation and degradation of these photodegradable gelatin hydrogels. (oNB-Gel incorporating the 4-(4-(1-hydroxyethyl)-2-methoxy-5-nitrophenoxy) butanoate linker (10) significantly attenuates light and is therefore better for surface modifications or self-folding gels, and was therefore not used to fabricate gels in this study.)

We fabricated photodegradable gels with three different compositions, all at 10 wt% macromer: 10 wt% *o*NB - Gel/0wt% GelMA; 6.7 wt% *o*NB - Gel /3.3wt% GelMA, and 5 wt% *o*NB - Gel /5wt% GelMA. For comparison, we also fabricated 5 wt% and 10 wt% GelMA gels. We also produced 10 wt% sulfo-GelMA gels. Notably, gels incorporating *o*NB-Gel require more initiator, presumably due to radical chain transfer to the nitro- group.

All gels were transparent. The 10% GelMA gel exhibited the highest modulus, which is not surprising given that its degree of functionalization is higher than that of *o*NB- Gel. The sulfo-GelMA gel was significantly softer than the corresponding GelMA gel (10 wt%), which is surprising given the higher degree of functionalization. We hypothesize two possible reasons. First, the negative charge on the sulfo-GelMA chains will likely result in a more extended solution conformation (due to charge charge repulsion), and thus reduce interchain crosslinking. Furthermore, because sulfo-GelMA is less hydrophobic than GelMA, it may exhibit less physical crosslinking [198], which is known to play a role in GelMA stiffness.

4.5.7 AFM of hydrogels

To characterize the mechanical properties of our gels, we used atomic force microscopy (AFM) with a colloid (3.5 μm diameter bead) tip to indent the gels. AFM is optimally suited for these gels since photodegradation creates a gradient across thick samples due to light attenuation. Table 4.2 displays the as-fabricated (before photodegradation) Young's modulus of the gels described above as measured by AFM. Gels incorporating o-NB were exposed to 365 nm light (7.8 mW/cm^2) to demonstrate their photodegradability.

Table 4.2: Properties of gels made from GelMA (**11**), sulfo-*o*NB-gelatin (**9**) and modified sulfo-GelMA (**12**) hydrogels as measured by AFM. Values for photodegradable gels are the initial modulus.

Gel type	Modulus via AFM (kPa)
10 wt% GelMA	35.9±2.8
5 wt% GelMA	3.1±0.3
10 wt% sulfo-GelMA	22.7±3.8
10 wt% *o*NB-Gel	15.8±1.1
6.7/3.3% *o*NB-Gel/GelMA	31.3±2.0
5/5% *o*NB-Gel/GelMA	34.4±3.8

As depicted in Figure 4.7, the modulus of these gels monotonically decreases as a function of exposure time. Importantly, the range of dynamically achievable moduli is ≈5 kPa to 35 kPa using 10 wt% gelatin macromer. This stiffness range can be further expanded to include different compositions such as a greater or lesser wt% gelatin macromer. This is significant because this range is biologically relevant for soft and hard tissues[199, 200, 2, 201].

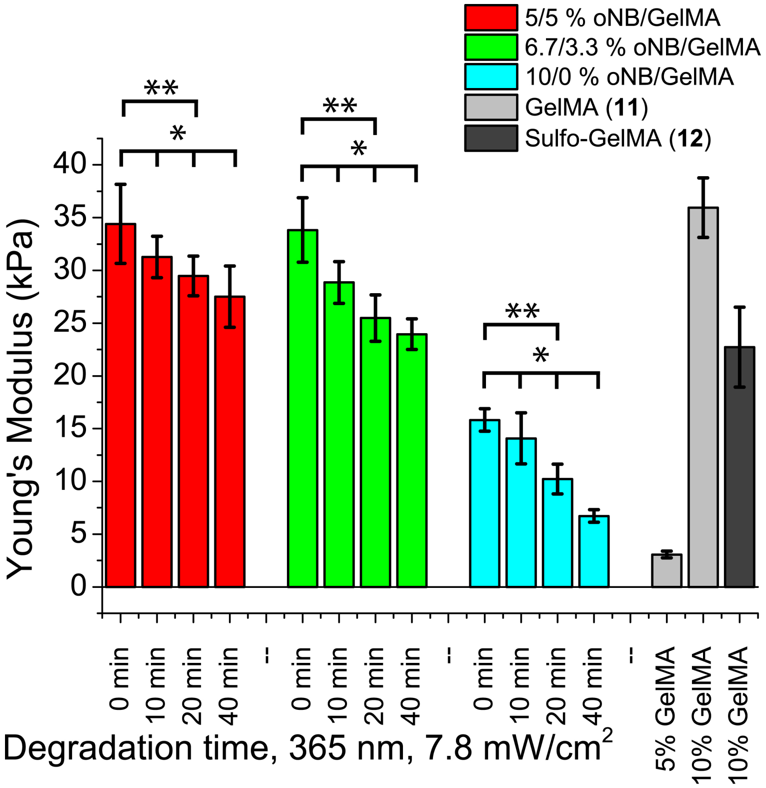

Figure 4.7: **Young's modulus of the respective gels as measured by atomic force microscopy.**

Gels containing photodegradable linkages monotonically decrease in modulus as a function of exposure to light. Photodegradable gels also have modulus values similar to that of gelatin methacrylamide at similar wt%. At each degradation time, the modulus of the gels are significantly different from one another. **: $P < 0.01$, *: $P < 0.05$, $n > 15$ independent locations on each gel were probed.

Furthermore, this stiffness range has not been achieved with any of the previously reported photodegradable gelatins. For example, Truong et. al, conjugated *o*-NB groups to gelatin, and reported a storage modulus of 0.8 ± 0.1 kPa at 5 wt/v% [63].

4.5.8 Cell Compatibility

While GelMA is widely used and known to be compatible with live cell encapsulation, the compatibility of photodegradable *o*NB-sulfo-gelatin (**9**) is unknown.

2D. To demonstrate biocompatibility of the *o*NB-Gel and its photodegradation, we seeded 3T3 fibroblasts onto the surface of 10 wt% gels that were either undegraded or degraded prior to seeding (either homogenously or topographically patterned); we subsequently exposed the undegraded gels to light to degrade them in situ. In situ exposure was divided into four incremental exposures (365 nm, 10 min per exposure, 7.8 mW/cm^2) to prevent heat build-up in the samples. Figure 4.8 shows that the cells adhere to and spread on the undegraded and pre-degraded gels, with organized actin cytoskeletal networks; more stress fibers can be observed on the stiffer, undegraded gels. The cells that experience in situ degradation remain adhered to the gel, although their morphology changes. The cells generally become more compact, presumably due to the softer substrate. This experiment highlights an important aspect of dynamically controllable materials. Even though the pre-degraded gel and the in situ degraded gel have the same mechanical and chemical properties, the dynamic modulation of the latter gel results in a markedly different cell morphology. That is, the absolute properties (such as stiffness) may not be the only factor in determining cell fate. Cells were also seeded on gels with a topographically and mechanically striped pattern fabricated using a photomask containing 50 μm wide opaque stripes separated by 100 μm wide transparent stripes. In Figure 4.8, we see a clear patterning of the cells. While the cell body can be found in both the degraded and non-degraded regions, both the phalloidin and DAPI stains show a clear preference towards the undegraded, stiffer regions of the gel.

3D. To further demonstrate biocompatibility, we encapsulated 3T3s in *o*NB-Gel/GelMA gels of varying composition, and exposed them to light. As depicted in Figure 4.9, cell viability after encapsulation was generally good, although somewhat lower in the o-NB modified gels than those containing GelMA only. This is due to the need for a higher concentration of photoinitiator, but can be optimized further. The cells also survive in situ light exposure.

Figure 4.10 shows phase contrast micrographs of encapsulated cells after one, five and eight days of culture using 6.7 wt% *o*NB-Gel/3.3wt% GelMA gels. We found that gels made up of purely *o*NB-Gel tended to degrade more rapidly than desired, thus, some (non-photodegradable) GelMA component was incorporated. A set of the gels were degraded in-situ after one day in culture (365 nm, 7.8 mW/cm^2 for 20 minutes). After only one day in culture, the cells exhibited a rounded morphology with some very small protrusions visible.

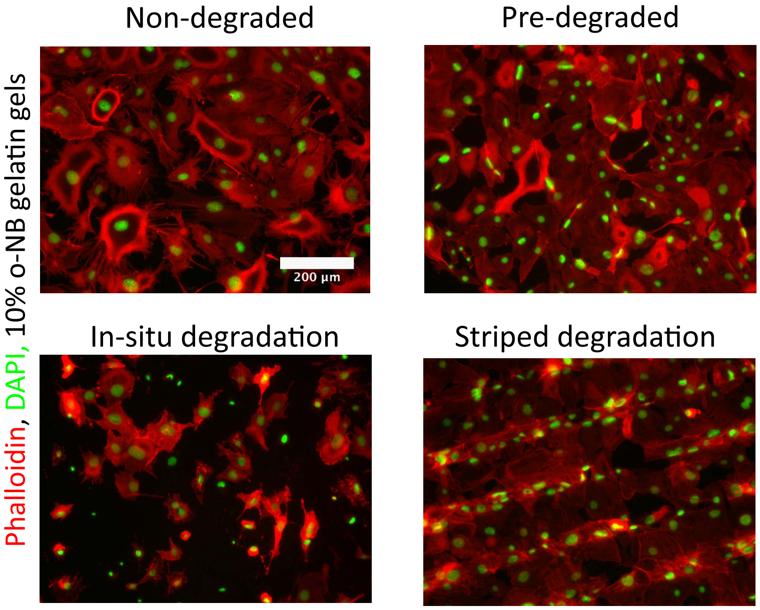

Figure 4.8: **Cells seeded on top of 10 wt% *o*NB-Gel gels respond to the matrix stiffness.**

Cells seeded on nondegraded gels exhibit a well spread morphology with stress fibers clearly visible. Cells seeded on gels that had been pre-degraded for 40 min at 7.8 mW/cm^2 showed a less spread morphology with more diffuse actin structure and less stress fibers. Cells seeded on initially stiff gels which were subsequently exposed to 365 nm light for 40 min at 7.8 mW/cm^2 one day after culture exhibited a shrunken morphology. Cells seeded on gels with a pre-degraded stripped pattern tended to collect in the stiffer, undegraded regions, especially the cell nuclei. Scale bar is 200 μm.

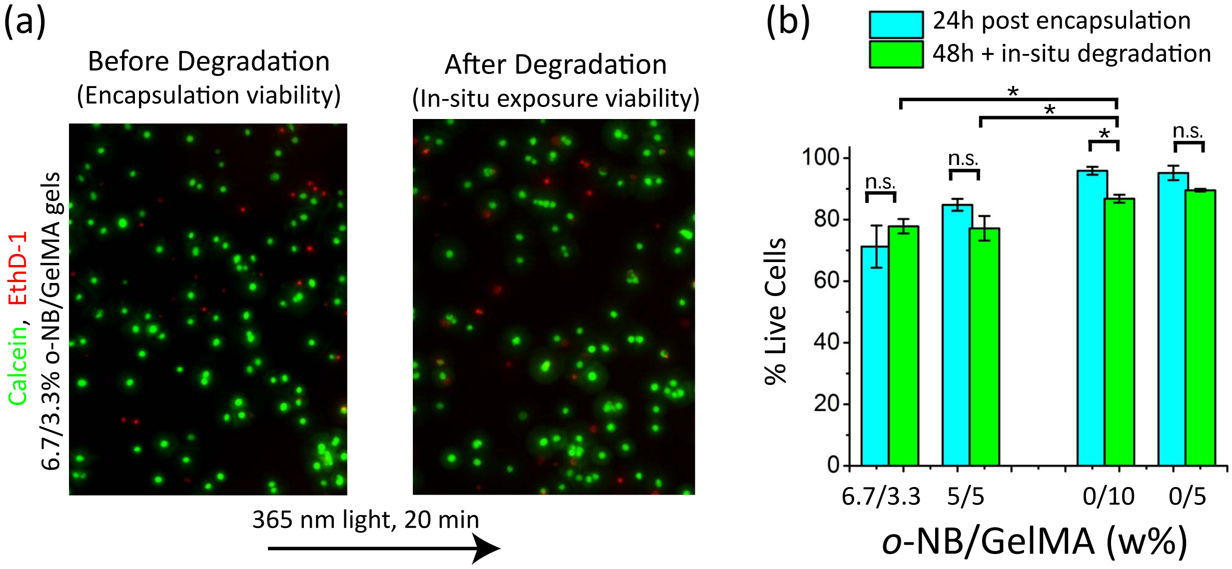

Figure 4.9: **Cell viability of cells encapsulated in 3D.**

(a) LIVE/DEAD staining of encapsulated 3T3s and **(b)** quantification of LIVE/DEAD assay demonstrate that cells maintain viability during encapsulation and after in situ exposure to 365 nm light. In-situ exposure of the gels did not significantly affect cell viability in all but one (the 10% GelMA samples). In-situ exposed *o*-NB gels did show significantly less viability than in-situ exposed 10% GelMA gels, but the p-values were not especially low: P = 0.04 and 0.009 for the 5/5 and 6.7/7.3 *o*-NB gels, respectively. *: $P < 0.05$, n = 3 independent gels were tested with 5 different locations imaged per gel.

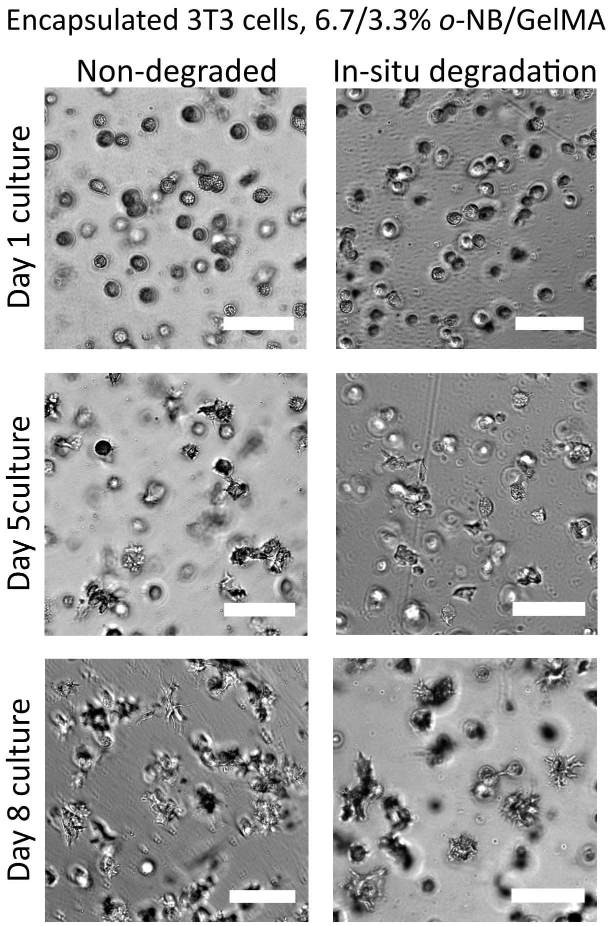

Figure 4.10: **Cell behavior in photodegradable gels as a function of culture time and degradation state.**
Cells were encapsulated in 6.7 wt% oNB-Gel /3.3wt% GelMA gels. After one day in culture a subset of the gels were exposed to 365 nm light at 7.8 mW/cm^2 for 20 minutes. The progression of the cell morphology was observed as a function of time (1, 5, and 8 days in culture). Scale bar for this figure is 100 μm.

After five days in culture, the cells started to spread into the gel volume, a process that was not hindered by the in-situ degradation. After eight days of culture the cells are well spread and some appear to have a stellate morphology. Differences in morphology are seen between Day 1 and Day 8 for both experimental groups (photodegraded and unexposed), implying that some enzymatic degradation is happening, allowing cells to spread. That is, the cells exhibit the morphological changes equally in photodegraded and unexposed samples so any changes must be due to a common effect.

Further supporting our hypothesis of cellular remodelling of the gel, the mechanical difference seen between the unexposed (33.8 ± 3.1 kPa) and photodegraded (25.5 ± 2.2 kPa) samples is not expected to significantly affect the fully differentiated fibroblasts used in this study. However, this modulus range is important to investigate certain cell types [199], including stem cells. From these experiments, we can conclude that cells can be cultured in these gels over the course of weeks, survive in situ modification of the gels, and are able to remodel their environment independently as well.

4.6 Conclusions

Protein modification for use in tissue engineering is both desirable an challenging, due to the limited solubility and solution stability of many proteins. Many modifications, such as modification with crosslinkable groups, increase the hydrophobicity of a protein and therefore reduce its aqueous solubility. Herein we report modification of gelatin with a cysteic acid group to increase its aqueous solubility. We characterized the modified gelatin via 1H NMR, an amine assay, acid base titration and isoelectric point determination, demonstrating that the lysine groups were modified. This modification allowed conjugation of methacryloyl groups and photodegradable acrylate groups to the gelatin. These modifications resulted in a (photo)crosslinkable gelatin with good water solubility, tunable mechanical properties and good cell compatibility in both 2D and 3D experiments. This chemistry is widely applicable to other proteins and polypeptides, and may enable a broader range of synthetic modifications useful in biomedical applications.

4.7 Acknowledgements

This work was funded by the National Institutes of Health through the NIH Director's New Innovator Award Program, 1-DP2-OD008533. S.C.P.N gratefully acknowledges support from a Ruth L. Kirschstein Predoctoral Fellowship (NIH - F31DE026356). S.M.D gratefully acknowledges the support of Eugene Cota Robles Fellowship. The authors acknowledge the use of instruments at the Nano & Pico Characterization Lab at the California NanoSystems

Institute.

4.8 Supporting Information

Table 4.3: Amino acid composition of Red Tilapia.

Amino Acid	Composition (mg/g)	Composition (mmol/g)	# NMR Protons	mmol/g Protons	AA type	mmol/g Protons
Aspartic acid	38.9±4.59	0.292			Val, Ile, leu	2.124
Glutamic acid	71.7±1.08	0.488			lys	0.292
Serine	Not detected	0			tyr, phe	0.697
Glycine	308±12.1	4.107				
Histidine	Not detected	0				
Arginine	29.5±0.84	0.17				
Threonine	134±8.35	1.126				
Alanine	76.1±5.20	0.855				
Proline	Not detected	0				
Tyrosine	5.95±0.78	0.033	4	0.132		
Valine	17.7±1.60	0.151	6	0.906		
Methionine	14.2±2.03	0.095				
Cysteine	1.51±0.14	0.012				
Isoleucine	8.39±0.14	0.064	6	0.384		
Leucine	18.2±1.27	0.139	6	0.834		
Phenylalanine	18.6±0.51	0.113	5	0.565		
Lysine	21.3±2.21	0.146	2	0.292		
Tryptophan	Not detected	0				

Amino acid composition of Red Tilapia according to a previous study quantifying the amino acid composition of red tilapia (*Oreochromis nilotica*) [202], we calculate the molar amount of each amino acid per gram of gelatin. Once this data is known, we can calibrate the NMR spectrum to the expected molar amount of protons detected at each peak. In particular we calculate three specific peaks: 1) the methyl protons on Val (6 protons), Leu (6 protons), and Ileu (6 protons)located at 0.84 ppm; 2) the ethylene protons attached to the carbon next to the primary amine on lysine (2 protons) located at at 2.93 ppm; and 3) the aromatic protons of phe (5 protons) and tyr (4 protons) at 7.25 ppm. We can then calculate the mmol protons/g gelatin for these three respective regions (last column).

Figure 4.11: ***o*-NB gelatin precipitation.**
Early attempts to produce photodegradable gelatin were unsuccessful. In these experiments, we attempted to directly attach the o-NB acrylate moiety **(1)** directly to the lysine primary amine using DMSO as a solvent. However, upon dialysis of the product, we found that the product crashed out of solution, and could not be dissolved, even at elevated temperatures or by using DMSO as the solvent.

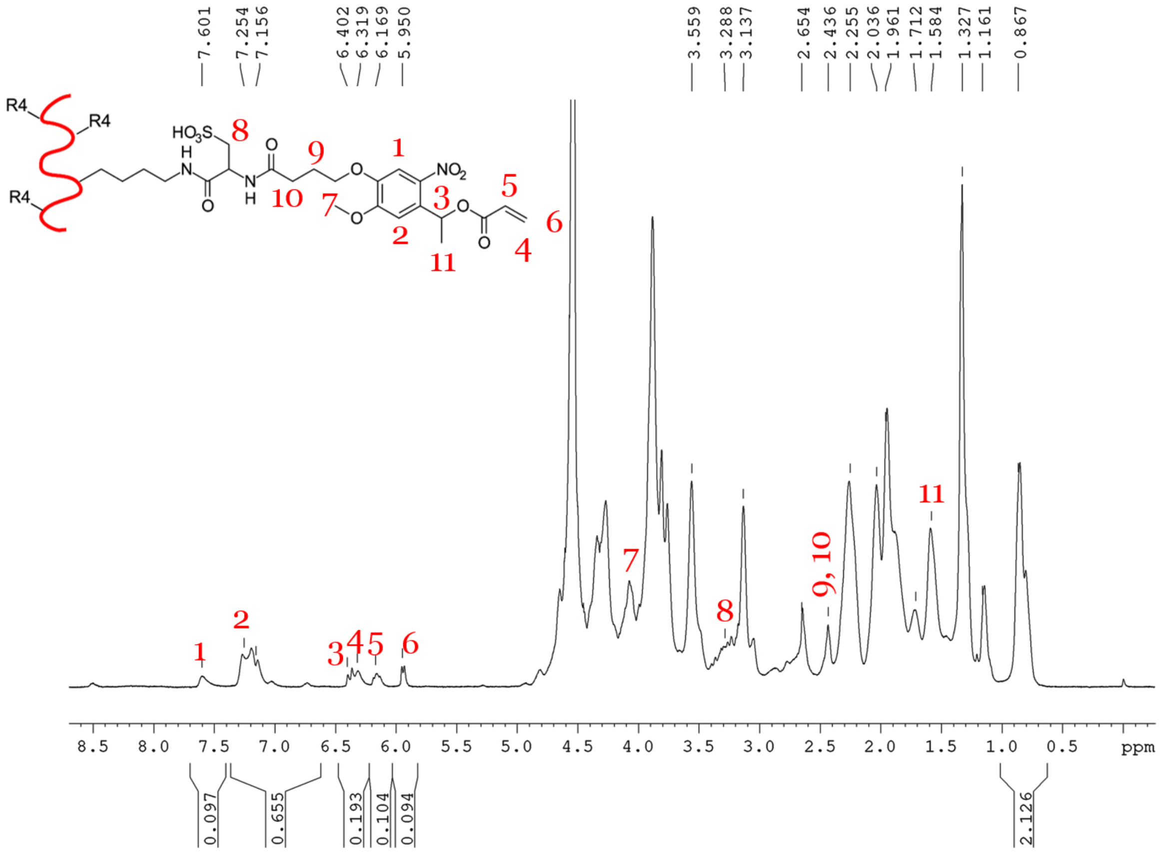

Figure 4.12: ^{1}**H NMR Spectrum of acryl-*o*NB-sulfo-gelatin (10)**

Synthesis Acryl-oNB-sulfo-gelatin (oNB-Gel) (10).

A mixture of **8** (433 mg, 0.0632 mmol primary amine) was dissolved in DMSO (20 mL) at 65^o C. Once dissolved, the reaction mixture was brought down to 35^o C. Compound **1** (76 mg, 0.168 mmol) was added and the reaction mixture was stirred overnight. The conjugation of the *o*-NB group to the gelatin was checked by TLC. The reaction mixture was precipitated in acetone (200 mL) and acidified with 2 M HCl until the gelatin was fully precipitated. The product was collected by centrifugation, washed twice with 20 mL acetone, dissolved in water, and then titrated with 0.1 M NaOH (aq.) till the solution reached pH=7.0. The solution was then dialyzed against water for 36 hours with 4 water changes and lyophilized to yield a colorless foam 10 (yield 427 mg, 90.7%, 0.098 mmol *o*-NB per gram gelatin).

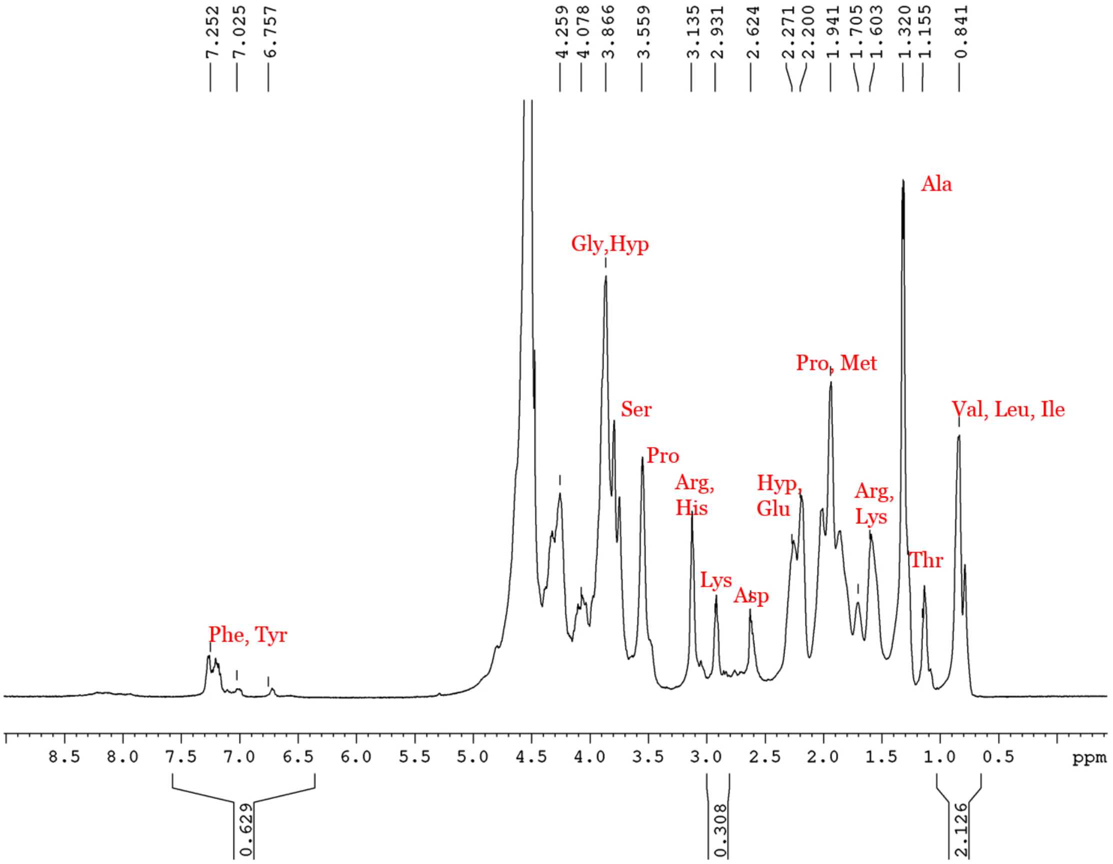

Figure 4.13: ^{1}**H NMR spectrum of Native Fish gelatin.**
Location of the peaks according to Billiet et al. [197]. We pay particular attention to 1) the methyl protons on Valine, Leucine, and Isoleucine at 0.84 ppm; 2) the ethylene protons attached to the carbon next to the primary amine on lysine at 2.93 ppm; and 3) the aromatic protons of phenylalanine and tyrosine at 7.25 ppm. These peaks can be used to quantify the conjugation efficiency to the gelatin macromer. The integrated peaks of the NMR matches well with the calculated proton concentration calculated above. For this study, we use the Val, Leu, Ile proton peak as an internal standard.

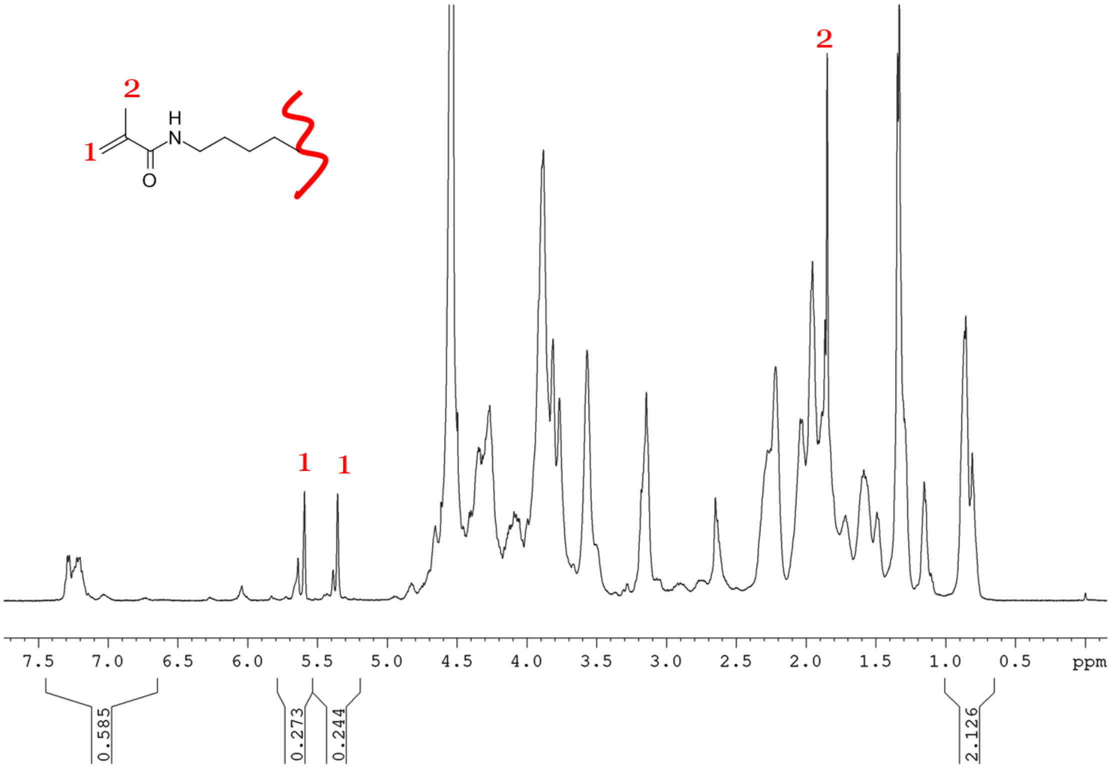

Figure 4.14: ^{1}**H NMR spectrum of gelatin methacrylamide (GelMA) (11)**

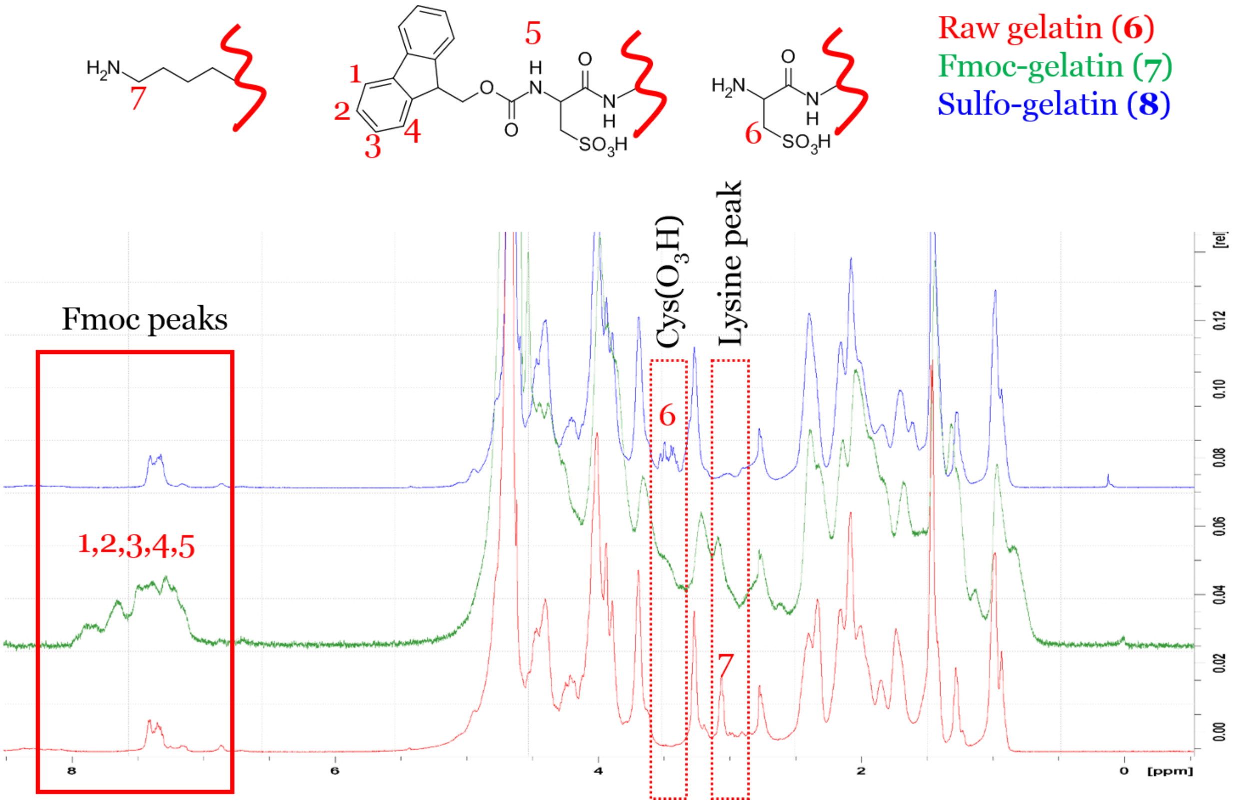

Figure 4.15: **Comparison of ^{1}H NMR spectra of different gelatins.**
^{1}H NMR spectra of native gelatin **(6)**, Gelatin-Cys(O_3H)-NH-Fmoc **(7)**, and deprotected Gelatin-Cys(O_3H)-NH_2 **(8)**. In the native gelatin, we can see the ethylene proton peak corresponding to the protons on the carbon adjacent to the amine of the lysine. Once Fmoc-Cys(O_3H)-OH **(4)** is conjugated, this peak disappears and we find the proton peaks corresponding to the fmoc group. After deprotection of the fmoc group, we show that they peak corresponding to lysine is still not present and the peak corresponding to the cysteic acid appears. The fmoc proton peaks have disappeared, showing the successful deprotection.

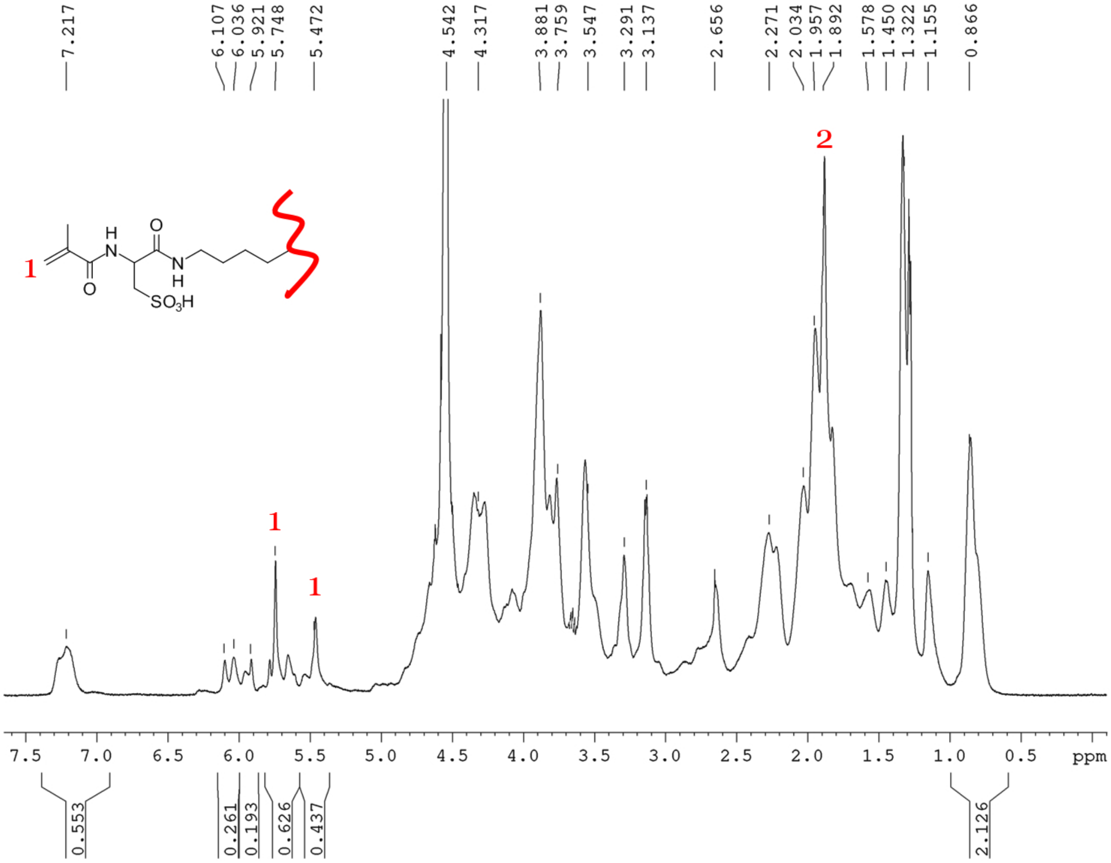

Figure 4.16: ^{1}**H NMR spectrum of sulfo- gelatin methacrylamide (12).** We notice how the protons on the methacrylamide peak shift now that the methacrylamide is attached to cysteic acid rather than lysine. We also find the presence of other methacryl protons around 6 ppm. These are likely methacryl groups attached to alcohol side chains in the gelatin (serine, threonine, and tyrosine) or possibly to histidine since we see an extra peak at 3.29 ppm.

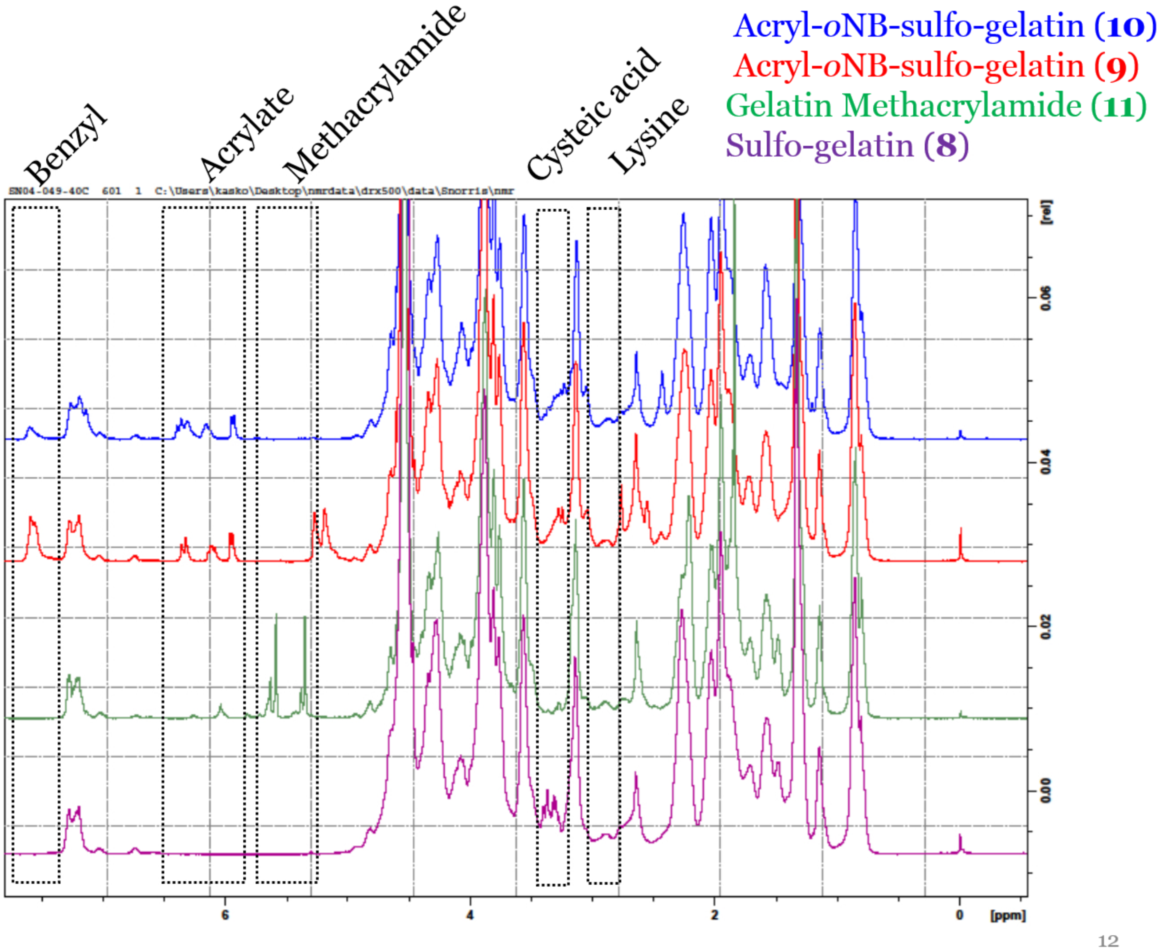

Figure 4.17: **Comparison of the ^{1}H NMR spectra of conjugated gelatins.** Comparison of the ^{1}H NMR spectra of gelatin-Cys(O_3H)-NH_2 **(8)**, gelatin methacrylamide **(11)** and the two acryl-*o*-NB-sulfo-gelatin samples (**9** & **10**). We pay special attention to the appearance and disappearance of several peaks corresponding to: 1) the benzyl peaks of the *o*-NB moieties; 2) the acrylate peaks of the *o*-NB moieties; 3) the methacrylamide peaks of GelMA; 4) the proton peaks on the cysteic acid; and 5) the lack of the lysine proton peaks on all samples.

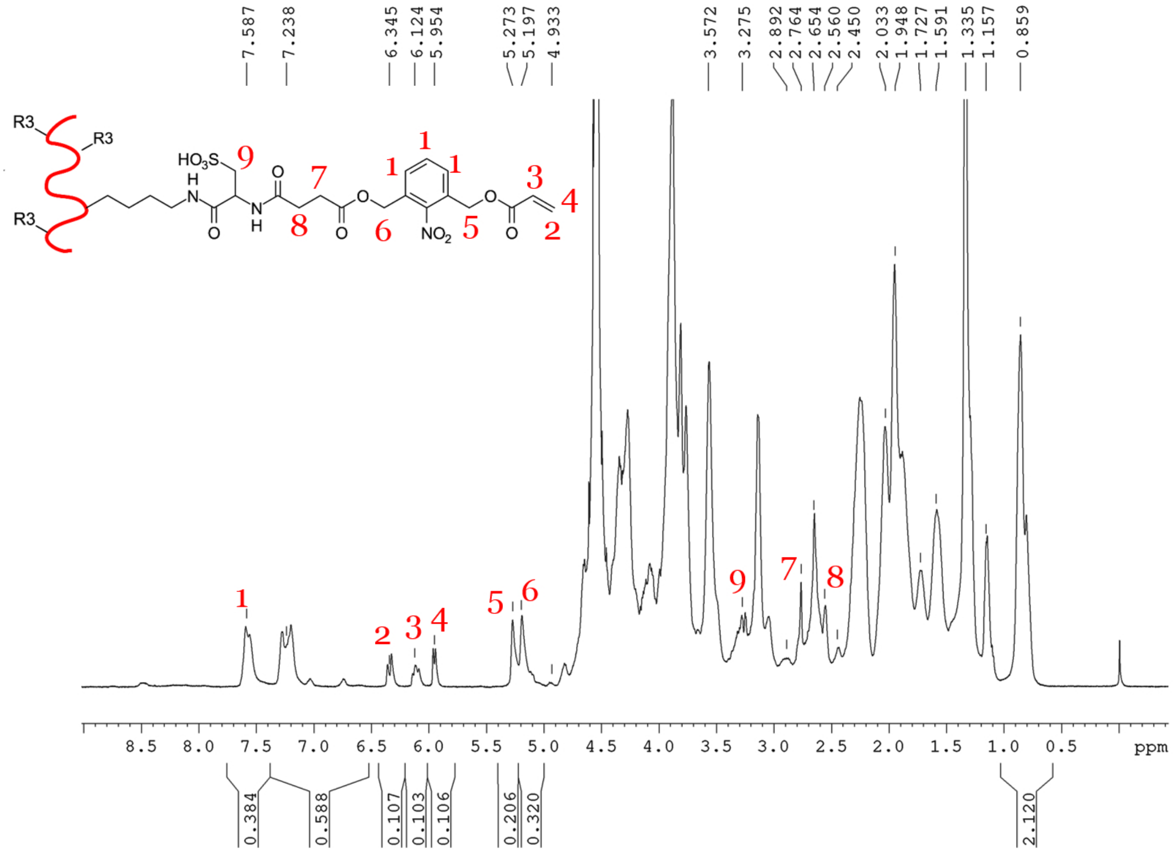

Figure 4.18: ^{1}**H NMR spectrum of acryl-*o*NB-sulfo-gelatin (9)**

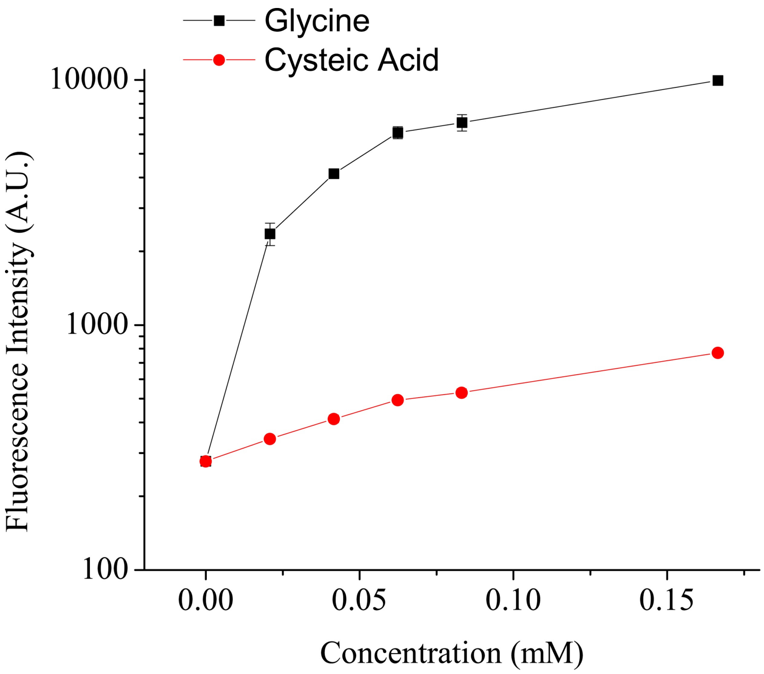

Figure 4.19: **Standard curves for glycine and cysteic acid for the CBQCA assay.** As noted above, we noticed that the primary amines of cysteic acid tend to react less readily than the primary amines of glycine. Thus, we produced a standard curve using cysteic acid and found that it reacted with the CBQCA assay orders of magnitude less than glycine. We paid special attention that the pH of the two amino acid solutions was the same. Thus, we recalibrated the calculation of primary amines remaining for the sulfo-gelatin **(8)** and the *o*NB-gelatin **(9)** using the cysteic acid standard curve.

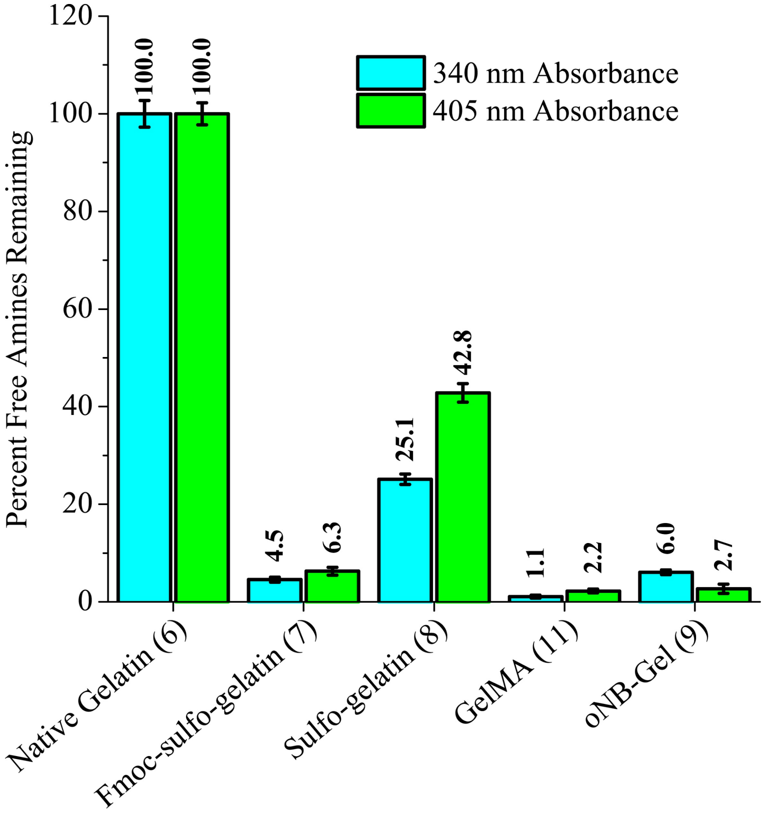

Figure 4.20: **TNBS assay as measured using the absorbance of two different wavelengths of light.**

We found that if the reaction of the TNBS reagent when analyzed by the absorbance of 405 nm light (instead of 340 nm as suggested by the manufacturer), the sulfo-gelatin **(8)** showed a relatively higher signal, which could indicate that the chromogenic derivative of the assay is different when assaying cysteic acid residues. We do not believe that there is only a partial recovery of the amine group after Fmoc removal, but rather, the TNBS amine assay does not properly assay for amines on cysteic acid residues.

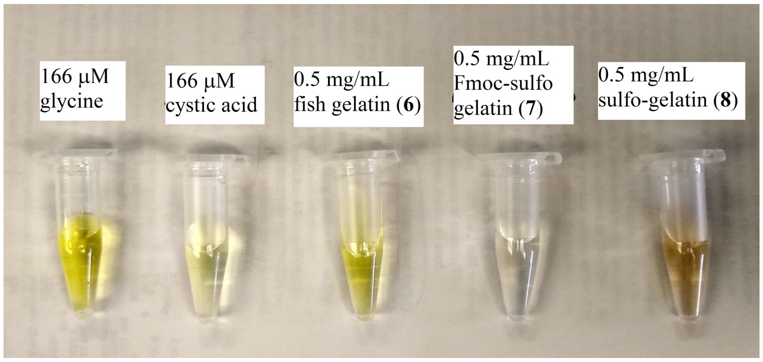

Figure 4.21: **Images of TNBS assay solutions.**

During the TNBS assay, we noticed that the sulfo-gelatin (**8**) has a pinkish hue, as opposed to the yellow color of the glycine standards and the native fish gelatin (**6**). We have observed this difference in color across several independent experiments and multiple batches of sulfo-gelatin (**8**). We believe that the conjugated cysteic acid moieties may interact with the TNBS assay differently than the primary amines of either gelatin's lysines or the primary amine on glycine (the typical/suggested source of primary amines for TNBS assay standard curves). This is supported by the above image showing the 166 μM cysteic acid sample, noticeably less saturated than the 166 μM glycine sample, even though they contain the same number of primary amines (the pH of the two solutions was the same).

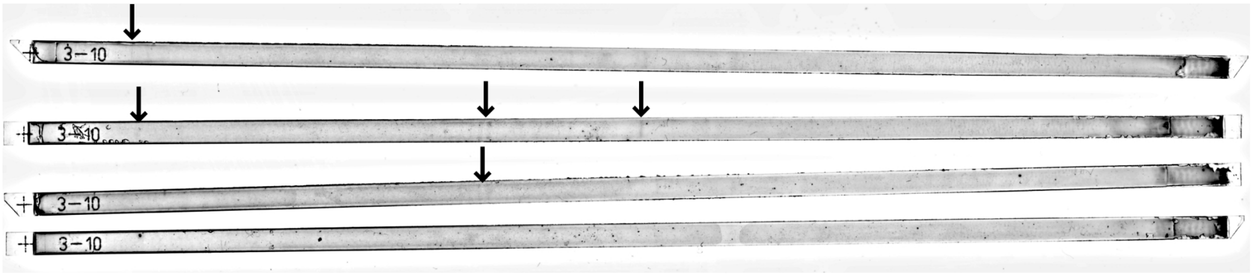

Figure 4.22: **Iso Electric focusing gels.**

The top most gel is of the acryl-*o*NB-sulfo-gelatin (**9**) sample. The second from the top is the native fish gelatin (**6**). The second from the bottom is the Gelatin-Cys(O_3H)-NH-Fmoc (**7**) sample. The bottom most gel is of the deprotected Gelatin-Cys(O_3H)-NH_2 (**8**) sample. In the native fish gelatin, we find a prominent band at pH 6.6. This corresponds well to the pH range given by the manufacturer. There is a less prominent band at pH 5.7 which could correspond to different molecular weight gelatin strands, and another very faint band at pH 3.7, which we disregard. The gelatin-Cys(O_3H)-NH-Fmoc (**7**) sample has a faint peak at pH 5.6, which is very similar to the peak found in the native fish gelatin, which indicates that it could be an artifact. For the deprotected gelatin-Cys(O_3H)-NH_2 (**8**) sample we found no observable bands. In the acryl-*o*NB-sulfo-gelatin (**9**) sample we found possibly one faint band at pH 3.6, but this could again be an artifact since it also exists in the native gelatin sample. Altogether, this results suggests that addition of the cysteic acid moiety reduces the isoelectric point so strongly, that it is out of the range of this testing method. These isoelectric focusing strips had the lowest pH range we could find.

CHAPTER 5

Photodegradable polyacrylamide gels for dynamic modulus control of cell culture platforms

5.1 Abstract

Crosslinked polyacrylamide hydrogels are commonly used in biotechnology and cell culture applications. These hydrogels are easily fabricated, with precise control over the material stiffness, using readily available reagents, resulting in their widespread popularity. Furthermore, specific proteins or cell binding domains can be covalently attached to the surface of polyacrylamide hydrogels to allow for precise control of the chemical environment. However, once fabricated, the chemical and physical properties of polyacrylamide gels cannot be altered. To this end, we have developed a photodegradable polyacrylamide gel system that allows for dynamic control of the polyacrylamide gel stiffness with exposure to light. Photodegradable polyacrylamide gels were produced by copolymerizing acrylamide and a photocleavable *ortho*-nitrobenzyl (*o*-NB) bis-acrylate crosslinker. Adhesive proteins were covalently attached using standard functionalization techniques for polyacrylamide gels. Upon polymerization, hydrogel networks were readily formed, where the initial stiffness could be precisely tuned by changing the concentrations of acrylamide and *o*-NB bis-acrylate molecules, respectively. When the hydrogels were exposed to light, the *o*-NB crosslinks cleaved and the stiffness of the photodegradable polyacrylamide gels decreased. We were able to control the dynamic range of the modulus by the exposure time and intensity of light. Fibroblast cells were successfully cultured on these materials and exhibited similar proliferation and viability to cells cultured on non-degradable polyacrylamide gels. In situ exposure of light decreased the modulus of the gels while maintaining cell attachment

and viability. In-situ softening led to changes in cell behavior that were not observed when cells were cultured on pre-softened gels, indicating that both dynamic and static environments, influence cell fate. Notably, we observed significant changes to nuclear localization of YAP and cytoskeletal organization after in-situ softening. To further explore the capabilities of polyacrylamide gels, we conjugated different amounts of the binding protein collagen or laminin and compare how the combination of binding protein and in-situ softening affects cell behavior. In this work, we have incorporated the simplicity and well-established protocols of standard polyacrylamide gel fabrication with the dynamic control of photodegradable systems. This will allow cell biologists and engineers to study more complex cellular behaviors that were previously inaccessible using standard polyacrylamide gels.

5.2 Introduction

Cells feel and respond to the physical properties of their surrounding environment. Processes such as embryonic development, metastasis, morphology, tissue architecture, and cell differentiation are all regulated, in some part, by their mechanical environment [7]. Through a variety of pathways and mechanisms cells are able to convert physical stimuli into chemical and electrochemical signals; a process generally termed as mechanotransduction. In order to study the biophysical environment and to elucidate how mechanics can dictate cell fate, researchers have utilized advances in hydrogel development [2, 203, 204, 1, 4]. Hydrogels, which are water-swollen polymer networks, are ideal materials to study how cells respond to their surrounding environment. Both the chemical and physical properties of hydrogels can be easily and controllably tuned, allowing for a wide variety of processes to be studied.

While such studies using static mechanical environments have been transformative, cells and tissues do not live in a static world, but rather continuously develop and remodel their environment. Interest in dynamic mechanical environments, and how time-dependent changes in the cells' physical microenvironment play a role in cellular development, has grown [18, 19]. In response, researchers have looked to improve upon classic hydrogel systems, and added the ability for their physical properties hydrogels to be tuned in both time and space [178, 179, 180]. One such method to achieve dynamic mechanics is to incorporate photodegradable *ortho*-nitrobenzyl (*o*-NB) linkers into the backbone of poly(ethylene glycol) (PEG) diacrylate macromers which are polymerized by free radical polymerization to form photodegradable hydrogels [38, 39]. This modification allows users to control the number of intact network strands and thus the elastic modulus of the gels as a function of exposure to light [131, 42]. Since this process uses non-toxic wavelengths of light, this matrix softening process can be performed on-demand and in the presence of cells [40, 41]. These photodegradable gels have been used to control cell behavior by controlling the matrix mechanics spatially [81, 78, 60], or temporally [48, 77, 58], through macroscale changes in hydrogels shape [53], and have been modified to better suit 3D culture [59, 205, 63].

While current PEG-based photodegradable hydrogels can examine cell behavior with in-situ changes to the matrix stiffness, we are interested to expand the photodegradable hydrogel system. Inspired by the flexibility of polyacrylamide (PAAm) gels, breadth of current research, and desire to compare to current literature, this work explores the use of photodegradable PAAm gels. Polyacrylamide gels are easy to fabricate and heavily used in cell biology either as cell substrates or for polyacrylamide gel electrophoresis (PAGE). Without modification, they are relatively chemically inert and do not nonspecifically bind to proteins [64]. Important to mechanobiologists, the elastic modulus of PAAm gels can be controllably and precisely tuned during fabrication [206]. Through various types of heterobifunctional linkers, researchers are able to attach full length proteins (rather than short synthetic peptide sequences [207, 208]) to the gel surface that allow for cell binding.

Thus far, polyacrylamide gels have been mechanically static and do not allow for researchers to study cell behavior in response to dynamic mechanical environments. In this study, we synthesize homobifunctional photodegradable bis-acrylate linkers that can be substituted for the bisacrylamide linkages typically used in PAAm gels. We derive a relatively simple, high yielding chemical synthesis (Figure5.1) that utilizes *o*-NB chemistries currently used for photodegradable PEG gels [39, 38, 35]. In order to incorporate the hydrophobic photodegradable linkages, we use a process previously reported to incorporate hydrophobic moieties into polyacrylamide gels [209, 66, 210, 211] and demonstrate the hydrogel fabrication of the photodegradable polyacrylamide gels (Figure 5.2). While other groups have previously reported the fabrication of some forms of photodegradable PAAm, they were not suited for live-cell applications [66, 54]. In this study, we demonstrate the flexibility of photodegradable PAAm hydrogels for cell culture. Using primary mouse ear fibroblasts (MEF), we dynamically modulate matrix mechanics to dictate cell behavior. We probe whether photodegradable PAAm gels are suitable to study the interplay between delivering dynamic matrix mechanical cues and cell-matrix interactions.

5.3 Materials and Methods

5.3.1 Materials

Deuterated solvents ($(CD_3)_2SO$ and $CDCl_3$) (Cambridge Isotope Laboratories), borane-THF (BH_3-THF) (Acros, 1 M), ethyl acetate (EtOAc) (Fisher, 99.9%), sodium bicarbonate (Amresco, ACS grade), sodium chloride (NaCl) (Fisher, ACS grade), anhydrous magnesium sulfate ($MgSO_4$) (Fisher, certified), tetramethylethylenediamine (TEMED) (OmniPur), ammonium persulfate (APS) (Acros Organics, 99%), sodium hydroxide (NaOH) (Fisher, ACS grade), Dulbecco's Phosphate Buffered Saline (DPBS) (Corning, 1×), 3-(3-Dimethylaminopropyl)-1-ethyl-carbodiimide hydrochloride (EDCl) (Chem-Impex, 99.23%), N-hydroxysuccinimide (NHS) (Alfa Aesar, 98+%), 3-(trimethoxysilyl)propyl methacrylate (Acros Organics, 98%), sodium dodecylsulfate (SDS) (OmniPr), acrylamide (AAm) (Fisher, Electrophoresis Grade), Bis-acrylamide (BAAm) (Fisher, Electrophoresis Grade), HEPES (Sigma), and 2-(*N*-morpholino)ethanesulfonic acid (MES) (Chem-Impex, 99.23%) were used as supplied. Acryloyl chloride (Alfa Aesar, 96% stabilized with 400 ppm phenothiazine), and dichloromethane (DCM) (Fisher, 99.9%) were distilled under Ar and stored under Ar in a dry, air-free flask. Triethylamine (TEA) (Omnipur, 99.0%) was distilled under Ar and stored over KOH pellets. Anhydrous tetrahydrofuran (THF) was dispensed from a Grubb's-type Phoenix Solvent Drying System and stored under Ar in a dry, air-free flask.

5.3.2 Chemical synthesis techniques

All reactions were performed under argon atmosphere using a Schlenk line unless noted otherwise. ^1H NMR spectra (δ ppm) of the small molecules were recorded on a Bruker Biospin Ultrashield (either 300 or 500 MHz) NMR spectrometer. All spectra were recorded in $CDCl_3$ or $(CD_3)_2SO$ using tetramethylsilane (TMS) as an internal standard. 4-(4-Acetyl-2-methoxy-5-nitrophenoxy)butanoic acid and 1,3-di(hydroxymethyl)-2-nitrobenzene **(3)** photodegradable precursors were synthesized as described previously [39]. 6-Acrylamidohexylaminohexanoic (N6) acid was also synthesized as described previously [212]

5.3.3 Synthesis of 4-(4-(1-hydroxyethyl)-2-methoxy-5-nitrophenoxy)butan-1-ol (1)

4-(4-Acetyl-2-methoxy-5-nitrophenoxy)butanoic acid (8.000 g, 26.91 mmol) was dissolved in 200 mL of THF in an argon atmosphere. The reaction mixture was cooled in a hexanes/liquid nitrogen bath (-20 ^oC) and 1 M BH_3-THF (95 mL, 95 mmol) was added dropwise. The reaction mixture was allowed to come to room temperature slowly and stirred overnight at room temperature (RT). The reaction mixture was cooled in an ice bath and 50 mL of water was added dropwise to quench any unreacted BH_3. The reaction mixture was concentrated by a rotary evaporator and 300 mL of ethyl acetate was added. The mixture was washed 5× with a saturated aqueous solution of sodium bicarbonate followed by three washes with brine. The organic layer was dried over $MgSO_4$, filtered, and concentrated to yield a yellow powder (6.715 g, 23.53 mmol, 87%). ^1H NMR (300 Mz, $CDCl_3$) $\delta = 7.56$ (1H, s, **ArH**), 7.26 (1H, s, **ArH**) , 5.52 (1H, q, Ar-$\mathbf{CH}(CH_3)O$), 4.11 (2H, t, $CH_2\mathbf{CH_2}OH$), 3.97 (3H, s, $ArO\mathbf{CH_3}$), 3.73 (2H, t, $ArO\mathbf{CH_2}CH_2CH_2$), 1.98 (2H, quin, $ArOCH_2CH_2\mathbf{CH_2}$), 1.77 (2H, quin, $ArOCH_2CH_2CH_2$), 1.55 (3H, d, $ArCH\mathbf{CH_3}$).

5.3.4 Synthesis of 1-(4-(4-(acryloyloxy)butoxy)-5-methoxy-2-nitrophenyl)ethyl acrylate (*o*-NB-bis-acrylate) (2)

4-(4-(1-Hydroxyethyl)-2-methoxy-5-nitrophenoxy)butan-1-ol **(1)** (1.845 g, 6.467 mmol) was dissolved in a mixture of DCM (20 mL), THF (20 mL), and TEA (3.6 mL, 26 mmol). The mixture was cooled in an ice bath and acryloyl chloride (2.1 mL, 26 mmol) was added dropwise. The reaction mixture was allowed to warm to room temperature and stirred overnight. TLC shows the formation of the product and no left over starting compound (DCM, R_f 0.49). Methanol was added to the reaction mixture to quench the acryloyl chloride and the mixture was concentrated under reduced pressure. The subsequent compound was dissolved in DCM washed twice with a saturated aqueous solution of sodium bicarbonate followed by two washes with brine. The organic layer was dried over $MgSO_4$, filtered, and concentrated to yield a yellow oil. Product was further purified by column chromatography in DCM (1.248 g, 3.172 mmol, 49%). ^{1}H NMR (300 Mz, $CDCl_3$) δ = 7.62 (1H, s, **ArH**), 7.06 (1H, s, **ArH**), 6.59 (1H, q, Ar-**CH**(CH_3)O), 6.49 (1H, d, CHO(CO)CH$\mathbf{CH_2}$), 6.45 (1H, d, CH_2O(CO)CH$\mathbf{CH_2}$), 6.21 (1H, q, CHO(CO)**CH**CH_2), 6.17 (1H, q, CH_2O(CO)**CH**CH_2), 5.92 (1H, d, CHO(CO)CH$\mathbf{CH_2}$), 5.88 (1H, d, CH_2O(CO)CH$\mathbf{CH_2}$), 4.30 (2H, t, $\mathbf{CH_2}$O(CO)CHCH_2), 4.14 (2H, t, ArO$\mathbf{CH_2}$$CH_2$$CH_2$), 3.98 (3H, s, ArO$\mathbf{CH_3}$), 1.97 (2H, quin, ArO$CH_2$$CH_2$$\mathbf{CH_2}$), 1.95 (2H, quin, ArO$CH_2$$\mathbf{CH_2}$$CH_2$), 1.71 (3H, d, ArCH$\mathbf{CH_3}$).

5.3.5 Synthesis of (2-nitro-1,3-phenylene)bis(methylene) diacrylate (4)

We previously described the synthesis of 2-acryloxymethyl-6-hydroxymethyl-nitrobenzene, which uses acryloyl chloride as a limiting reagent [39]. This reaction produces a statistical mixture of mono-functionalized (29.8 %), di-functionalized (27.1 %), and unfunctionalized (12.8 %) products which are purified via column chromatography. We previously utilized the mono-functionalized product [39, 81, 213], however, in this work we used the di-functionalized side product. This product could be synthesized more efficiently using a slight excess of acryloyl chloride. Briefly, 1,3-di(hydroxymethyl)-2-nitrobenzene

(3.385 g, 18.5 mmol) and TEA (5.20 mL, 37.3 mmol) were dissolved in a mixture of DCM (10 mL) and THF (20 mL) and cooled with an ice bath. Acryloyl chloride (1.50 mL, 18.5 mmol) was added dropwise. The reaction was allowed to warm to room temperature and stirred overnight. The reaction mixture was concentrated under reduced pressure and dissolved in 100 mL DCM. The organic layer was washed twice with brine and once with water. The organic layer was dried over $MgSO_4$, filtered, and concentrated to yield a yellow oil. The three products (TLC: diacrylate – DCM, R_f 0.34; monoacrylate – DCM/EtOAc 9:1, v/v, R_f 0.46; diol – DCM/EtOAc 1:1, v/v, R_f 0.54) were separated by gradient column chromatography (DCM to 1:1 DCM:EtoAc). The bis-acrylate product **(4)** was collected as colorless powder (1.459 g, 5.009 mmol, 27.1%,). ^{1}H NMR (300 Mz, $(CD_3)2SO$) $\delta = 7.71$ (3H, m, **ArH**), 6.34 (2H, d, OC(O)CH**CH_2**), 6.17 (2H, q, OC(O)**CH**CH_2), 6.01 (2H, d, OC(O)CH**CH_2**), 5.28 (4H, s, Ar**CH_2**).

5.3.6 Glass functionalization

(a) To covalently adhere the hydrogels to a glass substrate, round pieces of coverglass (12 mm diameter, Fisher) were functionalized with methacrylate groups using the following procedure. The coverglass was first cleaned with hexanes, acetone, water and methanol (in that order), dried, and activated with oxygen plasma (Plasma Prep II, SPI Supplies) for 5 minutes. The activated coverglass was then reacted with 3-(trimethoxysilyl)propyl methacrylate (0.5 mL) in 25 mL of a conjugation solvent solution (95 vol% Ethanol, 5 vol% water, adjusted to pH = 5 with acetic acid) for 30 minutes. The coated coverglass was then washed with methanol three times before drying. Silanized coverglass pieces were used within two hours of functionalization.

(b) Glass slides were rendered hydrophobic, and thus non-adherent to the polymerized hydrogels, by wiping a drop of Gel Slick (Lonza) on the slide surface. This process was repeated once to ensure a sufficient coating. The slides were then briefly rinsed with DI water to clean the surface and dried before use.

5.3.7 Fabrication of hydrogels

To overcome the hydrophobicity of the two *o*-NB-bis-acrylate linkers, we adopted previous procedures for incorporating hydrophobic moieties into polyacrylamide gels [214, 66, 209]. Photodegradable *o*-NB-bis-acrylate linkers (**2** & **4**) were mixed with a 25 w/v% sodium dodecylsulfate (SDS) in water. These mixtures were heated in a 55 ^{o}C water bath and vigorous vortexed. Rounds of heating and vortexing were repeated until the monomers were solubilized. The mixtures were centrifuged before further use to remove any air bubbles.

We first prepared stock solutions of acrylamide (40 w/v% in water), bis-acrylamide (2 w/v% in water), *o*-NB-bis-acrylate (5.1 mg **2** +100 μL 25% SDS or 3.7 mg **4** + 100 μL 25% SDS), N6 (100 mg + 510 μL water + 134 μL 10× HEPES buffer pH 8 + 27 μL 10 M NaOH), APS (10 mg + 100 μL water). TEMED was used in its pure form. The stock solutions were mixed together in the ratios given in Table 5.1, where APS and TEMED were added last. The prepolymer solutions were quickly and gently vortexed, paying special attention to not to create any bubbles, and 13 μL/gel was pipetted onto a hydrophobically modified glass slide. 12 mm methacrylate functionalized glass cover slips were then placed on top of the prepolymer solutions to create a glass slide/prepolymer/coverglass sandwich. The prepolymer solutions were allowed to polymerize for 20 minutes. Gels attached to the 12 mm coverglass were peeled off the glass slide and placed into a wash solution (3:1 1× PBS:isopropanol). Gels were then washed on a shaker plate in the PBS/isopropanol solution[215] for five days with two changes of the wash solution per day.

5.3.8 Protein conjugation

To conjugate specific proteins to the gel surface, previously reported procedures were adapted [216, 212]. Briefly, after washing the gels in the PBS/isopropanol solution, gels were washed with 100% 1× PBS twice, with the second washing spanning overnight. The next day gels were submersed in a MES buffer solution (0.1 M, pH = 6) for at least 2 hours. The MES buffer was aspirated off, and 100 μL of an EDC/NHS solution (76 mg EDC + 115 mg NHS + 2 mL MES buffer) was added to the surface of the gel and incubated for 30 minutes. The EDC/NHS solution was then aspirated off and the gels were washed in 1× PBS for 5 minutes. The PBS was aspirated off and 100 μL of the desired protein solution (1 μg/mL collagen, 10 μg/mL collagen, 100 μg/mL collagen (Type I, rat tail, Millipore), or 100 μg/mL laminin (Engelbreth-Holm-Swarm mouse tumor, Corning) in 1× PBS) was added to the gel surface. Gels were placed into the cell culture incubator overnight. The following day, gels were sterilized in 70% ethanol and rehydrated in sterile 1× PBS. Cells were cultured on these gels within the same day after sterilization.

5.3.9 Gel degradation and exposure conditions

Gels were degraded using a 365 nm Black Ray Bench Lamp light source; 115V 60 Hz, 0.68 Amps (UVP, LLC) with an output intensity of 7.8 mW/cm^2 (integrated between 300 and 500 nm) as measured by a spectroradiometer (International Light Technologies, ILT950). All samples receiving irradiation were exposed for 40 minutes in four increments of 10 minutes. Between degradations, the samples were placed in the incubator for 10 minutes to minimize heat build-up and control pH.

5.3.10 Atomic force microscopy

After gel polymerization and subsequent washing steps, the gels were submersed in 1× PBS to swell overnight. The next day, the gels were exposed to 365 nm light or left unexposed for a prescribed amount of time. The gels were then submersed in 1× PBS to swell overnight. Elastic modulus was measured using Atomic Force Microscopy (AFM) in PBS using a JPK Nanowizard 4a BioScience AFM using the force spectroscopy mode in the Nano and Pico Characterization Laboratory at the California Nanosystems Institute, UCLA. A CP-qp-CONT-SiO-B probe with a 3.5 μm diameter SiO2 sphere (sQube) was used to indent the sample. For the quantitative measurements of moduli, the spring constant of the cantilever was measured using the AFM's internal contact-free thermal tuning method. Single indentations were performed with a total force of 4.0 nN. At least 15 indentations were performed at 15 unique locations across the gel surface. All AFM force curve analysis was performed using the JPK Data Processing software. The Young's modulus was calculated by using a Hertz/Sneddon spherical fit with a Poisson's ratio of $\nu = 0.5$.

5.3.11 Cell culture

Ear tissues from adult C57BL/6 mice were minced and then partially digested in a solution of Liberase (0.025mg/ml, Roche) for 45 minutes under constant agitation at 37^{o}C. Partially digested tissues were plated and fibroblasts were allowed to migrate out (passage 0). Isolated fibroblasts were expanded in MEF medium (DMEM (GIBCO +10% FBS (GIBCO) and 1% penicillin/streptomycin (GIBCO)) and used exclusively at passage 2 for all experiments. Cells were trypsinized and passaged onto gels at a density of 1,000 cells per cm^2 in phenol red-free MEF medium and allowed to attach overnight before initiating degradation experiments. Two hours before the in-situ gel degradations occurred, 0.2 mg/mL glutathione reduced (GSH) (Fisher) and 220 U/mL catalase from bovine liver (Thermo Scientific) were added to all gels (those experiencing an in-situ degradation or not) in order to reduce any possible oxidative stress in the culture media during exposure. For a subset of samples, cell culture media was replaced with 20 μM Y-27632 ROCK inhibitor in low serum media two hours before gel degradation.

5.3.12 Immunostaining

For immunostaining, cells were fixed with 4% paraformaldehyde (Electron Microscopy Sciences) and washed with 1× PBS three times (each 5 minutes). Samples were then permeabilized with 0.5% Triton X-100 (Sigma) in PBS, washed with PBS three times, and blocked with 5% donkey serum (Jackson Immunoresearch) in PBS for 30 minutes. Primary antibodies were incubated overnight in blocking solution at 4^{o}C, followed by 1h incubation with Alexa 488- and/or Alexa 546-labelled secondary antibodies (Molecular Probes). For actin-cytoskeleton staining, samples were incubated with fluorescein-isothiocyanate-conjugated phalloidin (Invitrogen) for 1 hour. Nuclei were stained with DRAQ5$^{\text{TM}}$(ThermoFisher). Stained samples were mounted using Fluoromount (Southern Biotech).

5.3.13 Image acquisition and preparation

All samples were imaged with a fluorescence microscope (10×, Axiovert Observer Z1, Zeiss). Tiled images (7×7) were acquired at resolution of 0.645 μm/pixel. Image acquisition times and intensity were kept constant for all samples. Tiles were stitched together using the Zeiss Zen software and exported as TIF files without any histogram modification. In order to automate the cell image processing procedure and remove user bias, we implemented a series of machine learning and automatic cell classification processes. We found that simply thresholding the fluorescent images did not suffice. Imperfections such as dust lead to false positives, and image shading errors lead to low sensitivity and specificity, which can lead researchers to count cells and cell properties by hand. Such non-automated procedures produce low sample numbers and can induce user error and bias. In this work, individual pixels of the fluorescent images were classified (via a machine learning algorithm – ilastik software [217]) as belonging to the nucleus, cytosol, background, or false positive stained gel imperfections. These segmented images were used to isolate single cells and define the boundary between the nucleus-cytosol, cytosol-background, and the boundary between two cells using a custom pipeline in CellProfiler [218]. Once the cell boundaries are determined, cell morphology parameters (cell/nucleus area, perimeter, morphology,...) could be determined on a cell-by-cell basis.

5.3.14 Calculation of nuclear/cytosolic YAP ratio

Once individual cells were classified, we measured the YAP staining intensity ratio between the nucleus and cytosol. Specifically, we wrote a custom pipeline in CellProfiler that segmented the nucleus and a region 20 pixels dilated directly outside nucleus border. Any part of the dilated region that fell into the background was removed so that the dilated region only contained cell body. YAP staining intensities were then measured in these three regions for each individual cell. Since YAP staining is not necessarily consistent between samples, the median YAP staining intensity in pixels classified as background was subtracted from the YAP staining intensities in the regions described above. The ratio of the median YAP staining intensity between the nucleus and the region 20 pixels outside the nucleus was calculated for every cell.

5.3.15 Calculation of actin orientation

To quantify the degree of stress fiber formation and degree of actin fiber orientation at a certain length scale we applied a Fourier transform (FT) image analysis technique called the orientation index (OI). Details on the calculation of the orientation index can be found as used previously [219, 220, 221]. In this work, we were interested in fiber orientation within a 22.58 × 22.58 um space (35 × 35 pixels) which is a length scale we found to be most appropriate to quantify stress fiber formation. Briefly, a custom Matlab program was written that randomly selected 35 × 35 pixel regions within the phalloidin stained images, with the requirement that all pixels comprised cell body. Each 35 × 35 pixel region was mean subtracted and multiplied by a two-dimensional Gaussian function to remove edge effects in the discrete FT. The absolute value of the shifted FT was converted into polar coordinates around the center of the FT (r, ϕ). The magnitude of the FT was calculated as a function of ϕ by integrating across r. Here, the strength of the different angle bands within the FT are an indicator of fiber alignment. The orientation index typically spans between 0 and 100, where an index of 100 indicates perfectly aligned, strong fibers, and an index of 0 indicates a completely flat, homogeneous, and isotropic distribution of actin with no directionality. For each sample imaged, a total of 50 35 × 35 pixel regions were analyzed. Since each condition was repeated in three independent experiments, a total of 150 total regions were analyzed per condition.

5.3.16 Statistical analysis

All statistical calculations were performed in Origin(Pro), OriginLab Corporation. All plots were made in Origin(Pro), Adobe Illustrator, and ChemDraw.

To compare the YAP ratio, cell size, and cell form factor between samples, we randomly selected (via a computer algorithm) 50 cells for every sample tested. Each condition was tested in three independent experiments, thus a total of 150 cells per condition were analyzed. The data for each condition are displayed as a box-and-whisker plots. The box is drawn with ends at the quartiles, the statistical median as a horizontal line in the box, and the whiskers are extended to the farthest points that are not outliers. The max and min are represented by (–) symbols, the 99 and 1 percentile are represented by (×) symbols, and the mean is represented by a solid box symbol.

To determine the degree to which the population means are different we apply a Student's two-sample t-test assuming equal variance with the null hypothesis that the sample means are equal. For each pair of samples the p-value is calculated as a measure of the difference between the two sample populations. The p-value can be used to test statistical significance if it is below a set significance value (usually < 0.05, 0.01, 0.001, or less). Due to the sample size in this work, we use the p-value of 0.01 as a threshold for statistical significance, but examine the p-value more generally as an indication of the degree to which the sample means are different.

5.4 Results and Discussion

5.4.1 Fabrication of hydrogels

Typically, PAAm gels are crosslinked using the bis-acrylamide (BAAm) small molecule. BAAm has good water solubility, and can be easily polymerized into the PAAm backbone, linking chains together through its homobifunctional vinyl end groups. To replicate this monomer, we synthesized the diol version of two photodegradable moieties (**1** & **3**) and reacted them with acryloyl chloride to produce the photodegradable *ortho*-nitrobenzyl bis-acrylate crosslinkers (**2** & **4**). Once synthesized, we examined methods for incorporating them into PAAm gels where they act as crosslinkers.

A major limitation in the production of photodegradable polyacrylamide gels is that the photodegradable crosslinkers used have very low solubility in aqueous solutions. We initially made stock solutions of the *o*-NB linkages in dimethyl sulfoxide and other water miscible

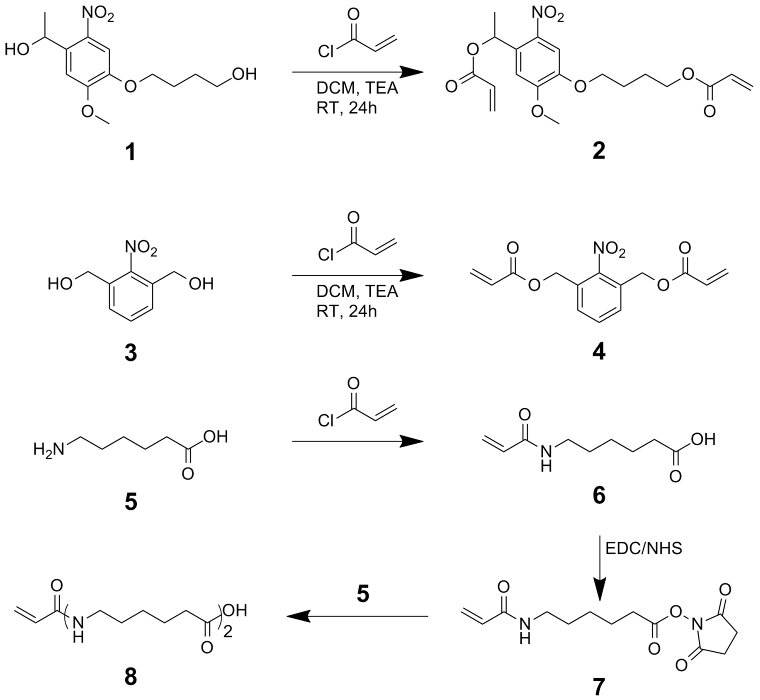

Figure 5.1: **Synthesis of photodegradable crosslinkers(2 & 4) and protein attachment linker (8).**

organic solvents, and added this stock solution to the overall aqueous gel solutions. However, the *o*-NB monomers either precipitated out of solution, or produced gels with very irregular and heterogeneous swelling. Following these experiments, we adopted previous procedures to incorporate hydrophobic moieties into PAAm gels [214, 66, 209] and first solubilized the *o*-NB linkages in a 25 w/v% solution of sodium dodecyl sulfate (SDS). The *o*-NB linkages readily went into solution after several rounds of vigorous vortexing and incubating in a 55 ^{o}C water bath. Once dissolved, the *o*-NB solutions were centrifuged to remove bubbles. From here, the *o*-NB SDS solution could be readily mixed with the other gel components in various ratios as outlined in Table 5.1. Once the gels were produced, we paid special attention to insure that all SDS had been removed. SDS is an ionic detergent that readily breaks up cell membranes. To remove SDS, the gels were submerged into PBS with 25% isopropanol and washed over the course of 5 days with multiple changes of the wash solution to ensure complete removal of SDS [215]. In addition, since SDS is ionic, it increases the osmotic pressure of the gels[209]. We found that washing with an aqueous solvent alone, caused too much swelling, leading to gel creasing [222, 223]. Since isopropanol is a poorer

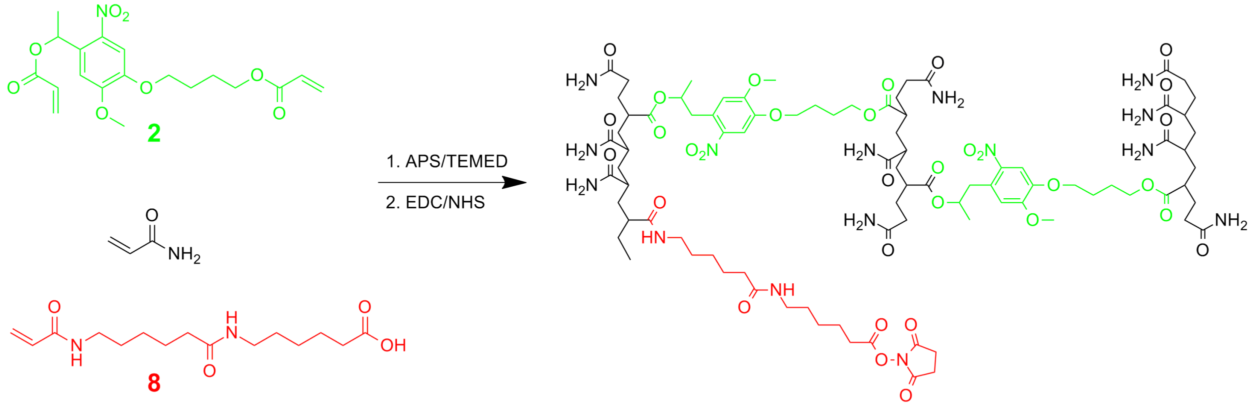

Figure 5.2: **Fabrication of photodegradable hydrogels.** Photodegradable polyacrylamide gels are formed by the copolymerization of acrylamide, photodegradable *o*-NB-bis-acrylate and 6-Acrylamidohexylaminohexanoic acid. A standard free radical initiator system (APS and TEMED) are used to polymerize the vinyl groups of the monomers. Acrylamide polymerizes into linear chains which are crosslinked together with *o*-NB-bis-acrylate. In order to attach cell binding proteins, 6-Acrylamidohexylaminohexanoic acid copolymerized into the gel and provides free carboxyl groups. After polymerization, the pendent carboxyl groups in the gel reacted with EDC to form an intermediate o-acylisourea ester that reacts with NHS to form an NHS ester.

solvent than water for PAAm chains, swelling is reduced and the gels do not crease.

We found that gels with *o*-NB crosslinker incorporated required more of the APS/TEMED initiator, presumably due to more radical chain transfer to the nitro-group [224]. We have observed this effect previously for both PEG-based [39, 81] and gelatin-based [213] photodegradable hydrogels incorporating *o*-NB moieties. We also found that gels made with the *o*-NB linker based on 1,3-di(hydroxymethyl)-2-nitrobenzene (**4**) were mechanically weaker than those using the 4-(4-(1-hydroxyethyl)-2-methoxy-5-nitrophenoxy) butanoate linker (**2**). Gels made with **4** did not degrade as rapidly (as observed previously for PEG-based gels [39] and swelled more, which led to gel creasing. For this reason, gels made with **4** were not examined for the rest of this study. During the production of these gels, we paid special attention to the total polymer content (%T) and the crosslinker concentration

($\%C$) given by:

$$\%T(\text{w/v}) = \frac{\text{AAm (g)} + \text{crosslinker (g)}}{\text{total volume (mL)}} \times 100\% \tag{5.1a}$$

$$\%C(\text{w/v}) = \frac{\text{crosslinker (g)}}{\text{AAm (g)} + \text{crosslinker (g)}} \times 100\%, \tag{5.1b}$$

where the crosslinker refers to either the *o*-NB-bis-acrylate or bis-acrylamide di-vinyl crosslinkers. These values, along with the gel compositions, are reported in Table 5.1. As is commonly known for PAAm gels, increasing both $\%T$ and $\%C$ will increase the elastic modulus of the subsequent gels [206, 222]. It is also well known that the osmotic pressure of polymer networks and solutions increase as a function of polymer concentration. The osmotic pressure is balanced with the stored elastic energy to determine the volumetric swelling ratio [50]. Increasing the crosslinker concentration while keeping the polymer concentration constant, however, does not increase osmotic pressure. Thus, both properties $\%T$ and $\%C$ can be tuned to achieve optimal gel properties. In Table 5.1 we show the compositions of a variety of gels that were fabricated and tested. To name the gels, we used the following scheme: standard PAAm gels have a "b" prefix (for bis-acrylamide) followed by a number that represents the total μL of AAm stock; gels incorporating *o*-NB groups have an "*o*" prefix (for *o*-NB), followed by the μL of AAm stock, and a suffix that indicates the $\%C$ value (LL = 2.25, L = 2.75, M = 3.23, H = 3.75). We found that when we fixed $\%C = 3.23$ we achieved optimal properties: for $\%C < 3.23$ gels attached to pieces of coverglass tended to crease when swollen (especially after degradation); and for $\%C > 3.23$ the dynamic range of the elastic modulus was reduced. Thus, we fixed $\%C = 3.23$ and controlled the mechanical properties of the gels by modifying $\%T$ (See Table 5.2 & Figure 5.4).

5.4.2 AFM of hydrogels

To characterize the mechanical properties of our gels, we used atomic force microscopy (AFM), indenting the surface of the gels with a 3.5 μm diameter colloid probe. Since degradation of the gels occurs mostly at the surface (due to optical attenuation of the *o*-NB

Table 5.1: Composition of different polyacrylamide gels, both photodegradable and non-degradable. All volumes in μL.

Name	Water (μL)	AAm Stock (μL)	Bis Stock (μL)	*o*-NB Stock (μL)	N6 Stock (μL)	APS Stock (μL)	TEMED (μL)	%T (w/v)%	%C (w/v)%	Initial Modulus (kPa)
b150	774	150	25	n/a	40	10	1	6.05	0.830	2.49 ± 0.04
b200	617	200	132	n/a	40	10	1	8.26	3.19	27.8 ± 1.5
*o*300M	416	300	n/a	200	40	40	4	12.4	3.23	21.6 ± 3.0
*o*262M	479	262	n/a	175	40	40	4	10.9	3.23	16.1 ± 0.9
*o*225M	541	225	n/a	150	40	40	4	9.30	3.23	14.7 ± 1.6
*o*169M	634	169	n/a	113	40	40	4	7.00	3.23	7.25 ± 1.60
*o*145M	674	145	n/a	97	40	40	4	6.00	3.23	2.81 ± 0.11
*o*121M	714	121	n/a	81	40	40	4	5.00	3.23	1.33 ± 0.14
*o*097M	755	97	n/a	64	40	40	4	4.00	3.23	0.286 ± 0.028
*o*339L	385	339	n/a	192	40	40	4	14.0	2.75	42.6 ± 17.1
*o*301L	444	301	n/a	171	40	40	4	12.4	2.75	30.3 ± 13.5
*o*264L	503	264	n/a	149	40	40	4	10.9	2.75	11.8 ± 1.1
*o*341LL	418	341	n/a	157	40	40	4	14.0	2.25	16.7 ± 2.9
*o*303LL	473	303	n/a	140	40	40	4	12.4	2.25	6.11 ± 0.65
*o*261H	452	261	n/a	203	40	40	4	10.9	3.75	73.3 ± 2.3
*o*224H	518	224	n/a	174	40	40	4	9.30	3.75	13.2 ± 1.0

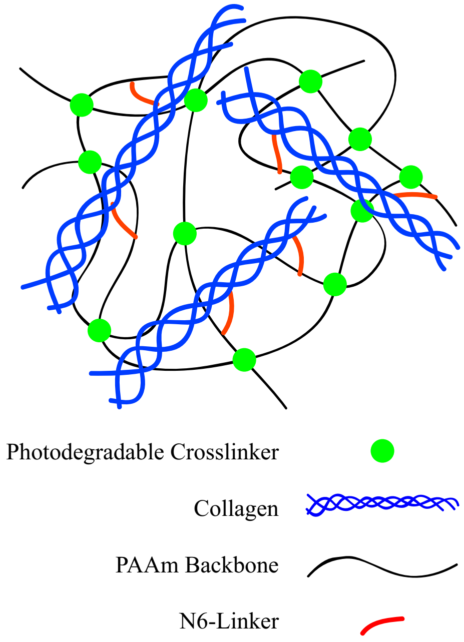

Figure 5.3: **Structure of photodegradable polyacrylamide hydrogels with attached cell binding proteins.**
Free primary amines of the protein of choice (e.g., collagen, laminin...) react with the NHS ester shown in Figure 5.2 to couple the protein to the gel surface.

linker), light-induced changes in the gel mechanical properties occur only at the surface. AFM is an optimal suited technique to measure surface properties. In Figure 5.4 we show a simple example of how increasing either $\%T$ (while keeping $\%C$ constant) increases elastic modulus of the photodegradable PAAm gels. We demonstrate that *o*-NB-PAAm gels achieve the same range of mechanical properties as traditional PAAm gels – a range relevant in cell mechanobiology [200]. Once fabricated, gels incorporating the *o*-NB crosslinker were exposed to 365 nm light (7.8 mW/cm^2 – a previously identified cytocompatible dose [40, 38, 41]) for different amounts of time (0, 10, 20, and 40 minutes). The Young's modulus E of the gels was measured to demonstrate their on-demand photodegradability and softening. In Table 5.2, we present seven different gel compositions, all with $\%C = 3.23$, while increasing $\%T$ between gels. For each gel composition, we measured the initial elastic modulus and the subsequent moduli after set periods of degradation, exhibiting a wide range of mechanical properties. In Figure 5.5, we graphically display a subset of this data, showing the monotonic decrease in Young's modulus as a function of exposure time.

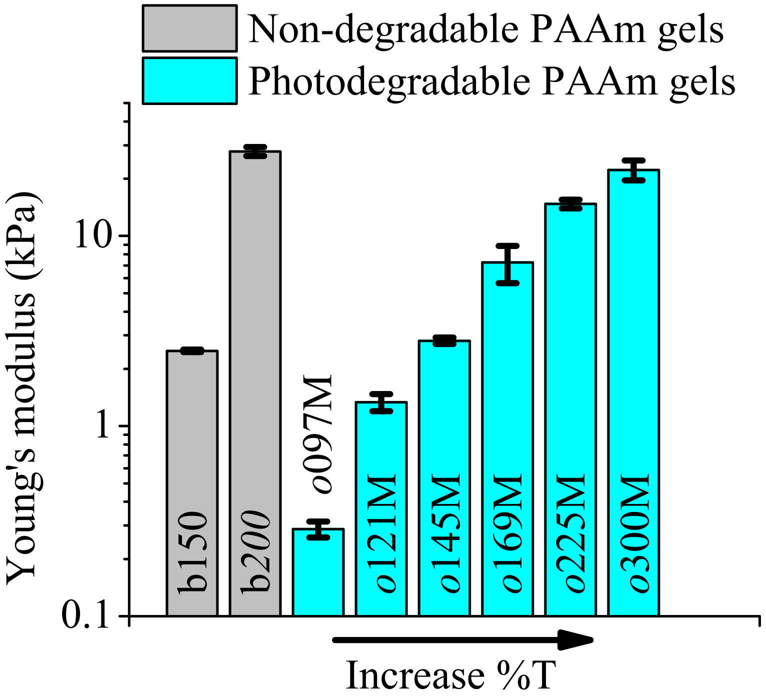

Figure 5.4: **Controlling gel mechanics by composition.**
Photodegradable gels can be stiffened by increasing the total polymer content ($\%T$) of the gel while keeping the fraction of crosslinker fixed ($\%C = 3.23$) . [206] The initial mechanics of a subset of gels displayed in Table 5.1 are plotted here with corresponding labels. The gel composition can be tailored to match the mechanical properties of standard non-photodegradable PAAm gels. Error bars represent the standard deviation, $n \geq 15$ independent indentations per sample.

Table 5.2: Gel mechanics as a function of composition and degradation time (kPa).

Gel Designation	Degradation time			
	0 min	10 min	20 min	40 min
*o*097M	0.287 ± 0.028	0.0922 ± 0.0329	0.0317 ± 0.0102	n/a
*o*121M	1.13 ± 0.14	0.873 ± 0.266	0.0407 ± 0.0600	0.235 ± 0.025
*o*145M	2.81 ± 0.11	1.84 ± 0.09	1.22 ± 0.08	0.804 ± 0.029
*o*169M	7.25 ± 1.60	5.85 ± 1.45	3.32 ± 0.67	2.23 ± 0.27
*o*225M	14.7 ± 0.8	11.0 ± 0.5	7.91 ± 0.30	6.12 ± 0.39
*o*300M	21.6 ± 3.0	15.4 ± 1.6	12.0 ± 0.7	9.42 ± 0.69

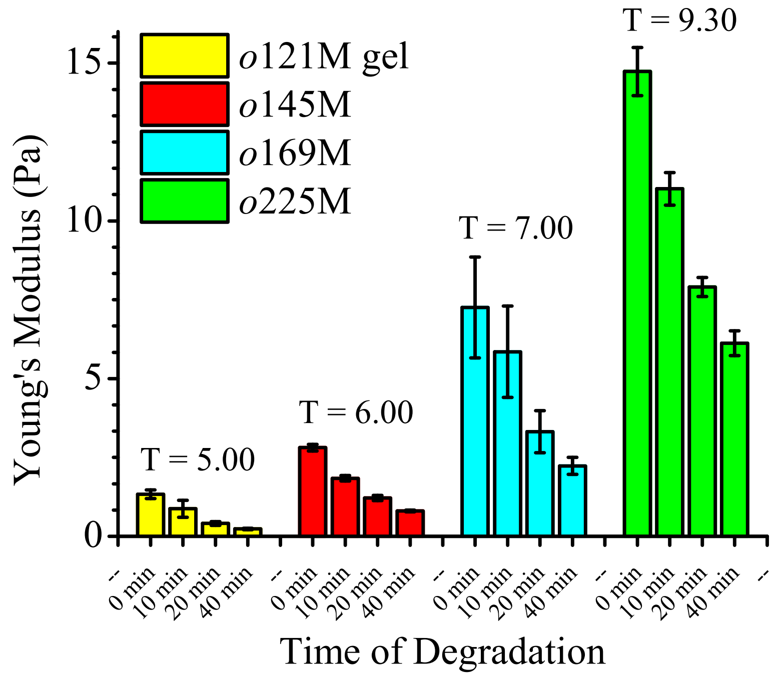

Figure 5.5: **Gel mechanics as a function of exposure time.**
Upon exposure to light, the *o*-NB crosslinkers cleave and the modulus of the photodegradable PAAm gels decrease. Gel modulus as a function of exposure time is plotted. The moduli of four different gel types (Tables 5.1) are shown. Initial modulus is controlled by increasing $\%T$ while maintaining $\%C = 3.23$. Individual modulus values can found in Table 5.2. Using both gel composition and exposure time, we can probe a large range of gel mechanics. Error bars represent the standard deviation, $n \geq 15$ independent indentations per sample.

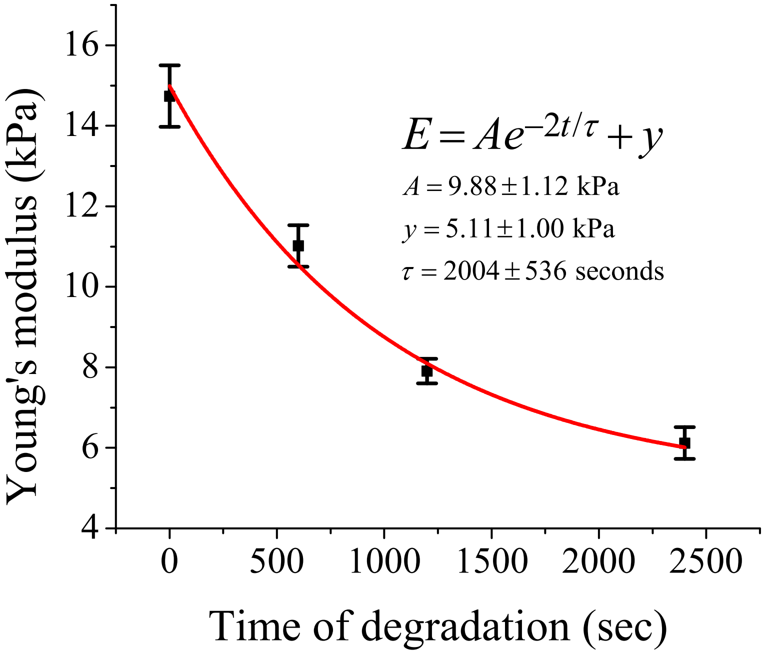

Figure 5.6: **Fit of elastic modulus with exponential decay.** The young's modulus is fit to an exponential decay function. The o225M gel is exposed to 365 nm 7.8 mW/cm^2 light that softens the gel as determined by AFM. Error bars represent the standard deviation, $n \geq 15$ independent indentations per sample.

Using the o225M gels as an example, we calculated the rate constant of degradation. Researchers have shown the elastic shear modulus G (which is proportional to the Young's modulus E) for PAAm hydrogels is proportional to $\%C$ given that $\%C \lessapprox 4$ [225]. Since the cleavage of o-NB crosslinkers follow first order rate kinetics, the elastic modulus data was fit to an exponential decay function as a function of the exposure time t:

$$E = Ae^{-2t/\tau} + y, \tag{5.2}$$

where A is the amplitude, y is the offset and τ is the characteristic degradation time. According to Figure 5.6, for the o225M gels, we calculate τ to be equal to 2004 ± 536 seconds for an irradiation intensity of 7.8 mW/cm^2 using 365 nm light. Since the characteristic degradation time is inversely proportional to the irradiation intensity, we can compare to other photodegradable hydrogels currently in the literature by using the parameter $\tau \cdot I_0$, where I_0 is the incident light intensity at the gel surface. For these photodegradable PAAm gels, we found that $\tau \cdot I_0 = 15631$ mW$\cdot s$/cm^2. In comparison, Griffin and Kasko measured

$\tau \cdot I_0 = 3030$ mW$\cdot s/\text{cm}^2$ for PEG-based hydrogels [39], and for hyaluronic acid-based photodegradable hydrogels, Rosales et. al measured $\tau \cdot I_0 = 8000$ mW$\cdot s/\text{cm}^2$ [58]. The τ for these photodegradable PAAm gels is large in comparison to the PEG gels. We note, however, that each PAAm chain has many crosslinks attached to it. Cleaving a single crosslink on a PAAm chain will not drastically alter the elastic effectiveness of that chain. In PEG-based photodegradable gels, cleaving a single end group renders the respective network strand elastically ineffective, thus the gels degrade rapidly. In this regard, the mechanical behavior of photodegradable PAAm gels more closely resembles that of photodegradable hyaluronic acid gels, which also likely have more than two linkages per chain, and are more likely to contain physical entanglements than PEG-based gels [58].

Furthermore, since the *o*-NB crosslinkers are solubilized using SDS, they likely become grouped together in micelles. Upon polymerization the photodegradable crosslinks likely group to form multi-monomer blocks along the polymer backbone [66]. The individual crosslinks in the group will not individually crosslink to separate PAAm strands, rather, they will likely bind to the same adjacent strand. If a single one of these crosslinks in the group is cleaved, the two PAAm chains will remain bound at the "grouped crosslink" and the mechanical properties of the network will not change. Moreover, the Beer–Lambert law does not apply if local photoabsorbing species concentration is high, leading to irregular behavior. Considering these factors, we aim to improve upon the degradation speed of these photodegradable PAAm gels in the future.

5.4.3 Cell Response

While generally accepted that 365 nm light does not adversely modify cell function and downstream effects [41, 40, 58, 77] we tested the exposure conditions used in this study and determined the cytocompatibility of this system. To do this, primary mouse ear fibroblast cells were cultured on non-photodegradable PAAm gels coated with 100 μg/mL collagen. After 24 hours of culture, the cells were exposed to three conditions: 1) cells received no irradiation; 2) cells received the prescribed 40 minutes of irradiation; or 3) cells

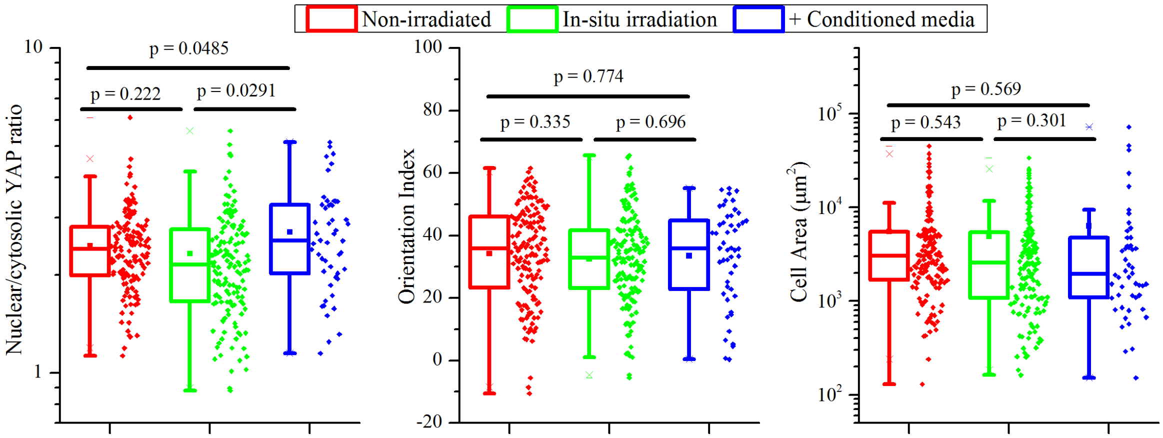

Figure 5.7: **Light controls on non-photodegradable PAAm hydrogels.** Nuclear/cytosolic YAP, orientation index, and cell area are examined for cells cultured on non-photodegradable hydrogels. Hydrogels with cultured cells were either not exposed to light, exposed to light in-situ, or culture media is replaced with media from an exposed photodegradable o-NB gel. We found no significant change in the cell area, orientation index, or the nuclear/cytosolic YAP ratio given these conditions. $n = 150$ cells per condition. We consider p-values where $p < 0.01$ indicates statistical significance.

received no irradiation, but after the irradiation period their media was replaced with a “conditioned” media. This “conditioned” media was produced by incubating a set of o225M photodegradable PAAm gels in culture media without any cells. We decided to transfer the “conditioned” media immediately after exposure in order to test if any irradiation-induced oxidative stress components were present, which can quench quickly. These cell-less gels received the same irradiation conditions. The media in the presence of these irradiated gels was labeled “conditioned”. Since the irradiation period lasted a total of 70 minutes (due to 10 minute incubation periods without light between irradiations) we estimate that this was sufficient time for any photodegradation products to diffuse out into the media as well. Cells were fixed and stained 48 hours after seeding. In Figure 5.7, we show that nuclear/cytosolic YAP ratios, actin orientation index, and cell area do not significantly change between these three conditions. These results indicate that the irradiation conditions alone, and any potential byproducts from the photodegradation reaction, do not adversely affect cell behavior. In Figure 5.7, we show the box plots and the data points for individual cells. For each plot, we indicate the p-value between the three different conditions, using $p < 0.01$ as the condition for statistical significance.

Next, we examined primary mouse ear fibroblast (MEF) cell behavior using o225M gels with 100 μg/mL collagen attached. We examined how cell behavior responded to mechanically dynamic environments. In general, all cell data on photodegradable PAAm gels presented in this work used the o225M composition. These gels had an initial Young's modulus of 14.7 ± 0.8 kPa and, after 40 minutes of exposure/degradation, had a Young's modulus of 6.12 ± 0.39 kPa (Table 5.2). Three different mechanical environments were tested. Cells were seeded on: 1) gels that received no degradation – "non-degraded" (14.7 kPa); 2) gels degraded before cell seeding – "pre-degraded" (6.12 kPa); and initially stiff gels that were softened via photodegradation 24 hours after cell seeding – "in-situ degradation" (14.7 → 6.12 kPa). For all gel conditions, cells were fixed 48 hours after seeding.

For each gel condition, we examined cell properties shown previously to be mechanosensitive. Of particular interest, nuclear localization of the transcriptional regulator yes-associated protein (YAP) has been shown to be mechanosensitive for cells cultured on 2D substrates and increases a function of increasing matrix stiffness [204]. We tested if our photodegradable PAAm gels could induce a reversal of the nuclear translocation of YAP as the gels are softened – a process researchers have observed previously [77, 58]. To do this, we measured the median fluorescence intensity of stained YAP within the nucleus as well as within a 20 × 20 pixel region outside the nucleus (see image processing section). In Figure 5.8, we show both the statistical box–whisker plots as well as individual cell data points. For each plot, we indicate the p-value between the three different conditions. As shown in Figure 5.8, we found that YAP did not necessarily localize to the nucleus more in the non-degraded (14.7 kPa) gels as compared to the pre-degraded (6.12 kPa) gels. However, cells that experienced an in-situ softening markedly decreased the amount of nuclearized YAP (see Figure 5.9, first column). This result was counter to our inclination that nuclear localization of YAP would depend most strongly on the matrix stiffness felt by the cells [204], rather than the dynamics of the matrix stiffness alone.

Qualitatively, we observed that actin structures in cells experiencing in-situ softening of the underlying matrix were less organized, which could be correlated to the higher cytosolic levels of YAP [226, 227, 228]. To quantitatively examine this observation, we calculated the

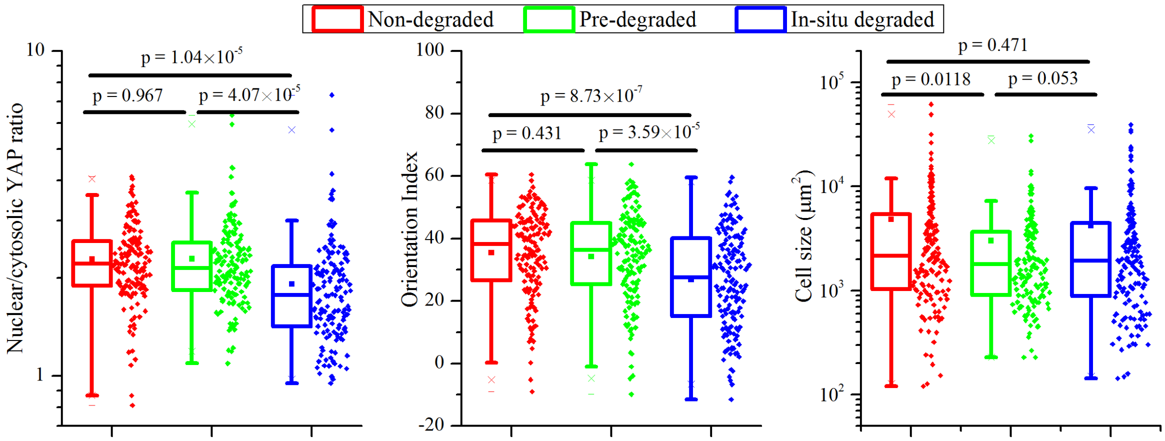

Figure 5.8: **Cell response on photodegradable PAAm gels.** Cells were cultured on initially stiff (non-degraded, 14.7 kPa) and initially soft (pre-degraded, 6.12 kPa) gels. A subset of the initially stiff gels were exposed to light 24 hours after cell seeding for 40 minutes to soften them (in-situ degraded, 14.7 → 6.12 kPa). All gels were coated with 100 μg/mL collagen. For each condition, the nuclear/cytosolic YAP intensity ratio, orientation index, and cell area were calculated. Individual data points represent data for a single cell, and the box plots display the variation of the statistical populations. $n = 150$ cells per condition. We consider p-values where $p < 0.01$ indicates statistical significance.

orientation index (OI) of randomly selected 35 × 35 pixel (22.58 × 22.58 μm) regions of the fluorescently-labeled phalloidin stain within the cells. The orientation index is a measure of the power distribution of the spatial-frequency-averaged, two-dimensional Fourier transform [229], allowing for measurement of local organization of actin fibers. We found that the window size of 35 × 35 pixels was the best length scale to quantify localized bundles of actin and stress fibers. Similar to the nuclear localization of YAP, we found that the actin orientation index of cells cultured non-degraded (14.7 kPa) gels did not markedly differ from that of cells cultured on pre-degraded (6.17 kPa) gels as shown in Figure 5.8. In Figure 5.13 (first column) we see that actin structure is generally preserved between cells on non-degraded and pre-degraded gels. However, once cells experience an in-situ softening, the actin structure becomes more diffuse.

Cells have long been known to gradually spread more as matrix stiffness increases within a range of $\approx 1 - 40$ kPa [1]. In addition to nuclearization of YAP and actin structure, we looked to see if the dynamic mechanical environment affected cell area. As shown in Figure 5.8, we found that average cell size decreased when cells were cultured on softer (pre-degraded

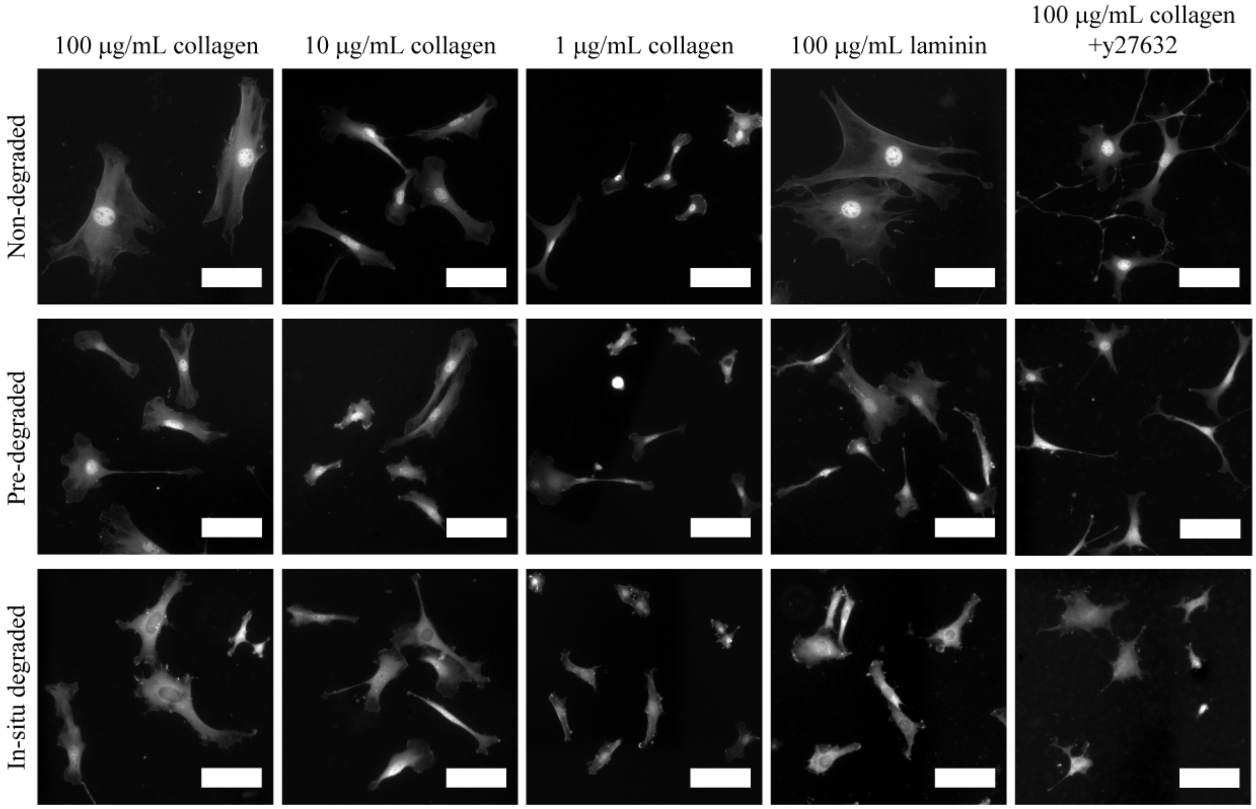

Figure 5.9: **Examples of YAP staining.**
Cells cultured on gels with the same conditions as in Figure 5.10 are shown stained for YAP. For each culture condition (100, 10, and 1 μg/mL collagen; 100 μg/mL laminin; and 100 μg/mL collagen + y27632) we show examples of gels that are either non-degraded (top row), pre-degraded (middle row), or in-situ degraded (bottom row). Clear examples of cytosolic and nuclear YAP can be seen. Error bars are 100 μm.

$\approx 3000\ \mu\text{m}^2$) substrates compared to cells cultured on stiffer substrates (non-degraded $\approx 4800\ \mu\text{m}^2$), however, we do not consider this decrease to be statistically significant given the relatively high p-value ($p = 0.0118$) between the two conditions when using $p < 0.01$ to indicate significance. More surprisingly, the area of cells exposed to in-situ softening did not further decrease ($\approx 4200\ \mu\text{m}^2$). Taken together, and given the relatively high p-values, we do not conclude that cell area for this particular cell type, under these specific gel conditions, was significantly affected by matrix mechanics – static or dynamic.

Next, we looked at the behavior of cells cultured on photodegradable PAAm gels with variable conjugated protein density and different proteins types – an attractive versatility of the polyacrylamide gels system. In Figure 5.9, we show example images of cells with YAP staining, and in Figure 5.13 we show example images of cells stained with phalloidin (actin) and DRAQ5 (nucleus) for each condition. In all conditions, we observe that cells undergoing in-situ softening of their matrix lose nuclear YAP and that cell size typically decreases with lower surface ligand concentration. Measured data from the cells corroborates this observation as seen in Figure 5.10. For the three different collagen densities (100, 10, and 1 μg/mL) and gels with 100 μg/mL laminin, the nuclear/cytosolic YAP ratio of the cells drops with in-situ matrix softening. For gels with laminin attached and lower collagen densities (10 and 1 μg/mL), cells seem to respond more to both the pre-degraded and in-situ conditions. That is, cells respond differently to their surrounding mechanics when the binding ligand density or type is different.

Similar to the results seen in Figure 5.8, Figure 5.12 shows that neither cells on initially soft pre-degraded gels nor on in-situ softened gels have a significantly different cell area from the non-degraded gels. Ligand type and density play a role in cell area, but for this cell type and stiffness range, the elastic modulus of the gels does not. Upon examination of the actin orientation index, we find that reducing the ligand density generally reduces the degree to which actin is organized. Again, we observe that actin organization is approximately the same in cells cultured on non-degraded gels and pre-degraded gels. However, the orientation index drops for cells cultured on gels with in-situ softening (see Figure 5.13 for examples).

To further explore this behavior, we incubated cell cultures in Y-27632, a rho-associated

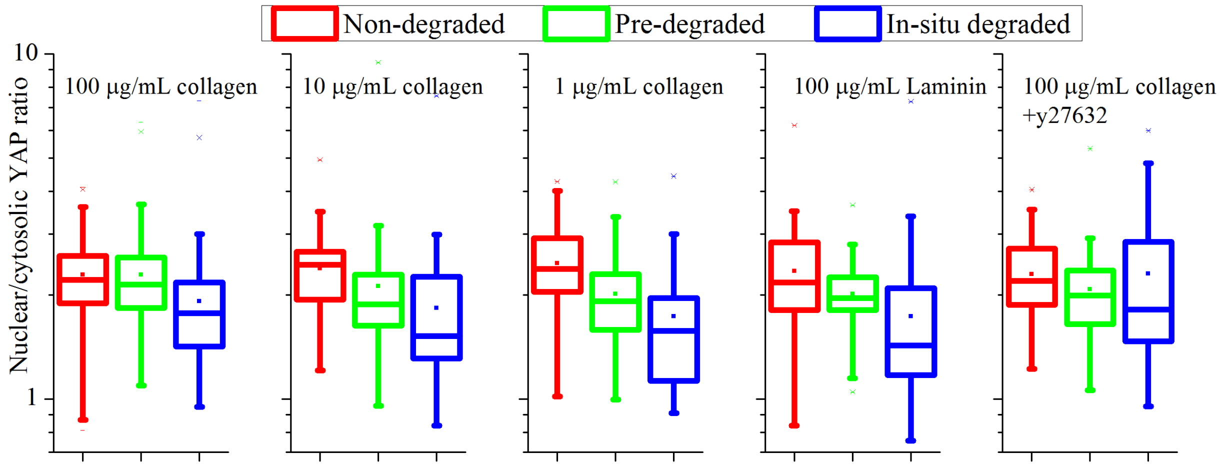

Figure 5.10: **Quantification of nuclear/cytosolic YAP for different gel conditions.** We subsequently examine cells cultured on gels with different concentrations of collagen (100, 10, and 1 μg/mL), laminin (100 μg/mL), and collagen coated gels (100 μg/mL) where ROCK inhibitor y27632 was added into the culture. Again cells were cultured on non-degraded (14.7 kPa) pre-degraded (6.12 kPa) and in-situ degrade (14.7 → 6.12 kPa) gels. Data is represented as box plots.

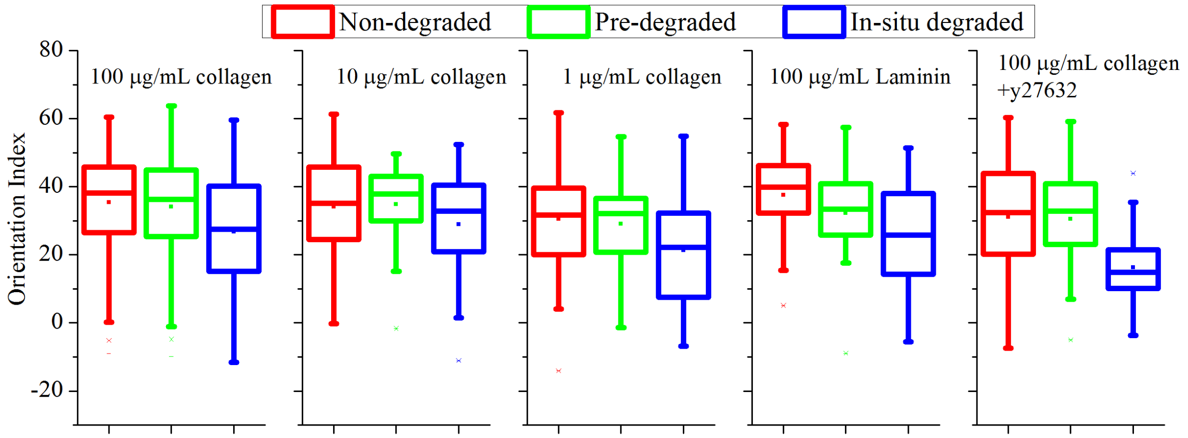

Figure 5.11: **Quantification of orientation Index.**
Given the same conditions outlined in Figure 5.7, the calculated orientation index is displayed as box plots. (Again, only one sample was analyzed for the collagen

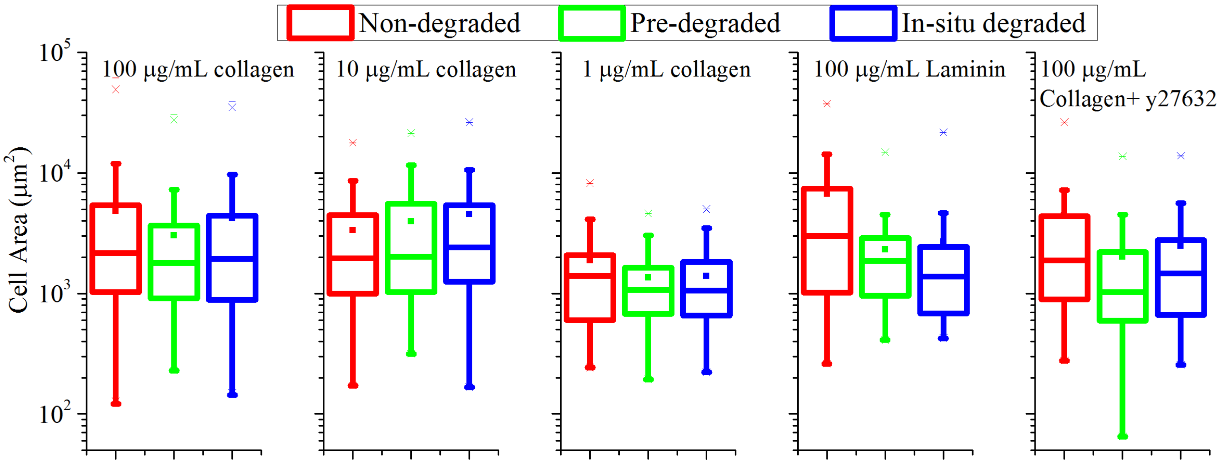

Figure 5.12: **Quantification of cell area.**
Given the same conditions outlined in Figure 5.10, the measured cell area is displayed as box plots.

protein kinase (ROCK) inhibitor, which reduces actin organization and contraction. As shown in Figure 5.10, addition of Y-27632 removed the effect of in-situ softening on lowering the nuclear/cytosolic YAP ratio. This indicates that the cell behavior we observe, for cells experiencing an in-situ matrix softening, is related to how cells are feeling the mechanical changes to the surrounding matrix. By reducing the cells' ability to organize and contract their actin filaments, we reduce their ability to sense the dynamic mechanical cues. Accordingly cell area does not differ significantly as a function of matrix mechanics when Y-27632 is added. We do notice, however, that actin organization as measured by the orientation index very drastically diminishes for cells experiencing in-situ matrix softening that have been treated with Y-27632. We are not exactly sure of the reason behind this drastic reduction in actin organization. However, the result points to the fact that both chemical and physical cues produce a combined effect on the organization of cellular actin. Photodegradable PAAm gels may be uniquely suited to study the combined cues on cell behaviour.

5.5 Conclusions

In this work we demonstrate the synthesis and cell biology applications of photodegradable polyacrylamide gels. We simply present a new tool for analyzing cell behaviour and

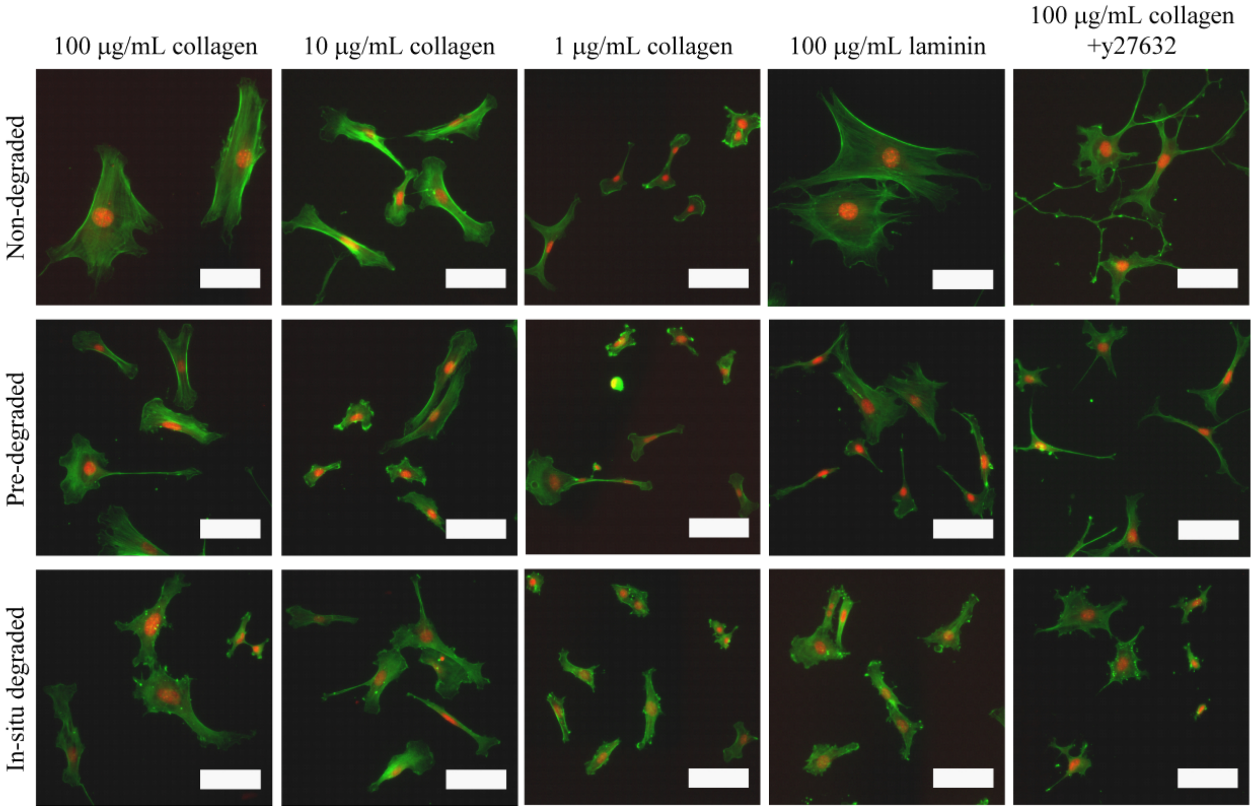

Figure 5.13: **Examples of nuclear and cytoskeleton stained cells.**
Cells were stained with phalloidin (cytoskeleton - green) and DRAQ5 (nucleus - red). We show example cells as the same conditions as Figure 5.10. Clear examples of actin fiber orgainization and cell size/morphology can be seen. Error bars are 100 μm.

demonstrate potential applications. We utilized the classic *ortho*-nitrobenzyl chemistry to produce two different *o*-NB-bis-acrylate linkers. These linkers were used to crosslink polyacrylamide chains during hydrogel formation. They hydrogel formation process is simple and analogous to that of the traditional PAAm gels already used for cell culture. In this work, we focused on the feasibility of photodegradable polyacrylamide gels to study dynamic matrix softening on cell behavior. Our main objective was to be able to take the well-established PAAm system for cell culture and expand its utility by adding the ability to dynamically tune the matrix mechanics in the presence of cells. Our goal is to be able to broaden the already expansive set of results obtained using standard PAAm gels and add an extra dimension to the questions that can be asked. Furthermore, unlike the already established PEG-based photodegradable hydrogels, we show that the photodegradable PAAm system allows researchers to quickly and easily test different cell binding ligands, and important feature when studying the interaction between cells and their surrounding matrix.

As a brief introduction to the usefulness of the photodegradable polyacrylamide gels, we examine the behavior of primary mouse ear fibroblasts and their response to gel mechanics. In general, we show that under the conditions tested, these cells respond more to in-situ changes in matrix mechanics than they do to the static mechanical environment alone. Overall, since we use primary cell lines, which are quite heterogeneous, we may not expect that their response to static mechanical cues will show statistical differences in the cell behavior. We also examine the roll of cell binding ligand type and density. Here, we show that there exists a complex interplay between static mechanics, dynamic mechanics and cell binding domains. The results point to the fact that both chemical and physical cues produce a combined effect on the organization of cellular actin. Photodegradable PAAm gels may be uniquely suited to study the combined cues on cell behavior.

CHAPTER 6

Direct Gradient Photolithography of Photodegradable Hydrogels with Patterned Stiffness Control with Sub-Micron Resolution

6.1 Abstract

Cell response to matrix mechanics is well known; however, the ability to spatially pattern matrix stiffness to a high degree of control has been difficult to attain. This study describes the use of maskless photolithography as a flexible process for direct, non-contact gradient patterning of photodegradable hydrogels with custom graphics. Any input gray scale image can be used to directly chart hydrogel crosslink density as a function of spatial position. Hydrogels can be patterned with submicron resolution, with length-scales within a single substrate spanning several orders of magnitude. A quantitative relationship between input grayscale image pixel intensity and output gel stiffness is validated, allowing for direct gradient patterning. Such physical gradient hydrogel constructs are rapidly produced in a highly controlled fashion with measured stiffness ranges and length-scales that are physiologically relevant. Mesenchymal stem cells cultured on these physical gradients matrices congregate and align orthogonal to the gradient direction along iso-degraded lines. This approach results in a robust and high throughput platform to answer key questions about cell response in heterogeneous physical environments.

6.2 Introduction

In tissue biology it is well known that cell organization, boundaries, and interfaces are important in tissue formation and repair.[4] For example, changes in tissue stiffness occur naturally, such as the bone to cartilage interface in the articular surface. Additionally, changes in composition and mineral density give rise to gradients in material stiffness in teeth.[21] As such, cell behavior, in the context of the surrounding physical environment of the extracellular matrix (ECM), has been well studied.[1, 4] In vivo, the cellular microenvironment is highly heterogeneous. Spatial variations in extracellular matrix stiffness from neighboring cells and tissues can occur at subcellular lengthscales,[5] but, the mechanisms by which cells spatially organize and form tissue interfaces (as triggered by the mechanically heterogeneous ECM) are still unknown. The investigation, of how such interfaces form, has been limited by a lack of materials that allow real-time, on demand control of the mechanical environment across a broad range of physiologically relevant length scales. Photodegradable hydrogels, a novel class of polymeric biomaterials exhibiting precisely controlled on-demand degradation, have been recently developed and optimized by our group.[38, 39] *ortho*-Nitrobenzyl (*o*-NB) linkers are easily incorporated into polymerizable poly(ethylene glycol) diacrylate (PEG-DA) macromers that can be crosslinked via a number of chemical approaches (ie. free radical polymerization, Michael addition, etc.) to yield photodegradable hydrogels (6.1). The outstanding benefit of these materials is that their physical and chemical properties can be altered externally, in real-time, without the presence of small molecule catalysts or other toxic compounds, allowing cells to be present during fabrication as well as modification. In addition, the degradation, and hence the material property of interest, is a strict function of the exposure to light (exposure time and intensity) such that precise spatial and temporal control of the degree of degradation can be achieved to an extent far surpassing other mechanisms (such as hydrolysis and enzymolysis).

To date, controlled photodegradation has been limited to using physical photomasks[48, 230, 52] and two-photon techniques.[48, 49, 45] A physical photomask blocks light from reaching certain regions of the substrate, thus, creating a binary, degraded/non-degraded

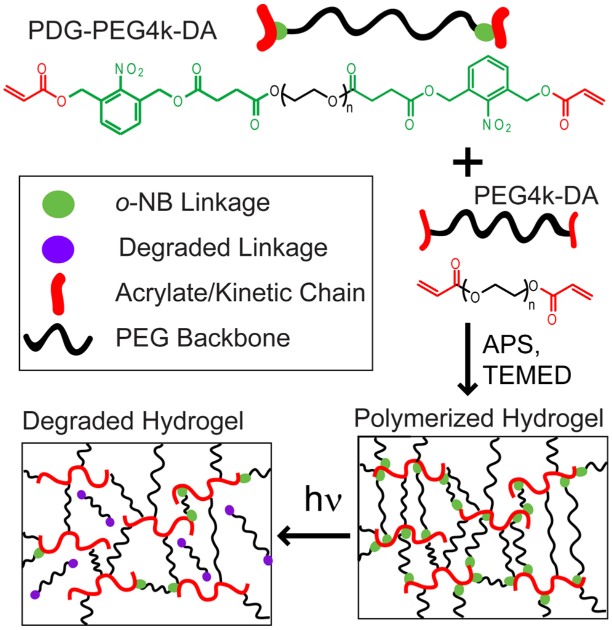

Figure 6.1: **Fabrication of photodegradable hydrogels.**
A combination of photodegradable PDG-PEG4k-DA and non-degradable PEG4k-DA were polymerized by redox-initiated (APS and TEMED) radical chain polymerization into network form. After exposure to light, photodegradable o-NB linkages degrade and the PDG-PEG4k-DA chains are released from the network.

substrate. While hydrogels with very fine feature size and resolution can be produced, direct gradation between fully exposed and non-exposed regions is not possible. Methods have been developed using non-photodegradable hydrogels systems to produce mechanical gradient patterns using a moving photomask,[231, 232] microfluidic techniques,[233] or a peristaltic pump,[234, 235] but these methods produce relatively large gradient sizes (on the order of millimeters) and the gradient strength and shape is difficult to control, thus reducing the potential complexity of the engineered substrate. More recently, researchers have been able to produce smaller mechanical gradient patterns on the order of 50 μm, however, the methods still rely on the physical movement of a photomask.[236] In two-photon lithography, a focused laser beam scans in a raster-like manner. This method is prohibitively slow when degrading a three-dimensional gel. Furthermore, since most current two-photon systems have been designed for confocal microscopy, the software is insufficient for complex three-dimensional photolithography.

As an alternative to physical photomasks and multi-photon patterning, maskless, projection-based lithography, which has been used with photopolymerizable biomaterials to create topological features,[237, 238, 239, 240, 241] offers several advantages. First, lithographic pattern creation only requires an 8-bit grayscale image file, which can be easily, quickly and inexpensively created by most graphics editors. Second, implementation is immediate: image files are directly loaded into the system for use. Thus, a hydrogel with an entirely new degradation pattern can be produced within minutes to hours, rather than waiting days to weeks for a custom physical mask to be manufactured. Third, the degree of degradation is direct: the system imposes a spatial map of crosslink density and matrix stiffness as a function of the input grayscale image's pixel intensity values and their spatial position. This system is not limited to movement of photomasks or controlled mixing to achieve gradation of crosslink density. Fourth, length scales of the resultant lithograph can scale many orders of magnitude. While the system presented here does not produce true 3D patterning like that of two-photon lithography, cells can be cultured in 3D where the projected 2D pattern spans the depth of the sample. Here spatial hydrogel patterning is orthogonal to the direction of light propagation across the sample depth. In this system, the purpose of the patterning is not to produce surface topology, like that of photopolymerized systems, but rather to spatially pattern the material stiffness with limited topology variation. Mask-less photolithography to modulate surface chemistry and mechanical properties allows experimentalists to assay biological response to a variety of conditions in high-throughput compared to traditional soft or hard lithographic techniques.[242, 243, 244, 245, 246, 247, 248] Such an adaptable approach significantly reduces experimental turn-around, and is thus a valuable tool to rapidly assay the biological and material responses to stimuli gradients.[249]

6.3 Materials and Methods

6.3.1 Materials.

2-Nitro-*m*-xylene (Alfa Aesar, 99%), hydrochloric acid (Fisher, concentrated), sodium hydroxide (Fisher, ACS grade), potassium permanganate (Alfa Aesar, 98%), tetrahydrofuran (THF) (EMD, anhydrous, 99.9%, ACS Grade, DriSolv), borane-THF (1M) (Acros), ethyl acetate (Fisher, 99.9%), succinic anhydride, (Alfa Aesar, 99%), 4-(dimethylamino)pyridine (DMAP) (Alfa Aesar, 99%), *N,N*-dimethylformamide (DMF) (BDF, ACS grade), thionyl chloride (Alfa Aesar, 99%), poly(ethylene glycol) (PEG) ($M_n = 4000$ g/mol) (Mallinckrodt), dichlorodimethylsilane (DMDCS) (Sigma 99.5%), di(isopropyl) ethyl amine (Alfa Aesar, 99%), Ammonium persulfate (APS) (Acros Organics, 99%), tetramethylethylenediamine (TEMED) (OmniPur), Dulbecco's Phosphate Buffered Saline (DPBS) (Corning, 1×), and RGD peptide (Ac-GCGYGRGDSPG-NH_2, GenScript) were used as received. Acryloyl chloride (Alfa Aesar, 96% stabilized with 400ppm phenothiazine), and dichloromethane (DCM) (Fisher, 99.9%) were distilled under Ar and stored under Ar in a dry, air-free flask. Triethylamine (TEA) (Omnipur, 99.0%) was distilled under Ar and stored over KOH pellets. MesenPro medium (Invitrogen), bone-marrow derived mesenchymal stem cells (Invitrogen), penicillin-streptomycin-glutamine solution (Invitrogen), slowfade with DAPI (Invitrogen), phalloidin 200 U/mL (Invitrogen), formaldehyde (4%, Boston Bioproducts), and triton-X 100 (invitrogen) were used as received for cell culture. Coverglass (Electron Microscopy Sciences) and micropore filters (0.22μm filter unit, Millex) were used for hydrogel fabrication. The PEG 4000 4-(3-(Acryloyloxymethyl)-2- nitrobenzyloxy)-4-oxobutanoate photo degradable macromer (PDG-PEG4k-DA) was synthesized as described previously.[39] PEG 4000 diacrylate (PEG4k-DA) PEG 4000 was synthesized according to a modified literature procedure.[250]

6.3.2 Chemical Synthesis Techniques.

All reactions were performed under Ar atmosphere using a Schlenk line unless noted otherwise. ^{1}H NMR spectra (δ ppm) were recorded on a Bruker Biospin Ultrashield 300 MHz NMR spectrometer. Unless noted otherwise, all spectra were recorded in $(CD_3)_2SO$ or $CDCl_3$ using tetramethylsilane (TMS) as an internal standard.

Table 6.1: Details of hydrogel compositions.

	20 wt% gel	10 wt% gel	39 wt% gel
Total PEG (wt%)	20%	9.9%	39%
PEG4k-DA (wt%)	10%	2.9%	35%
PDG-PEG4k-DA (wt%)	10%	7.0%	4.3%
APS (wt%)	1.9%	1.9%	1.7%
TEMED (wt%)	0.55%	0.55%	0.50%
RGD (wt%)	n/a	0.24%	n/a

6.3.3 Cover glass salinization.

Coverglass was cleaned with filtered water and methanol, dried, and cleaned with UV-light and ozone (UVO cleaner 42, Jelight Company) for 30 minutes. The activated coverglass was then reacted in a solution of toluene (25mL) and DCDMS (500 μL) for 30 minutes. The coated coverglass was then washed with clean toluene and filtered methanol before drying.

6.3.4 Hydrogel Fabrication.

All hydrogels were fabricated by dissolving PEG4k-DA and PDG-PEG4k-DA in water and radically polymerizing them into network form using solutions of APS and TEMED 6.1. All concentrations are given Table 1. For cell studies, PEG4K-DA was first pre-reacted with a peptide containing the cell binding motif Arg-Gly-Asp (RGD) and a cysteine residue via Michael addition. Solutions of the macromers, APS and TEMED were filtered through a microfilter. The components were combined, vortexed and quickly dispensed between two microscope cover glasses separated by a coverglass spacer (thickness 0.17 mm). The top cover glass was coated with dichlorodimethyl silane. These gels polymerized for 10 min then submersed in water for 30 min before removing the top cover glass. Each hydrogel was then allowed to swell in water at 4^o C overnight before further use.

6.3.5 Hydrogel Lithography.

All photolithography was performed on a SF-100 XPRESS maskless photolithography system (Intelligent Micro Patterning, LLC, St. Petersburg, FL) using its mercury arc lamp light source. For this study, no bandpass filter was used as to accelerate degradation times. Grayscale, 8-bit artworks were constructed in Photoshop or MATLAB. Grayscale light projection was provided by Smart Filter$^{\mathrm{TM}}$ Technology made up of a Digital Micro-Mirror Device (DMD). Hydrogel lithograph size could be controlled by the system objective power (see supporting information) or the artwork size. Exposure conditions for each sample presented here is included in the supporting information.

6.3.6 Cell Culture.

Bone marrow human mesenchymal stem cells at passage 6 were thawed and grown in MesenPro medium (2% serum, 1% penicillin/streptomycin glutamine). Cells were trypsinized and seeded onto substrates, and allowed to incubate and grow overnight at 37^o C, 5% CO_2. Samples were subsequently fixed in warm 4% formaldehyde solution for 15 minutes, and permeabilized in 0.5% triton-X 100. Samples were finally incubated for 20 minutes in 0.2 U/mL phalloidin in PBS at room temperature. Samples were mounted in slowfade with DAPI, and affixed to a glass slide with nail polish for imaging.

6.3.7 Hydrogel and Cell Imaging.

Degraded hydrogels were imaged by a reflected light microscope (LV100 Eclipse, Nikon). Cell-seeded samples were imaged with a Nikon, inverted fluorescent microscope with a 10× objective. Large image areas were captured using an ASI motorized stage (Applied scientific instrumentation). Images were minimally edited through contrast adjustments and a high pass filter for shading correction. Measurements of the cell density as a function of the spatial position along the gradient were performed with a custom algorithm produced with MATLAB. Cell material was segregated from the background by using the phalloidin cytoskeletal stain to produce a binary image of location of cellular material. The binary image was then averaged over the iso-degraded lines to give the cell density as a function of the gradient position. This data was then averaged across the numerous repeated gradient features.

6.3.8 Atomic Force Microscopy.

Surface topography and elastic modulus were measured using Atomic Force Microscopy (AFM) in deionized water using a Bioscope Catalyst AFM (Bruker) in the Nano and Pico Characterization Laboratory at California Nanosystems Institute, UCLA. Images were acquired in peak force tapping mode with MLCT probes (Bruker), tip E or D. For the quantitative measurements of moduli, the spatial sensitivity of the AFM photodetector was first calibrated against a clean glass slide. The spring constant of the cantilever was measured using the thermal tuning method. All AFM force curve analysis was performed with a custom MATLAB algorithm adopted from previously published procedures.[251] The Young's modulus was calculated by using a Sneddon fit with a Poisson's ratio of $\nu = 0.3$.[252] For each sample, the topology, PeakForce error, deformation, and elastic modulus images were collected at a digital resolution of 256 pixels × 256 pixels. AFM images found in Figure 6.4 and Figure 6.5 were edited by subtracting each line by its mean as to remove scan lines. Details for determining the pattern resolution are found in the Supporting Information.

6.4 Results and Discussion

6.4.1 Grayscale "Printing" of Photodegradable Hydrogels.

To demonstrate the use of the maskless lithography system, photodegradable hydrogels were prepared with varying concentrations (Table 1) of the photodegradable PEG 4000 4-(3-(acryloyloxymethyl)-2- nitrobenzyloxy)-4-oxobutanoate macromer (PDG-PEG4k-DA) and PEG 4000 diacrylate (PEG4k-DA) in water. Non-degradable PEG4k-DA was incorporated into the sample to prevent de-gelation and increase the basal stiffness of the gel (Figure 6.1). Figure 6.2 shows the basic schematic of the maskless photolithography procedure. In this technique a UV light source with a band pass filter illuminates a digital micromirror device (DMD). The DMD device uses an array of fluctuating mirrors to spatially regulate the output light intensity of the projected image. A grayscale image is loaded into the system where the image pixel intensity values are transcoded by the DMD into a grayscale pattern. The

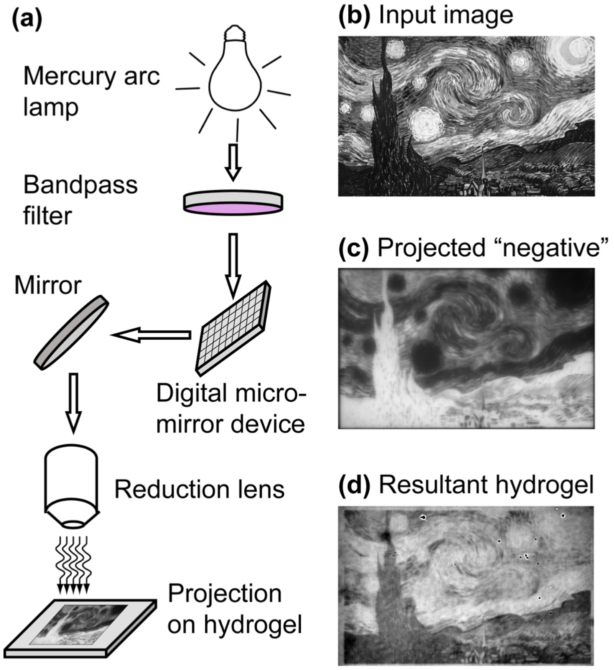

Figure 6.2: **Photolithograpy schematic.**
(a) A schematic of the maskless photolithography process for fabrication of hydrogels with grayscale degradation. (b) An input 8-bit image file is loaded into the system, transcoded by the DMD, and (c) projected down onto the hydrogel surface as a "negative" which gives (d) the resultant hydrogel where the degraded regions absorb more light and appear darker.

patterned light is then directed through a reduction lens as a projection of collimated UV light on the desired surface. Unlike digital movie or presentation projectors, which use an enlarging lens, the maskless lithography system uses a reduction lens to project the image in to a small 1 mm^2 or less area.

The projected pixel and single exposure window size depends on the power of the reduction lens where smallest projected pixel size is 250 nm using a 20× lens. Hence, compared to other lithographic techniques, resolution and feature sizes are not compromised in this system. This allows for hydrogel stiffness to be controllably altered over very small distances. For example, a stiffness gradient can be easily applied across the length of a single cell. Furthermore, many exposure windows can be stitched together to form larger structures on the order of centimeters. To show the capabilities of this system to "print" patterns with length-scales spanning many orders of magnitude, a combination of different input pattern sizes and reduction lens powers was used (Figure 6.3). Figure 6.3a shows a hydrogel de-

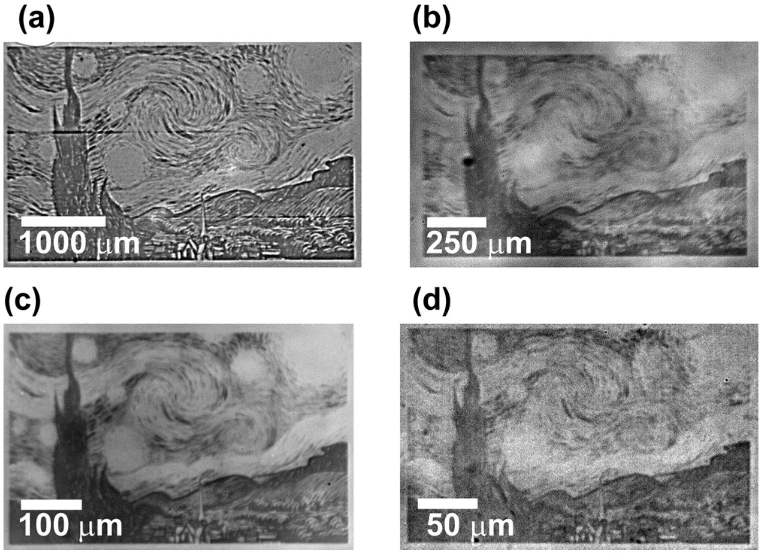

Figure 6.3: **Photolithograpy lengthscales.**
Variation of hydrogel lithograph length scales can be achieved using (a) the 4× reduction lens with nine exposure windows stitched together (3 × 3), or using a single exposure window with the (b) 4× reduction lens (c) 10× reduction lens, and (d) 20× reduction lens. The 20 wt% gel was used for these images.

graded using the 4× lens and is made up of nine exposure windows stitched together. The total pattern size is 3.84 × 2.40 mm. An even greater number of exposure windows can be stitched together with any lens to yield patterns on the order of centimeters. Figure 6.3b, c, and d show hydrogels degraded using the 4×, 10×, and 20× lenses, respectively, but only a single exposure window. As shown in Figure 6.5f, the minimum resolution and feature size achieved is less than a single micron, hence, hydrogel physical properties can be directly patterned across length-scales spanning five order of magnitudes (single microns – tens of centimeters) all within a single substrate and degradation pattern. Any apparent differences in the darkness/brightness/contrast of the degraded hydrogels in Figure 6.3 are attributed to the imaging lens used as well as illumination/shading effects with reflected light microscopy. Furthermore, when using different lenses, the exposure time needs to be calibrated to achieve similar exposure conditions across reduction lens powers (see Supplementary Information for details). For subsequent cell studies, the lens power and exposure conditions were fixed across all samples.

6.4.2 Direct Mechanical Patterning.

To directly characterize the sample material properties, atomic force microscopy (AFM) in PeakForce Tapping^{TM} mode was used. Two different regions of interest (ROI) of the hydrogel lithograph presented in Figure 6.3c were examined and are presented in Figure 6.4: the top of the cypress tree (Figure 6.4a-e) and part of the central spiral (Figure 6.4f-j). Figure 6.4 shows representative input grayscale image (a, f), the resultant hydrogel lithograph (b, g), the peak force error (PFE) images (c, h), the DMT Modulus maps (d, i), and the deformation maps (e,j). The gels presented in Figure 6.4 have the "20 wt%" composition (Figure 6.4). Upon preliminary inspection, it is clear that the degree of degradation—indicated by the shading of the hydrogel in the visible light images (Figure 6.4b, g)—is a function of the original image pixel intensity value Figure 6.4a, f). This patterned degradation is further observed by the PFE (Figure 6.4c, h), which is data derived from the constant force feedback control of the machine and allows for visualization of the stiffness variation—i.e., any contrast indicates a change of substrate stiffness. Here, sharp changes in the substrate modulus are observed to the extent that even individual brushstrokes of the original artwork can be discerned from one another (Figure 6.4f, h). DMT Modulus (Figure 6.4d, i) and deformation maps (Figure 6.4e, j) of the hydrogels were also obtained to better quantify the mechanical environment. The DMT Modulus is the Young's Modulus obtained by fitting the retract force curves using the Derjaguin, Muller, Toropov [253] model and the deformation is the maximum deformation of the sample caused by the probe under a constant force: softer regions will deform more. For these images, data was centered line-by-line around the mean value of each line to reduce misaligned scan lines as to better visualize the change of mechanical environment. Thus, the modulus and deformation values are only relative (absolute stiffness values of this system were measured in the experiment in Figure 6.5 described below). It is clear from these images that in regions of increased degradation, the DMT Modulus decreases and the deformation increases. Again, fine artwork features can be resolved and artwork pixel intensity generally corresponds to a change in the material's local stiffness. The AFM, however, struggles to map modulus and deformation in scanning mode properly on soft (<1MPa, according to the manufacturer), hydrated materials, so the resolution and contrast are noise-limited.

To better understand the quantitative relationship between input image pixel intensity and output gel stiffness, a gradient pattern was produced and exposed on the sample surface in a repeated pattern. Figure 6.5a shows the grayscale photomask used, which is a linear gradient of pixel intensities. Lighter pixels of the photomask correspond to more degradation since the image is inverted during exposure. This pattern is then repeated in a grid-like fashion where each gradient block is $\approx 130 \times 100\mu$m, as shown in a reflected light image of the gel (Figure 6.5b). First, the 20 wt% gel was exposed with the 10× reduction lens (the same gel composition and reduction lens as Figure 6.4). Single indentations were performed with the AFM and the Young's Modulus was calculated (Figure 6.5c) as a function of the position along the gradient. The red box in Figure 6.5b indicates the approximate ROI examined by the AFM. The resultant modulus depends on the input pattern pixel intensities and monotonically decreases from 220.8 ± 1.4 to 151.0 ± 1.1 kPa for this particular gel composition and degradation conditions. From this, the modulus of any grayscale hydrogel lithograph pattern—such as the Starry Night gels shown previously—is assumed to correspond to the input pattern pixel intensities. Next, the experiment above was repeated for a softer gel (10 wt% - Table 1) exhibiting more physiologically/biologically relevant moduli. The 4× reduction lens was used (to match conditions of subsequent cell studies) to expose the repeated gradient pattern. Figure 6.5c shows the Young's Modulus decreases from 52.7 ± 1.6 to 12.9 ± 0.3 kPa as a function of position. This stiffness range has been found to be useful for studying the cell fate in response to substrate stiffness.[1, 2]

6.4.3 Resolution and Feature Size Determination.

After confirming the direct gradient patterning capabilities, the resolution and minimum feature size of this photodegradable hydrogel/maskless lithography system was determined. To do this, a simple photomask was created by alternating white (on/exposed pixels) and black lines (off/non-exposed pixels) of increasing size (Figure 6.5d). Using the 20× lens, the width of a single projected pixel is 0.25μm. For this experiment, the gel density was

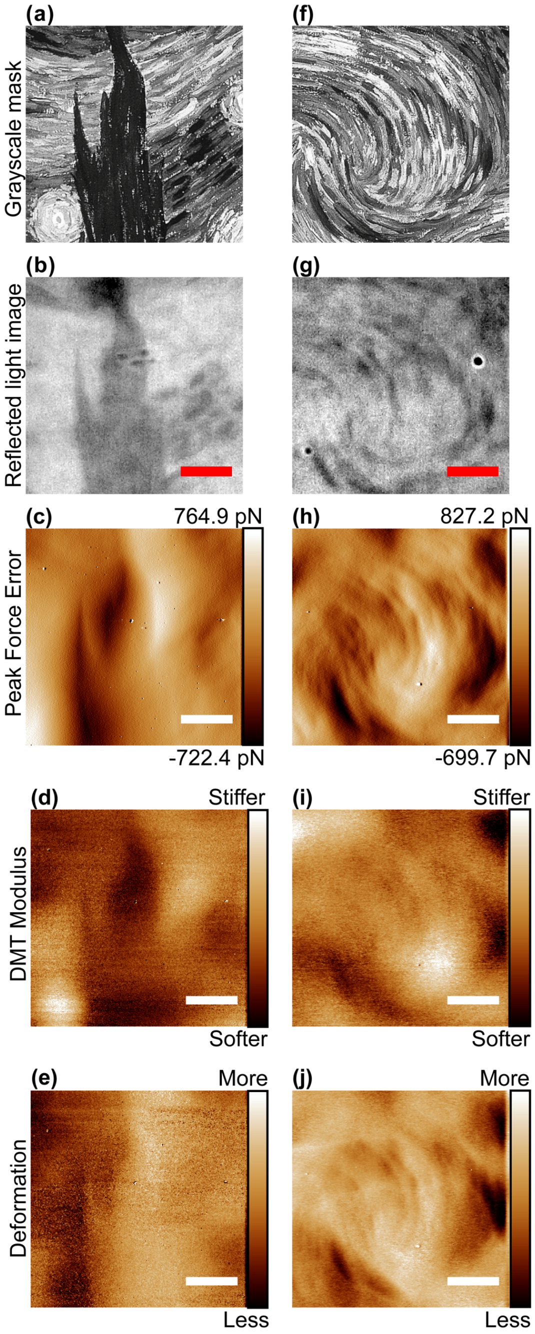

Figure 6.4: **Hydrogel mechanical lithography.**
Selected ROIs of the (a-e) top of the cypress tree and (f-j) central spiral of the Starry Night image. (a, f) Input grayscale images, (b, g) reflected light images, (c, h) the peak force error, (d, i) DMT Modulus, and (e,j) deformation maps of the resultant hydrogel. Scale bars are 30 μm, 20 wt% gels.

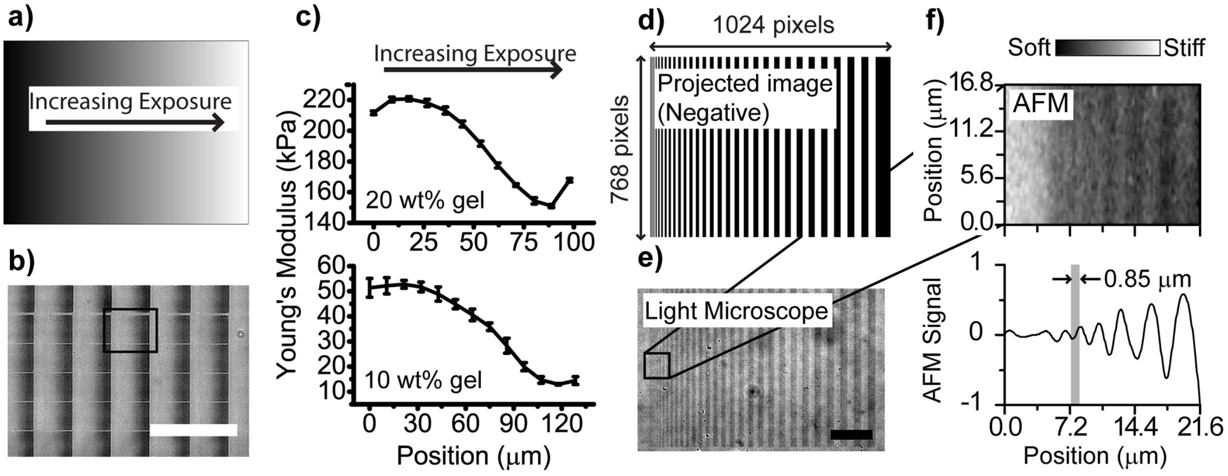

Figure 6.5: **Hydrogel mechanical gradients.**
Stiffness gradients that are created from (a) a linear gradient mask and (b) exposed on a hydrogel's surface in a repeated fashion—scale bar 250 μm. (c) AFM force measurements across the degradation gradient for the 20 and 10 wt% gels. (d) The image negative (projected image) created to test the resolution of this system. Smallest line width is one pixel ($\approx 0.25\mu$m). (e) Reflected light image of the degraded hydrogel—scale bar 50 μm. (f) AFM Young's modulus image of the selected region and the line-spread function of the AFM image showing the variations in modulus. The finest resolution/feature size was measured to be 0.85 μm.

increased to 39 wt% (see Table 1) which increases the modulus of the gel and allows the AFM to better measure the DMT modulus in scanning mode. Figure 6.5e shows a reflected light image of the degraded hydrogel, where lines of decreasing size are clearly observed. To measure the resolution/feature size, the DMT modulus was measured in the region of smallest line sizes (Figure 6.5e—black box) using the AFM in scanning mode (Figure 6.5f). The darker vertical lines of the AFM image correspond to the degraded regions. Data from this image was processed (see Supplementary Information for details) and presented as a line spread function (Figure 6.5f) where the peaks and valleys correspond to the degraded and non-degraded lines. As marked in Figure 6.5f, the smallest distinguishable line size is 0.85μm that corresponds to the three pixel wide line. The following lines were measured to be 1.02, 1.27, 1.61 and 1.86μm which seemingly correspond to the 4, 5, 6, and 7 pixel wide lines, where the size of a single pixel is 0.25μm. The 1 and 2 pixel wide lines apparently merged together and cannot be distinguished in the AFM image.

6.4.4 Influence of Stiffness Gradients on Mesenchymal Stem Cell Response.

Next, the response of human mesenchymal stem cells (hMSCs) to patterned hydrogels was examined (Figure 6.6). Similar to that of Figure 6.5a,b, a repeated linear gradient pattern was used as the input "negative" (Figure 6.6a) and projected down on the hydrogel surface (10 wt% gels, incorporating the cell adhesive RGD peptide motif). The darker, more exposed regions were visualized by reflected light microscopy (Figure 6.6b) and corresponded well to the input projected image. The stiffness of the gradient exposed 10 wt% hydrogels was measured by AFM (Figure 6.5c), as described above, where the measured substrate moduli correlated well with the input image pixel intensities. hMSCs were seeded on the surface of samples with the same composition and exposure conditions as those measured by AFM. The hMSCs were observed to line up orthogonal to the gradient direction (along iso-degraded lines). Simultaneous phase contrast imaging shows the patterned hydrogel underneath where the degraded regions appear raised due to network degradation-induced swelling. Figure 6.6d shows a magnified view of a single gradient pattern with the position of the cells and the superimposed, corresponding stiffness measurements. To align the AFM stiffness measurements with the corresponding degraded hydrogel gradient, the sharp edge of the saw-tooth gradient pattern was lined up with the sharp stiffness transition of the AFM measurements with reasonable accuracy. Furthermore, the size of the modulus gradient observed by AFM directly matches the exposed gradient observed by the phase contrast and reflected light images. Here hMSCs were observed to congregate in the most degraded, softest region of the gel. That is, faced with a choice of moduli ranging from $\approx$ 13-53 kPa, the hMCs preferentially align along the softest region (confirmed via AFM, Figure 6.6d).

To test the lengthscale dependence of this behavior, the size of the gradient pattern was increased. The lengths of the gradients patterns tested were measured to be 1340 μm (Figure 6.6e), 445 μm (Figure 6.6f), 268 μm (Figure 6.6g) and 134 μm (Figure 6.6h). The measured gradient sizes were within 5% of the predicted values given by maskless lithography machine manufacturer. In Figure 6.6e-h, the fluorescently labeled phalloidin cytoskeleton stain is shown to adsorb slightly more in the degraded regions, as confirmed by comparison to

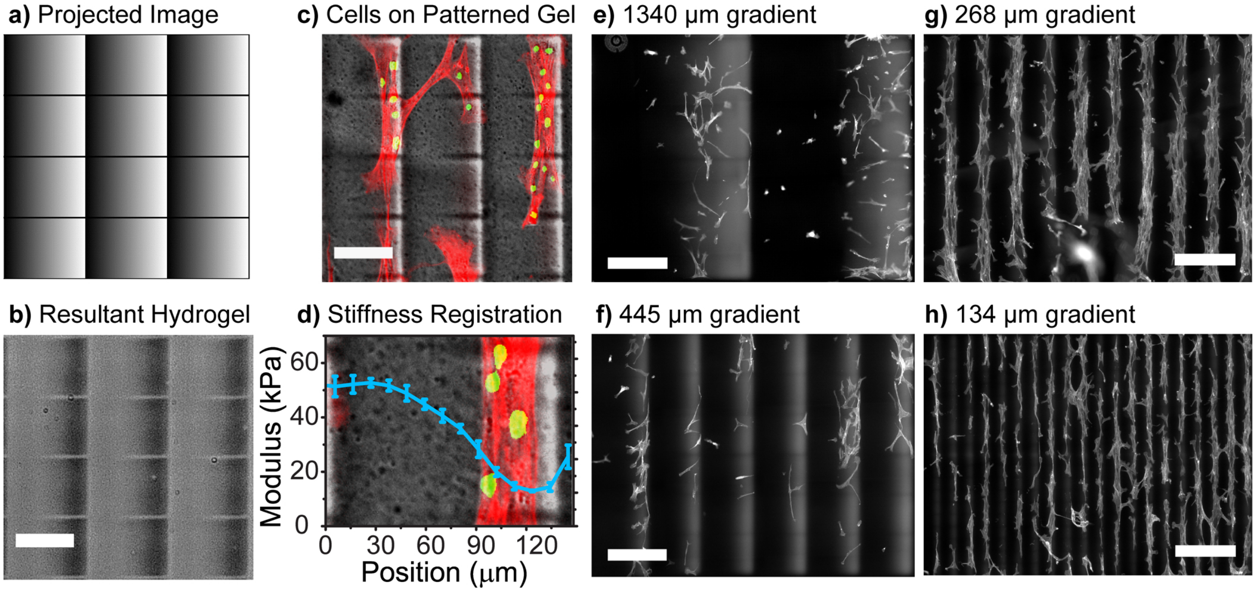

Figure 6.6: **Cell response to mechanical gradients.**
Stiffness gradients that are created from (a) a linear gradient mask and (b) exposed on a hydrogel's surface in a repeated fashion—scale bar 100 μm—(c) were created to test hMSC response—scale bar 100 μm. Phalloidin cytoskeleton staining is labeled in red and DAPI is labeled in green. Phase contrast imaging shows the patterned hydrogel underneath where the degraded regions appear raised due to network degradation-induced swelling. These cells lined up along iso-degraded lines in a position that was both the softest and topologically highest on the hydrogel surface. (d) A close up view of a single gradient pattern with the position of the cells and the superimposed, corresponding stiffness measurements. (e-h) Wide-field images of cell behavior stained with phalloidin—scale bars 500 μm—with pattern sizes of: (e) 1340 μm; (f) 445 μm; (g) 268 μm; and (h) 134 μm.

the phase contrast images. This contrast was used as an indicator of the gradient direction and pattern edges. Importantly, this slight difference in fluorescent molecule adsorption did not affect the cell imaging, but rather, the difference was considered useful background fluorescence. Similar to the cells shown in Figure 6.6c,d, the hMSCs prefer the more degraded regions of the hydrogel. Interestingly the alignment and shape of the cells is a function of the scale: larger gradient sizes show much different behavior than the smaller gradient sizes. When the gradient size is the small ($\cong 134$ μm—Figure 6.6h) the hMSCs lose their ability to exclusively follow the iso-degraded lines and jump across the gradient from one pattern to another, although the cytoskeleton remains aligned orthogonal to the gradient. As the gradient size is increased ($\cong 268$ μm—Figure 6.6g), the cells congregate on iso-degraded lines and do not cross from one gradient to the next. When the gradient size is increased further ($\cong 445$ μm—Figure 6.6f and $\cong 1340$ μm—Figure 6.6e), the hMSCs congregate in the most degraded regions but become more randomly aligned as the pattern becomes larger.

To better understand the spatial distribution and orientation of the cells along the gradient patterns, Figure 6.7 shows a magnified view of the individual, different lengthscale gradient patterns ($\cong 1340$ μm—Figure 6.7a; $\cong 445$ μm—Figure 6.7b; $\cong 268$ μm—Figure 6.7c; $\cong 134$ μm—Figure 6.7d). As shown, the cells congregate in regions with similar degrees of degradation and appear to prefer the more degraded side. In addition the orientation of the cell cytoskeleton as a function of the pattern size is more clearly observed. Arrows within the gradient patterns of Figure 6.7 show the direction of increasing degradation. To quantify this effect, the fraction of surface covered with cell matter was calculated as a function of the spatial position along the gradient pattern (Figure 6.7e). Figure 6.7e shows that the fraction of the surface covered by cells (or cell density) is maximzed in the most degraded region, regardless of the gradient pattern lengthscale. While the magnitude of the cell densities might be different across different lengthscale patterns, the shape of the cell density curves are strikingly similar. This effect shows that the cell adhesion and preference is strongly correlated with the degree of hydrogel degradation. To relate the underlying substrate stiffness to the cell density, the Young's Modulus as a function of the normalized spatial position anlong the gradient, was superimposed over the cell density curves in Figure 6.7e. While the substrate modulus was only measured for the 134 μm gradient pattern, we assume that the shape and magnitude of the gradient modulus maps are largely similar across the different lengthscales. Since the gradient exposure pattern is the same for each lengthscale, only stretched over a larger distance, the corresponding modulus measurements should also be the same. As alluded to above, Figure 6.7e shows a clear pattern of the cell density increasing with decreasing substrate modulus. Here, individual cells are seen to span across distances with significant changes in the hydrogel degradation and modulus. This approach uniquely allows highly controlled gradient creation on the order of the size of a single cell, where a single cell can span a range of modulus on the order of $\approx$ 10 kPa across its body. In fact, across a single $\approx$ 130 μm pattern, we recapitulate a large fraction of microelasticities observed in soft tissues ($\approx$ 10-50 kPa, compared to $\approx$ 1-40 kPa in Discher et al.[200] as well as the modulus range used to differentiate cells as a function of the matrix elasticity ($\approx$ 1-40 kPa in Engler et al.([2])). As demonstrated, this modulus range can be easily modified by changing the exposure conditions and gel composition (Figure 6.5; and supplementary information) Furthermore, no contact guidance of hMSCs in the stiffer grooves was observed as confirmed by an AFM height map (Figure 6.7—softer, more degraded regions swell).

In order to determine how robust the effect of substrate degradation on hMSC behavior is, a large 4096 × 3072 pixel projected image (negative) file containing both linear and curved gradients of differing dimensions was produced and exposed to the surface of a gel to produce a large ($\approx$ 5.5 × 4.0 mm) precisely patterned hydrogel construct (Figure 6.8). Notably, this patterning allows the direct comparison of multiple conditions all on a single hydrogel substrate, which is much more difficult to achieve (rapidly) in traditional masked photolithography. hMSCs were seeded on the surface of the patterned gels, and their behavior was observed (Figure 6.8b). Again, the hMSCs followed the gradient pattern and congregated in the most degraded region (as indicated by the increased background fluorescence of the cytoskeletal stain) even when the path was curved (Figure 6.8c,d—magnified view). When the dimension of the repeated gradient is decreased from 200 μm to 100 μm (right and left side of Figure 6.8a,b, respectively) the hMSCs are able to cross from one gradient square to another (magnified view in Figure 6.8c,d). We cannot attribute a single cause to this unusual

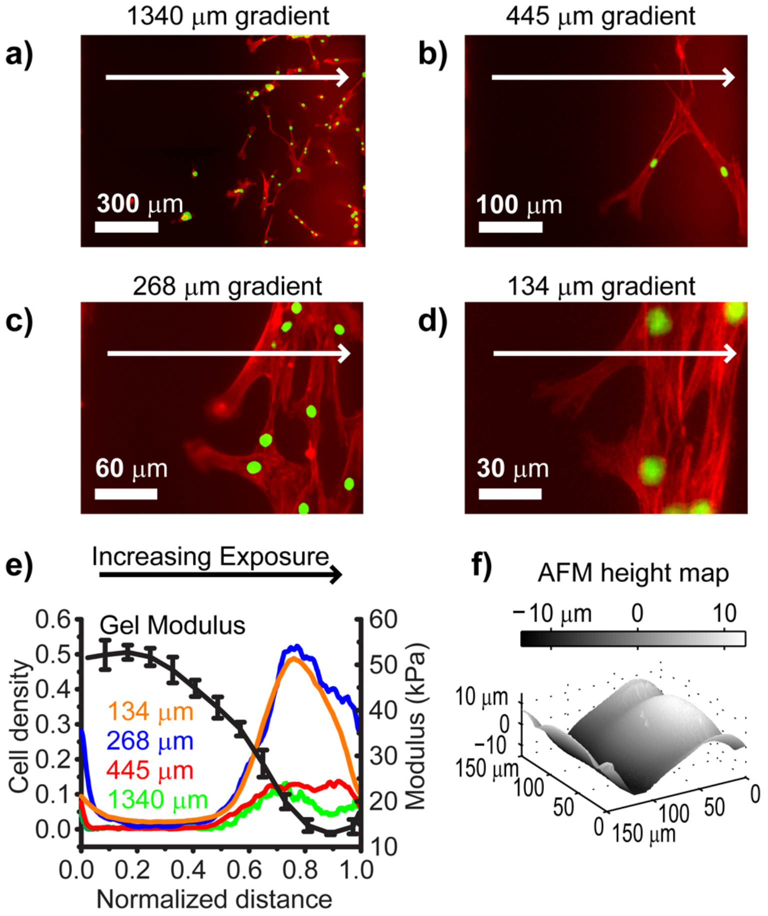

Figure 6.7: **Cell alignment on mechanical gradients.**

(a-d) Magnified imags of the cell behavior of the individual gradient patterns sizes of: (a) 1340 μm; (b) 445 μm; (c) 268 μm; and (d) 134 μm. Cells congregate in the most degraded portion of the pattern as indicated by the arrows. (e) The corresponding cell density is plotted as a function of the normalized spatial position along the gradient with corresponding modulus measurement. (f) An AFM height map showing swelling-induced height changes of the degraded gels (more degradation leads to more swelling.)

behavior, as many factors such as change in gel modulus, geometry, mesh size, cell binding domain accessibility, and protein absorption could influence cell adhesion. Regardless, the effect is both reproducible and robust. We have shown that cells distribute themselves similarly along the gradient pattern regardless of the lengthscale of the gradient. However, cell orientation and spreading are highly correlated to the lenghtscales of patterning.

Typically cells migrate in the direction of greater stiffness[231, 232, 254, 255, 236] (durotaxis) and/or align along topographical grooves, so this result was somewhat unexpected. However, some reports have shown that non-degradable PEG hydrogels with low crosslink density and containing the cell-adhesive RGD peptide sequence promote more cell spreading, migration, and better formation of cellular networks than more highly crosslinked PEG hydrogels.[256] While not directly comparable to the results presented herein (where cells are seeded in 2D) this work also demonstrates that softer networks may provide a better environment for cell attachment and spreading. The authors postulate that cells exploit macroscopic defects or propagate cracks within the mechanically fragile PEG hydrogels. In a 2D cell culture system such as ours, one could then postulate that cells may be able to "dig in" to the softer regions of the hydrogel by exploiting such defects (that is, extend processes slightly below the surface and into the gel), or that the RGD binding domains simply become more accessible for cell binding in a less dense network. Similarly, studies using hMSCs, have also shown that lower gel density leads to better cell spreading and migration.[257, 258]

To this end, pure matrix elasticity[2] may not be the dominating matrix factor in hMSC behavior as demonstrated recently in the literature. Issues such as the viscoelasticity and the cells ability to reorganize the matrix,[259] lamin-A content,[260] the mechanism of cell tethering to the matrix,[261, 262] and construct topology[263] have been identified as potentially influencing cell fate. It is therefore becoming clear that the complex interplay of several factors, and not simply elastic modulus alone, may dictate cell response to its material environment. These discussions about matrix mechanics and other environmental factors, and the widespread interesting in using materials to control cell fate demonstrate the need and importance of a technique such as the one reported here to rapidly and repeatable test multiple conditions.

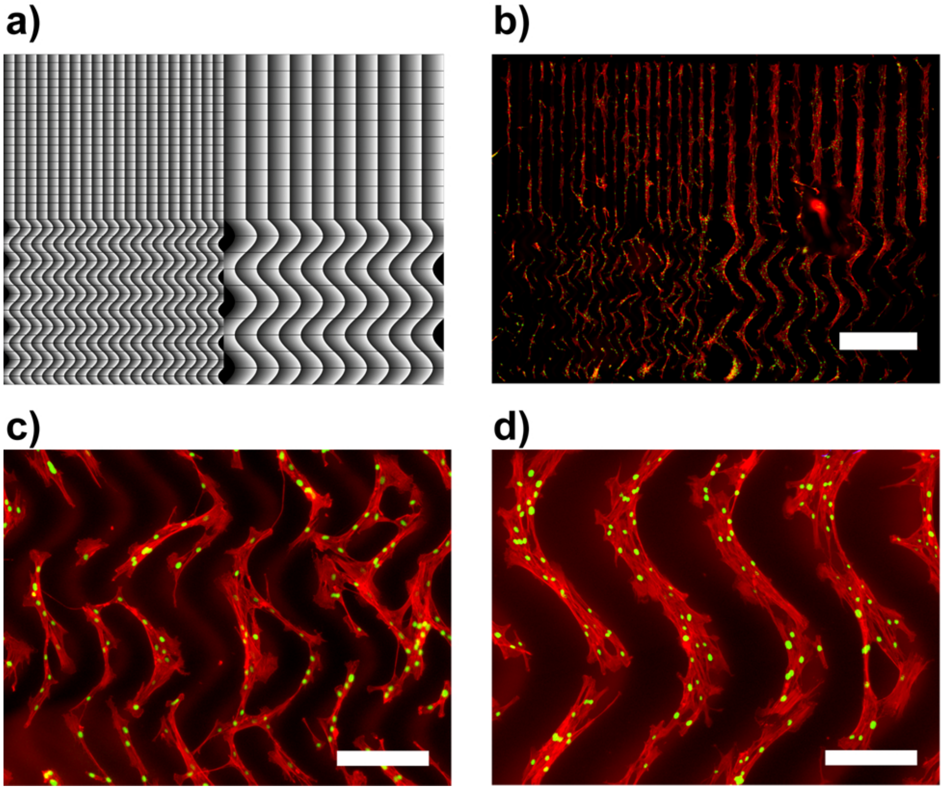

Figure 6.8: **Cell response to curved mechanical gradients.**
(a) A large 4096 × 3072 pixel projected image (negative) file was produced and exposed to the surface of a gel. (b) Subsequent seeded hMSCs behavior was observed—scale bar 1000 μm. (c,d) When the pattern was curved, the hMSC maintain their ability to follow the gradient pattern and congregated in the most degraded region. When the dimension of the repeated gradient is decreased from (d) 268 μm to c) 134 μm the hMSCs are able to cross from one gradient square to another.

6.4.5 Limitations.

Maskless photolithography for hydrogel degradation does have limitations since it uses a projection-based method to expose the sample to light. At short length scales, on the order of ≈100 m, the projected light is relatively collimated. The projected image, however, quickly becomes defocused as the distance from the focal plane is increased. To this end, this method is limited to only two-dimensional variations in degradation. It is not possible to achieve controllable three-dimensional degradation patterns where each projection plane has a different degradation pattern. Such patterning is best implemented using a scanning focused laser beam combined with multi-photon excitation. Additionally, the total time of degradation necessary for large patterns is long compared to traditional mask-based lithography techniques. In traditional photolithography, the entire mask, which can span hundreds of square centimeters in size, can be exposed all at once. With maskless lithography, large images need to be broken down into multiple exposure windows which have to be individually exposed. However, accessibility to traditional photomasks is low, and often requires several weeks to produce an entirely new pattern. The system presented here is immediate, where an entirely new hydrogel with patterned degradation can be produced on the order of hours. Furthermore, system modifications, including higher lamp power, can significantly reduce the degradation time. More importantly, we demonstrate that this technique in combination with our hydrogel gives gradient modulus as a function of the spatial position. This is not accessible with traditional lithography.

6.5 Conclusions

Grayscale projection-based methods for patterning hydrogels are currently utilized due to speed, rapid turn-around, direct gradient capabilities, and the ability to pattern a large range of length scales within a single substrate. In nature, materials of varying properties seamlessly transition from one to another. Replication of such environments requires sophisticated stimuli-responsive materials as well as the tools to induce such environments in a direct and controllable fashion. Moreover, living organisms are made of structures with length scales spanning many orders of magnitude. Macroscopic objects on the order of centimeters, are constructed of smaller structures whose organization is on the order of microns or less. For these reasons, this technique is optimally suited to explore the relationship between cellular systems and their surrounding physical environment. Exploring this cellular behavior is an integral part of our ongoing and future investigations.

6.6 Acknowledgment

Funding for this work was provided by the National Institutes of Health through the NIH Director's New Innovator Award Program, 1-DP2-OD008533. The authors would like to thank Professor Dino Di Carlo for his assistance during discussions and access to his laboratory equipment. The authors would also like to thank Adam Stieg of the Nano & Pico Characterization Lab (NPC) at the California NanoSystems Institute (CNSI) for assistance with atomic force microscopy. All lithography work was performed in the Integrated Systems Nanofabrication Cleanroom (ISNC), CNSI.

6.7 Supporting Information

6.7.1 Exposure Conditions.

Table 6.2: Design Guidelines of the SF-100 as provided by the manufacturer.

	2× Reduction Lens	4× Reduction Lens	10× Reduction Lens	20× Reduction Lens
Maximum Recommended Design Size	6 × 6 inches	6 × 6 inches	4 × 4 inches	4 × 4 inches
Approximate Pixel Size	2.5μm	1.25μm	0.50μm	0.25μm
Single Exposure Window Area	2.56× 1.92 mm	1.28× 0.96 mm	0.512× 0.384 mm	0.256× 0.192 mm

For the hydrogels presented in this paper, certain exposure condition were used. For the 4×, 10×, and 20× reduction lenses of the maskless lithography machine, exposure times of 720 seconds, 240 seconds, and 60 seconds were used, respectively, for each exposure window unless otherwise noted.

For the gradient hydrogels, the 20 wt% gels used the 10× reduction lens and a gradient size of 204 × 147 pixels with the 8-bit grayscale pixel intensities ranging from 0-255. The 10 wt% gels used the 4× reduction lens and a gradient size of 101 × 71 pixels with the 8-bit grayscale pixel intensities ranging from 50-255. The 10 wt% gels used for the cell studies used a variation of gradient sizes and patterns, but the 8-bit grayscale pixel intensities still ranged from 50-255. For the 10 wt% gels, the lower 8-bit pixel intensity of the gradient was raised to 50 since it was noticed that pixel intensity values below that were not substantially degrading the substrate. Since cells were being seeded on top of the gels, the value was raised. The lower 8-bit pixel intensity of the gradient for the 10 wt% gel was raised to match that of the cell studies.

For the cell study, the exposure pattern was composed of a total of 16 exposure windows

(4 × 4) stitched together.

For the 39 wt% hydrogel used for the resolution test, the 20× reduction lens was used with an exposure time of 240 seconds.

6.7.2 Resolution Calculation.

To calculate the resolution of this system, the 20× reduction lens with the 39 wt% gel was used. The DMT modulus from the atomic force microscope (AFM) was collected in scanning mode to find the minimum distances the modulus of the gel could be altered controllably. The DMT modulus image was first corrected by subtracting the mean of each scan line from its self to remove scan line artifacts. The modulus pixel values were then averaged in the vertical direction to get an average modulus value for each exposed line (Figure 6.9a). This averaged line is called the line spread function (LSF) of the hydrogels resolution. The LSF was then processed by two low pass filters (Figure 6.9b) – one to capture background changes in the modulus map, and the other to capture the variations of the modulus caused by the degraded lines. The lower frequency filtered data was then subtracted from the higher frequency filtered data and divided by the lower frequency filtered data (Figure 6.9c,d):

$$\text{Filtered AFM Signal} = \frac{\text{Higher frequency data} - \text{Lower frequency data}}{\text{Lower frequency data}} \tag{6.1}$$

Figure 6.9c shows a series of dips and peaks corresponding to the degraded (lower modulus) and undegraded (higher modulus) regions. The resolution (Figure 6.9e) pattern is constructed such that there are lines of increasing size from left to right: 1 pixel on, 1 pixel off, 2 pixels on, 2 pixels off, 3 pixels on, 3 pixels off, and so on… until all 1024 pixels have been filled. These pixel-based line widths correspond to projected line widths of 0.25μm, 0.50μm, 0.75μm…, respectively using the 20× lens. The distance from a dip to the next peak in Figure 6.9d gives the width of the degraded line. The dip to peak distances recorded in Figure 6.9d correspond to the pixel widths given in Figure 6.9e.

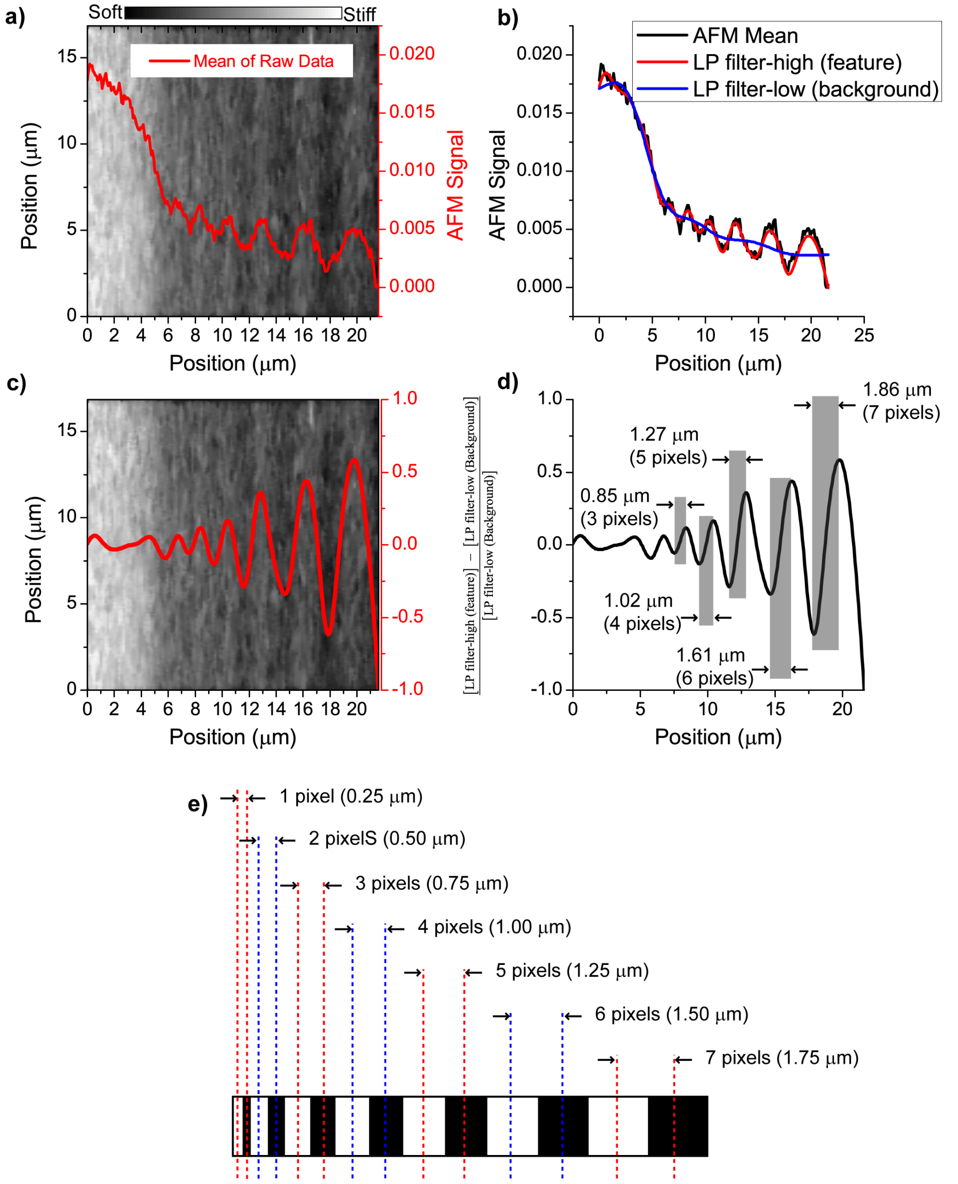

Figure 6.9: **Resolution test.**
(a) AFM modulus image and mean modulus in the vertical direction. (b) mean modulus (black), with low pass filter following substrate features (red) and general background (blue). (c) AFM modulus image with calculated line spread function. (d) Line spread function with corresponding degraded line widths. (e) Pixel distance of input mask and corresponding projected size.

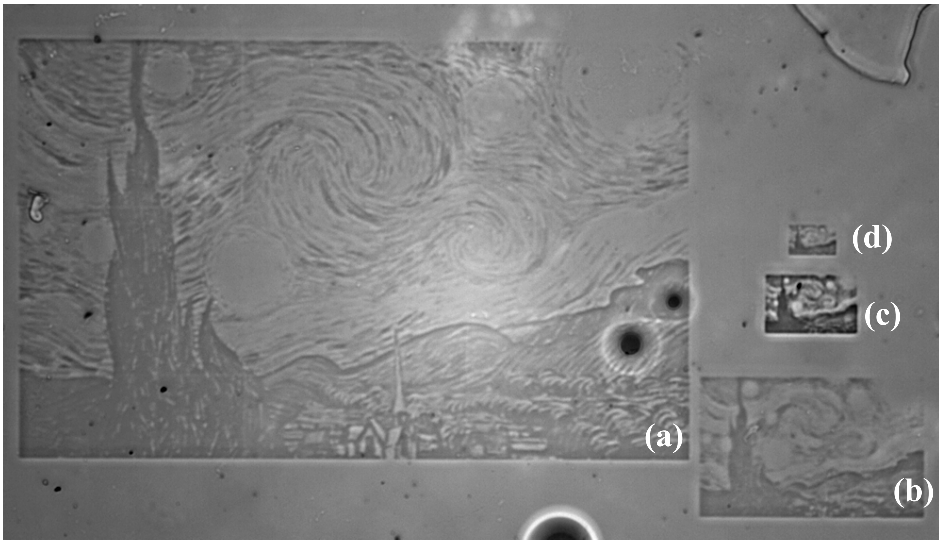

Figure 6.10: **Resolution test.**
(a) Variation of hydrogel lithograph length scales can be achieved using a) the 4× reduction lens with nine exposure windows stitched together (3 × 3), or using a single exposure window with the b) 4× reduction lens c) 10× reduction lens, and d) 20× reduction lens. The 20 wt% gel was used for these images.

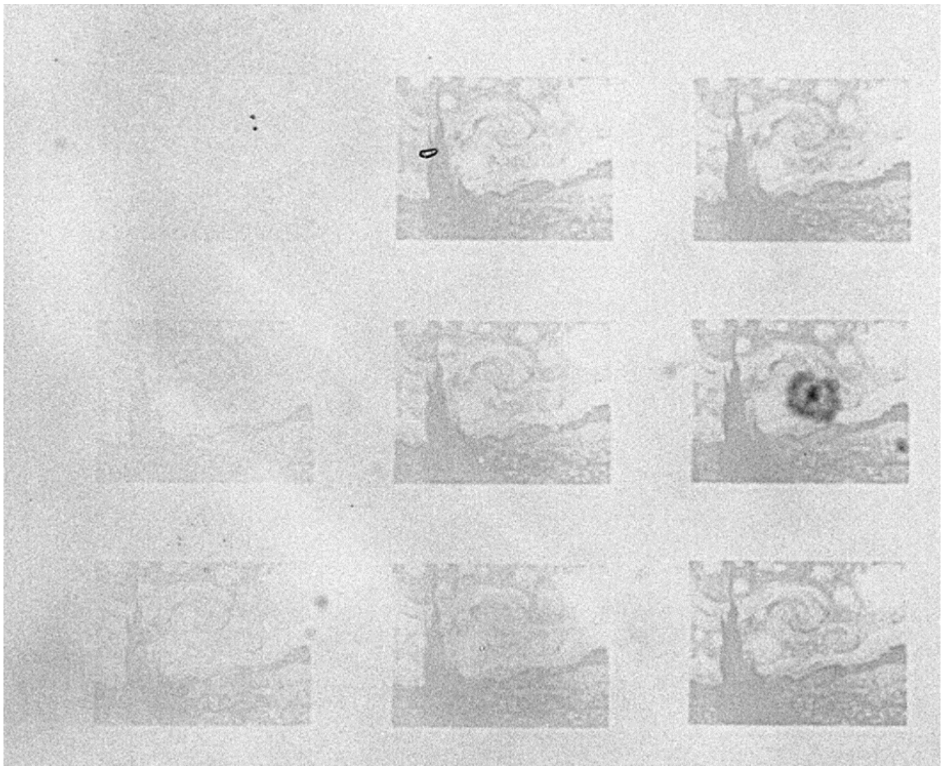

Figure 6.11: **Variation of degradation time.**
Variation of hydrogel lithograph degradation using the 10× reduction lens ranging from 30 to 270 seconds at 30 second intervals. This can be used to calibrate the exposure condition for a particular experimental setup. The 20 wt% gel was used for these images.

CHAPTER 7

Conclusions

7.1 Motivation and Summary

In this dissertation, I looked to reinforce our ability to ask and answer questions in cell biology that are currently inaccessible. By expanding on current photodegradable hydrogel research, I further characterized the networks through mathematical modeling, developed new photodegradable materials to expand the potential applications, and optimized precision patterning techniques of photodegradable hydrogels. Together, I hope that the topics and tools developed in this dissertation will help researchers study and understand fundamental principles of cell biology.

7.1.1 Mathematical modeling of photodegradable hydrogels

In the second and third chapters of this dissertation, I devised mathematical models to better predict how photodegradable polymer networks are formed and subsequently degraded. As cells are sensitive to subtle changes to their physical environment, proper materials characterization to fully understand the mechanical environment is needed. We found that current models of photodegradable hydrogels were not sufficiently detailed in their findings to properly predict and explain the physical properties of photodegradable hydrogels.

In particular, as demonstrated in Chapter 2, we found that diffusion of degradation byproducts during photodegradation severely affected the output properties of the gels, a characteristic that was previously assumed to be negligible. Since the process of free diffusion has both a spatial and temporal component, the exact conditions under which the network is degraded proved highly important (regardless if the total exposure energy density was kept constant.) Parameters such as the time of degradation, spatial dimensions of the gels, and diffusion coefficients of the network strands all played a significant role.

To further explore models of network gelation/degelation, Chapter 3 of this dissertation specifically examined the micro/nano-structure of polymeric gels. More specifically, I examined how micro-regions within the gels are formed during an end-linking process, and how this leads to heterogeneity of the gel microstructure. Many processes in cell biology, from the molecular interactions with the extracellular matrix, to the movement of nutrients and proteins are dependent on the microstructure of their surrounding matrix. Thus, I examined the stochastic nature in which networks are formed to obtain a better picture of gel micro-heterogeneities. We found that simply due to the randomness of network strand end-linking, micro-regions within the gel are high variability in terms of their crosslink density and topology. Adding to the strength of this model, we explored how such micro-regions are affected by the dynamics of end-linking gelation. By controlling the reactivity of the end groups and the ability of the end groups to bind and unbind, we were able to better characterize the heterogeneous topology of polymer network microstates.

7.1.2 Expansion of photodegradable materials

In the next two chapters of this dissertation, I expanded the library of materials that could be used for photodegradable hydrogels. While the existing materials used for photodegradable hydrogels have been revolutionary, many of these materials have not allowed researchers to properly ask questions important in fundamental cell biology. Our ability to asses the complex problems, which we hope photodegradable hydrogels can help solve, have still lacked from a materials standpoint. In this respect I expanded the photodegradable hydrogel toolbox by developing new photodegradable materials.

In Chapter 4 of this dissertation, I developed a protein-based photodegradable hydrogel system . While current photodegradable hydrogels have been sufficient for two-dimensional cell culture, they have not been optimal for three-dimensional culture. Photodegradable hydrogels have been composed of polymers that prevent cells from proliferating and restructuring their surrounding environment. In response, I developed a photodegradable hydrogel made up entirely of natural proteins. Proteins, however, are highly complex and unstable. Slight changes to their structure, charge density, and interaction with water drastically affect their conformation and solubility. We found that when we conjugated nitro-benzyl-based photodegradable moieties to the backbone of gelatin, the protein irreversibly crashed out of aqueous solution. This loss of solubility has prevented protein based materials from being used as photodegradable hydrogels. To counter this issue, I looked to change the charge density, and thus the solubility of the base protein through the addition of a sulfonic acid group. Thus, conjugation of highly hydrophobic groups to the backbone of gelatin was made possible. I explored the photodegradability of gelatin-based gels and three-dimensional culture of cells.

In Chapter 5 of this dissertation I successfully fabricated and demonstrated the applicability of photodegradable polyacrylamide gels. For decades, polyacrylamide hydrogels have been the standard material to study how cells interact with their surrounding physical environment. While tissue-culture plastic has been optimized for cell culture, its material modulus is supraphysiologically stiff and can not be modified. With polyacrylamide-based gels, researchers have been able to study cell behavior on physiologically soft materials. Just as important, polyacrylamide gels have allowed researchers to modify the binding proteins cells interact with. For these reasons, I expanded the use of polyacrylamide gels by incorporating photodegradable linkages that allowed for dynamic tuning of the gel elastic modulus. I first synthesized a set of photodegradable bis-acrylate groups in order to crosslink the linear polyacrylamide chains. Again, the hydrophobicity of the nitro-benzyl moiety made the gel synthesis difficult. I applied a micellar polymerization technique by first solubilizing the photodegradable crosslinkers using a surfactant (sodium dodecyl sulfate). Once soluble, the hydrophobic crosslinkers were easily co-polymerized into the backbone of the polyacrylamide gels. Due to the outstanding flexibility of these gels, I explored cellular response to the dynamic mechanical environment. I showed that, at least for the particular cell type studied, dynamic changes to the matrix mechanical properties, significantly affect cell behavior, beyond that of static material stiffness alone. Since the binding protein attached to the surface of polyacrylamide gels could be readily modified, I also examined the interplay between dynamic material modulus and cell-ligand interaction.

7.1.3 Advanced photolithography of photodegradable hydrogels

In Chapter 6 of this dissertation, I demonstrated the use of maskless photolithography to pattern precise, high-resolution, grayscale patterns into photodegradable hydrogels. Light is highly controllable in both time and space. For hundreds of years, researchers have used light as a method to pattern materials through photo-chemical reactions. Over this time, the techniques and tools of photographic patterning have expanded exponentially, allowing the user extreme control over where, when, and at what intensity light can illuminate a substrate. For these reasons I utilized such advances to pattern our photodegradable hydrogels. The outstanding benefit of photodegradable hydrogels is that the material modulus is a strict function of the degree of exposure. Thus, within the same material, a range of elastic moduli can be patterned in both time and space. Grayscale and gradient patterns can be formed. To accomplish grayscale patterning of photodegradable hydrogels, I used a process termed "maskless photolithography" where a grayscale pattern of light was projected on the gel surface. As a result, I showed that gradients of material modulus can be rapidly patternened into photodegradable hydrogels in a highly controlled fashion, with stiffness patterns at the sub-micron scale. Due to the flexibility of this process, any grayscale image/pattern could be rapidly patterned into the gel, simply by uploading a new bitmap image. Using this combination of materials a lithographic process, I studied how human mesenchymal stem cells responded gradient patterns of different sizes and shapes.

7.2 Future Directions and Outlook

While this dissertation has addressed many challenges that have faced photodegradable hydrogels, numerous unresolved issues and potential applications exist.

7.2.1 Advancing models of gel photodegradation

While the mathematical models devised in this dissertation, examine the intricacies of photodegradable hydrogels, they are still imperfect. For a model to properly predict network properties physical values, such as the modulus E, swelling ratio Q, and network mesh size ξ, should be calculated and tested experimentally. The model I have presented directly calculates the number of respective network strand types (intact, dangling, free), which can be used to estimate these parameters [100]. However, experimental verification still needs to be performed. Furthermore, polymer networks are not ideal, and do not perfectly behave according to theoretical predictions such as the phantom or affine network theory. As networks form, dangling chains and loops of varying degrees form, and negatively impact the networks [136]. A more advanced model should take these factors into account.

During our exploration of how diffusion of photoabsorbing species affects the photodegradation process, we only modeled the problem in one dimension. While this simplification may be appropriate if the networks are uniformly irradiated in the plane orthogonal to the direction of light, any two-dimensional patterns of light will cause the model to progressively break down. Flux of freely diffusing network strands will no longer only move along the path of light, but also in the plane of the gel from more to less degraded regions. Two or three-dimensional models are possible, but require more complicated models and computational power. We also realize that dynamic changes to the gel structure during degradation will affect the degradation kinetics. As degradation proceeds, the mesh size increases and the gel swells more. As a result, polymer network strand diffusion speed increases and becomes spatially heterogeneous. As the network swells, the distances strands need to travel also become longer. Thus an estimation of the diffusion coefficient and volume change as a function of the network degradation should be incorporated.

In the study of gel microstates, I simply looked at the different fractions of network strands states. I did not examine the exact micro-gel topology that was formed, nor did I take into consideration any variance of network strand concentration within the microstate. In real polymer networks, these two factors play a significant role in the gel nano/micro-heterogeneity, and should be considered. Since the Master Equation only calculates the probabilities that certain numbers of different network strands exist, variance of both topology and network strand concentration can be easily incorporated. The Master Equation can also be applied towards modeling the spatial heterogeniety of larger polymer networks. The Master Equation outputs a histogram of microstate probabilities that can be directly interpreted as a histogram of gel microstates spread out in space.

7.2.2 New photodegradable materials

The ultimate purpose of the photodegradable hydrogels developed in this dissertation is to create more complex environments in which we can study cell behavior. By synthesizing photodegradable gelatin gels, my goal was to replicate an environment that more closely resembles the in vivo environment: cells can be cultured in a three-dimensional environment composed of proteins. To study cells in 3D culture is inherently difficult. Cells need to proliferate and restructure their environment. However, during restructuring, the matrix mechanics change. Since the purpose of photodegradable gelatin is to structure and tune the cellular mechanical environment, researchers must take this uncontrolled dynamic interaction into account. While a material such as photodegradable gelatin may be intriguing as a tissue engineering material, it's ability to be used as a material to study fundamental cell biophysics is limited. The techniques developed in this work are also not limited to only attaching photodegradable groups to gelatin. We believe that this work has opened the door towards conjugating a broader range of hydrophobic groups to a breadth of other proteins and polypeptides. In particular, collagen, laminin, elastin, and fibronectin are all structural proteins used to recreate extracellular matricies. Since the structure of these proteins is so conserved, chemical modification, especially with hydrophobic groups (such as photofluors), is difficult. By dictating the placement of charged groups on the protein structure, we hope this limitation will be alleviated.

While we demonstrated the successful production of photodegradable polyacrylamide gels, several improvements should be made in the future. First, the degradation kinetics should be improved. We found that a total of 40 minutes of exposure was needed to produce the range of elastic moduli desired. Although we found that length of degradation did not adversely affect cultured cells, shorter degradation times are preferable for logistic reasons, and to potentially work with more sensitive cell types. We believe that the slow degradation is linked to the clustering of photodegradable groups during micellar polymerization. In addition, gels should ideally be fabricated without the aid of a surfactant. Addition of a surfactant also requires the gels to be washed over a period of days before cell culture, which is inconvenient. Even given these limitation, one of the brightest future applications of this work is the ability to study the complex interplay between mechanical environment and cell adhesion. With the development of photodegradable polyacrylamide gels, the dimension of time-dependent mechanics is possible.

7.2.3 Utilizing photolithographic techniques

Since the purpose of the photodegradable hydrogels developed in this dissertation is to create dynamic and heterogeneous cellular environments, I also sought out the necessary techniques to properly pattern these gels. While I explore and highlight the application of maskless photolithography for hydrogel degradation it is inherently limited since it uses a projection-based method expose the surface of the gels. The patterns created are two-dimensional, thus, full three-dimensional control over the matrix mechanics is not possible. Depending on the application, the speed of degradation using the maskless photolithography technique is also limiting. While in traditional photolithography an entire mask, which can span hundreds of square centimeters, can be exposed all at once, maskless photolithography requires that the sample surface be exposed window by window. Since the window size was only ≈ 1 mm^2 in this study, many degradations are needed to expose a large surface. We expect, however, with increasing popularity of this technique, machines will be developed to expose larger surface areas more rapidly. Despite these limitations, the combination of material and patterning technique is powerful. Cell response to simple high-resolution one-dimensional gradients is still not well studied, especially in three-dimensional culture.

REFERENCES

[1] Discher DE (2005) Tissue Cells Feel and Respond to the Stiffness of Their Substrate. *Science* 310(5751):1139–1143.

[2] Engler AJ, Sen S, Sweeney HL, Discher DE (2006) Matrix Elasticity Directs Stem Cell Lineage Specification. *Cell* 126(4):677–689.

[3] Huebsch N et al. (2010) Harnessing traction-mediated manipulation of the cell/matrix interface to control stem-cell fate. *Nature Materials* 9(6):518–526.

[4] Mikos AG et al. (2006) Engineering Complex Tissues. *Tissue Engineering* 12(12):3307–3339.

[5] Orr AW, Helmke BP, Blackman BR, Schwartz MA (2006) Mechanisms of Mechanotransduction. *Developmental Cell* 10(1):11–20.

[6] Bonnans C, Chou J, Werb Z (2014) Remodelling the extracellular matrix in development and disease. *Nature Reviews Molecular Cell Biology* 15(12):786–801.

[7] Mammoto T, Ingber DE (2010) Mechanical control of tissue and organ development. *Development* 137(9):1407–1420.

[8] Levental KR et al. (2009) Matrix Crosslinking Forces Tumor Progression by Enhancing Integrin Signaling. *Cell* 139(5):891–906.

[9] Acerbi I et al. (2015) Human breast cancer invasion and aggression correlates with ECM stiffening and immune cell infiltration. *Integrative Biology* 7(10):1120–1134.

[10] Paszek MJ et al. (2005) Tensional homeostasis and the malignant phenotype. *Cancer Cell* 8(3):241–254.

[11] Kraning-Rush CM, Califano JP, Reinhart-King CA (2012) Cellular Traction Stresses Increase with Increasing Metastatic Potential. *PLoS ONE* 7(2):e32572.

[12] Geiger B, Spatz JP, Bershadsky AD (2009) Environmental sensing through focal adhesions. *Nature Reviews Molecular Cell Biology* 10(1):21–33.

[13] Reddy KL, Feinberg AP (2013) Higher order chromatin organization in cancer. *Seminars in Cancer Biology* 23(2):109–115.

[14] Kumar S, Weaver VM (2009) Mechanics, malignancy, and metastasis: The force journey of a tumor cell. *Cancer and Metastasis Reviews* 28(1-2):113–127.

[15] Chaudhuri O et al. (2014) Extracellular matrix stiffness and composition jointly regulate the induction of malignant phenotypes in mammary epithelium. *Nature Materials* 13(10):970–978.

[16] Mekhdjian AH et al. (2017) Integrin-mediated traction force enhances paxillin molecular associations and adhesion dynamics that increase the invasiveness of tumor cells into a three-dimensional extracellular matrix. *Molecular Biology of the Cell* 28(11):1467–1488.

[17] Butcher DT, Alliston T, Weaver VM (2009) A tense situation: forcing tumour progression. *Nature Reviews Cancer* 9(2):108–122.

[18] Balestrini JL, Chaudhry S, Sarrazy V, Koehler A, Hinz B (2012) The mechanical memory of lung myofibroblasts. *Integrative Biology* 4(4):410.

[19] Li CX et al. (2017) MicroRNA-21 preserves the fibrotic mechanical memory of mesenchymal stem cells. *Nature Materials* 16(3):379–389.

[20] Nasrollahi S et al. (2017) Past matrix stiffness primes epithelial cells and regulates their future collective migration through a mechanical memory. *Biomaterials* 146:146–155.

[21] Ho SP, Marshall SJ, Ryder MI, Marshall GW (2007) The tooth attachment mechanism defined by structure, chemical composition and mechanical properties of collagen fibers in the periodontium. *Biomaterials* 28(35):5238–5245.

[22] Di Luca A, Van Blitterswijk C, Moroni L (2015) The osteochondral interface as a gradient tissue: From development to the fabrication of gradient scaffolds for regenerative medicine. *Birth Defects Research Part C: Embryo Today: Reviews* 105(1):34–52.

[23] Thesleff I (2008) Tooth organogenesis and regeneration. *StemBook* pp. 1–12.

[24] Yamazaki H, Tsuneto M, Yoshino M, Yamamura KI, Hayashi SI (2007) Potential of Dental Mesenchymal Cells in Developing Teeth. *STEM CELLS* 25(1):78–87.

[25] Volponi AA, Pang Y, Sharpe PT (2010) Stem cell-based biological tooth repair and regeneration. *Trends in Cell Biology* 20(12):715–722.

[26] Khademhosseini A, Langer R (2007) Microengineered hydrogels for tissue engineering. *Biomaterials* 28(34):5087–5092.

[27] Sands RW, Mooney DJ (2007) Polymers to direct cell fate by controlling the microenvironment. *Current Opinion in Biotechnology* 18(5):448–453.

[28] Lutolf MP et al. (2003) Synthetic matrix metalloproteinase-sensitive hydrogels for the conduction of tissue regeneration: Engineering cell-invasion characteristics. *Proceedings of the National Academy of Sciences* 100(9):5413–5418.

[29] Ifkovits JL, Burdick Ja (2007) Review: photopolymerizable and degradable biomaterials for tissue engineering applications. *Tissue engineering* 13(10):2369–2385.

[30] Rajasekharan Pillai VN (1980) Photoremovable Protecting Groups in Organic Synthesis. *Synthesis* 1980(01):1–26.

[31] Patchornik A, Amit B, Woodward RB (1970) Photosensitive protecting groups. *Journal of the American Chemical Society* 92(21):6333–6335.

[32] Bochet CG (2002) Photolabile protecting groups and linkers. *Journal of the Chemical Society, Perkin Transactions 1* (2):125–142.

[33] Nivens DA, Conrad DW (2002) Photoactive Poly(ethylene glycol) Organosilane Films for Site-Specific Protein Immobilization. *Langmuir* 18(2):499–504.

[34] Chiang WY, Lee ML (2003) Synthesis and characterization of novel copolymers of carboxyphenylmaleimide and methacrylates with trimethylsiloxy groups for deep-UV photoresists. *Journal of Applied Polymer Science* 90(4):1032–1037.

[35] Johnson Ja, Finn MG, Koberstein JT, Turro NJ (2007) Synthesis of Photocleavable Linear Macromonomers by ATRP and Star Macromonomers by a Tandem ATRP?Click Reaction:? Precursors to Photodegradable Model Networks. *Macromolecules* 40(10):3589–3598.

[36] Zhao Y et al. (2004) New Caged Coumarin Fluorophores with Extraordinary Uncaging Cross Sections Suitable for Biological Imaging Applications. *Journal of the American Chemical Society* 126(14):4653–4663.

[37] Luo Y, Shoichet MS (2004) A photolabile hydrogel for guided three-dimensional cell growth and migration. *Nature Materials* 3(4):249–253.

[38] Kloxin AM, Kasko AM, Salinas CN, Anseth KS (2009) Photodegradable Hydrogels for Dynamic Tuning of Physical and Chemical Properties. *Science* 324(5923):59–63.

[39] Griffin DR, Kasko AM (2012) Photodegradable Macromers and Hydrogels for Live Cell Encapsulation and Release. *Journal of the American Chemical Society* 134(31):13103–13107.

[40] Wong DY, Ranganath T, Kasko AM (2015) Low-Dose, Long-Wave UV Light Does Not Affect Gene Expression of Human Mesenchymal Stem Cells. *PLOS ONE* 10(9):e0139307.

[41] Ruskowitz ER, DeForest CA (2019) Proteome-wide Analysis of Cellular Response to Ultraviolet Light for Biomaterial Synthesis and Modification. *ACS Biomaterials Science & Engineering* 5(5):2111–2116.

[42] Tibbitt MW, Kloxin AM, Anseth KS (2013) Modeling controlled photodegradation in optically thick hydrogels. *Journal of Polymer Science Part A: Polymer Chemistry* 51(9):1899–1911.

[43] Pasparakis G, Manouras T, Argitis P, Vamvakaki M (2012) Photodegradable Polymers for Biotechnological Applications. *Macromolecular Rapid Communications* 33(3):183–198.

[44] Kloxin AM, Tibbitt MW, Kasko AM, Fairbairn JA, Anseth KS (2010) Tunable Hydrogels for External Manipulation of Cellular Microenvironments through Controlled Photodegradation. *Advanced Materials* 22(1):61–66.

[45] Wong DY, Griffin DR, Reed J, Kasko AM (2010) Photodegradable Hydrogels to Generate Positive and Negative Features over Multiple Length Scales. *Macromolecules* 43(6):2824–2831.

[46] LeValley PJ et al. (2018) Fabrication of Functional Biomaterial Microstructures by in Situ Photopolymerization and Photodegradation. *ACS Biomaterials Science & Engineering* 4(8):3078–3087.

[47] LeValley PJ et al. (2019) Immunofunctional photodegradable poly(ethylene glycol) hydrogel surfaces for the capture and release of rare cells. *Colloids and Surfaces B: Biointerfaces* 174(May 2018):483–492.

[48] Kloxin AM, Benton JA, Anseth KS (2010) In situ elasticity modulation with dynamic substrates to direct cell phenotype. *Biomaterials* 31(1):1–8.

[49] Tibbitt MW, Kloxin AM, Dyamenahalli KU, Anseth KS (2010) Controlled two-photon photodegradation of PEG hydrogels to study and manipulate subcellular interactions on soft materials. *Soft Matter* 6(20):5100.

[50] Rubinstein M, Colby RH (2003) *Polymer Physics.* (Oxford University Press, New York) No. June.

[51] Macosko CW, Miller DR (1976) A New Derivation of Average Molecular Weights of Nonlinear Polymers. *Macromolecules* 9(2):199–206.

[52] Xue C, Wong DY, Kasko AM (2014) Complex Dynamic Substrate Control: Dual-Tone Hydrogel Photoresists Allow Double-Dissociation of Topography and Modulus. *Advanced Materials* 26(10):1577–1583.

[53] Käpylä E, Delgado SM, Kasko AM (2016) Shape-Changing Photodegradable Hydrogels for Dynamic 3D Cell Culture. *ACS Applied Materials & Interfaces* 8(28):17885–17893.

[54] Liao Y et al. (2015) Photoactive Self-Shaping Hydrogels as Noncontact 3D Macro/Microscopic Photoprinting Platforms. *Macromolecular Rapid Communications* 36(24):2129–2136.

[55] Peng K et al. (2011) Dextran based photodegradable hydrogels formed via a Michael addition. *Soft Matter* 7(10):4881.

[56] Kharkar PM et al. (2017) Controlling the Release of Small, Bioactive Proteins via Dual Mechanisms with Therapeutic Potential. *Advanced Healthcare Materials* 6(24):1700713.

[57] McKinnon DD, Brown TE, Kyburz KA, Kiyotake E, Anseth KS (2014) Design and Characterization of a Synthetically Accessible, Photodegradable Hydrogel for User-Directed Formation of Neural Networks. *Biomacromolecules* 15(7):2808–2816.

[58] Rosales AM, Vega SL, DelRio FW, Burdick JA, Anseth KS (2017) Hydrogels with Reversible Mechanics to Probe Dynamic Cell Microenvironments. *Angewandte Chemie International Edition* 56(40):12132–12136.

[59] Kloxin AM et al. (2012) Responsive culture platform to examine the influence of microenvironmental geometry on cell function in 3D. *Integrative Biology* 4(12):1540.

[60] Arakawa CK, Badeau BA, Zheng Y, DeForest CA (2017) Multicellular Vascularized Engineered Tissues through User-Programmable Biomaterial Photodegradation. *Advanced Materials* 29(37):1703156.

[61] Tsang KMC et al. (2015) Facile One-Step Micropatterning Using Photodegradable Gelatin Hydrogels for Improved Cardiomyocyte Organization and Alignment. *Advanced Functional Materials* 25(6):977–986.

[62] Tamura M et al. (2014) Optical cell separation from three-dimensional environment in photodegradable hydrogels for pure culture techniques. *Scientific Reports* 4:1–6.

[63] Truong VX et al. (2015) Photodegradable Gelatin-Based Hydrogels Prepared by Bioorthogonal Click Chemistry for Cell Encapsulation and Release. *Biomacromolecules* 16(7):2246–2253.

[64] Kandow CE, Georges PC, Janmey PA, Beningo KA (2007) Polyacrylamide Hydrogels for Cell Mechanics: Steps Toward Optimization and Alternative Uses. *Methods in Cell Biology* 83(07):29–46.

[65] White EM et al. (2013) Switching the Adhesive State of Catecholic Hydrogels using Phototitration. *Macromolecules* 46(22):8882–8887.

[66] Selen F, Can V, Temel G (2016) Preparation of photodegradable polyacrylamide hydrogels via micellar copolymerization and determination of their phototunable elasticity and swelling behaviors FT-IR analysis :. *RSC Advances* 6:2–4.

[67] Ercole F, Thissen H, Tsang K, Evans RA, Forsythe JS (2012) Photodegradable Hydrogels Made via RAFT. *Macromolecules* 45(20):8387–8400.

[68] Zhu C, Bettinger CJ (2013) Light-Induced Disintegration of Robust Physically Cross-Linked Polymer Networks. *Macromolecular Rapid Communications* 34(18):1446–1451.

[69] Zhu C, Bettinger CJ (2014) Light-induced remodeling of physically crosslinked hydrogels using near-IR wavelengths. *J. Mater. Chem. B* 2(12):1613–1618.

[70] Ninh C, Cramer M, Bettinger CJ (2014) Photoresponsive hydrogel networks using melanin nanoparticle photothermal sensitizers. *Biomaterials Science* 2(5):766.

[71] Zhu C, Bettinger CJ (2015) Photoreconfigurable physically cross-linked triblock copolymer hydrogels: Photodisintegration kinetics and structure-property relationships. *Macromolecules* 48(5):1563–1572.

[72] Zhao D et al. (2018) A photo-degradable injectable self-healing hydrogel based on star poly(ethylene glycol)- b -polypeptide as a potential pharmaceuticals delivery carrier. *Soft Matter* 14(36):7420–7428.

[73] Kloxin AM, Tibbitt MW, Anseth KS (2010) Synthesis of photodegradable hydrogels as dynamically tunable cell culture platforms. *Nature Protocols* 5(12):1867–1887.

[74] Wang H, Haeger SM, Kloxin AM, Leinwand LA, Anseth KS (2012) Redirecting Valvular Myofibroblasts into Dormant Fibroblasts through Light-mediated Reduction in Substrate Modulus. *PLoS ONE* 7(7):e39969.

[75] Elbert DL, Hubbell Ja (2001) Conjugate Addition Reactions Combined with Free-Radical Cross-Linking for the Design of Materials for Tissue Engineering. *Biomacromolecules* 2(2):430–441.

[76] Kirschner CM, Alge DL, Gould ST, Anseth KS (2014) Clickable, Photodegradable Hydrogels to Dynamically Modulate Valvular Interstitial Cell Phenotype. *Advanced Healthcare Materials* 3(5):649–657.

[77] Yang C, Tibbitt MW, Basta L, Anseth KS (2014) Mechanical memory and dosing influence stem cell fate. *Nature Materials* 13(6):645–652.

[78] Yang C et al. (2016) Spatially patterned matrix elasticity directs stem cell fate. *Proceedings of the National Academy of Sciences* 113(31):E4439–E4445.

[79] Lewis KJR et al. (2015) In vitro model alveoli from photodegradable microsphere templates. *Biomaterials Science* 3(6):821–832.

[80] Lewis KJ et al. (2018) Epithelial-mesenchymal crosstalk influences cellular behavior in a 3D alveolus-fibroblast model system. *Biomaterials* 155:124–134.

[81] Norris SCP, Tseng P, Kasko AM (2016) Direct Gradient Photolithography of Photodegradable Hydrogels with Patterned Stiffness Control with Submicrometer Resolution. *ACS Biomaterials Science & Engineering* 2(8):1309–1318.

[82] Hu X, Shi J, Thomas SW (2015) Photolabile ROMP gels using ortho-nitrobenzyl functionalized crosslinkers. *Polym. Chem.* 6(27):4966–4971.

[83] Griffin DR, Kasko AM (2012) Photoselective Delivery of Model Therapeutics from Hydrogels. *ACS Macro Letters* 1(11):1330–1334.

[84] DeForest Ca, Tirrell Da (2015) A photoreversible protein-patterning approach for guiding stem cell fate in three-dimensional gels. *Nature Materials* 14(5):523–531.

[85] de Gracia Lux C et al. (2012) Single UV or Near IR Triggering Event Leads to Polymer Degradation into Small Molecules. *ACS Macro Letters* 1(7):922–926.

[86] Metters AT, Anseth KS, Bowman CN (2000) Fundamental studies of a novel, biodegradable PEG-b-PLA hydrogel. *Polymer* 41(11):3993–4004.

[87] Metters AT, Bowman CN, Anseth KS (2000) A Statistical Kinetic Model for the Bulk Degradation of PLA- b -PEG- b -PLA Hydrogel Networks. *The Journal of Physical Chemistry B* 104(30):7043–7049.

[88] Terrones G, Pearlstein AJ (2001) Effects of Optical Attenuation and Consumption of a Photobleaching Initiator on Local Initiation Rates in Photopolymerizations. *Macromolecules* 34(10):3195–3204.

[89] Terrones G, Pearlstein AJ (2001) Effects of Kinetics and Optical Attenuation on the Completeness, Uniformity, and Dynamics of Monomer Conversion in Free-Radical Photopolymerizations. *Macromolecules* 34(26):8894–8906.

[90] Reddy SK, Cramer NB, Bowman CN (2006) ThiolVinyl Mechanisms. 1. Termination and Propagation Kinetics in ThiolEne Photopolymerizations. *Macromolecules* 39(10):3673–3680.

[91] Reddy SK, Cramer NB, Bowman CN (2006) ThiolVinyl Mechanisms. 2. Kinetic Modeling of Ternary ThiolVinyl Photopolymerizations. *Macromolecules* 39(10):3681–3687.

[92] Terrones G, Pearlstein AJ (2004) Diffusion-Induced Nonuniformity of Photoinitiation in a Photobleaching Medium. *Macromolecules* 37(4):1565–1575.

[93] Andrzejewska E (2001) Photopolymerization kinetics of multifunctional monomers. *Progress in Polymer Science* 26(4):605–665.

[94] Cabral JT, Hudson SD, Harrison C, Douglas JF (2004) Frontal Photopolymerization for Microfluidic Applications. *Langmuir* 20(23):10020–10029.

[95] Hennessy MG, Vitale A, Cabral JT, Matar OK (2015) Role of heat generation and thermal diffusion during frontal photopolymerization. *Physical Review E* 92(2):022403.

[96] Hennessy MG, Vitale A, Matar OK, Cabral JT (2015) Controlling frontal photopolymerization with optical attenuation and mass diffusion. *Physical Review E* 91(6):062402.

[97] Norris SCP et al. (2011) Raster image correlation spectroscopy as a novel tool to study interactions of macromolecules with nanofiber scaffolds. *Acta Biomaterialia* 7(12):4195–203.

[98] Wegscheider R (1923) Articles on the photochemical kinetics. *Zeitschrift fur Physikalische Chemie–Stochiometrie und Verwandtschaftslehre* 103(3/4):273–306.

[99] Lin CC, Metters AT (2006) Hydrogels in controlled release formulations: Network design and mathematical modeling. *Advanced Drug Delivery Reviews* 58(12-13):1379–1408.

[100] Peppas NA, Hilt JZ, Khademhosseini A, Langer R (2006) Hydrogels in Biology and Medicine: From Molecular Principles to Bionanotechnology. *Advanced Materials* 18(11):1345–1360.

[101] De Gennes PG (1979) *Scaling concepts in polymer physics.* (Cornell University Press).

[102] Flory PJ (1953) *Principles of polymer chemistry.* (Cornell University Press).

[103] Stauffer D, Coniglio A, Adam M (1982) Gelation and critical phenomena in *Polymer Networks*, ed. Dušek K. (Springer Berlin Heidelberg, Berlin, Heidelberg), pp. 103–158.

[104] Sangeetha NM, Maitra U (2005) Supramolecular gels: Functions and uses. *Chemical Society Reviews* 34(10):821.

[105] Laftah WA, Hashim S, Ibrahim AN (2011) Polymer Hydrogels: A Review. *Polymer-Plastics Technology and Engineering* 50(14):1475–1486.

[106] Nicolson PC, Vogt J (2001) Soft contact lens polymers: an evolution. *Biomaterials* 22(24):3273–3283.

[107] Hild G (1998) Model networks based on 'endlinking' processes: synthesis, structure and properties. *Progress in Polymer Science* 23(6):1019–1149.

[108] Mark JE, Sullivan JL (1977) Model networks of end-linked polydimethylsiloxane chains. I. Comparisons between experimental and theoretical values of the elastic modulus and the equilibrium degree of swelling. *The Journal of Chemical Physics* 66(3):1006–1011.

[109] Metters AT, Bowman CN, Anseth KS (2000) A Statistical Kinetic Model for the Bulk Degradation of PLA- b -PEG- b -PLA Hydrogel Networks. pp. 7043–7049.

[110] Tonelli AE, Helfand E (1974) Elastically Ineffective Cross-Links in Rubbers. *Macromolecules* 7(1):59–63.

[111] Bibbo MA, Valles EM (1982) Calculation of average properties of the pendant chains in a network. *Macromolecules* 15(5):1293–1300.

[112] Dušek K et al. (2002) Polyurethane networks with controlled architecture of dangling chains. *Macromolecular Chemistry and Physics* 203(13):1936–1948.

[113] Seiffert S (2017) Origin of nanostructural inhomogeneity in polymer-network gels. *Polymer Chemistry* 8(31):4472–4487.

[114] Bastide J, Leibler L (1988) Large-scale heterogeneities in randomly cross-linked networks. *Macromolecules* 21(8):2647–2649.

[115] Ikkai F, Shibayama M (2005) Inhomogeneity control in polymer gels. *Journal of Polymer Science Part B: Polymer Physics* 43(6):617–628.

[116] Kroll D, Croll S (2017) Heterogeneity in polymer networks formed by a single copolymerization reaction: II. Post-gelation structure and pendants. *Polymer* 116:113–123.

[117] Kroll D, Croll S (2015) Influence of crosslinking functionality, temperature and conversion on heterogeneities in polymer networks. *Polymer* 79:82–90.

[118] Balabanyan A, Kramarenko E, Ronova I, Khokhlov A (2005) Monte Carlo study of structure and kinetics of formation of end-linked polymer networks. *Polymer* 46(12):4248–4257.

[119] Gilra N, Cohen C, Panagiotopoulos AZ (2000) A Monte Carlo study of the structural properties of end-linked polymer networks. *The Journal of Chemical Physics* 112(15):6910–6916.

[120] Leung Y, Eichinger BE (1984) Computer simulation of end-linked elastomers. II. Bulk cured tetrafunctional networks. *The Journal of Chemical Physics* 80(8):3885–3891.

[121] Leung Y, Eichinger BE (1984) Computer simulation of end-linked elastomers. I. Trifunctional networks cured in the bulk. *The Journal of Chemical Physics* 80(8):3877–3884.

[122] Hosono N, Masubuchi Y, Furukawa H, Watanabe T (2007) A molecular dynamics simulation study on polymer networks of end-linked flexible or rigid chains. *The Journal of Chemical Physics* 127(16):164905.

[123] Stanford JL, Stepto RFT (1975) Rate theory of irreversible linear random polymrisation. Part 1.—Basic theory. *Journal of the Chemical Society, Faraday Transactions 1: Physical Chemistry in Condensed Phases* 71:1292.

[124] Stanford JL, Stepto RFT, Waywell DR (1975) Rate theory of irreversible linear random polymerisation. Part 2.—Application to intramolecular reaction in A—A + B—B type polymerisations. *Journal of the Chemical Society, Faraday Transactions 1: Physical Chemistry in Condensed Phases* 71:1308.

[125] Ahmad Z, Stepto RFT (1980) Approximate theories of gelation. *Colloid and Polymer Science* 258(6):663–674.

[126] Wang R, Alexander-Katz A, Johnson JA, Olsen BD (2016) Universal Cyclic Topology in Polymer Networks. *Physical Review Letters* 116(18):188302.

[127] Chou T, D'Orsogna MR (2011) Coarsening and accelerated equilibration in mass-conserving heterogeneous nucleation. *Physical Review E* 84(1):011608.

[128] D'Orsogna MR, Lakatos G, Chou T (2012) Stochastic self-assembly of incommensurate clusters. *The Journal of Chemical Physics* 136(8):084110.

[129] Miller DR, Macosko CW (1976) A New Derivation of Post Gel Properties of Network Polymers. *Macromolecules* 9(2):206–211.

[130] Macosko CW, Miller DR (1976) A New Derivation of Average Molecular Weights of Nonlinear Polymers. *Macromolecules* 9(2):199–206.

[131] Norris SCP, Chou T, Kasko AM (2017) Diffusion of Photoabsorbing Degradation Byproducts in Photodegradable Polymer Networks. *Macromolecular Theory and Simulations* 26(4):1700007.

[132] Bowman CN, Kloxin CJ (2012) Covalent Adaptable Networks: Reversible Bond Structures Incorporated in Polymer Networks. *Angewandte Chemie International Edition* 51(18):4272–4274.

[133] Roberts MC, Hanson MC, Massey AP, Karren EA, Kiser PF (2007) Dynamically Restructuring Hydrogel Networks Formed with Reversible Covalent Crosslinks. *Advanced Materials* 19(18):2503–2507.

[134] Yang B et al. (2012) Facilely prepared inexpensive and biocompatible self-healing hydrogel: a new injectable cell therapy carrier. *Polymer Chemistry* 3(12):3235.

[135] Rodell CB, Wade RJ, Purcell BP, Dusaj NN, Burdick Ja (2015) Selective Proteolytic Degradation of Guest–Host Assembled, Injectable Hyaluronic Acid Hydrogels. *ACS Biomaterials Science & Engineering* 1(4):277–286.

[136] Zhong M, Wang R, Kawamoto K, Olsen BD, Johnson JA (2016) Quantifying the impact of molecular defects on polymer network elasticity. *Science* 353(6305):1264–1268.

[137] Guillame-Gentil O et al. (2010) Engineering the Extracellular Environment: Strategies for Building 2D and 3D Cellular Structures. *Advanced Materials* 22(48):5443–5462.

[138] Baroli B (2007) Hydrogels for Tissue Engineering and Delivery of Tissue-Inducing Substances. *Journal of Pharmaceutical Sciences* 96(9):2197–2223.

[139] Fussenegger M et al. (2003) Stabilized Autologous Fibrin-Chondrocyte Constructs for Cartilage Repair in Vivo. *Annals of Plastic Surgery* 51(5):493–498.

[140] Matsusaki M, Yoshida H, Akashi M (2007) The construction of 3D-engineered tissues composed of cells and extracellular matrices by hydrogel template approach. *Biomaterials* 28(17):2729–2737.

[141] Bryant SJ, Nicodemus GD, Villanueva I (2008) Designing 3D Photopolymer Hydrogels to Regulate Biomechanical Cues and Tissue Growth for Cartilage Tissue Engineering. *Pharmaceutical Research* 25(10):2379–2386.

[142] Tibbitt MW, Anseth KS (2009) Hydrogels as extracellular matrix mimics for 3D cell culture. *Biotechnology and Bioengineering* 103(4):655–663.

[143] Möller S, Weisser J, Bischoff S, Schnabelrauch M (2007) Dextran and hyaluronan methacrylate based hydrogels as matrices for soft tissue reconstruction. *Biomolecular Engineering* 24(5):496–504.

[144] Discher DE (2005) Tissue Cells Feel and Respond to the Stiffness of Their Substrate. *Science* 310(5751):1139–1143.

[145] Mikos AG et al. (2006) Engineering Complex Tissues. *Tissue Engineering* 12(12):3307–3339.

[146] Caliari SR, Burdick JA (2016) A practical guide to hydrogels for cell culture. *Nature Methods* 13(5):405–414.

[147] Streeter HB (1987) Fibroblast adhesion to RGDS shows novel features compared with fibronectin. *The Journal of Cell Biology* 105(1):507–515.

[148] Fong E, Tirrell DA (2010) Collective Cell Migration on Artificial Extracellular Matrix Proteins Containing Full-Length Fibronectin Domains. *Advanced Materials* 22(46):5271–5275.

[149] Chaudhuri O et al. (2016) Hydrogels with tunable stress relaxation regulate stem cell fate and activity. *Nature Materials* 15(3):326–334.

[150] Khetan S et al. (2013) Degradation-mediated cellular traction directs stem cell fate in covalently crosslinked three-dimensional hydrogels. *Nature Materials* 12(5):458–465.

[151] Jonker AM, Löwik DWPM, van Hest JCM (2012) Peptide- and Protein-Based Hydrogels. *Chemistry of Materials* 24(5):759–773.

[152] Silva NHCS et al. (2014) Protein-based materials: from sources to innovative sustainable materials for biomedical applications. *Journal of Materials Chemistry B* 2(24):3715.

[153] Aigner T (2003) Collagens—major component of the physiological cartilage matrix, major target of cartilage degeneration, major tool in cartilage repair. *Advanced Drug Delivery Reviews* 55(12):1569–1593.

[154] Scherzer T, Beckert A, Langguth H, Rummel S, Mehnert R (1997) Electron beam curing of methacrylated gelatin. I. Dependence of the degree of crosslinking on the irradiation dose. *Journal of Applied Polymer Science* 63(10):1303–1312.

[155] Van Den Bulcke AI et al. (2000) Structural and Rheological Properties of Methacrylamide Modified Gelatin Hydrogels. *Biomacromolecules* 1(1):31–38.

[156] Benton Ja, DeForest Ca, Vivekanandan V, Anseth KS (2009) Photocrosslinking of gelatin macromers to synthesize porous hydrogels that promote valvular interstitial cell function. *Tissue engineering. Part A* 15(11):3221–3230.

[157] Nichol JW et al. (2010) Cell-laden microengineered gelatin methacrylate hydrogels. *Biomaterials* 31(21):5536–5544.

[158] Yue K et al. (2015) Synthesis, properties, and biomedical applications of gelatin methacryloyl (GelMA) hydrogels. *Biomaterials* 73:254–271.

[159] Klotz BJ, Gawlitta D, Rosenberg AJ, Malda J, Melchels FP (2016) Gelatin-Methacryloyl Hydrogels: Towards Biofabrication-Based Tissue Repair. *Trends in Biotechnology* 34(5):394–407.

[160] Lai TC, Yu J, Tsai WB (2016) Gelatin methacrylate/carboxybetaine methacrylate hydrogels with tunable crosslinking for controlled drug release. *Journal of Materials Chemistry B* 4(13):2304–2313.

[161] Shin SR et al. (2013) Carbon-Nanotube-Embedded Hydrogel Sheets for Engineering Cardiac Constructs and Bioactuators. *ACS Nano* 7(3):2369–2380.

[162] Bertassoni LE et al. (2014) Hydrogel bioprinted microchannel networks for vascularization of tissue engineering constructs. *Lab Chip* 14(13):2202–2211.

[163] Zhao X et al. (2016) Photocrosslinkable Gelatin Hydrogel for Epidermal Tissue Engineering. *Advanced Healthcare Materials* 5(1):108–118.

[164] Annabi N et al. (2017) Engineering a sprayable and elastic hydrogel adhesive with antimicrobial properties for wound healing. *Biomaterials* 139:229–243.

[165] Gauvin R et al. (2012) Microfabrication of complex porous tissue engineering scaffolds using 3D projection stereolithography. *Biomaterials* 33(15):3824–3834.

[166] Loessner D et al. (2016) Functionalization, preparation and use of cell-laden gelatin methacryloyl–based hydrogels as modular tissue culture platforms. *Nature Protocols* 11(4):727–746.

[167] Huang S, Ingber DE (2005) Cell tension, matrix mechanics, and cancer development. *Cancer Cell* 8(3):175–176.

[168] Nelson CM, VanDuijn MM, Inman JL, Fletcher DA, Bissell MJ (2006) Tissue Geometry Determines Sites of Mammary Branching Morphogenesis in Organotypic Cultures. *Science* 314(5797):298–300.

[169] Lu P, Weaver VM, Werb Z (2012) The extracellular matrix: A dynamic niche in cancer progression. *The Journal of Cell Biology* 196(4):395–406.

[170] Vukmirovic-Popovic S et al. (2002) Morphological, histomorphometric, and microstructural alterations in human bone metastasis from breast carcinoma. *Bone* 31(4):529–35.

[171] Davies SR et al. (2008) Expression of the cell to cell adhesion molecule, ALCAM, in breast cancer patients and the potential link with skeletal metastasis. *Oncology reports* 19(2):555–61.

[172] Ruppender NS et al. (2010) Matrix Rigidity Induces Osteolytic Gene Expression of Metastatic Breast Cancer Cells. *PLoS ONE* 5(11):e15451.

[173] Humphrey JD (2008) Vascular Adaptation and Mechanical Homeostasis at Tissue, Cellular, and Sub-cellular Levels. *Cell Biochemistry and Biophysics* 50(2):53–78.

[174] Griffith LG, Swartz MA (2006) Capturing complex 3D tissue physiology in vitro. *Nature Reviews Molecular Cell Biology* 7(3):211–224.

[175] Discher DE, Mooney DJ, Zandstra PW (2009) Growth Factors, Matrices, and Forces Combine and Control Stem Cells. *Science* 324(5935):1673–1677.

[176] Burdick JA, Murphy WL (2012) Moving from static to dynamic complexity in hydrogel design. *Nature Communications* 3(1):1269.

[177] Cui J, Del Campo A (2014) Photo-responsive polymers: properties, synthesis and applications in *Smart Polymers and their Applications*, eds. Aguilar MR, San Román J. (Elsevier), pp. 93–133.

[178] Rosales AM, Anseth KS (2016) The design of reversible hydrogels to capture extracellular matrix dynamics. *Nature Reviews Materials* 1(2):15012.

[179] Brown TE, Anseth KS (2017) Spatiotemporal hydrogel biomaterials for regenerative medicine. *Chemical Society Reviews* 46(21):6532–6552.

[180] Liang Y, Li L, Scott RA, Kiick KL (2017) 50th Anniversary Perspective : Polymeric Biomaterials: Diverse Functions Enabled by Advances in Macromolecular Chemistry. *Macromolecules* 50(2):483–502.

[181] Smith Callahan L (2018) Gradient Material Strategies for Hydrogel Optimization in Tissue Engineering Applications. *High-Throughput* 7(1):1.

[182] Griffin DR, Patterson JT, Kasko AM (2010) Photodegradation as a mechanism for controlled drug delivery. *Biotechnology and Bioengineering* 107(6):1012–1019.

[183] DeForest CA, Anseth KS (2011) Cytocompatible click-based hydrogels with dynamically tunable properties through orthogonal photoconjugation and photocleavage reactions. *Nature Chemistry* 3(12):925–931.

[184] Badeau BA, Comerford MP, Arakawa CK, Shadish JA, DeForest CA (2018) Engineered modular biomaterial logic gates for environmentally triggered therapeutic delivery. *Nature Chemistry* 10(3):251–258.

[185] Tamura M et al. (2015) Click-crosslinkable and photodegradable gelatin hydrogels for cytocompatible optical cell manipulation in natural environment. *Scientific Reports* 5(October):15060.

[186] Hutson CB et al. (2011) Synthesis and Characterization of Tunable Poly(Ethylene Glycol): Gelatin Methacrylate Composite Hydrogels. *Tissue Engineering Part A* 17(13-14):1713–1723.

[187] Romieu A et al. (2008) Postsynthetic Derivatization of Fluorophores with α-Sulfo-β-alanine Dipeptide Linker. Application to the Preparation of Water-Soluble Cyanine and Rhodamine Dyes. *Bioconjugate Chemistry* 19(1):279–289.

[188] Romieu A et al. (2011) N-Fmoc-α-sulfo-β-alanine: a versatile building block for the water solubilisation of chromophores and fluorophores by solid-phase strategy. *Organic & Biomolecular Chemistry* 9(15):5337.

[189] Shirahama H, Lee BH, Tan LP, Cho NJ (2016) Precise Tuning of Facile One-Pot Gelatin Methacryloyl (GelMA) Synthesis. *Scientific Reports* 6(1):31036.

[190] KENCHINGTON AW, WARD AG (1954) The titration curve of gelatin. *The Biochemical journal* 58(2):202–7.

[191] Griffiths PC, Fallis IA, Teerapornchaisit P, Grillo I (2001) Hydrophobically Modified Gelatin and Its Interaction in Aqueous Solution with Sodium Dodecyl Sulfate. *Langmuir* 17(9):2594–2601.

[192] Magdassi S, Kamyshny A, Baszkin1† A (2001) Interfacial Properties of Hydrophobically Modified Biomolecules: Fundamental Aspects and Applications. *Journal of Dispersion Science and Technology* 22(4):313–322.

[193] Matsuda M, Inoue M, Taguchi T (2012) Adhesive properties and biocompatibility of tissue adhesives composed of various hydrophobically modified gelatins and disuccinimidyl tartrate. *Journal of Bioactive and Compatible Polymers* 27(5):481–498.

[194] Taguchi T, Endo Y (2014) Crosslinking Liposomes/Cells Using Cholesteryl Group-Modified Tilapia Gelatin. *International Journal of Molecular Sciences* 15(7):13123–13134.

[195] Yoshizawa K, Taguchi T (2014) Enhanced Bonding Strength of Hydrophobically Modified Gelatin Films on Wet Blood Vessels. *International Journal of Molecular Sciences* 15(2):2142–2156.

[196] Yoon HJ et al. (2016) Cold Water Fish Gelatin Methacryloyl Hydrogel for Tissue Engineering Application. *PLOS ONE* 11(10):e0163902.

[197] Billiet T et al. (2013) Quantitative Contrasts in the Photopolymerization of Acrylamide and Methacrylamide-Functionalized Gelatin Hydrogel Building Blocks. *Macromolecular Bioscience* 13(11):1531–1545.

[198] Bode F et al. (2013) Hybrid gelation processes in enzymatically gelled gelatin: impact on nanostructure, macroscopic properties and cellular response. *Soft Matter* 9(29):6986–6999.

[199] Buxboim A, Ivanovska IL, Discher DE (2010) Matrix elasticity, cytoskeletal forces and physics of the nucleus: how deeply do cells 'feel' outside and in? *Journal of Cell Science* 123(3):297–308.

[200] Discher DE, Mooney DJ, Zandstra PW (2009) Growth factors, matrices, and forces combine and control stem cells. *Science (New York, N.Y.)* 324(5935):1673–1677.

[201] Panciera T, Azzolin L, Cordenonsi M, Piccolo S (2017) Mechanobiology of YAP and TAZ in physiology and disease. *Nature Reviews Molecular Cell Biology* 18(12):758–770.

[202] Jamilah B, Harvinder KG (2002) Properties of gelatins from skins of fish - Black tilapia (Oreochromis mossambicus) and red tilapia (Oreochromis nilotica). *Food Chemistry* 77(1):81–84.

[203] Lo CM, Wang HB, Dembo M, Wang Yl (2000) Cell Movement Is Guided by the Rigidity of the Substrate. *Biophysical Journal* 79(1):144–152.

[204] Dupont S et al. (2011) Role of YAP/TAZ in mechanotransduction. *Nature* 474(7350):179–184.

[205] Norris SCP, Delgado SM, Kasko AM (2019) Mechanically robust photodegradable gelatin hydrogels for 3D cell culture and in situ mechanical modification. *Polymer Chemistry* 10(23):3180–3193.

[206] Denisin AK, Pruitt BL (2016) Tuning the Range of Polyacrylamide Gel Stiffness for Mechanobiology Applications. *ACS Applied Materials & Interfaces* 8(34):21893–21902.

[207] Streeter HB (1987) Fibroblast adhesion to RGDS shows novel features compared with fibronectin. *The Journal of Cell Biology* 105(1):507–515.

[208] Fong E, Tirrell DA (2010) Collective Cell Migration on Artificial Extracellular Matrix Proteins Containing Full-Length Fibronectin Domains. *Advanced Materials* 22(46):5271–5275.

[209] Abdurrahmanoglu S, Can V, Okay O (2009) Design of high-toughness polyacrylamide hydrogels by hydrophobic modification. *Polymer* 50(23):5449–5455.

[210] Dowling KC, Thomas JK (1990) A novel micellar synthesis and photophysical characterization of water-soluble acrylamide-styrene block copolymers. *Macromolecules* 23(4):1059–1064.

[211] Hill A, Candau F, Selb J (1993) Properties of Hydrophobically Associating Polyacrylamides : Influence of the Method of Synthesis. *Macromolecules* 26(17):4521–4532.

[212] Pless DD, Lee YC, Roseman S, Schnaar RL (1983) Specific cell adhesion to immobilized glycoproteins demonstrated using new reagents for protein and glycoprotein immobilization. *The Journal of biological chemistry* 258(4):2340–9.

[213] Norris SCP, Delgado SM, Kasko AM (2019) Mechanically robust photodegradable gelatin hydrogels for 3D cell culture and in situ mechanical modification. *Polymer Chemistry.*

[214] Algi MP, Okay O (2014) Highly stretchable self-healing poly(N,N-dimethylacrylamide) hydrogels. *European Polymer Journal* 59:113–121.

[215] Phillips HM (1981) Method for rapid removal of sodium dodecyl sulfate from polyacrylamide gels. *Analytical Biochemistry* 117(2):398–401.

[216] Poellmann MJ, Wagoner Johnson AJ (2013) Characterizing and Patterning Polyacrylamide Substrates Functionalized with N-Hydroxysuccinimide. *Cellular and Molecular Bioengineering* 6(3):299–309.

[217] Sommer C, Straehle C, Kothe U, Hamprecht FA (2011) Ilastik: Interactive learning and segmentation toolkit. *Proceedings - International Symposium on Biomedical Imaging* pp. 230–233.

[218] Carpenter AE et al. (2006) CellProfiler: image analysis software for identifying and quantifying cell phenotypes. *Genome biology* 7(10):R100.

[219] Petroll MW, Cavanagh DH, Barry P, Andrews P, Jester JV (1993) Quantitative Analysis of Stress Fiber Orientation During Corneal Wound Contraction. *Journal of Cell Science* 104:353–63.

[220] Chaudhuri S, Nguyen H, Rangayyan RM, Walsh S, Frank CB (1987) A Fourier Domain Directional Filtering Method for Analysis of Collagen Alignment in Ligaments. *IEEE Transactions on Biomedical Engineering* BME-34(7):509–518.

[221] Kim A, Lakshman N, Petroll WM (2006) Quantitative assessment of local collagen matrix remodeling in 3-D Culture: The role of Rho kinase. *Experimental Cell Research* 312(18):3683–3692.

[222] Saha K et al. (2010) Surface Creasing Instability of Soft Polyacrylamide Cell Culture Substrates. *Biophysical Journal* 99(12):L94–L96.

[223] Trujillo V, Kim J, Hayward RC (2008) Creasing instability of surface-attached hydrogels. *Soft Matter* 4(3):564.

[224] Pugh C, Fan G, Kasko AM (2005) Measurement of Chain Transfer Constants to Polymer Using Oligomers and Model Compounds: Chain Transfer to Poly[11-(4‘-cyanophenyl-4‘ ‘-phenoxy)undecyl acrylate] in Radical Polymerization. *Macromolecules* 38(19):8071–8077.

[225] Calvet D, Wong JY, Giasson S (2004) Rheological Monitoring of Polyacrylamide Gelation: Importance of Cross-Link Density and Temperature. *Macromolecules* 37(20):7762–7771.

[226] Aragona M et al. (2013) A Mechanical Checkpoint Controls Multicellular Growth through YAP/TAZ Regulation by Actin-Processing Factors. *Cell* 154(5):1047–1059.

[227] Matsui Y, Lai ZC (2013) Mutual regulation between Hippo signaling and actin cytoskeleton. *Protein & Cell* 4(12):904–910.

[228] Wada KI, Itoga K, Okano T, Yonemura S, Sasaki H (2011) Hippo pathway regulation by cell morphology and stress fibers. *Development* 138(18):3907–3914.

[229] Bayan C, Levitt JM, Miller E, Kaplan D, Georgakoudi I (2009) Fully automated, quantitative, noninvasive assessment of collagen fiber content and organization in thick collagen gels. *Journal of Applied Physics* 105(10):102042.

[230] Kloxin AM, Kloxin CJ, Bowman CN, Anseth KS (2010) Mechanical properties of cellularly responsive hydrogels and their experimental determination. *Advanced Materials* 22(31):3484–3494.

[231] Marklein RA, Burdick JA (2010) Spatially controlled hydrogel mechanics to modulate stem cell interactions. *Soft Matter* 6(1):136–143.

[232] Tse JR, Engler AJ (2011) Stiffness Gradients Mimicking In Vivo Tissue Variation Regulate Mesenchymal Stem Cell Fate. *PLoS ONE* 6(1):e15978.

[233] Vincent LG, Choi YS, Alonso-Latorre B, del Álamo JC, Engler AJ (2013) Mesenchymal stem cell durotaxis depends on substrate stiffness gradient strength. *Biotechnology Journal* 8(4):472–484.

[234] Chatterjee K et al. (2010) The effect of 3D hydrogel scaffold modulus on osteoblast differentiation and mineralization revealed by combinatorial screening. *Biomaterials* 31(19):5051–5062.

[235] Nemir S, Hayenga HN, West JL (2010) PEGDA hydrogels with patterned elasticity: Novel tools for the study of cell response to substrate rigidity. *Biotechnology and Bioengineering* 105(3):636–644.

[236] Kidoaki S, Sakashita H (2013) Rectified Cell Migration on Saw-Like Micro-Elastically Patterned Hydrogels with Asymmetric Gradient Ratchet Teeth. *PLoS ONE* 8(10):e78067.

[237] Lu Y, Chen S (2008) Direct write of microlens array using digital projection photopolymerization. *Applied Physics Letters* 92(4):041109.

[238] Lee SA, Chung SE, Park W, Lee SH, Kwon S (2009) Three-dimensional fabrication of heterogeneous microstructures using soft membrane deformation and optofluidic maskless lithography. *Lab on a Chip* 9(12):1670.

[239] Gauvin R et al. (2012) Microfabrication of complex porous tissue engineering scaffolds using 3D projection stereolithography. *Biomaterials* 33(15):3824–3834.

[240] Soman P, Chung PH, Zhang aP, Chen S (2013) Digital microfabrication of user-defined 3D microstructures in cell-laden hydrogels. *Biotechnology and Bioengineering* 110(11):3038–3047.

[241] Zhu W et al. (2015) 3D-Printed Artificial Microfish. *Advanced Materials* 27(30):4411–4417.

[242] Suh KY, Seong J, Khademhosseini A, Laibinis PE, Langer R (2004) A simple soft lithographic route to fabrication of poly(ethylene glycol) microstructures for protein and cell patterning. *Biomaterials* 25(3):557–563.

[243] Théry M, Pépin A, Dressaire E, Chen Y, Bornens M (2006) Cell distribution of stress fibres in response to the geometry of the adhesive environment. *Cell Motility and the Cytoskeleton* 63(6):341–355.

[244] Fink J et al. (2007) Comparative study and improvement of current cell micro-patterning techniques. *Lab on a Chip* 7(6):672.

[245] Rape AD, Guo Wh, Wang Yl (2011) The regulation of traction force in relation to cell shape and focal adhesions. *Biomaterials* 32(8):2043–2051.

[246] Tseng Q et al. (2011) A new micropatterning method of soft substrates reveals that different tumorigenic signals can promote or reduce cell contraction levels. *Lab on a Chip* 11(13):2231.

[247] Tseng P, Judy JW, Di Carlo D (2012) Magnetic nanoparticle–mediated massively parallel mechanical modulation of single-cell behavior. *Nature Methods* 9(11):1113–1119.

[248] Tseng P, Di Carlo D (2014) Substrates with Patterned Extracellular Matrix and Subcellular Stiffness Gradients Reveal Local Biomechanical Responses. *Advanced Materials* 26(8):1242–1247.

[249] Seidi A, Ramalingam M, Elloumi-Hannachi I, Ostrovidov S, Khademhosseini A (2011) Gradient biomaterials for soft-to-hard interface tissue engineering. *Acta Biomaterialia* 7(4):1441–1451.

[250] Cruise GM, Scharp DS, Hubbell Ja (1998) Characterization of permeability and network structure of interfacially photopolymerized poly(ethylene glycol) diacrylate hydrogels. *Biomaterials* 19(14):1287–1294.

[251] Lin DC, Dimitriadis EK, Horkay F (2007) Robust Strategies for Automated AFM Force Curve Analysis—I. Non-adhesive Indentation of Soft, Inhomogeneous Materials. *Journal of Biomechanical Engineering* 129(3):430.

[252] Geissler E, Hecht AM (1981) The Poisson ratio in polymer gels. 2. *Macromolecules* 14(1):185–188.

[253] Derjaguin B, Muller V, Toporov Y (1975) Effect of contact deformations on the adhesion of particles. *Journal of Colloid and Interface Science* 53(2):314–326.

[254] Kuo CHR, Xian J, Brenton JD, Franze K, Sivaniah E (2012) Complex Stiffness Gradient Substrates for Studying Mechanotactic Cell Migration. *Advanced Materials* 24(45):6059–6064.

[255] Plotnikov SV, Pasapera AM, Sabass B, Waterman CM (2012) Force Fluctuations within Focal Adhesions Mediate ECM-Rigidity Sensing to Guide Directed Cell Migration. *Cell* 151(7):1513–1527.

[256] Ehrbar M et al. (2011) Elucidating the Role of Matrix Stiffness in 3D Cell Migration and Remodeling. *Biophysical Journal* 100(2):284–293.

[257] Kyburz Ka, Anseth KS (2013) Three-dimensional hMSC motility within peptide-functionalized PEG-based hydrogels of varying adhesivity and crosslinking density. *Acta Biomaterialia* 9(5):6381–6392.

[258] Blache U et al. (2016) Dual Role of Mesenchymal Stem Cells Allows for Microvascularized Bone Tissue-Like Environments in PEG Hydrogels. *Advanced Healthcare Materials* 5(4):489–498.

[259] Chaudhuri O et al. (2016) Hydrogels with tunable stress relaxation regulate stem cell fate and activity. *Nature Materials* 15(3):326–334.

[260] Swift J et al. (2013) Nuclear Lamin-A Scales with Tissue Stiffness and Enhances Matrix-Directed Differentiation. *Science* 341(6149):1240104–1240104.

[261] Trappmann B et al. (2012) Extracellular-matrix tethering regulates stem-cell fate. *Nature Materials* 11(8):742–742.

[262] Wen JH et al. (2014) Interplay of matrix stiffness and protein tethering in stem cell differentiation. *Nature Materials* 13(10):979–987.

[263] Viswanathan P et al. (2015) 3D surface topology guides stem cell adhesion and differentiation. *Biomaterials* 52:140–147.